

**BLOCKAGE CORRECTIONS FOR DIFFERENT
GEOMETRIES IN ENCLOSED FREE-JET TEST
SECTION OF HIGH ALTITUDE TEST SYSTEM**

**YÜKSEK İRTİFA BENZETİM SİSTEMİNİN KAPALI
SERBEST-JET TEST BÖLÜMÜ İÇERİSİNE
YERLEŞTİRİLEN FARKLI GEOMETRİLER İÇİN
BLOKAJ DOĞRULAMA ÇALIŞMALARI**

HALİL ARSLAN

Assoc. Prof. Dr. Bilsay SÜMER

Dr. Bülent SÜMER

Submitted to

Graduate School of Science and Engineering of Hacettepe University

As a Partial Fulfillment to the Requirements

For the Award of the Degree of Master

In Mechanical Engineering

2021

ABSTRACT

BLOCKAGE CORRECTIONS FOR DIFFERENT GEOMETRIES IN ENCLOSED FREE-JET TEST SECTION OF HIGH ALTITUDE TEST SYSTEM

Halil ARSLAN

Master of Science, Department of Mechanical Engineering

Supervisor: Assoc. Prof. Dr. Bilsay SÜMER

Co-Supervisor: Dr. Bülent SÜMER

September 2021, 145 Pages

High altitude simulation tests are of great importance for missile systems to be tested on the ground in their working altitude pressure environment. These altitude simulation tests of tactical missile systems particularly at supersonic speeds need ‘High Altitude Test System’. The missile systems can be tested in two different ways of external flow over the missile systems using the free-jet nozzle at different Mach numbers and the nozzle of the missile system itself. The ‘HATS’ consists of a test chamber that isolates the test article from the outside atmosphere and simulates the high altitude environment. Typically, the test article is installed inside the test chamber through appropriate support systems. This thesis focused on the effects of blockage of the test articles that have different area ratios for determination of the working characteristics of the ‘HATS’. The blockage ratios were chosen as 8%, 15% and 25% according to the exit area for two different free-jet nozzles, ‘Mach 2 and Mach 2.5’. Vacuum test chamber for different

blockage area ratios has been studied for cold flow conditions with experimental and CFD analyses. Within the framework of the cold flow tests, Schlieren images were recorded with high speed camera and static pressures and temperatures of the test chamber were also be collected. Results from experimental tests and numerical analyses have been compared in terms of both test chamber pressure and Schlieren images. In the first case, the CFD analyses have been performed to simulate the flow conditions inside the modified ‘HATS’ facility without any test article in the test section and in the second case, the CFD analyses have been performed for the test articles inside the test chamber with different blockage areas. The working characteristics of the ‘HATS’ have been determined according to the different blockage ratios by using experimental results and experimental results have been used both as inputs to the CFD analyses and CFD analyses corrections.

Keywords: High Altitude Test System, Test Chamber, Altitude Simulation, Blockage, CFD Analysis, Schlieren Imaging

ÖZET

YÜKSEK İRTİFA BENZETİM SİSTEMİNİN KAPALI SERBEST-JET TEST BÖLÜMÜ İÇERİSİNE YERLEŞTİRİLEN FARKLI GEOMETRİLER İÇİN BLOKAJ DOĞRULAMA ÇALIŞMALARI

Halil ARSLAN

Yüksek Lisans, Makina Mühendisliği Bölümü

Tez Danışmanı: Doç. Dr. Bilsay SÜMER

Eş Danışman: Dr. Bülent SÜMER

Eylül 2021, 145 Sayfa

Yüksek irtifa benzetim testleri, füze sistemlerinin çalışma irtifa basınç ortamlarında yerde test edilmesi için büyük önem arz etmektedir. Taktik füze sistemlerinin özellikle süpersonik hızlarda yapılan bu irtifa simülasyon testleri, “Yüksek İrtifa Test” sistemine ihtiyaç duymaktadır. Test düzeneğinin serbest-jet lülesi kullanılarak farklı Mach sayılarında füze sistemlerine dış akış sağlanmasıyla ve füze sistemlerinin kendi lülelerinin test düzeneği içerisinde test edilmesiyle iki farklı şekilde test imkanı bulunmaktadır. “Yüksek İrtifa Benzetim Sistemi”, içerisinde konulan test kalemini dış atmosfer koşullarından izole ederek, irtifa koşulunu benzeten test odasından oluşmaktadır. Test edilecek kalem bu test odasına uygun bağlantı elemanları yardımıyla sabitlenmektedir. Bu tez kapsamında, benzetim sisteminin çalışma karakteristiğini belirlemek amacıyla, farklı kesit alanlarına sahip test kalemlerinin blokajlarının etkileri

incelenmektedir. İki farklı serbest-jet lülesi, '2 Mach ve 2.5 Mach' için; blokaj oranları her bir lülenin lüle çıkış kesit alanına göre %8, %15 ve %25 olarak seçilmektedir. Vakum test odası, tüm bu farklı blokaj test kalemleri için soğuk hava koşullarında hem deneysel hem de "Hesaplamalı Akışkanlar Dinamiği" analizleri yardımıyla çalışılmaktadır. Deneysel testler kapsamında, hızlı kamera ile Schlieren görüntüleri kaydedilmekte, test odası statik basınç ve sıcaklık değerleri ölçülmektedir. Deneysel testler ve nümerik analizlerden elde edilen sonuçlar hem test odası basıncı hem de Schlieren görüntüleri kapsamında karşılaştırılmaktadır. "Hesaplamalı Akışkanlar Dinamiği" analizleri ilk olarak test odasında herhangi bir blokaj olmadığı durumda yapılmaktadır. Daha sonra, farklı blokaj oranlarındaki test kalemlerinin test odasına yerleştirilmiş durumları için tekrar edilmektedir. "Yüksek İrtifa Benzetim Sistemi"nin deneysel testlerden elde edilen sonuçlara göre çalışma karakteristiği belirlenmekte ve deneysel testlerden elde edilen bu sonuçlar hem "Hesaplamalı Akışkanlar Dinamiği" analizlerine girdi olarak kullanılmakta hem de analiz sonuçlarının doğrulanmasında kullanılmaktadır.

Anahtar Kelimeler: Yüksek İrtifa Benzetim Sistemi, Test Odası, İrtifa Benzetimi, Blokaj, Hesaplamalı Akışkanlar Dinamiği Analizi, Schlieren Görüntüleme

ACKNOWLEDGMENTS

First, I would like to express my deep and sincere gratitude to my thesis supervisor, Assoc. Prof. Dr. Bilsay SÜMER for giving me the opportunity to study and providing invaluable guidance throughout this study. It was a great privilege and honor to study under his guidance.

Also, I would like to thank to my thesis co-supervisor, Dr. Bülent SÜMER for sharing his experience and providing all kinds of convenience.

And my special thanks to Mr. Bora YAZICI for his great contributions, invaluable efforts during both the experimental and numerical process and discussion on the subject during the preparation of this thesis.

I would like to say thanks to my friends and colleagues for their constant encouragement. I express my special thanks to Mr. Mustafa PELİT, Mr. Mahmut DOĞRUDİL and Mr. Ataman AYDOĞDU for their genuine support throughout this thesis. I also would like to thank to the technicians of the facility, Mr. Ali İhsan AKBAŞ and Mr. Mehmet Fatih BOZYİĞİT for their great efforts to install the experimental test setup.

I am extremely grateful to my parents for their love, caring and sacrifices for educating and preparing me for my future. My special thanks go to my sister for her support and the keen interest shown to complete this thesis successfully.

Finally, my thanks go to all the people who have supported me to complete this thesis directly or indirectly.

TABLE OF CONTENTS

ABSTRACT	i
ÖZET	iii
ACKNOWLEDGMENTS	v
TABLE OF CONTENTS.....	vi
LIST OF FIGURES	viii
LIST OF TABLES	xii
SYMBOLS AND ABBREVIATIONS	xiv
1. INTRODUCTION	1
1.1. Motivation	1
1.2. High Altitude Test System	2
1.2.1. Test Chamber and Diffuser System	3
1.2.3. Ejector System	5
1.3. Literature Survey	7
2. EXPERIMENTAL INVESTIGATION	20
2.1. Introduction	20
2.2. Experimental Test Setup	20
2.2.1. TÜBİTAK-SAGE HATS Setup.....	21
2.2.2. Test Articles and Support Design	22
2.2.3. Measurements	25
2.2.3.1. Pressure.....	26
2.2.3.2. Temperature	26
2.2.3.3. Mass Flow Rate.....	27
2.2.3.4. Schlieren Imaging.....	27
2.2.4. Mach 2.5 Free-Jet Nozzle Design	30
2.3. Experimental Results	35
2.3.1. Experimental Data from Tests	42
3. NUMERICAL INVESTIGATION	45
3.1. Introduction	45

3.2. Governing Equations	45
3.3. Turbulence Model.....	47
3.4. Solution Domain.....	49
3.4.1. Fluent CFD Solver Setup	53
3.4.2. Grid Sensitivity	54
3.5. Numerical Results.....	57
3.6. Comparison of the Experimental and Numerical Results	73
3.6.1. Test Chamber Pressure	73
3.6.2. Schlieren Imaging	83
4. CONCLUSION AND FUTURE STUDY	103
4.1. Conclusion.....	103
4.2. Future Study	105
5. REFERENCES.....	106
APPENDIX.....	108
1 - Test Setup and Measurement Locations	108
2 - Atmospheric Pressure Data.....	110
3 - Test Matrix.....	111
4 - Experimental Data from Tests	113

LIST OF FIGURES

Figure 1-1. HATS with Ejector Diffuser System.	2
Figure 1-2. Enclosed Free-Jet Test Section.	3
Figure 1-3. Detailed View of the Test Chamber.	4
Figure 1-4. Ejector System with Own Separate Nozzle.	5
Figure 1-5. Operation Modes of the Ejector System [4].	6
Figure 1-6. Design Procedure of HATS [5].	7
Figure 1-7. Solution Domain and Boundary Conditions for Test Section of HATS [5]. .	7
Figure 1-8. Subscaled Rocket Test Article [5].	8
Figure 1-9. Free-Jet Nozzle-Diffuser System Installation Concepts [8].	9
Figure 1-10. High Temperature Hypersonic Gas Dynamics Facility [9].	10
Figure 1-11. Schlieren Images of Some Typical Test Articles [9].	10
Figure 1-12. Effect of Test Article on Test Chamber Static Pressure [9].	11
Figure 1-13. Test Results and Blockage Effect on Test Chamber Pressure [3].	11
Figure 1-14. Test Chamber Pressure for Ideal and Real Gas Modelled Ejectors [3].	12
Figure 1-15. Test Article and Supporting Mechanism [10].	12
Figure 1-16. Minimum Test Chamber Pressure Limits: (a) Jet Plume Limit, (b) Base Flow Limit [10].	13
Figure 1-17. Sketch of a High Altitude Test System Facility [11].	14
Figure 1-18. Boundary Conditions for Ejector System [11].	14
Figure 1-19. Boundary Conditions for Diffuser System [12].	15
Figure 1-20. Performance of Simple Cylindrical Ejector-Diffuser System [13].	16
Figure 1-21. Schematics of Refinements to Cylindrical Ejector-Diffuser System [13].	16
Figure 1-22. P6.2 Cold Gas Subscale Test Facility [14].	17
Figure 1-23. Color Schlieren Images of a Free-Jet Nozzle [14].	18
Figure 1-24. Test Section Diffuser Pressure [15].	19
Figure 2-1. Test Section Side View.	20
Figure 2-2. Test Section Isometric View.	20
Figure 2-3. TÜBİTAK-SAGE Test Setup.	21
Figure 2-4. von Karman Nosecone Geometry.	23
Figure 2-5. Optical Scanning Result.	24
Figure 2-6. Test Article and Placement Inside the Test Chamber.	24

Figure 2-7. Test Chamber Pressure and Temperature Sensors.	25
Figure 2-8. Kistler 4260A Piezoresistive Pressure Transducer.	26
Figure 2-9. K-Type Thermocouple.	26
Figure 2-10. SAGE 200 Thermal Mass Flow Meter.	27
Figure 2-11. Sketch of a Schlieren System [16].	27
Figure 2-12. Schlieren Image for Three Different Cutoffs: (a) Pinhole, (b) Knife-Edge Adjusted in Vertical, (c) Knife-Edge Adjusted in Horizontal [16].	28
Figure 2-13. Installation of Schlieren System in the Test Setup.	29
Figure 2-14. One-Dimensional Nozzle Flow.	30
Figure 2-15. Mach 2.5 Free-Jet Nozzle.	32
Figure 2-16. Closer View to the Grid.	33
Figure 2-17. Mach Number Distribution at the Free-Jet Nozzle Exit Plane.	33
Figure 2-18. Contour Plot of Mach Number on the Symmetry Plane.	34
Figure 2-19. Ejector Nozzle Feed Manifold Pressure.	35
Figure 2-20. Test Section Diffuser-Ejector Nozzle Feed Manifold Connection Pressure.	36
Figure 2-21. Vacuum Pressure vs. Mass Flow Rate.	37
Figure 2-22. Test Section Diffuser Pressure.	38
Figure 2-23. Test Chamber Pressure vs. Free-Jet Nozzle Mass Flow Rate [Mach 2]. ...	38
Figure 2-24. Test Chamber Pressure vs. Free-Jet Nozzle Mass Flow Rate [Mach 2.5].	39
Figure 2-25. Test Chamber Pressure vs. Free-Jet Nozzle Inlet Pressure [Mach 2].	39
Figure 2-26. Test Chamber Pressure vs. Free-Jet Nozzle Inlet Pressure [Mach 2.5].	40
Figure 2-27. Test Chamber Pressure vs. Blockage Area Ratio [Mach 2].	40
Figure 2-28. Test Chamber Pressure vs. Blockage Area Ratio [Mach 2.5].	41
Figure 2-29. Test Chamber Pressure.	42
Figure 2-30. Free-Jet Nozzle Air Mass Flow Rate.	43
Figure 2-31. Free-Jet Nozzle Inlet Pressure.	43
Figure 2-32. Test Chamber and Ejector Nozzle Inlet Temperature.	44
Figure 3-1. Solution Domain of the Test Chamber without Blockage Test Article and Boundary Conditions.	49
Figure 3-2. Solution Domain of the Test Chamber with Blockage Test Article and Boundary Conditions.	50
Figure 3-3. Half Model Solution Domain.	50

Figure 3-4. Closer View to the Grid of the Test Chamber and Mach 2.5 Free-Jet Nozzle without Blockage.	51
Figure 3-5. Closer View to the Grid of the Test Chamber for Mach 2.5 Free-Jet Nozzle with 8% Blockage.	52
Figure 3-6. Closer View to the Grid of the Test Chamber for Coarse Grid.	54
Figure 3-7. Closer View to the Grid of the Test Chamber for Medium Grid.	54
Figure 3-8. Closer View to the Grid of the Test Chamber for Fine Grid.	54
Figure 3-9. Test Chamber Pressure vs. Grid Count.	55
Figure 3-10. Mach Number Variation Along the X-Axis Throughout the Solution Domain and Mach Number Contour Plots for Coarse, Medium and Fine Grids. ...	56
Figure 3-11. Static Pressure Contour Plots for Mach 2.5 Free-Jet Nozzle.	58
Figure 3-12. Mach Number Contour Plots for Mach 2.5 Free-Jet Nozzle.	59
Figure 3-13. Static Temperature Contour Plots for Mach 2.5 Free-Jet Nozzle.	60
Figure 3-14. Static Pressure Contour Plots [Mach 2 - 750 g/s].	61
Figure 3-15. Static Pressure Contour Plots [Mach 2 - 1100 g/s].	61
Figure 3-16. Static Pressure Contour Plots [Mach 2 - 1500 g/s].	62
Figure 3-17. Static Pressure Contour Plots [Mach 2 - 1900 g/s].	62
Figure 3-18. Mach Number Contour Plots [Mach 2 - 750 g/s].	63
Figure 3-19. Mach Number Contour Plots [Mach 2 - 1100 g/s].	63
Figure 3-20. Mach Number Contour Plots [Mach 2 - 1500 g/s].	64
Figure 3-21. Mach Number Contour Plots [Mach 2 - 1900 g/s].	64
Figure 3-22. Static Temperature Contour Plots [Mach 2 - 750 g/s].	65
Figure 3-23. Static Temperature Contour Plots [Mach 2 - 1100 g/s].	65
Figure 3-24. Static Temperature Contour Plots [Mach 2 - 1500 g/s].	66
Figure 3-25. Static Temperature Contour Plots [Mach 2 - 1900 g/s].	66
Figure 3-26. Static Pressure Contour Plots [Mach 2.5 - 750 g/s].	67
Figure 3-27. Static Pressure Contour Plots [Mach 2.5 - 1300 g/s].	67
Figure 3-28. Static Pressure Contour Plots [Mach 2.5 - 1500 g/s].	68
Figure 3-29. Static Pressure Contour Plots [Mach 2.5 - 1900 g/s].	68
Figure 3-30. Mach Number Contour Plots [Mach 2.5 - 750 g/s].	69
Figure 3-31. Mach Number Contour Plots [Mach 2.5 - 1300 g/s].	69
Figure 3-32. Mach Number Contour Plots [Mach 2.5 - 1500 g/s].	70
Figure 3-33. Mach Number Contour Plots [Mach 2.5 - 1900 g/s].	70

Figure 3-34. Static Temperature Contour Plots [Mach 2.5 - 750 g/s].....	71
Figure 3-35. Static Temperature Contour Plots [Mach 2.5 - 1300 g/s].....	71
Figure 3-36. Static Temperature Contour Plots [Mach 2.5 - 1500 g/s].....	72
Figure 3-37. Static Temperature Contour Plots [Mach 2.5 - 1900 g/s].....	72
Figure 3-38. Test Chamber Pressure Sensor Locations.....	73
Figure 3-39. Comparison of the Test Chamber Pressure for Mach 2.5 and 15% Blockage Ratio.....	74
Figure 3-40. Experimental vs. Numerical Test Chamber Pressure.	75
Figure 3-41. Sketch of the Test Rhombus for Mach 2 and 2.5 Free-Jet Nozzles.	83
Figure 3-42. Sketch of Positioning the Test Article Inside the Test Chamber [10].....	84
Figure 3-43. Example Comparison of the Schlieren Images and Shock Angles.	85
Figure 3-44. Experimental vs. Numerical Schlieren Image [Test-5].	86

LIST OF TABLES

Table 1-1. Specifications of the Test Facility.	17
Table 2-1. Test Setup Main Parts List.	22
Table 2-2. Test Article Dimensions.....	23
Table 2-3. Measuring Equipment of the Test Setup.....	25
Table 2-4. Equipment of Schlieren System.	29
Table 2-5. Inputs for Mach 2.5 Free-Jet Nozzle Design.....	31
Table 2-6. Mass Flow Rate vs. Pressure [Mach 2 Free-Jet Nozzle].	37
Table 2-7. Mass Flow Rate vs. Pressure [Mach 2.5 Free-Jet Nozzle].....	37
Table 3-1. CFD Solver Setup.	53
Table 3-2. Boundary Conditions for Grid Sensitivity Analysis.	55
Table 3-3. Mach Cone Angle for Mach 2 and 2.5 Free-Jet Nozzles.....	83
Table 3-4. Experimental vs. Numerical Schlieren Image [Test-1].	87
Table 3-5. Experimental vs. Numerical Schlieren Image [Test-2].	87
Table 3-6. Experimental vs. Numerical Schlieren Image [Test-3].	88
Table 3-7. Experimental vs. Numerical Schlieren Image [Test-4].	88
Table 3-8. Experimental vs. Numerical Schlieren Image [Test-5].	89
Table 3-9. Experimental vs. Numerical Schlieren Image [Test-6].	89
Table 3-10. Experimental vs. Numerical Schlieren Image [Test-7].....	90
Table 3-11. Experimental vs. Numerical Schlieren Image [Test-8].....	90
Table 3-12. Experimental vs. Numerical Schlieren Image [Test-9].....	91
Table 3-13. Experimental vs. Numerical Schlieren Image [Test-10].....	91
Table 3-14. Experimental vs. Numerical Schlieren Image [Test-11].....	92
Table 3-15. Experimental vs. Numerical Schlieren Image [Test-12].....	92
Table 3-16. Experimental vs. Numerical Schlieren Image [Test-13].....	93
Table 3-17. Experimental vs. Numerical Schlieren Image [Test-14].....	93
Table 3-18. Experimental vs. Numerical Schlieren Image [Test-15].....	94
Table 3-19. Experimental vs. Numerical Schlieren Image [Test-16].....	94
Table 3-20. Experimental vs. Numerical Schlieren Image [Test-17].....	95
Table 3-21. Experimental vs. Numerical Schlieren Image [Test-18].....	95
Table 3-22. Experimental vs. Numerical Schlieren Image [Test-19].....	96
Table 3-23. Experimental vs. Numerical Schlieren Image [Test-20].....	96

Table 3-24. Experimental vs. Numerical Schlieren Image [Test-21].	97
Table 3-25. Experimental vs. Numerical Schlieren Image [Test-22].	97
Table 3-26. Experimental vs. Numerical Schlieren Image [Test-23].	98
Table 3-27. Experimental vs. Numerical Schlieren Image [Test-24].	98
Table 3-28. Experimental vs. Numerical Schlieren Image [Test-25].	99
Table 3-29. Experimental vs. Numerical Schlieren Image [Test-26].	99
Table 3-30. Experimental vs. Numerical Schlieren Image [Test-27].	100
Table 3-31. Experimental vs. Numerical Schlieren Image [Test-28].	100
Table 3-32. Experimental vs. Numerical Schlieren Image [Test-29].	101
Table 3-33. Experimental vs. Numerical Schlieren Image [Test-30].	101
Table 3-34. Experimental vs. Numerical Schlieren Image [Test-31].	102
Table 3-35. Experimental vs. Numerical Schlieren Image [Test-32].	102

SYMBOLS AND ABBREVIATIONS

Symbols

γ	Specific Heat Ratio
R_u	Universal Gas Constant
T	Temperature
P	Pressure
P_{ex}	Nozzle Exit Pressure
P_v	Vacuum Pressure
P_c	Test Chamber Pressure
P_{amb}	Ambient Pressure
\dot{m}	Mass Flow Rate
D_{th}	Nozzle Throat Diameter
D_{ex}	Nozzle Exit Diameter
A_{th}	Nozzle Throat Area
A_{ex}	Nozzle Exit Area
MW	Molecular Weight
ρ	Density
k	Turbulent Kinetic Energy
I	Turbulence Intensity
U	Mean Velocity
ω	Specific Turbulence Dissipation Rate
μ	Dynamic Viscosity
S_m	Mass Source
\vec{F}	External Body Force
\vec{g}	Gravitational Acceleration

$\bar{\tau}$	Stress Tensor
k	Conductivity
J_j	Diffusion Flux of Species
S_h	Volumetric Heat Source
E	Energy
u'	Root-Mean-Square of the Turbulence Velocity Fluctuations
Re	Reynolds Number
C_f	Skin Friction Coefficient
τ_{wall}	Wall Shear Stress
M	Mach Number
θ	Mach Cone Angle

Abbreviations

BR	Blockage Ratio
CFD	Computational Fluid Dynamics
CSPM	Color Schlieren Photography Method
ER	Entrainment Ratio
HATS	High Altitude Test System
MOC	Method of Characteristics
PIV	Particle Image Velocimetry
RANS	Reynolds Averaged Navier Stokes
TÜBİTAK-SAGE	The Scientific and Technological Research Council of Turkey Defense Industries Research and Development Institute

1. INTRODUCTION

1.1. Motivation

High Altitude Test System, 'HATS' has an important role to simulate the flight atmospheric conditions for aircrafts and missile systems by creating pressure of desired test altitude for ground level testing especially at supersonic speeds. Simulation of the atmospheric pressure is the main focus of the test system and the simulation of the temperature is achieved by other relatively simple solutions like using heat sources to produce the aimed heat flux [1].

High altitude testing is performed simply in two alternative ways in the sense of simulating vacuum pressure environment of different altitudes. First, nozzle itself can be tested in ground level that are used in missile systems or orbital movements of satellites and high altitude vehicles. Second, the aerodynamic tests can be executed using the free-jet nozzle to supply external flow over the test articles. Free-jet nozzles are designed for different Mach number test conditions. For both purposes, it is desired that the exit area of the nozzle used should be as high as possible. And any flow separation on the divergent section of the supersonic nozzles are not desired. Nozzle full flow condition must be satisfied while maintaining the vacuum pressure environment. Thus, larger nozzles and larger test articles can be tested in the vacuum pressure atmospheric environment on the ground.

A 'High Altitude Test System' has been previously designed in TÜBİTAK-SAGE without taking into account the blockage effect of the test articles that shall be tested inside the test chamber [2]. The main motivation of this thesis study is to study the effect of the blockage due to predefined test articles, which have different blockage ratios, by using experimental and numerical methods. The blockage effect has been studied for two different Mach numbers with three different test articles. It is shown that the blockage effect of the test articles changes working characteristics of the HATS.

1.2. High Altitude Test System

The main purpose of the ‘High Altitude Test System’ is to fulfill the requirement of the nozzle full-flow situation without any separation at the free-jet nozzle exit by maintaining the free-jet nozzle exit pressure equal or higher than the test chamber pressure. HATS shall generate this adequate low pressure situation inside the test chamber for performing high altitude testing flight situation [2]. HATS basically consists of an air storage tank, an air heater to heat the air before the free-jet nozzle, a test chamber for placing the test articles inside and a system for reducing pressure inside the test chamber to a determined value for successful operation of the free-jet nozzle. In order to create the aimed pressure levels inside the test section, an ‘Ejector Diffuser System’ is used which is given in Figure 1-1 schematically.

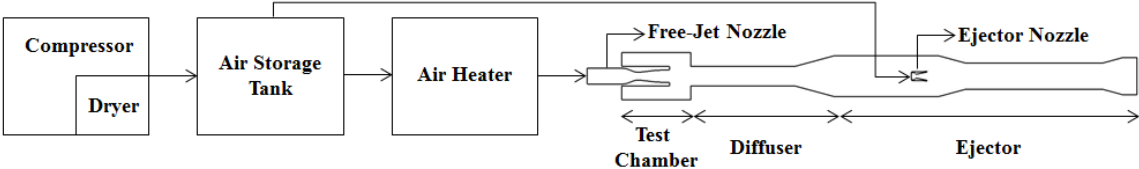


Figure 1-1. HATS with Ejector Diffuser System.

The ‘Ejector Diffuser System’ is opened to the atmosphere. Ejector is employed to pull air out of the test chamber. The test article is placed inside the test chamber through a supporting mechanism. The test articles like cones, hemisphericals or special nosecone geometries that have different blockage area ratios can be tested inside the test chamber at different test chamber pressure conditions.

1.2.1. Test Chamber and Diffuser System

Test section shown in Figure 1-2 is called as 'Enclosed Free-Jet Test Section' or 'Open Test Section' based on the structure of the free-jet nozzle and diffuser system.

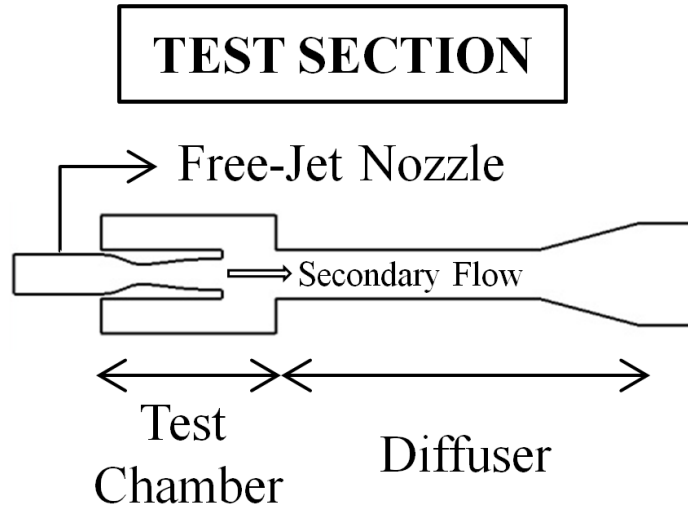


Figure 1-2. Enclosed Free-Jet Test Section.

The size of the test chamber does not affect the test setup performance at steady state operation, but it only matters in the transition period. So, the size of the test chamber is first defined in the design process of the HATS facility according to the test articles and measurement instrumentation requirements like Schlieren imaging or high speed camera usage. Once the size of the test chamber is determined by the prementioned considerations, the diffuser inlet area has to be stated. The higher diffuser inlet area means use of nozzles with larger exit area or lower test chamber pressure for nozzles with the same exit area. The basic design of the diffuser is called as constant-area exhaust diffuser system as shown in Figure 1-2. This system can also be used without ejector system after it. There is also another type of the diffuser system that is called second throat exhaust diffuser system. Both of the diffuser systems only use the momentum of the exhaust of the rocket nozzles or free-jet nozzles to lower the test chamber pressure.

Pressure and temperature data are collected by using proper meters installed up on the wall of the test chamber given in Figure 1-3.

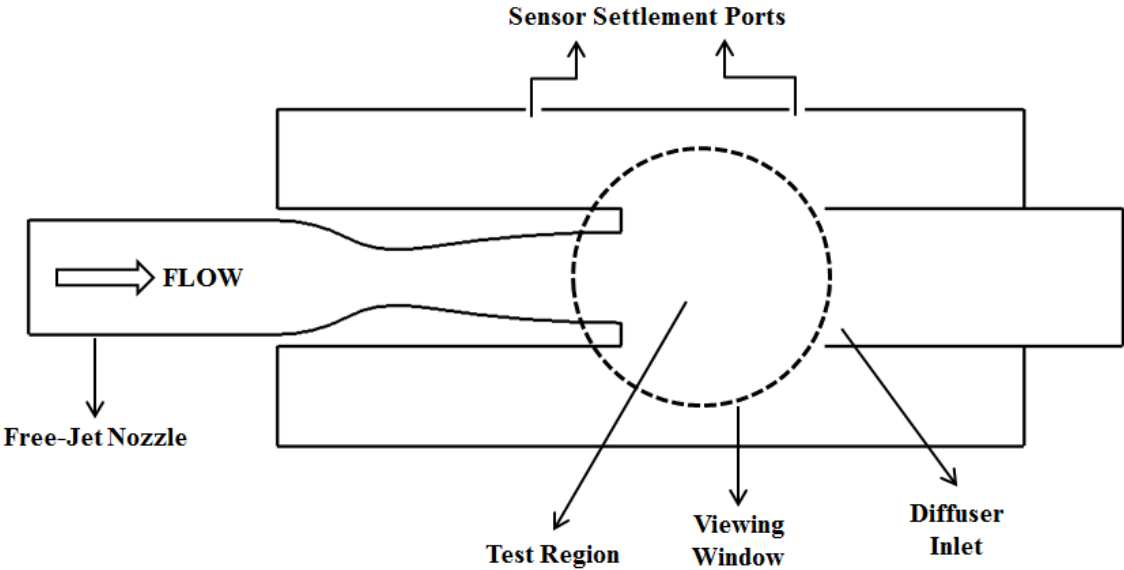


Figure 1-3. Detailed View of the Test Chamber.

Test region is also monitored through proper viewing window covering the free-jet nozzle exit and test articles. Plexiglass plates are generally used for monitoring the test chamber and quartz plates can also be used for a better view and high temperature applications. Sealing is a problem for vacuum pressure environment inside the test chamber. The test chamber wall material is chosen as steel to protect the outer environment in case of any failure and because of pressure-proof feature. The test chamber can be cooled with the help of water channels around for hot flow applications and it also has cable and pipe entry ports on the wall extending to the inside.

1.2.3. Ejector System

Ejectors can be thought of as simple pumps that are often used instead of some more complex rotary or reciprocating compressors where relatively hot combustion products exhausted from rockets or turbine engines are processed. The working principle of ejectors is based on momentum interchange in the boundary layer between a high velocity primary air flow and a low velocity secondary air flow [3]. The ejector system is given in Figure 1-4 schematically.

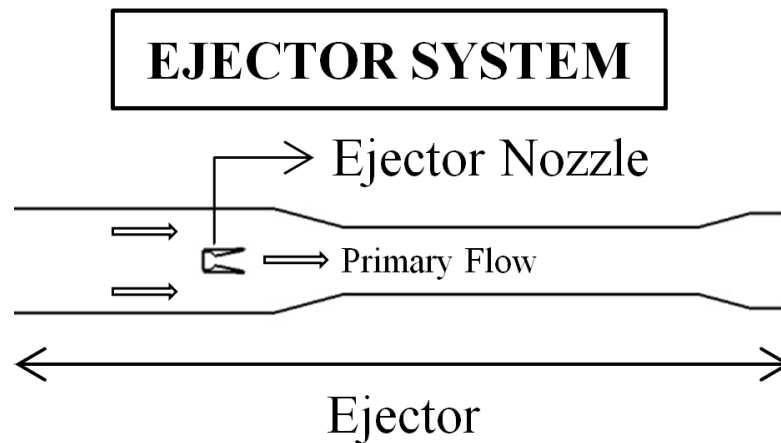


Figure 1-4. Ejector System with Own Separate Nozzle.

Actually, nozzle of a rocket engine or a turbine engine behaves as an ejector system using high speed gases from exhaust to draw air flow around itself for lowering the pressure inside the test chamber [3]. In Figure 1-4, ejector system has its own separate nozzle to lower the test chamber pressure for successful starting of the free-jet nozzle. Nitrogen gas or air are generally chosen as the primary flow for the ejector system. Ejector nozzle inlet is generally driven from the pipeline diverted from the main pipeline before the free-jet nozzle. Ejector system may consist of multiple ejectors arranged in a row. This multiple ejector system is employed to achieve lower pressure situation inside the test chamber. The diameter of the ejector system is determined according to the sum of the primary and secondary mass flow rates and that's exactly why an increase in the inlet total pressure of the ejector nozzle after fixing its optimum value generates an increase in the back pressure and an increase in the test chamber pressure as a result as well.

Ejectors have two major operation modes known as ‘started and unstarted mode’. In Figure 1-5, it can be seen that ‘State 1’ indicates the unstarted mode and ‘State 3’ is the started mode.

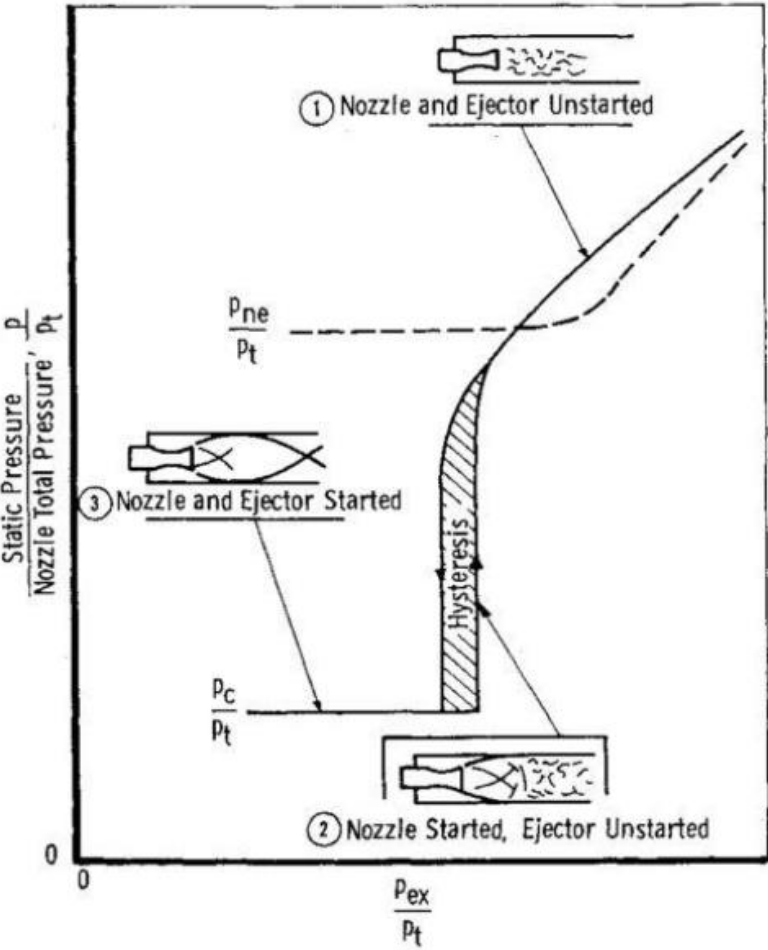


Figure 1-5. Operation Modes of the Ejector System [4].

While the ejector nozzle pressure increases, the flow accelerates from stagnant state which causes a decrease in static pressure shown as ‘State 1’ in Figure 1-5. When the ejector nozzle total pressure further increases, nozzle and ejector reaches the started mode and the pressure drops abruptly shown as ‘State 3’ in Figure 1-5 [2]. Once the ejector is started, further increase in pressure of the ejector nozzle increases the secondary flow pressure. Hence, the ejector nozzle will be considered as working at its optimum nozzle condition to help start free-jet nozzle satisfying lower pressure environment inside the test chamber. During CFD analyses and experimental tests, the ejector nozzle starting phenomena will not be covered and directly assumed as working in started mode.

1.3. Literature Survey

Rose et al. [5] have used the installed test setup presented in the testing facility for conducting aerodynamic simulation experiments with and without test articles under different operating conditions. The design process sequence of the HATS facility is given in Figure 1-6.

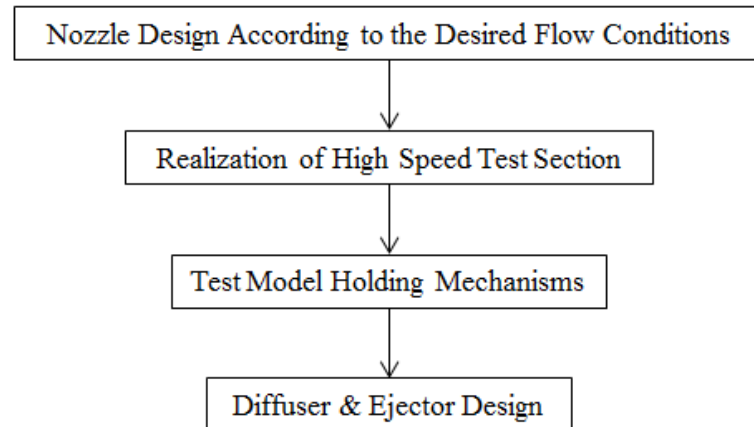


Figure 1-6. Design Procedure of HATS [5].

Mach 2.5 free-jet nozzle was designed by using Method of Characteristics, ‘MOC’ and numerically solved with perfect gas assumption for inviscid flow in 2D. According to the configuration of the test chamber, the free-jet nozzle and diffuser are placed with a specific distance between inside the enclosed free-jet test section of a subscale HATS facility. The flow simulation was performed for two cases, i.e with and without the test article. The solution domain of the test chamber and diffuser system is given in Figure 1-7 and the subscaled rocket test specimen is given in Figure 1-8.

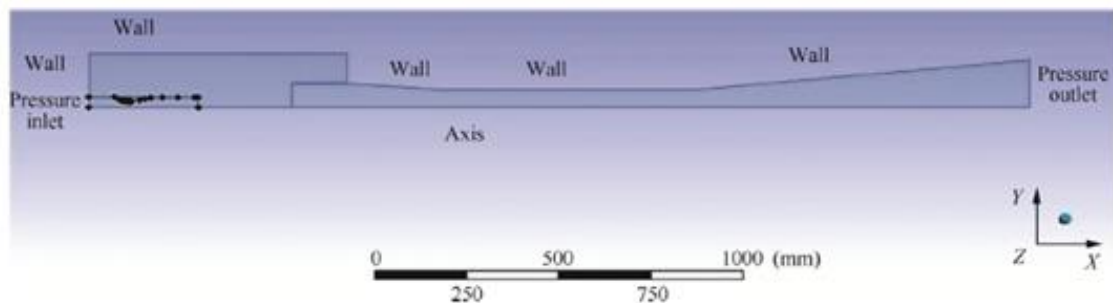


Figure 1-7. Solution Domain and Boundary Conditions for Test Section of HATS [5].

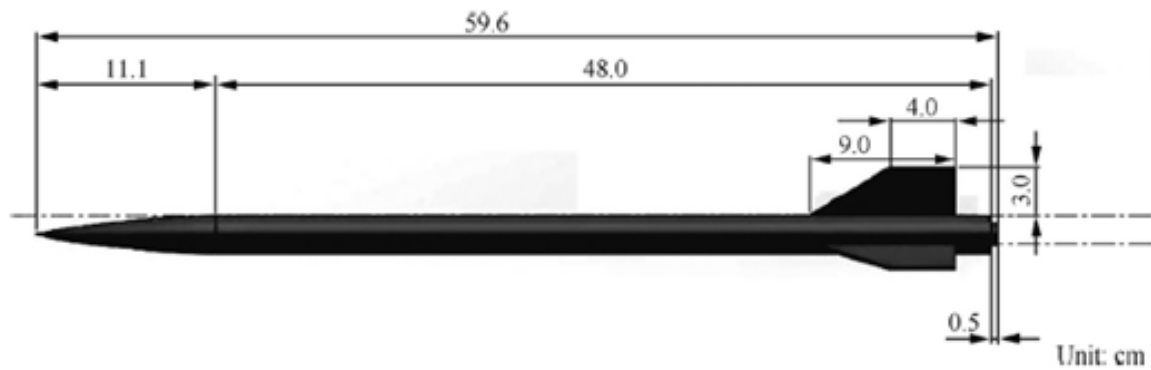


Figure 1-8. Subscaled Rocket Test Article [5].

Ejector section was not considered to analyze all different test conditions to lower the computational time because it is known that ejector nozzle is working at its optimum condition as designed. Hence, solution domain can be kept small from the beginning of the free-jet nozzle and the exit of the test section diffuser. In CFD analysis, an appropriate $k-\epsilon$ model for turbulent flow with pressure boundary conditions at free-jet nozzle inlet and diffuser outlet was used with Navier-Stokes equations combine conservation equations of mass, momentum and energy.

German and Bauer [6] have obtained such a result that 2D axisymmetric CFD analyses for ejectors are not sufficient in the results with error below 10% mostly and 20% in the largest compared to the experimental results. It was stated that there is a need for performing 3D CFD analyses in the future. Hence, CFD analyses are performed in 3D with half model because of the symmetry in this thesis.

Back pressure effect on the flow coming from the rocket nozzle as secondary flow has been worked by using numerical analyses. It was concluded that by lowering the back pressure, the shockwave moves away from the rocket nozzle and helps to create vacuum pressure inside the test chamber [7]. Hence, once the ejector starts to work, further increase in pressure of the ejector nozzle increases the back pressure of the test section diffuser used for the outlet boundary pressure condition in CFD analyses in this study.

Pruitt and Bates [8] have conducted an experimental research to identify the test rhombus characteristics of two-dimensional supersonic free-jet nozzle with Mach numbers of 1.7, 2.5 and 3.3. The four different free-jet nozzle-diffuser system installation concepts with test articles each illustrating several problems in the starting period of the free-jet nozzle as shown in Figure 1-9 were analyzed.

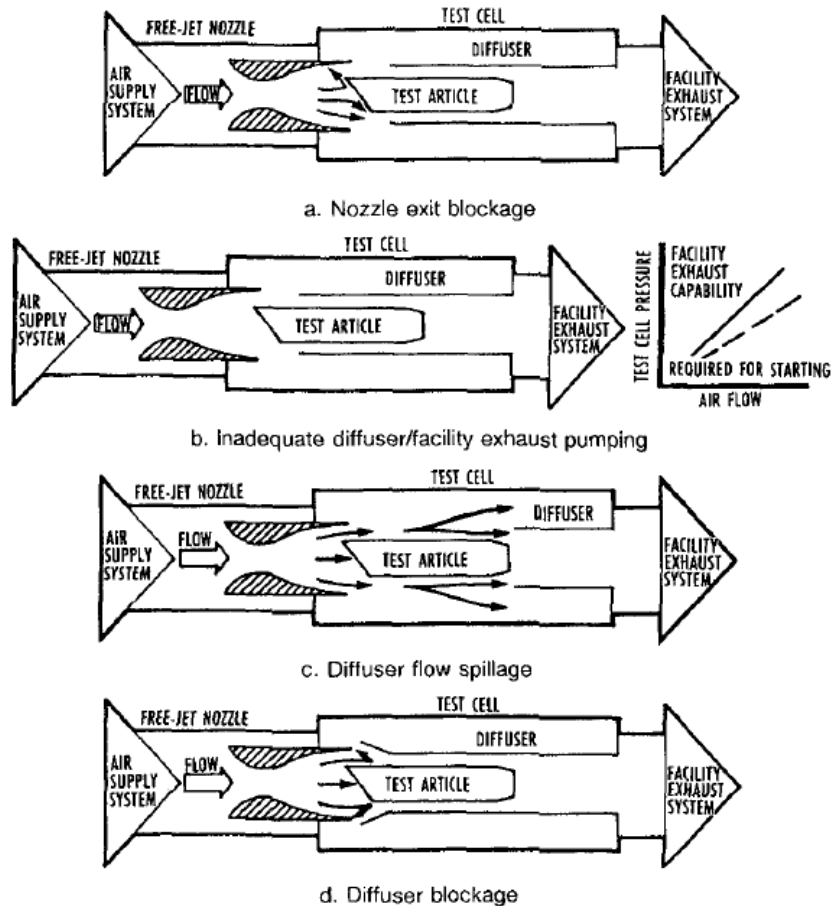


Figure 1-9. Free-Jet Nozzle-Diffuser System Installation Concepts [8].

The main purpose of the investigation was to determine the effect of the free-jet nozzle and test article placements on the characteristics of the free-jet nozzle starting period and to identify the test rhombus capability for these different configurations. The test chamber used for the research was capable of almost 4800 Pa vacuum pressure. The blockage ratio for Mach 1.7 in the range of 24-40%, for Mach 2.5 in the range of 34-67% and for Mach 3.3 in the range of 40-59% were tested successfully.

Czysz [9] has conducted an experimental study about the blockage effect on the working characteristics of the test setup for different test articles like cones, flat plates, hemisphericals up to 40° angle of attack with up to Mach 4 in the test facility given in Figure 1-10.

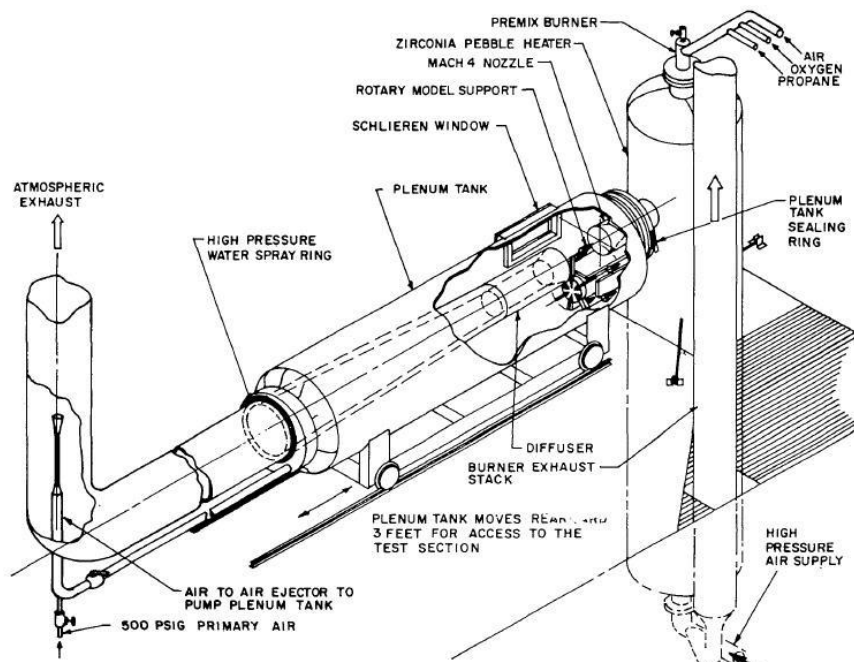


Figure 1-10. High Temperature Hypersonic Gas Dynamics Facility [9].

Schlieren photographs were also collected during the tests for different test articles at different flow conditions and example Schlieren images are given in Figure 1-11.

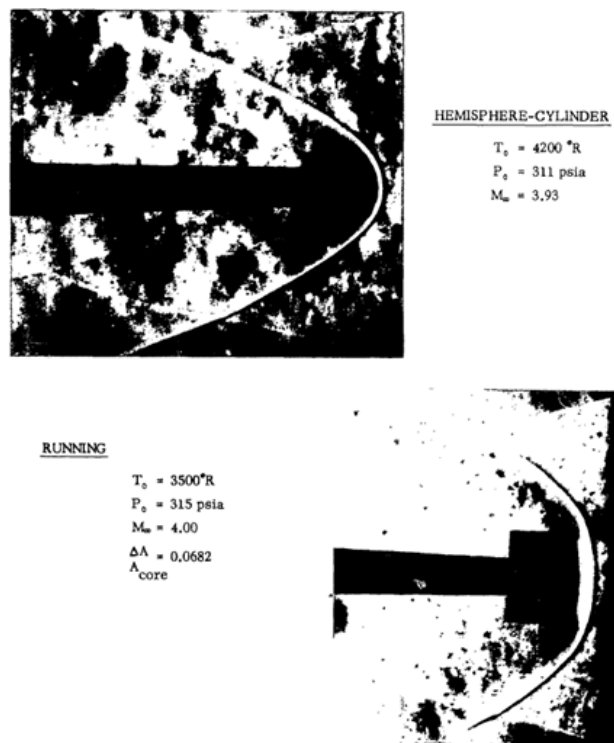


Figure 1-11. Schlieren Images of Some Typical Test Articles [9].

Effect of the test article on the test chamber pressure has been investigated during the research and some obtained results are given in Figure 1-12.

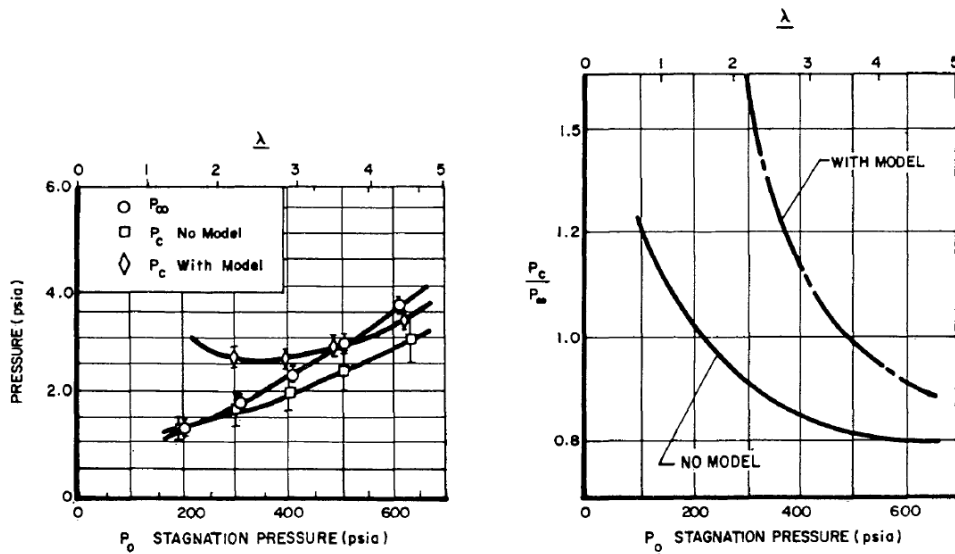


Figure 1-12. Effect of Test Article on Test Chamber Static Pressure [9].

Daniel [3] has improved the computer model to validate facility control systems during operation of the facility and compared the results with experimental test results. The started and unstarted modes of ejector were simulated by the model. Experimental test results and effect of the blockage on the test chamber pressure are given in Figure 1-13.

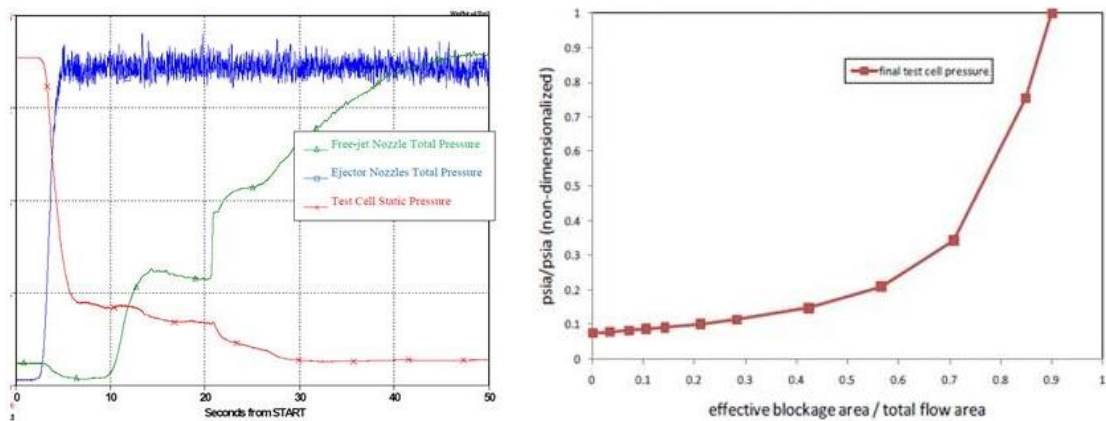


Figure 1-13. Test Results and Blockage Effect on Test Chamber Pressure [3].

It was concluded that real gas approach only diverges from the ideal gas during the early times of the operation of the ejector. In steady state, test chamber pressure for both real and ideal gas modelled ejectors gets closer to each other shown in Figure 1-14 [3].

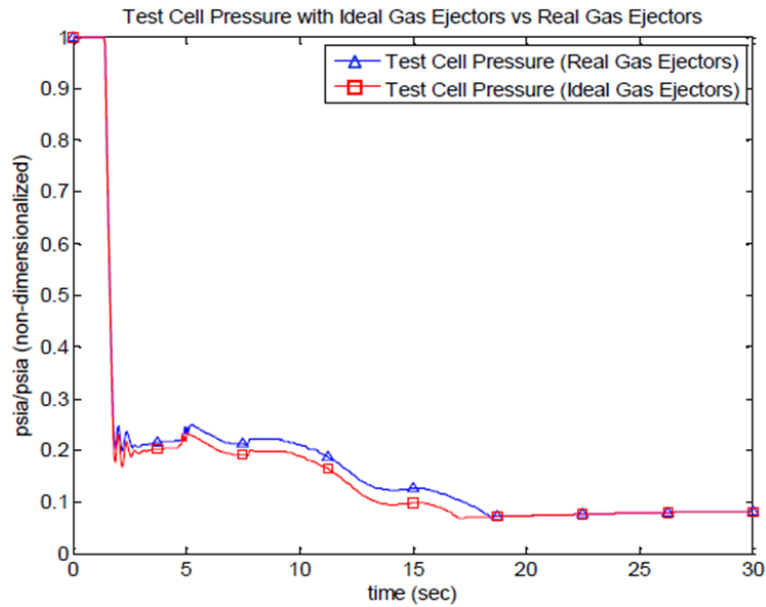


Figure 1-14. Test Chamber Pressure for Ideal and Real Gas Modelled Ejectors [3].

It is obvious that real gas deviates from ideal gas at high pressures and low temperatures. Hence, CFD analyses in steady state can be performed for ideal gas modelled free-jet nozzle flow in this thesis.

Bauer et al. [10] have conducted a performance analysis for the test facility with the chin inlet of a ramjet missile test article. The most important topics of the study were the position of the test article, performance prediction of the diffuser at starting and steady state operation for the test articles located with 0° and 11° of angle of attack. The basic test article and supporting mechanism are shown in Figure 1-15.

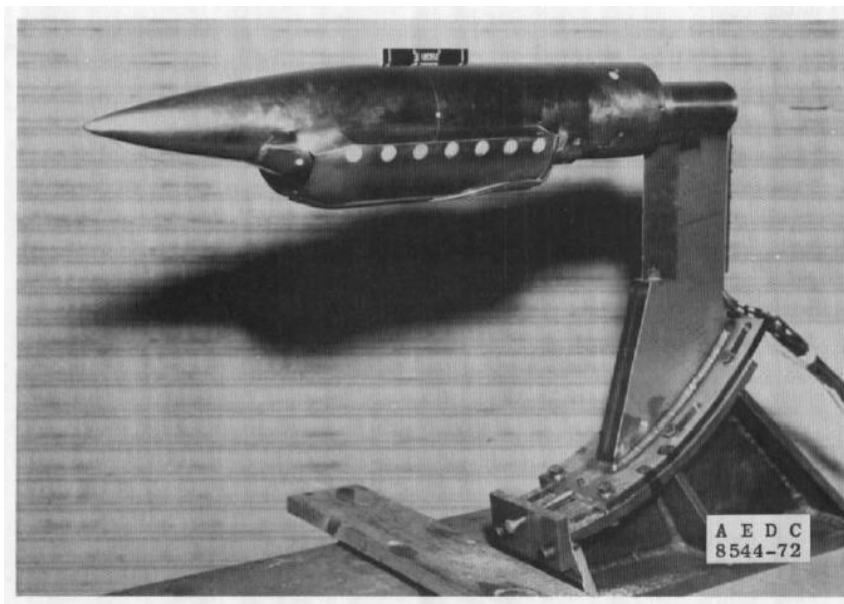


Figure 1-15. Test Article and Supporting Mechanism [10].

The test specimen is 3.5 inches in diameter and has a 2.92 von Karman forebody. The support of the test article has an aerodynamically shaped to minimize the extra drag caused by itself and a blocking area equal to around 14% of the frontal area of the test article. The free-jet nozzle, diffuser and the blockage test article are subscaled to 20.67% of the full scale models.

They have found that the pressure fluctuations are present during the start-up period but the fluctuations in the flow over the test article is lowered during operation. They have commented that these disturbances can be caused by the difference between the pressure of the free-jet nozzle exit and test chamber and also by excessive blockage ratio. In practice, the maximum test chamber pressure is determined according to the free-jet nozzle full flow condition, but the minimum test chamber pressure is limited either by the jet plume of the free-jet nozzle or the phenomena of base flow. This condition is shown in Figure 1-16.

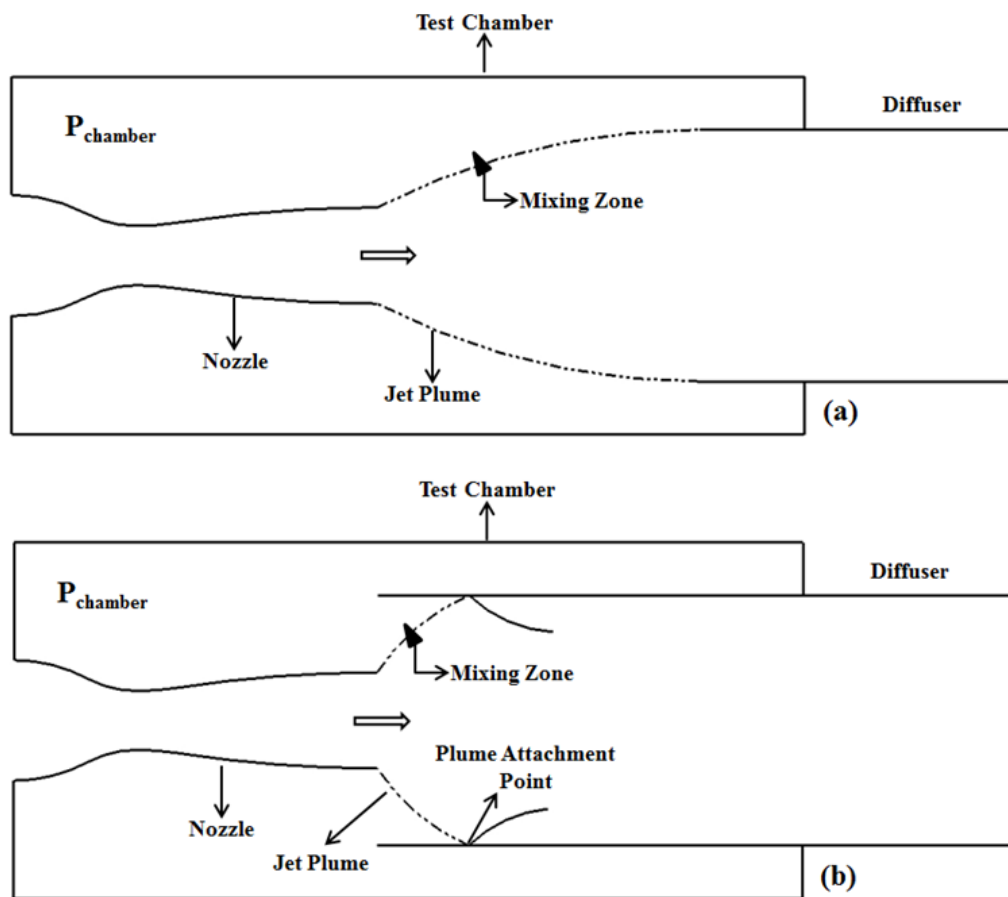


Figure 1-16. Minimum Test Chamber Pressure Limits: (a) Jet Plume Limit, (b) Base Flow Limit [10].

Kumaran et al. [11] have researched the effects of both geometrical and operational parameters on the performance of the second throat ejectors for HATS. That ejector system is utilized to achieve low vacuum pressure environment inside the test chamber for rocket motors with high nozzle area ratios. The study has shown that primary flow provided by the ejector nozzle just plays a supporting role when the rocket motor is in operation mode. Hence, the desired low pressure environment can be sustainable by the rocket motor nozzle exhaust itself. The HATS with second throat ejector system is given in Figure 1-17.

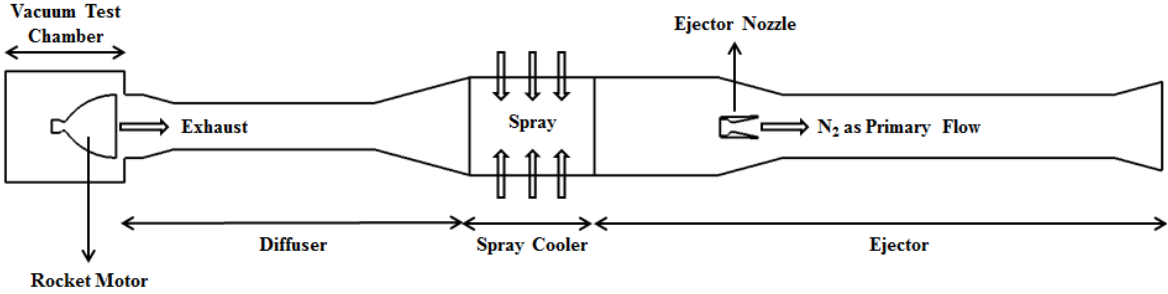


Figure 1-17. Sketch of a High Altitude Test System Facility [11].

It also has been found that there is a critical value for the primary flow of the ejector to lower the test chamber pressure and for flow rates lower or higher than this critical value, the test chamber pressure is affected adversely and the optimum condition is not satisfied. This situation is also taken into account in this thesis and the same amount of air flow is supplied to the ejector nozzle at each test condition. The boundary conditions used in the numerical analyses for ejector system is given in Figure 1-18.

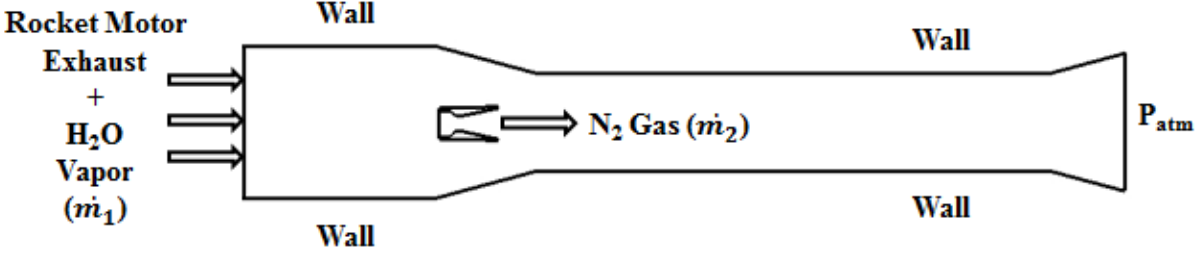


Figure 1-18. Boundary Conditions for Ejector System [11].

In the study, it is also observed that there is a spray cooler section of the test setup before the ejector section to cool down the high temperature exhaust of the rocket motor. In numerical analyses, the water vapor and rocket motor exhaust were both used as a mass flow inlet boundary condition for ejector system. The temperature must be below 3000 K for many compressible flow applications to assume perfect gas with constant properties. The assumption of perfect gas was also used in the study because it was stated that the stagnation temperature is almost 3500 K in the test setup [11].

Fernando et al. [12] have studied the performance of the diffuser system numerically for various back pressures. The ejector system consists of two ejectors arranged in a row. It is assumed that the ejector system works to provide different pressure values to analyze the diffuser system for a high area ratio nozzle numerically. The supersonic nozzle with area ratio of 114 was designed for altitude control of a satellite. The boundary conditions used in the numerical analyses for diffuser system is given in Figure 1-19.

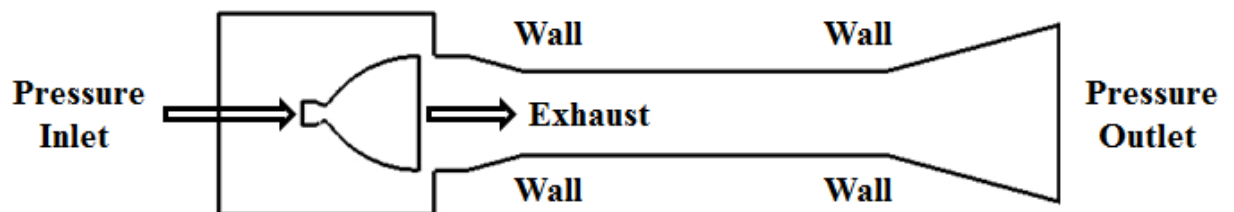


Figure 1-19. Boundary Conditions for Diffuser System [12].

The effect of the back pressure that is controlled by the pressure outlet boundary condition was analyzed numerically. This boundary condition is also used for numerical analyses of the diffuser section of the test setup in this thesis.

The design process of the high altitude test facilities for rocket engines ground level tests and the general working principles have been mentioned in the study [13]. The main problem area can be found as the exhaust gas handling and to achieve the desired pressure level before and after the test firings of the rocket engine. The pressure rise ratio, P_{ex}/P_c according to the ratio of the diffuser duct area to the rocket motor throat area was calculated for both hot and cold flow applications of rocket motor and the obtained data is given in Figure 1-20.

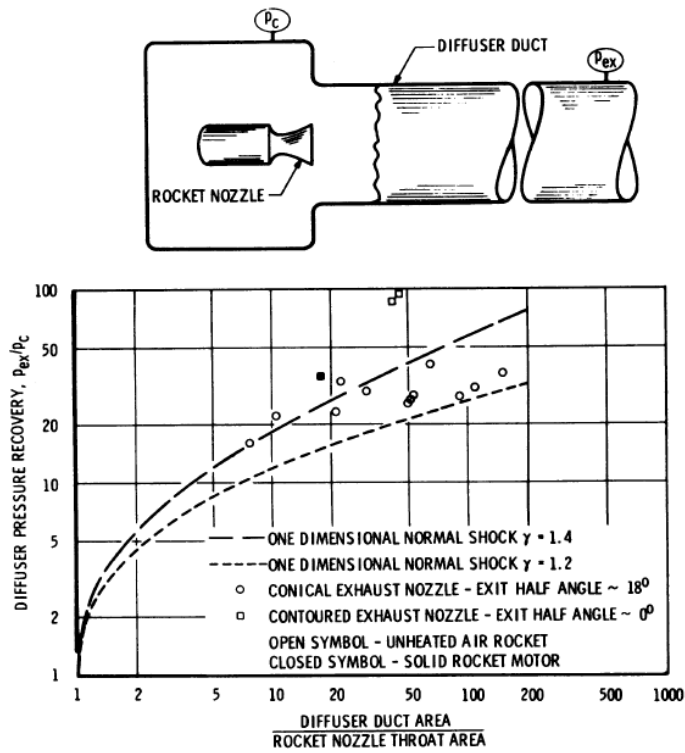


Figure 1-20. Performance of Simple Cylindrical Ejector-Diffuser System [13].

The result of the study is that the performance of the diffuser is severely affected by the ratio of the length to diameter of the diffuser up to 6. Because of this importance of the ejector-diffuser system, attention was given to the improvement of the diffuser performance. The performance improvement in terms of pressure rise ratio for different diffuser duct entry designs is shown in Figure 1-21.

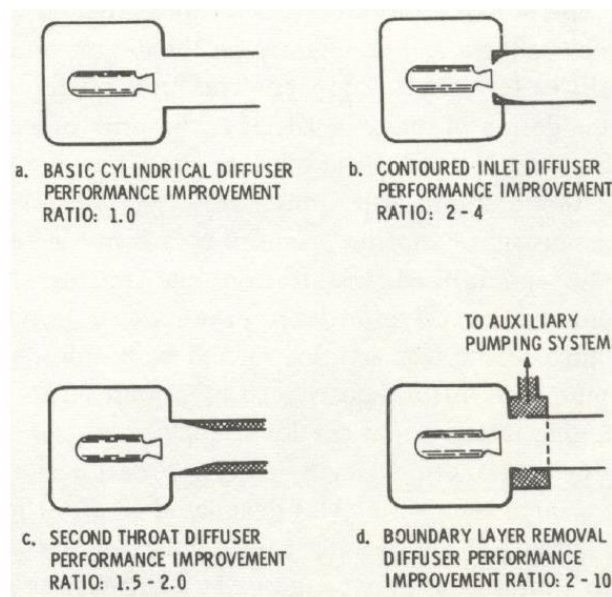


Figure 1-21. Schematics of Refinements to Cylindrical Ejector-Diffuser System [13].

If the performance improvement ratio is taken as 1 for basic cylindrical diffuser, the ratio can be increased up to 4 by just changing the entry duct geometrically and up to 10 by using auxiliary pumping system. In this thesis, there is a basic cylindrical diffuser system in the HATS setup which is examined both experimentally and numerically.

Kronmueller et al. [14] have shown the capability of the test facility and the measurement techniques like infrared camera and color Schlieren method used to obtain visual results during the experiments. The test facility is given in Figure 1-22.



Figure 1-22. P6.2 Cold Gas Subscale Test Facility [14].

The specifications of the subscale test facility is given in Table 1-1.

Table 1-1. Specifications of the Test Facility.

Test Chamber Pressure without Ejector System	< 4000 Pa
Test Chamber Pressure with Ejector System	< 2500 Pa
Free-Jet Nozzle Mass Flow Rate	2.8 - 4.2 kg/s
Ejector Nozzle Mass Flow Rate	2.8 - 4.2 kg/s
Free-Jet Nozzle Inlet Pressure	40 – 60 bar
Ejector Nozzle Inlet Pressure	40 – 60 bar
Length of the Test Chamber	1000 mm
Diameter of the Test Chamber	800 mm

As seen from Table 1-1, the test chamber pressure is lower than 4000 Pa and 2500 Pa without and with ejector system, respectively. Nitrogen gas was used for both ejector nozzle flow and free-jet nozzle flow. Mass flow rates of the free-jet nozzle and ejector nozzle are around 2.8 kg/s similar to the test setup used in this thesis.

Different types of the free-jet nozzle and diffuser system were tested in the test facility. Hence, the mathematical model was also verified by the comparison of the test results with the calculated ones. The flow pattern of the free-jet nozzle plume was also visually obtained by using color Schlieren method as a capability of the test facility. Color Schlieren method is an easier way to distinguish the differences in the flow than monochrome Schlieren method. Example images obtained using color Schlieren method are given in Figure 1-23.

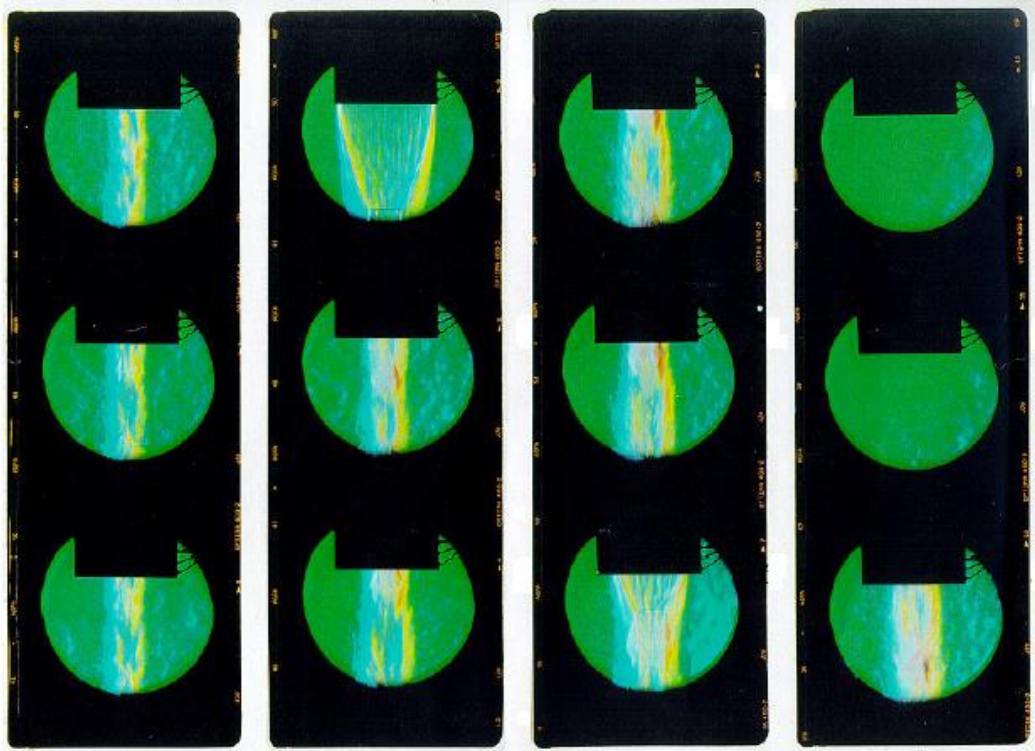


Figure 1-23. Color Schlieren Images of a Free-Jet Nozzle [14].

In this study [15], starting phenomena of the two-dimensional supersonic ejector for different inlet pressures of the air has been investigated experimentally. The result is that when the pressure of the ejector nozzle is on the critical pressure value, the shockwaves oscillate back and forth inside the ejector and this causes fluctuations in the pressure data. Then, if the pressure is higher than this critical starting pressure, the ejector starts and the pressure is lowered, the shockwaves inside the ejector have a lesser degree of oscillation and this causes also lesser fluctuations in the pressure data. This situation can be seen in Figure 1-24 as pressure oscillations for start and unstart status.

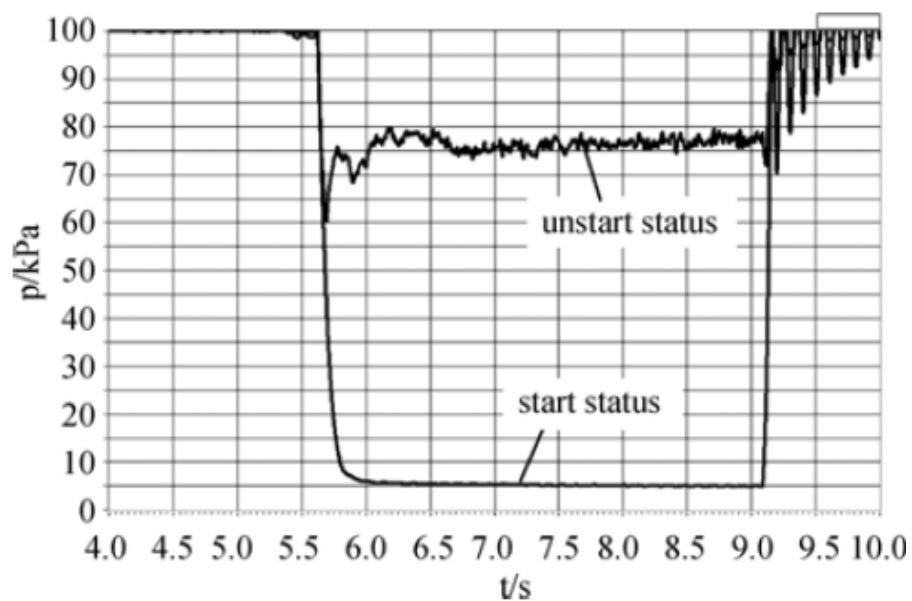


Figure 1-24. Test Section Diffuser Pressure [15].

2. EXPERIMENTAL INVESTIGATION

2.1. Introduction

The experimental test setup, test articles and supporting mechanism, measurements made during tests and Mach 2.5 free-jet nozzle design process are given in this chapter, respectively. The experimental test results are also given in the final section of this chapter.

The HATS setup which was already established in TÜBİTAK-SAGE is explained in detail in Section 2.2.1. The blockage test article and its supporting mechanism design and installation process inside the test chamber is also covered in Section 2.2.2. Measurement parameters and techniques are given in detail in Section 2.2.3. Studies to determine Mach 2.5 free-jet nozzle dimensions are given in Section 2.2.4. The experimental test results and example of the data sampled during tests for a specific test condition are finally given in Section 2.3.

2.2. Experimental Test Setup

In the scope of this study, the test section will be studied experimentally and numerically. Test section is given in right-side view and isometric view in Figure 2-1 and Figure 2-2, respectively.

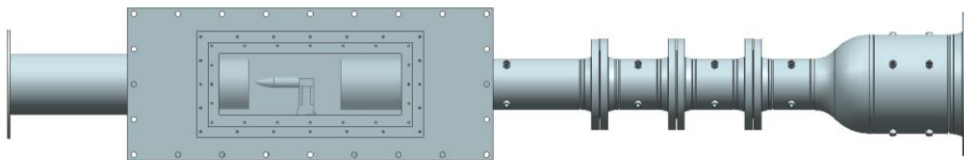


Figure 2-1. Test Section Side View.

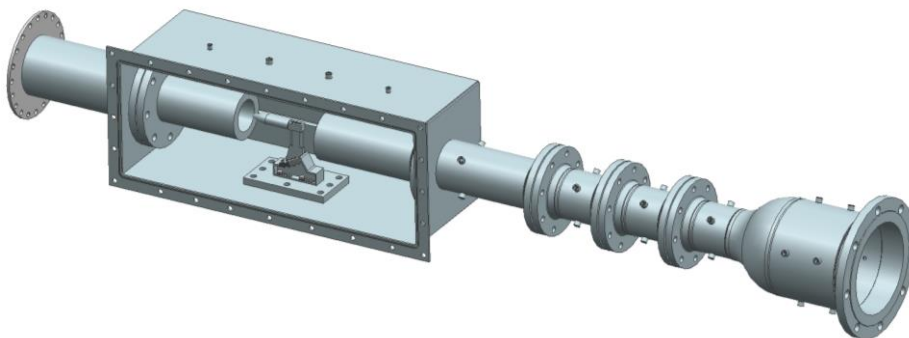


Figure 2-2. Test Section Isometric View.

Ejector system is considered as working at its optimum condition to lower the test chamber pressure as required to help start the free-jet nozzle. Hence, the ejector system after test section is not studied deeply and pressure outlet boundary condition will be given to the exit of the test section given in Figure 2-1.

Test section with test article and support mechanism can be seen in Figure 2-2. As seen, the test article does block the free-jet nozzle exit. Experimental tests and CFD analyses will be performed with and without test articles in this study.

2.2.1. TÜBİTAK-SAGE HATS Setup

‘TÜBİTAK-SAGE Test Setup’ was established in 2019 under another thesis about design parameters of the ‘High Altitude Test System’ which is given in Figure 2-3 [2].

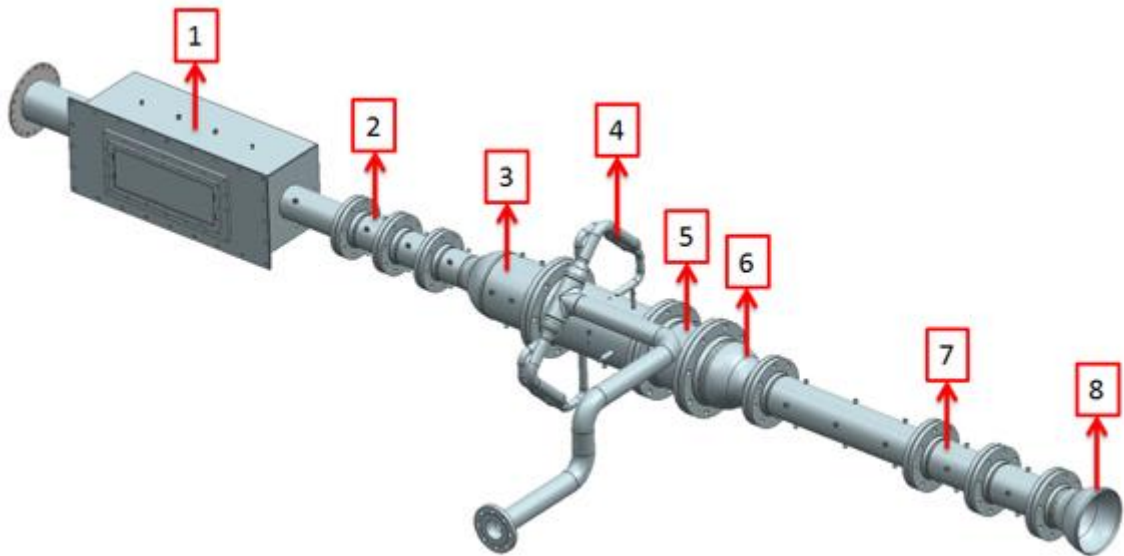


Figure 2-3. TÜBİTAK-SAGE Test Setup.

The test facility can supply most 2 kg/s for free-jet nozzle and 3 kg/s for ejector nozzle operation. The air is compressed to the air storage tank and also dried before entering the air storage tank. Some air after storage tank is also diverted from the main pipeline to the inlet of the ejector nozzle.

Experimental test setup consists of following sections given in Table 2-1.

Table 2-1. Test Setup Main Parts List.

Number	Section Name
1	Test Chamber
2	Test Section Diffuser
3	Test Section Diffuser-Ejector Nozzle Feed Manifold Connection
4	Ejector Nozzle Feed Manifold
5	Nozzle Exit Plane Extension
6	Transition Cone
7	Ejector Section Diffuser
8	Subsonic Diffuser

Test articles are located between the free-jet nozzle and diffuser entry duct inside the Section 1. There are 2 pressure sensors and 2 thermocouples on the upper wall of the Section 1. Test setup and all measurement locations are given in Appendix-1 in detail.

2.2.2. Test Articles and Support Design

Blockage ratio is defined as the ratio of the test article blocking area to the free-jet nozzle exit area and can be calculated easily in 2D by projecting the test article on the free-jet nozzle exit plane.

The special nosecone geometry called von Karman or LD-HAACK is designed to test the blockage effects on the pressure inside the test chamber. Equations 2-1 and 2-2 are used to design the nosecone geometries with different blockage area ratios.

$$\theta = \cos^{-1} \left(1 - \frac{2x}{L} \right) \quad (2-1)$$

$$y = \frac{R \sqrt{\theta - \frac{\sin(2\theta)}{2}} + C \sin^3(\theta)}{\sqrt{\pi}} \quad (2-2)$$

$C = 0$ for LD-HAACK, ‘Minimum Drag due to the Given Diameter and Length’

$C = 1/3$ for LV-HAACK, ‘Minimum Drag due to the Given Volume and Length’

The diameter of the test articles comes from the blockage ratios according to the free-jet nozzle exit diameter and because of the constricted area between the free-jet nozzle and diffuser inlet, the required length must also be kept as minimum as possible given in Figure 2-4.

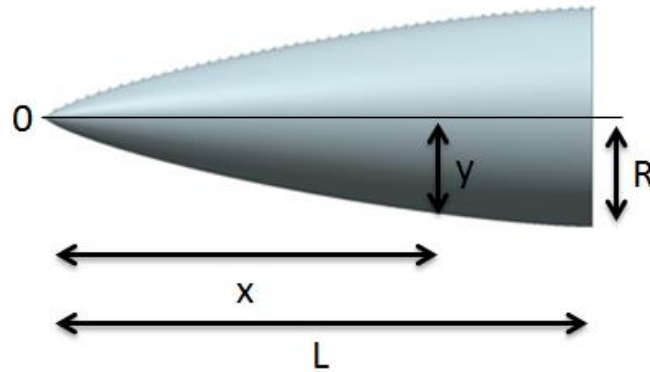


Figure 2-4. von Karman Nosecone Geometry.

Hence, LD-HAACK geometry which can be described as minimum drag due to the given diameter and length is selected as nosecone geometry.

By using Equation 2-2, y-axis coordinate against x-axis coordinate of the points can be found and it is obvious that at $x = L$, $y = R$. Nosecone geometry dimensions of the test articles are given in Table 2-2.

Table 2-2. Test Article Dimensions.

Blockage Ratio, BR	Mach 2 Free-Jet Nozzle		Mach 2.5 Free-Jet Nozzle	
	Length, L (mm)	Radius, R (mm)	Length, L (mm)	Radius, R (mm)
8%	50	10	50	7
15%	50	17.5	50	14.5
25%	50	25	50	21.5

All test articles are controlled by using optical scanning quality control process to check whether the geometry is out of tolerance in 3D. An example of the optical scanning results is given in Figure 2-5.

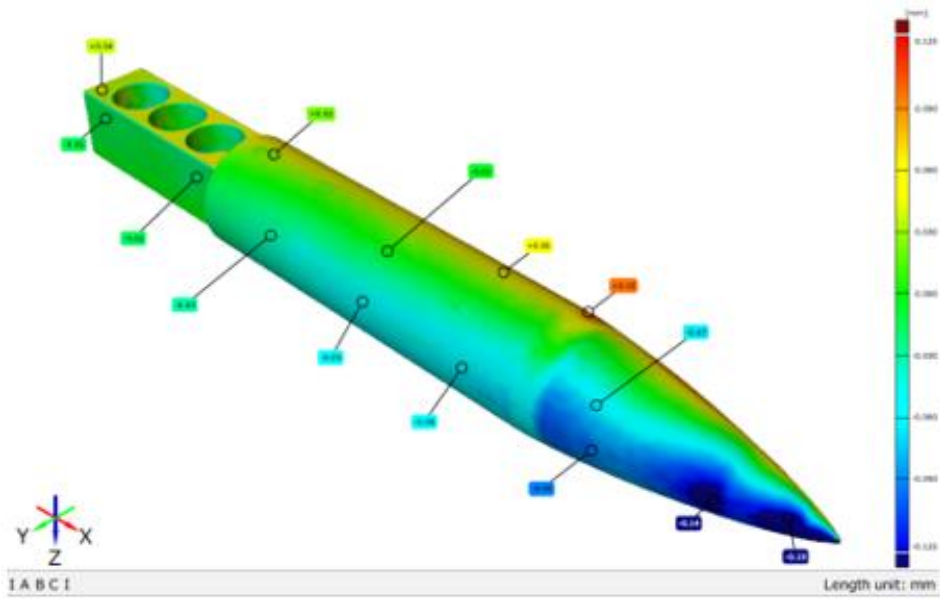


Figure 2-5. Optical Scanning Result.

The contour of optical scanning result shows the range of -0.125 to 0.125 mm. While the minus sign indicates that the manufactured part is inside the solid model, the plus sign indicates that it is outside the solid model. The supporting mechanism of the test articles is shown in Figure 2-6.

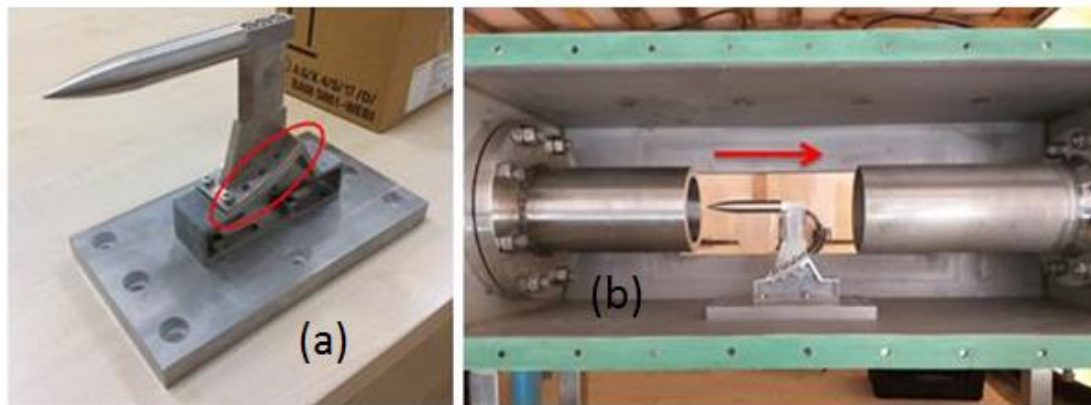


Figure 2-6. Test Article and Placement Inside the Test Chamber.

The red arrow indicates the flow direction. The support system marked in red circle allows the test article to be given angle of attack and that means also higher blockage ratios. This supporting mechanism also constricts the yaw and roll motion of the test articles. It is clearly observed that the test article is aligned with the free-jet nozzle axis and parallel to the ground almost 0.1° as a margin of error.

2.2.3. Measurements

Pressure, temperature and mass flow rate data are collected during the experimental tests by proper measuring equipment installed at different locations of the experimental test setup. The specifications of the sensors utilized in the test setup are given in Table 2-3.

Table 2-3. Measuring Equipment of the Test Setup.

Equipment	Description
Pressure Sensor	KISTLER 4260A Absolute
Thermocouple	OMEGA K-Type
Mass Flow Meter	SAGE 200 Thermal Mass Flow Meter

Locations of the pressure sensors and thermocouples up on the test chamber wall is given in Figure 2-7 as an example of sensor connections along the test setup.

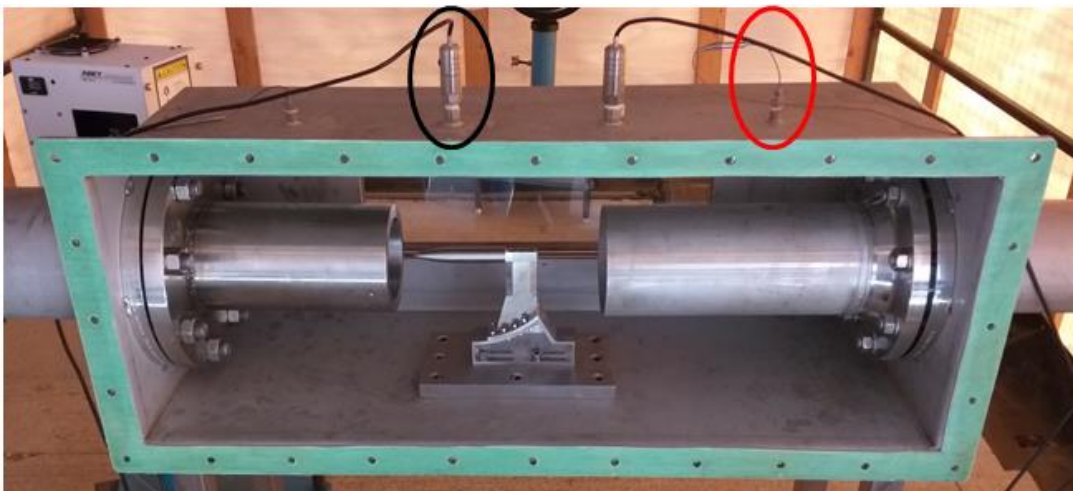


Figure 2-7. Test Chamber Pressure and Temperature Sensors.

All other pressure transducer and thermocouple locations are given in Appendix-1. Mass flow meter is also between the buffer tank and the free-jet nozzle on the main pipeline.

2.2.3.1. Pressure

Pressure data is collected with 0-1 bar and 0-35 bar piezoresistive pressure transducers from different locations along the experimental test setup during the experimental tests. 0-35 bar pressure transducer is used to measure ejector nozzle inlet total pressure while 0-1 bar pressure transducers are used at locations where vacuum condition is occurred especially in the test section. The data sampling rate is 25 kHz. Pressure transducer is shown in Figure 2-8.



Figure 2-8. Kistler 4260A Piezoresistive Pressure Transducer.

2.2.3.2. Temperature

Temperature data is collected with K-Type thermocouples at the test chamber and ejector nozzle inlet. The data sampling frequency is 1 kHz. K-Type thermocouple is shown in Figure 2-9.



Figure 2-9. K-Type Thermocouple.

2.2.3.3. Mass Flow Rate

The mass flow rate of the air is controlled by the valve opening ratio in the test setup. 'SAGE 200 Thermal Mass Flow Meter' is employed for mass flow rate measurements that is installed before the free-jet nozzle on the main pipeline and to check any occurring error of the operation of the valve. The data sampling rate is 1 Hz. Mass flow meter is shown in Figure 2-10.



Figure 2-10. SAGE 200 Thermal Mass Flow Meter.

2.2.3.4. Schlieren Imaging

Schlieren imaging is a classical method of visual processing that is used to photograph the flow of the fluid. While imaging the flow, it benefits from the change in the density of the fluid. This imaging technique is widely used in aerodynamic applications to obtain an image of air flow around objects. Schlieren system is given in Figure 2-11.

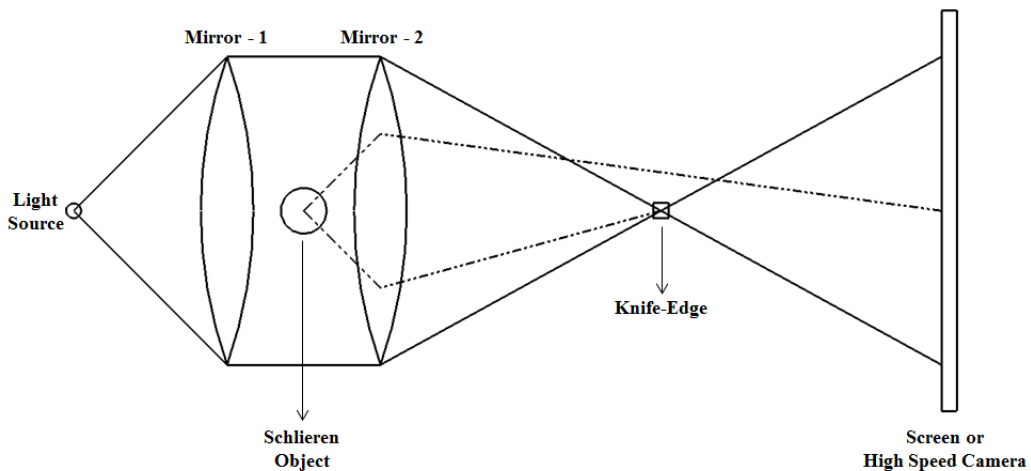


Figure 2-11. Sketch of a Schlieren System [16].

It basically consists of a light source, two mirrors to direct light beam, knife-edge as a cutoff and screen or high speed camera to project onto. The first mirror aligns the light beam coming from the light source. The light is then refocused after passing through the second mirror. The distance between the Schlieren object and second mirror and the distance between the second mirror and screen or high speed camera must be set before the installation in the test setup according to the focal length of the mirrors [16].

A blocking object is placed on the plane where the focus of the second mirror coincides. This object is called knife-edge and used to cut off the light rays that is bent while passing through the Schlieren object to increase the contrast and get the full Schlieren image. Knife-edge can be adjusted horizontal or vertical or a pin hole is used instead of the knife-edge as a cutoff [16]. Schlieren image for three types of the cutoffs is given in Figure 2-12.

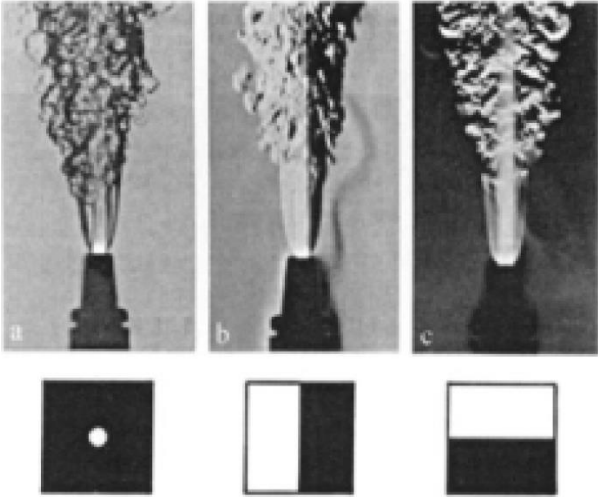


Figure 2-12. Schlieren Image for Three Different Cutoffs: (a) Pinhole, (b) Knife-Edge Adjusted in Vertical, (c) Knife-Edge Adjusted in Horizontal [16].

Horizontal or vertical placement of the knife-edge is just blocking a certain section along the x and y axes separately at the same time, but a pinhole or knife-edge adjusted both horizontal and vertical is used to achieve the full image of the Schlieren object [16].

The Schlieren system with the knife-edge adjustable in all three axes is used during the experimental tests to get full images. This Schlieren system used in the test setup and the equipment are given in Figure 2-13 and Table 2-4, respectively.

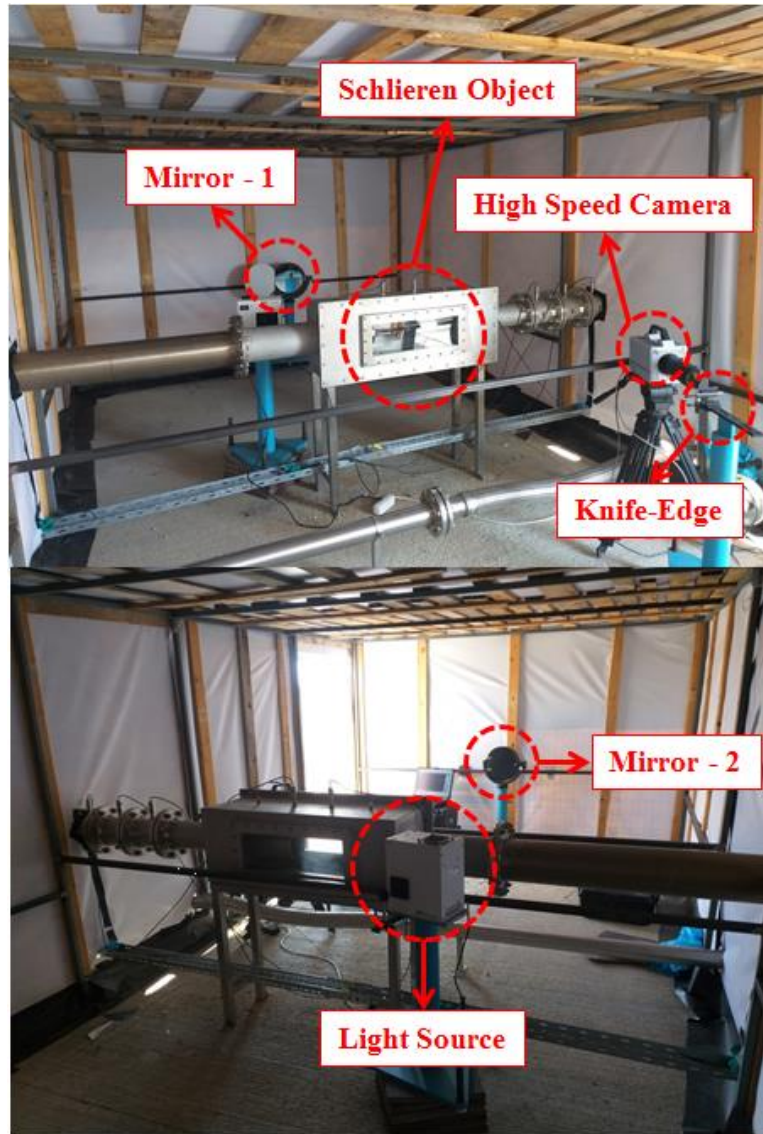


Figure 2-13. Installation of Schlieren System in the Test Setup.

Table 2-4. Equipment of Schlieren System.

Equipment	Description
High Speed Camera	Photron SA-X2
Light Source	Short-Arc Xenon Lamp
Mirror-1	Adjustable 10 in. Parabolic Mirror
Mirror-2	Adjustable 10 in. Parabolic Mirror
Knife-Edge	Adjustable in All Three Axes

2.2.4. Mach 2.5 Free-Jet Nozzle Design

The main function of a nozzle is to direct and accelerate the combustion products of the rocket motor and thus to obtain thrust. The concept of the nozzle design involves ‘steady state one-dimensional compressible fluid flow of an ideal gas’.

1D flow means that the flow is along the direction of the symmetry axis of the nozzle. The assumed flow direction for one-dimensional flow is shown in Figure 2-14.

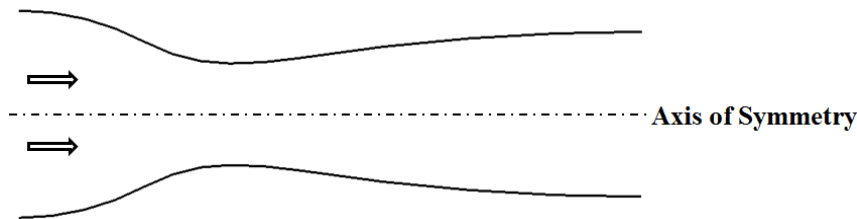


Figure 2-14. One-Dimensional Nozzle Flow.

Density, pressure and temperature are related to each other for an ideal gas assumption and they are affected by cross-sectional area, friction and heat losses to the surroundings in compressible fluid flow. Then, near isentropic flow assumption is considered for the design of the nozzle where the properties of the flow only changes with cross-sectional area and the effect of the friction and heat losses are assumed to be minimized [17]. It is considered that taking pressure data over the nozzle wall including both converging and diverging section and nozzle exit will be good in terms of proving that the nozzle designed by one-dimensional theory works as expected. But, only the nozzle inlet pressure was compared which was calculated using one-dimensional theory with measured pressure data in the experimental tests. The calculated nozzle outlet pressure is also given in Appendix-3.

Mach 2 free-jet nozzle was designed in the scope of the thesis about designing parameters of HATS [2]. Hence, Mach 2.5 free-jet nozzle is also designed and tested besides Mach 2 free-jet nozzle in this study. The free-jet nozzle dimensions are calculated by using inputs given in Table 2-5.

Table 2-5. Inputs for Mach 2.5 Free-Jet Nozzle Design.

γ	1.4
\dot{m} , kg/s	1
T_t , K	290
R_u , J/kmol.K	8314.3
MW , kg/kmol	28.96
P_{ex} , Pa	10000

The specific gas constant for dry air, R is calculated as 287 J/kg.K using Equation 2-3.

$$R = \frac{R_u}{MW} \quad (2-3)$$

Free-jet nozzle exit pressure must be equal or higher than the test chamber pressure. Hence, free-jet nozzle exit pressure input comes from the same condition for Mach 2. The exit pressure is taken as an input to obtain required total pressure at the inlet of the free-jet nozzle using Equation 2-4.

$$P_t = P_{ex} \left[1 + \frac{\gamma - 1}{2} M^2 \right]^{\frac{\gamma}{\gamma - 1}} \quad (2-4)$$

The free-jet nozzle inlet total pressure, P_t is calculated as 1.7 bar. Entrainment ratio, ER for HATS can be described as the ratio of secondary mass flow rate of the free-jet nozzle to primary mass flow rate of the ejector nozzle. The mass flow rate of the ejector nozzle is known from the capability of the test facility as 3 kg/s. So, by considering ER as 0.33, mass flow rate of the free-jet nozzle can be taken as 1 kg/s [2]. Then, the required throat area to choke this much mass flow rate can be calculated using Equation 2-5.

$$A_{th} = \frac{\dot{m}}{P_t} \sqrt{T_t} \frac{1}{\sqrt{\frac{\gamma}{R} \left(\frac{2}{\gamma + 1} \right)^{\frac{\gamma + 1}{\gamma - 1}}}} \quad (2-5)$$

The throat diameter is then calculated as 56.2 mm using Equation 2-6.

$$D_{th} = \sqrt{\frac{4A_{th}}{\pi}} \quad (2-6)$$

By using the calculated throat area, the exit area of the free-jet nozzle can be calculated using Equation 2-7.

$$A_{ex} = (A_{th}) \frac{1}{M} \left[\frac{1 + \left[\frac{\gamma - 1}{2} \right] M^2}{1 + \left[\frac{\gamma - 1}{2} \right]} \right]^{\frac{\gamma + 1}{2(\gamma - 1)}} \quad (2-7)$$

The exit diameter is then calculated as 91.2 mm using Equation 2-8.

$$D_{ex} = \sqrt{\frac{4A_{ex}}{\pi}} \quad (2-8)$$

The designed Mach 2.5 free-jet nozzle is given in Figure 2-15.

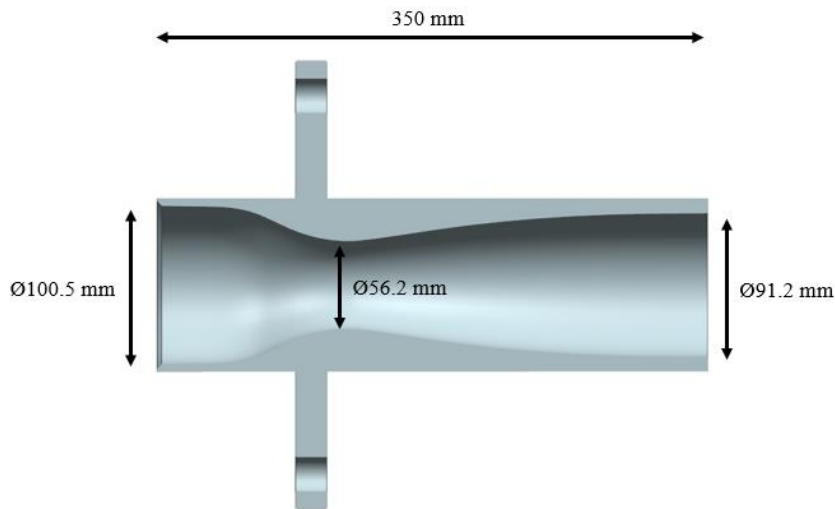


Figure 2-15. Mach 2.5 Free-Jet Nozzle.

The designed Mach 2.5 free-jet nozzle is also numerically analyzed to observe the full flow of the nozzle as expected according to the design condition. Half model solution domain is used for CFD analysis because of the symmetry. Closer view to the mesh of the free-jet nozzle is given on the symmetry plane in Figure 2-16.

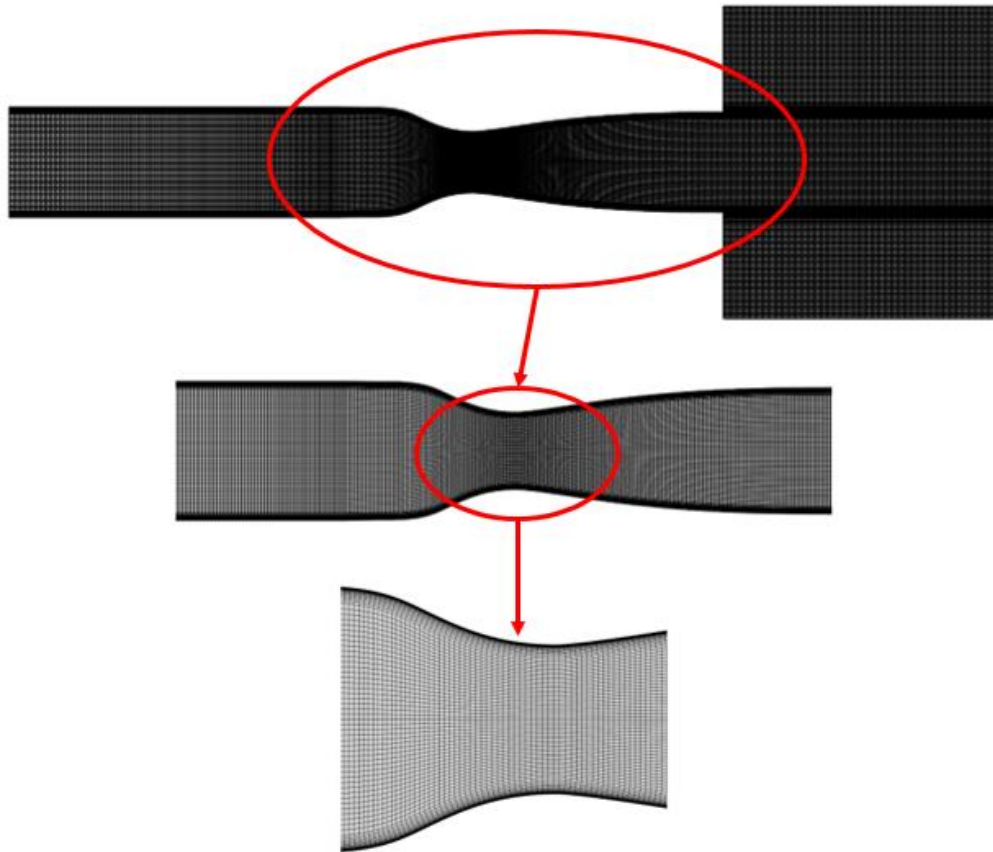


Figure 2-16. Closer View to the Grid.

Almost 2 million hexahedral elements with the size of around 2 mm are used for the mesh of Mach 2.5 free-jet nozzle exhausting to the atmosphere. Maximum skewness of the mesh elements is 0.6. The Mach number distribution at the free-jet nozzle exit plane is given in Figure 2-17.

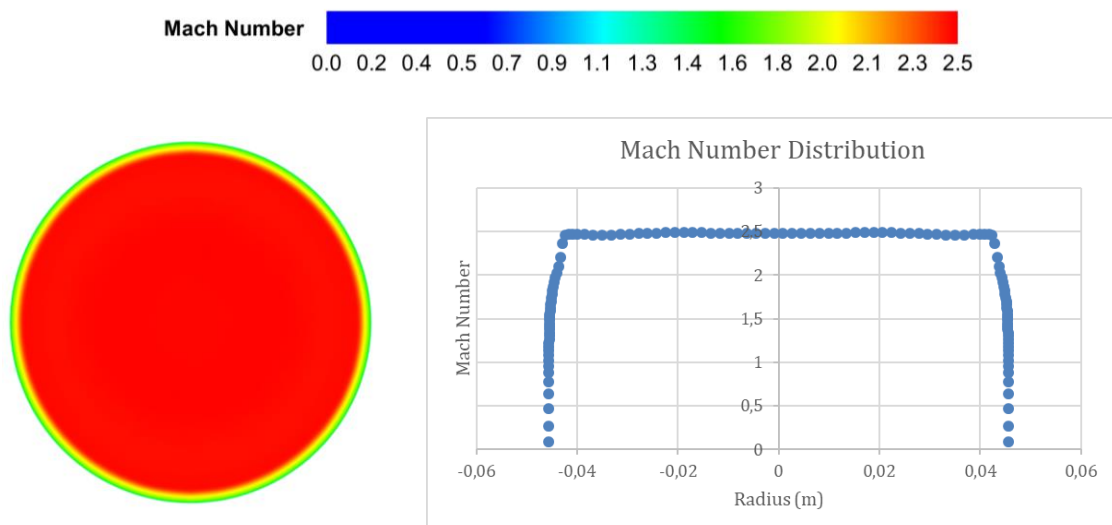


Figure 2-17. Mach Number Distribution at the Free-Jet Nozzle Exit Plane.

The distribution of Mach number can be clearly seen in the contour that the flow is full as expected according to the design condition of the free-jet nozzle with exit pressure is equal to the atmospheric pressure. Hence, flow is uniform and ideally expanded to the atmosphere at the exit of the free-jet nozzle. The effective free-jet nozzle exit diameter is calculated as 83.4 mm compared to the exact free-jet nozzle exit diameter of 91.2 mm calculated using one-dimensional nozzle theory. This condition can also be seen in the contour of Mach number in Figure 2-18 on the symmetry plane for Mach 2.5 free-jet nozzle.

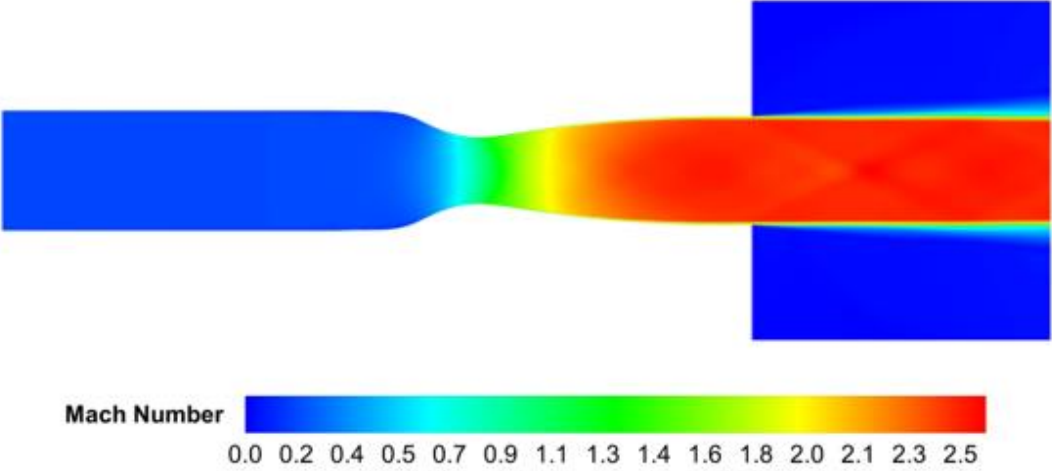


Figure 2-18. Contour Plot of Mach Number on the Symmetry Plane.

2.3. Experimental Results

In experimental tests, the ejector nozzle is pressurized first and then the free-jet nozzle starts to work. Ejector nozzle is considered as working at its optimum condition to satisfy the low pressure environment inside the test chamber. Ejector nozzle provides the primary flow of the test setup. Ejector nozzle inlet pressure is almost 20 bar and constant during all the tests. The pressure data is given in Figure 2-19.

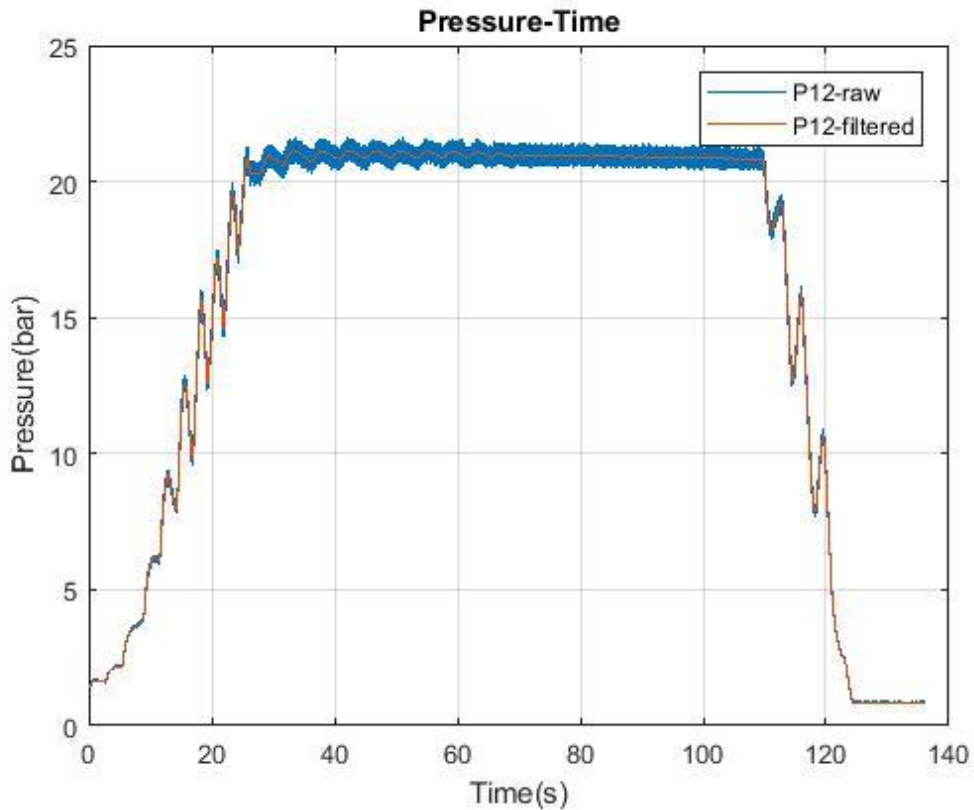


Figure 2-19. Ejector Nozzle Feed Manifold Pressure.

The mass flow rate corresponding to that pressure is 3 kg/s. Tests last 150 s on average. Pressure data is sampled at 25 kHz frequency and then filtered by allowing the passage of low frequency signals with 200 Hz cut-off frequency. Test Section Diffuser-Ejector Nozzle Feed Manifold Connection pressure is given in Figure 2-20.

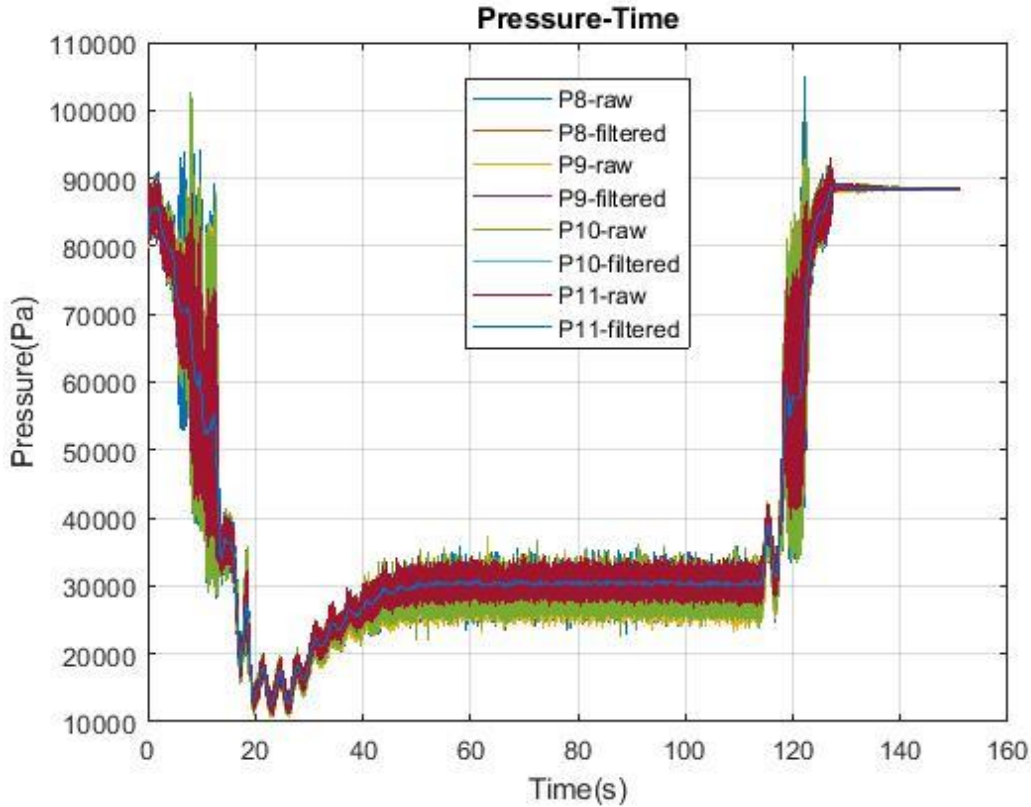


Figure 2-20. Test Section Diffuser-Ejector Nozzle Feed Manifold Connection Pressure.

Pressure data is sampled from different angular and axial locations to control any difference in the sampling data. The pressure value of this section is also used for CFD analyses as pressure outlet boundary condition. According to the design of HATS setup, 1 kg/s mass flow rate of secondary flow with ER of 0.33, pressure is obtained here as almost 28000 Pa for Mach 2 free-jet nozzle and 25000 Pa for Mach 2.5 free-jet nozzle.

The pressure changes with mass flow rate of the secondary flow and is constant for different blockage ratios of Mach 2 and 2.5 free-jet nozzles. The pressure values corresponding to the mass flow rate of secondary flow are given in Table 2-6 and Table 2-7.

Table 2-6. Mass Flow Rate vs. Pressure [Mach 2 Free-Jet Nozzle].

Valve Opening, %	Mass Flow Rate, g/s	Pressure, Pa
18	750	24000
25	1100	29000
35	1500	35500
40	1900	44000

Table 2-7. Mass Flow Rate vs. Pressure [Mach 2.5 Free-Jet Nozzle].

Valve Opening, %	Mass Flow Rate, g/s	Pressure, Pa
18	750	20500
30	1300	25500
35	1500	27700
40	1900	34500

The vacuum pressure measured in the test section diffuser-ejector nozzle feed manifold connection according to the increasing mass flow rate for both of Mach 2 and 2.5 free-jet nozzles is given in Figure 2-21.

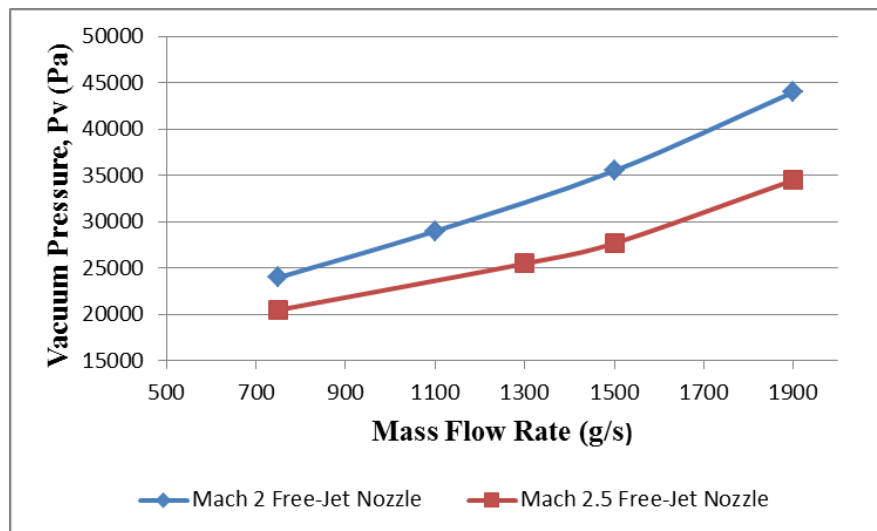


Figure 2-21. Vacuum Pressure vs. Mass Flow Rate.

The supersonic flow at the inlet of the diffuser turns into subsonic flow along the diffuser. Then, the subsonic flow pressure increases as expected throughout the connection as comparable between Figure 2-20 and Figure 2-22. Test Section Diffuser pressure is given in Figure 2-22.

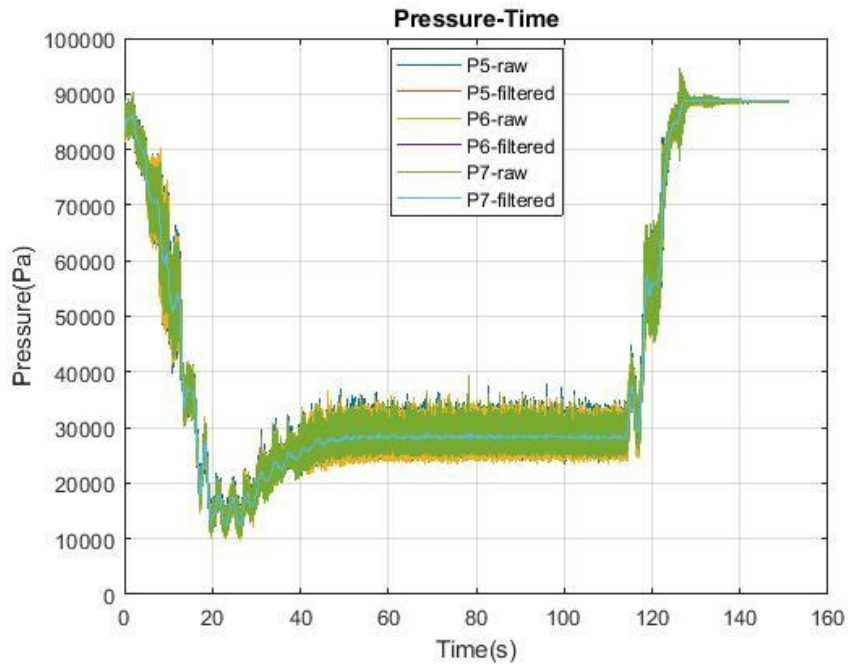


Figure 2-22. Test Section Diffuser Pressure.

The test chamber pressure is plotted according to the mass flow rate and inlet pressure of the free-jet nozzle and blockage ratio for Mach 2 and 2.5 free-jet nozzles as seen from Figure 2-23 to Figure 2-28.

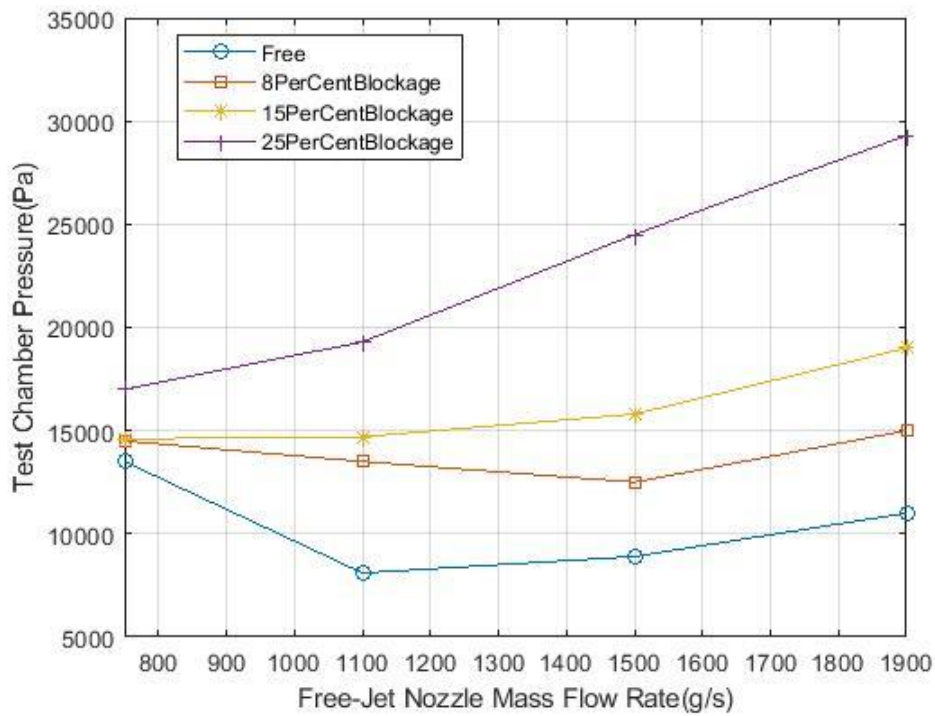


Figure 2-23. Test Chamber Pressure vs. Free-Jet Nozzle Mass Flow Rate [Mach 2].

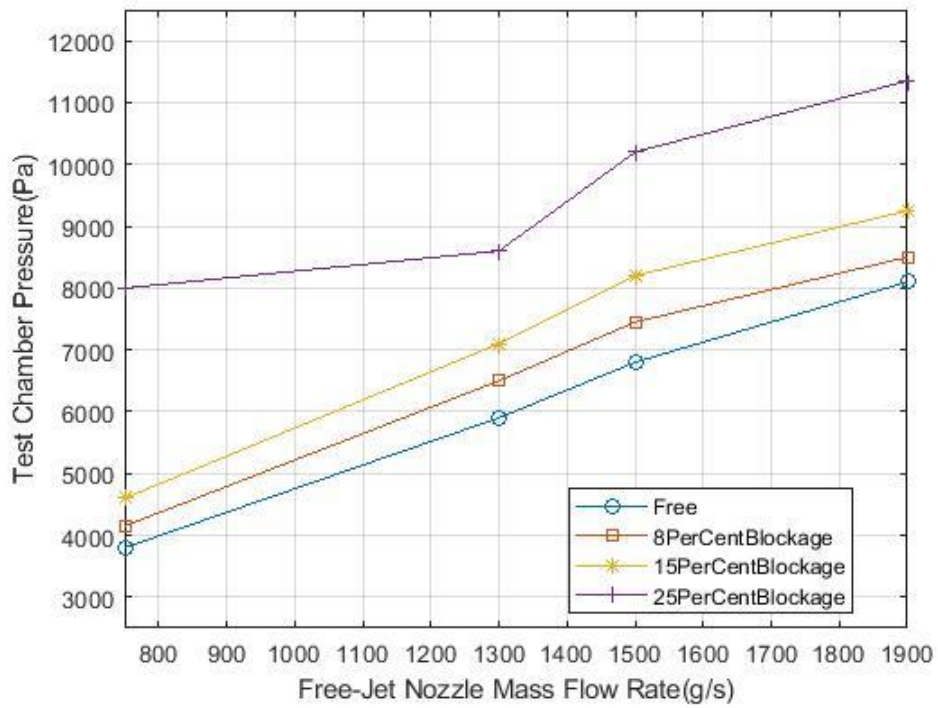


Figure 2-24. Test Chamber Pressure vs. Free-Jet Nozzle Mass Flow Rate [Mach 2.5].

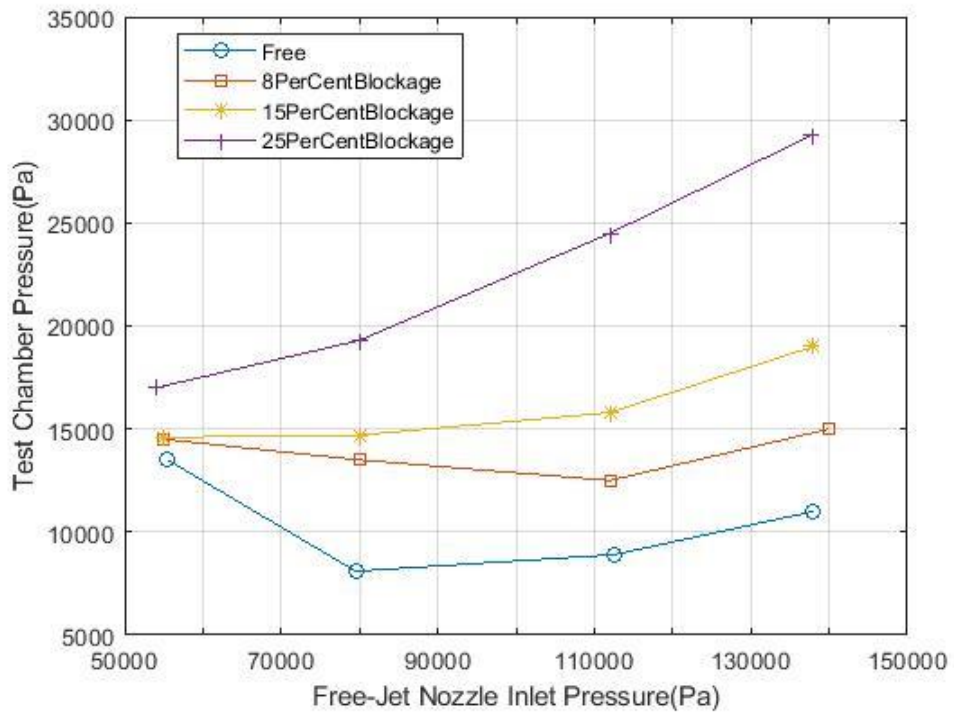


Figure 2-25. Test Chamber Pressure vs. Free-Jet Nozzle Inlet Pressure [Mach 2].

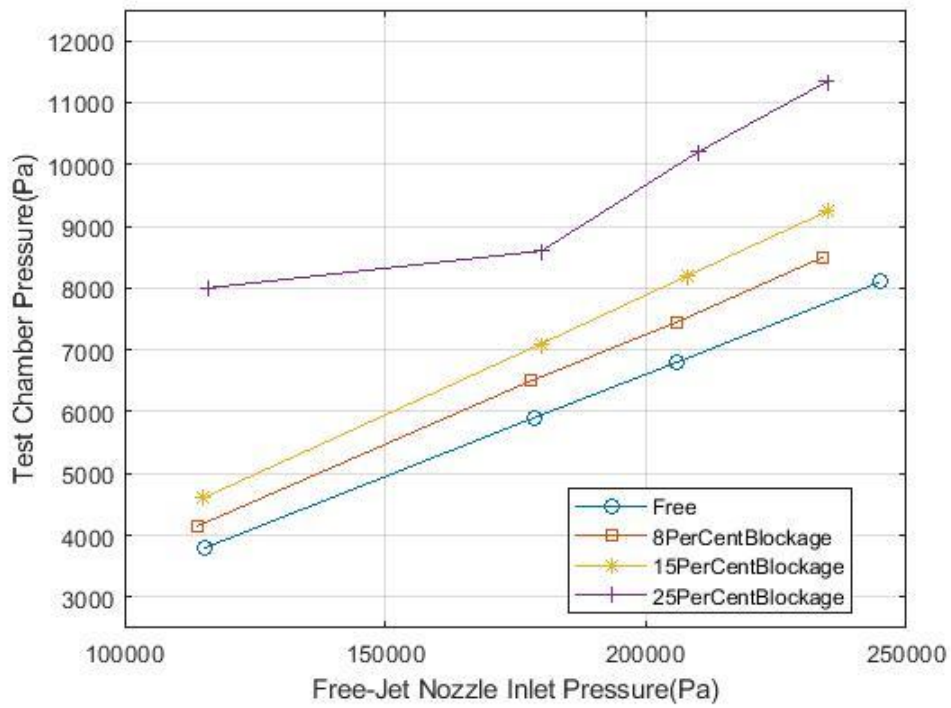


Figure 2-26. Test Chamber Pressure vs. Free-Jet Nozzle Inlet Pressure [Mach 2.5].

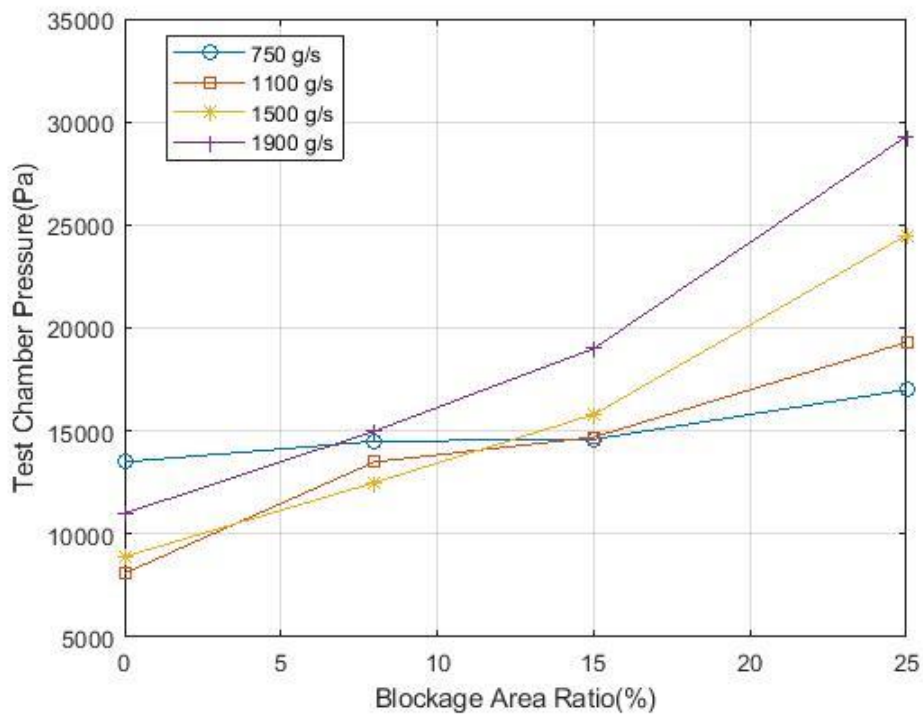


Figure 2-27. Test Chamber Pressure vs. Blockage Area Ratio [Mach 2].

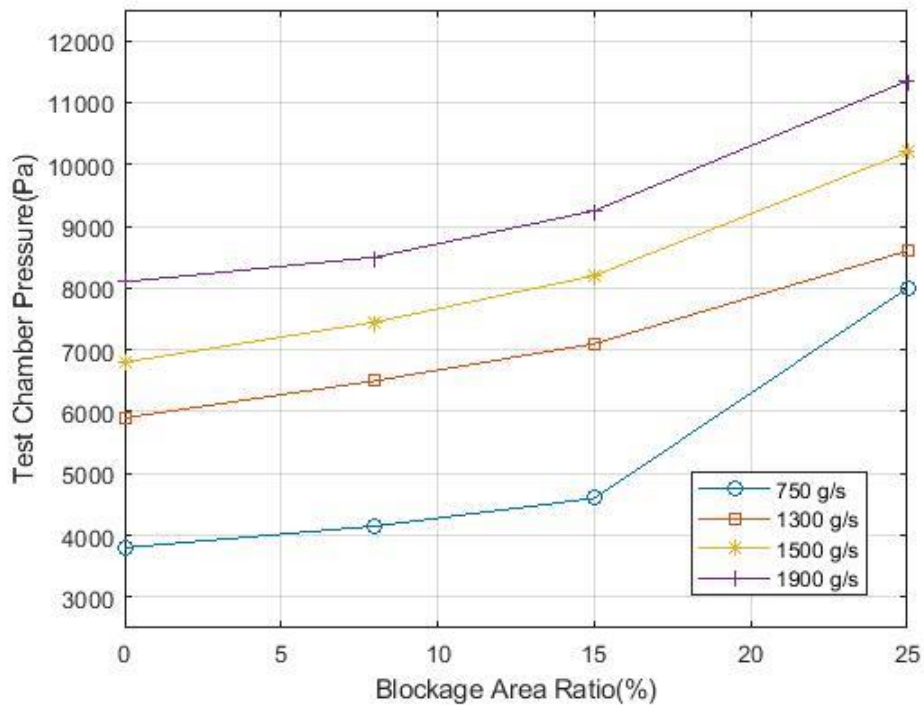


Figure 2-28. Test Chamber Pressure vs. Blockage Area Ratio [Mach 2.5].

Plot according to the free-jet nozzle mass flow rate is actually another form of the plot according to the free-jet nozzle inlet pressure. This can be seen from the similarity of the plots. Plots of the test chamber pressure according to the blockage ratio for different mass flow rates in Figure 2-27 and Figure 2-28 are achieved actually as the most important results to determine the characteristics of the test setup. It was seen that an almost linear curve can be fitted to the obtained data from the experimental test results for Mach 2.5 free-jet nozzle but not for Mach 2. This is also due to the unstart condition of the Mach 2 free-jet nozzle.

It is also expected that by increasing the mass flow rate, the test chamber pressure also increases as seen in Figure 2-24 for Mach 2.5 free-jet nozzle. But, Mach 2 free-jet nozzle does not fully comply with this rule as seen in Figure 2-23 and at some points of the plot, test chamber pressure falls under the pressure of the lower mass flow rate condition. This is also observed that the test chamber pressure increases proportionally up to 25% blockage rate. After 25% blockage rate, the test chamber pressure will increase at relatively higher rates and it is evaluated that the vacuum test condition cannot be achieved for the test articles to be tested both for Mach 2 and 2.5 free-jet nozzles.

2.3.1. Experimental Data from Tests

First the ejector nozzle starts working and reaches at steady state condition and then the free-jet nozzle starts to provide secondary flow as can be seen from the graphics. The most important one among these data is considered to be the test chamber pressure. The test chamber pressure is given in Figure 2-29 as an example.

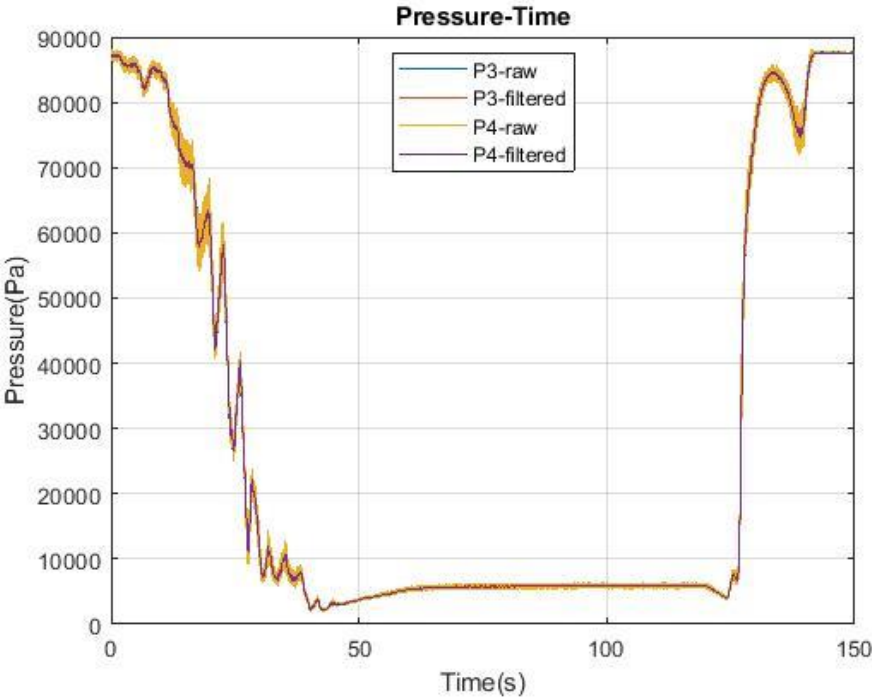


Figure 2-29. Test Chamber Pressure.

The pressure inside the test chamber drops to a lower pressure value from the stagnant ambient pressure during the start-up period when just the ejector operates and supplies the primary flow in the test setup. In this situation, some air is also drawn from the free-jet nozzle. But, the amount of the air is low compared to the operation mode and fails to meet the required Mach number test condition. The mass flow rate of the air for the free-jet nozzle is given in Figure 2-30 as an example.

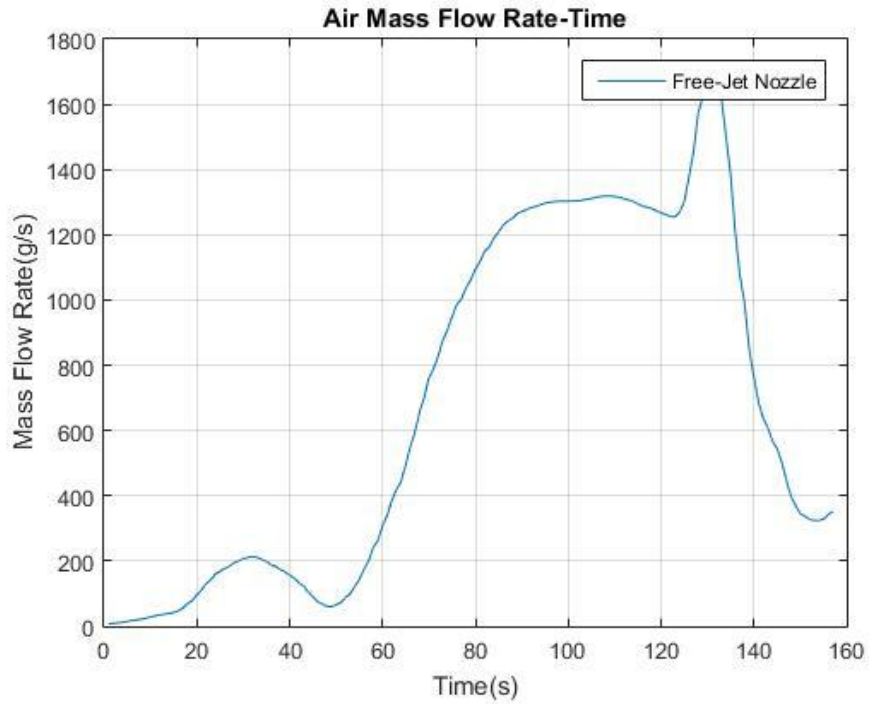


Figure 2-30. Free-Jet Nozzle Air Mass Flow Rate.

Then, the required Mach number test can be performed with the secondary flow from the free-jet nozzle. It is seen that the free-jet nozzle inlet pressure increases with the secondary flow. Inlet pressure of the free-jet nozzle is given in Figure 2-31 as an example.

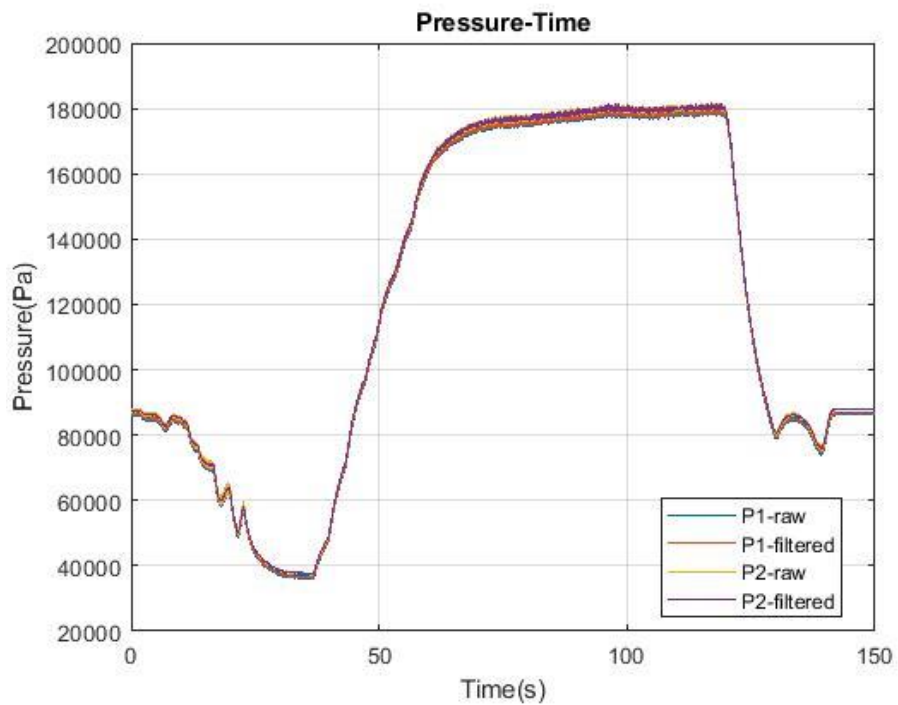


Figure 2-31. Free-Jet Nozzle Inlet Pressure.

During these experimental tests, temperature data from the test chamber and the ejector nozzle feed manifold connection is also collected. The temperature data appears to be similar and almost the same for all test conditions. Temperature data is given in Figure 2-32 as an example.

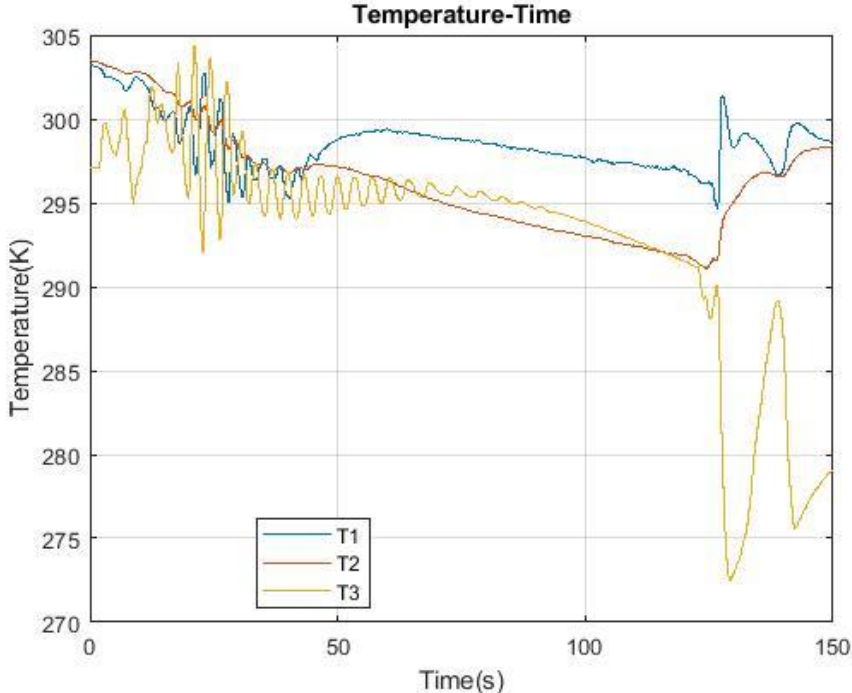


Figure 2-32. Test Chamber and Ejector Nozzle Inlet Temperature.

The mass flow rate and inlet pressure of the free-jet nozzle, test chamber pressure and temperature are collected for all test conditions separately and given in Appendix-4 by test order.

3. NUMERICAL INVESTIGATION

3.1. Introduction

The fluid flow of the HATS is numerically investigated utilizing the commercially available ANSYS Fluent software in this study. CFD analyses are performed in ANSYS Fluent 19.2 that has large capabilities to simulate flow, turbulence and heat transfer for many applications that the industry needs. Some essential notes about numerical methodology and its application to the solution of the HATS are given in this chapter. CFD solver settings and governing equations behind the solver is studied to obtain closer solutions to the experimental test results for the considered solution domain.

The governing equations and turbulence model are given lengthily in Section 3.2 and Section 3.3, respectively. The computational domain, CFD solver setup and grid sensitivity study are also presented in Section 3.4. The numerical results are given for each test conditions separately in Section 3.5. Finally, the comparison of these experimental test results with numerical results according to the test chamber pressure and Schlieren images are also given in Section 3.6.

3.2. Governing Equations

Conservation of mass, momentum and energy are the fundamental laws that are utilized to derive governing equations that are solved in a CFD analysis. Conservation of mass and momentum are solved for all flows in ANSYS Fluent. The extra equation of energy conservation is also solved for flows including compressibility. Density is related to pressure and temperature by using a special equation for compressible flows. Ideal gas equation is the most commonly used equation of state given in Equation 3-1. But when it comes to a situation as the non-ideal gas behavior, this equation of state can be very complex [18].

$$P = \rho RT \quad (3-1)$$

Conservation equations of mass, momentum and energy are solved coupled and simultaneously. There are 6 scalar unknowns totally which are density, pressure, temperature and 3 velocity components. These unknowns are obtained by using 6 scalar equations which are conservation of mass, conservation of energy, 3 components of conservation of momentum and equation of state.

Conservation of mass that is also known as continuity equation is given in Equation 3-2. This equation can be thought more precisely that net mass crossing the boundaries of the system must be balanced. Equation 3-2 is the general form of the continuity equation where S_m is the source of the mass added from the second phase to the continuous phase or any user defined sources [18].

$$\frac{\partial \rho}{\partial t} + \nabla \cdot (\rho \vec{V}) = S_m \quad (3-2)$$

Equation for the conservation of linear momentum can be expressed as given in Equation 3-3. Where \vec{F} is the external body force acting over the entire volume and $\rho \vec{g}$, the most common body force is the force due to the gravitational acceleration, \vec{g} [18].

$$\frac{\partial}{\partial t} (\rho \vec{V}) + \nabla \cdot (\rho \vec{V} \vec{V}) = -\nabla p + \nabla \cdot (\bar{\bar{\tau}}) + \rho \vec{g} + \vec{F} \quad (3-3)$$

$\bar{\bar{\tau}}$ is the stress tensor described in Equation 3-4. Where μ is the dynamic viscosity and I is the unit tensor [18].

$$\bar{\bar{\tau}} = \mu \left[(\nabla \vec{V} + \nabla \vec{V}^T) - \frac{2}{3} \nabla \cdot \vec{V} I \right] \quad (3-4)$$

The conservation of energy equation is used to obtain the temperature of the fluid for compressible flows and problems involving heat transfer. ANSYS Fluent solves the energy equation as given in Equation 3-5.

$$\frac{\partial}{\partial t} (\rho E) + \nabla \cdot (\vec{V} (\rho E + p)) = \nabla \cdot \left(k_{eff} \nabla T - \sum_j h_j \vec{J}_j + (\bar{\bar{\tau}}_{eff} \cdot \vec{V}) \right) + S_h \quad (3-5)$$

The first three terms on the right hand side of the equation represent conduction energy transfer, diffusion of species and viscous dissipation, respectively. E is described as given in Equation 3-6 [18].

$$E = h - \frac{p}{\rho} + \frac{V^2}{2} \quad (3-6)$$

3.3. Turbulence Model

The fundamental element for numerical solution involving fluid flow problems is modelling of the turbulence. It is very difficult to cover all the details of the turbulent flow with high Reynolds numbers in a complex 3D solution domain. This difficulty comes from the unsteady behaviour of the turbulent flow involving both large and extremely small eddies. Extremely small volume and time discretizations must be chosen in numerical analyses but this exceeds today's computational power. There are different turbulence models separately used today that can predict only some types of the turbulent flows more accurately. They all contain empiric constants which are fitted to the values so the numerical analyses predict the results closer to the known experimental results. The ANSYS Fluent enables use of different turbulence models, starting from one equation Spalart-Almaras Model to five equation Reynolds Transport Model.

Bartosiewicz et al. [19] have compared numerical analysis results with experimental results for different turbulence model approaches and indicated that SST $k-\omega$ model seems to be convenient for ejector analysis. Kolar and Dvorak [20] have also confirmed that SST $k-\omega$ model is well suited for ejector analysis by comparing the numerical analysis results with experimental results with regard to the vacuum pressure and color Schlieren images. The SST $k-\omega$ turbulence model is selected for use in this study due to the results of [19] and [20].

The SST $k-\omega$ turbulence model is a two-equation hybrid model combining the $k-\omega$ and the $k-\varepsilon$ models that is used for many aerodynamic applications. The $k-\omega$ model is appropriate for flow simulation in the viscous sublayer and the $k-\varepsilon$ model is well adapted for predicting turbulent region flow behavior away from the wall [21].

The SST $k-\omega$ model solves two transport equations in addition to the governing conservation equations. The turbulent kinetic energy, k and specific turbulent dissipation rate, ω are the two variables used in SST $k-\omega$ turbulence model.

The turbulent kinetic energy, k is given in Equation 3-7. The turbulence intensity, I is the level of the turbulence and is given in Equation 3-8 where u' is the root-mean-square of the turbulence velocity fluctuations given in Equation 3-9. The mean velocity, U is also calculated as given in Equation 3-10.

$$k = \frac{3}{2}(UI)^2 \quad (3-7)$$

$$I = \frac{u'}{U} \quad (3-8)$$

$$u' = \sqrt{\frac{1}{3}(u'_x{}^2 + u'_y{}^2 + u'_z{}^2)} \quad (3-9)$$

$$U = \sqrt{(U_x{}^2 + U_y{}^2 + U_z{}^2)} \quad (3-10)$$

The specific turbulent dissipation rate, ω can be calculated as given in Equation 3-11. C_μ is the constant of the turbulence model and the turbulent length scale, l defines the size of large energy-containing eddies in a turbulent flow which can be taken as $\sim 7\%$ of the hydraulic diameter for codes based on the mixing-length as used in Fluent, for instance [22].

$$\omega = C_\mu^{\frac{3}{4}} \frac{k^{\frac{1}{2}}}{l} \quad (3-11)$$

The dimensionless wall distance, y^+ should be approximately 1 for SST k- ω turbulence model because SST has no wall function and utilizes near wall model approach. It is a must that the mesh is properly sized near the wall to obtain an accurate simulation for the fluid flow. Therefore, some calculations should be performed to find the appropriate first cell height near the wall.

The calculations are based on flat-plate boundary layer theory [23]. First, the Reynolds number is calculated using Equation 3-12. Second, the skin friction coefficient, C_f is calculated using Equation 3-13.

$$Re = \frac{\rho UL}{\mu} \quad (3-12)$$

$$C_f = \frac{0.026}{Re^{\frac{1}{7}}} \quad (3-13)$$

Then, the wall shear stress and frictional velocity can be calculated using Equation 3-14 and Equation 3-15, respectively.

$$\tau_{wall} = \frac{C_f \rho U^2}{2} \quad (3-14)$$

$$U_{fric} = \sqrt{\frac{\tau_{wall}}{\rho}} \quad (3-15)$$

Finally, the height of the first mesh cell can be calculated using Equation 3-16 based on the predetermined value of y^+ of the selected turbulence model.

$$\Delta s = \frac{y^+ \mu}{U_{fric} \rho} \quad (3-16)$$

3.4. Solution Domain

The analysis model of the HATS consists of free-jet nozzle, test chamber and diffuser that is given schematically in Figure 3-1.

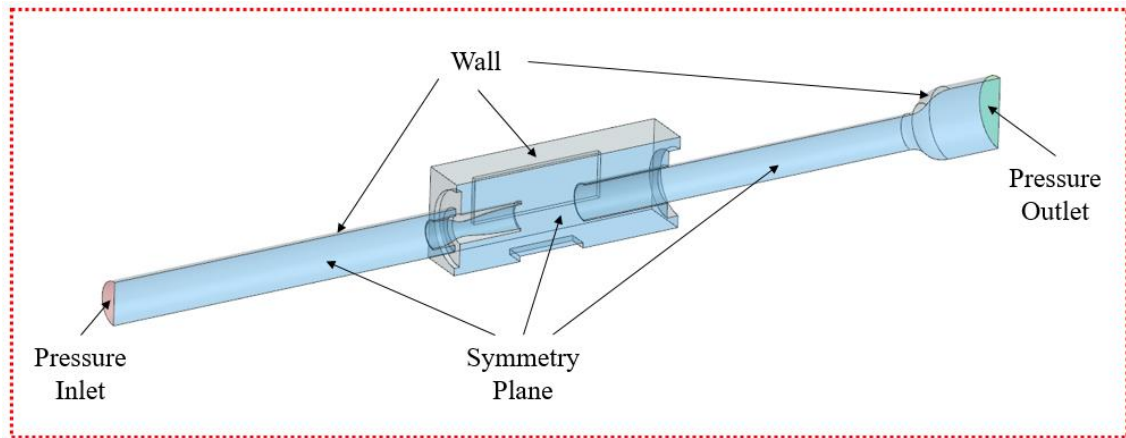


Figure 3-1. Solution Domain of the Test Chamber without Blockage Test Article and Boundary Conditions.

Ejector is assumed working at its optimum condition and gives the pressure outlet boundary condition to the analyses. The diffuser is cut from the exact position of the pressure transducer for pressure outlet boundary condition. Pressure inlet also comes from the experimental tests. Pressure transducer location is taken exactly as where the pressure is measured before the free-jet nozzle along the pipe. Free-jet nozzle supplies the secondary flow to the test chamber.

The blockage test articles are also supported between the free-jet nozzle exit plane and diffuser inlet plane inside the test chamber. Figure 3-2 shows the solution domain for Mach 2.5 free-jet nozzle and 8% blockage ratio as an example.

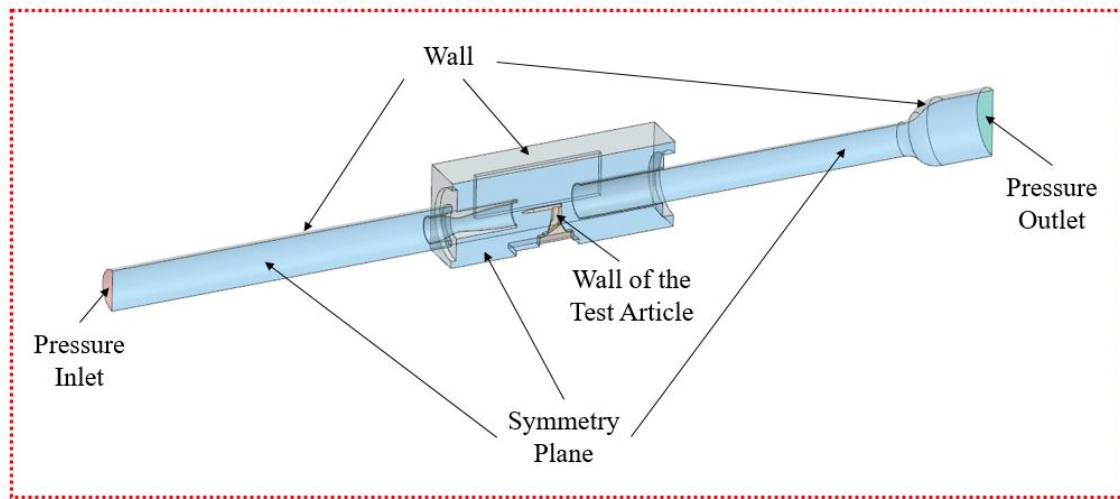


Figure 3-2. Solution Domain of the Test Chamber with Blockage Test Article and Boundary Conditions.

The solution domain for other blockage test articles is also prepared with the same manner. Half model solution domain that is given in Figure 3-3 can be used for 3D numerical analyses because of the symmetry.

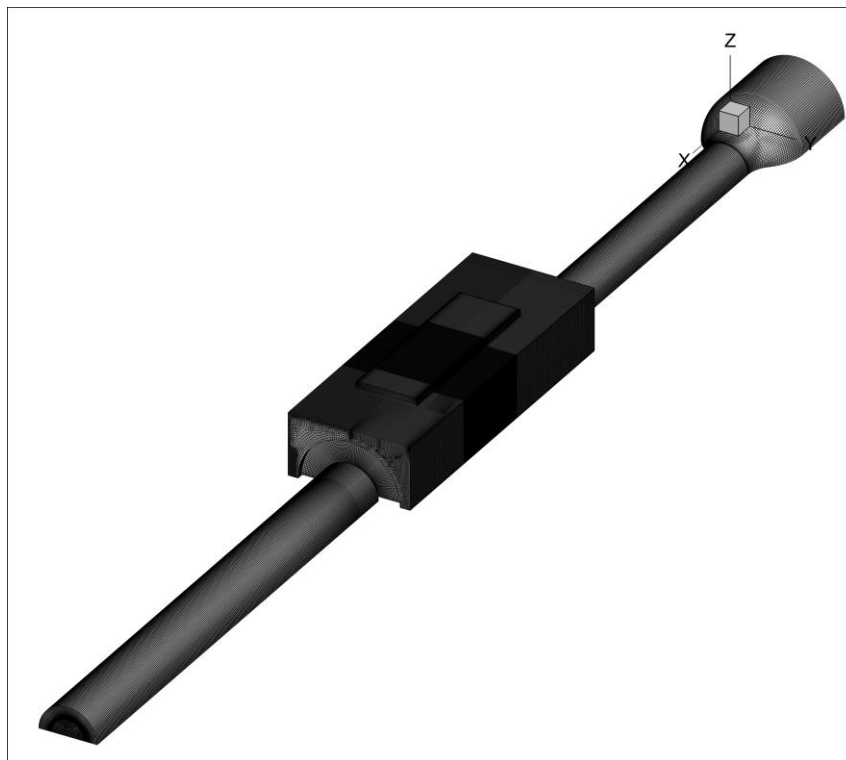


Figure 3-3. Half Model Solution Domain.

Almost 10 million hexahedral elements with the size of around 2 mm are used for the mesh of Mach 2.5 free-jet nozzle without blockage. There is no skewed elements above 0.7. Hex elements are easily used for the mesh because of the simplicity of the solution domain by splitting the analysis model at the right locations. The closer view to the grid of the test chamber and the free-jet nozzle is given in Figure 3-4 as an example.

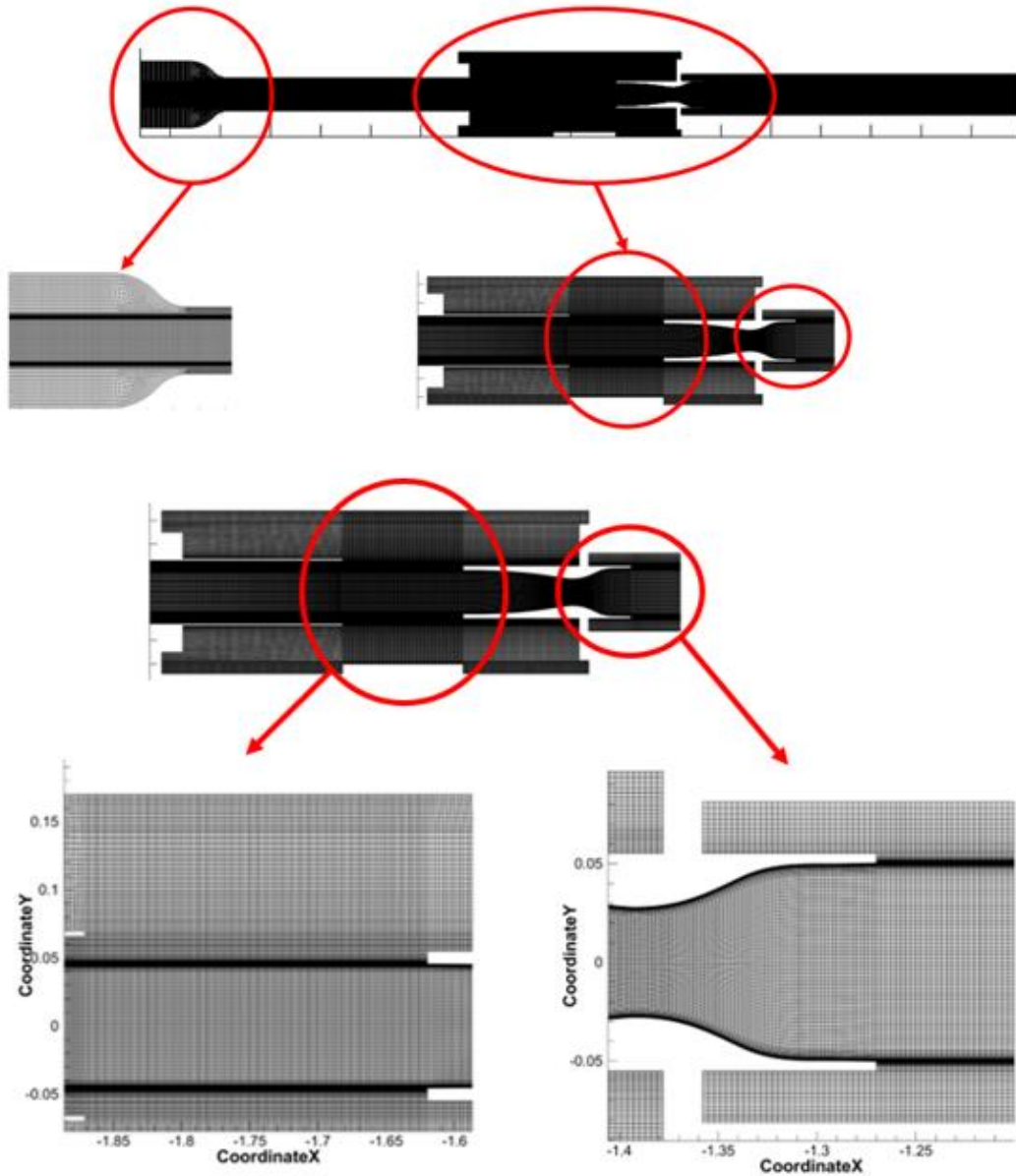


Figure 3-4. Closer View to the Grid of the Test Chamber and Mach 2.5 Free-Jet Nozzle without Blockage.

Almost 20 million hexahedral and tetrahedral elements with the size of around 2 mm are used for the mesh of Mach 2.5 free-jet nozzle with 8% blockage. Because of the use of the tet and hex elements, the size of the elements are tried to keep as minimum as possible. The average skewness is around 0.2, some skewed elements above 0.9 level are at the location of not affecting the main stream of the flow. The closer view to the grid of the test chamber with blockage and the free-jet nozzle is given in Figure 3-5 as an example.

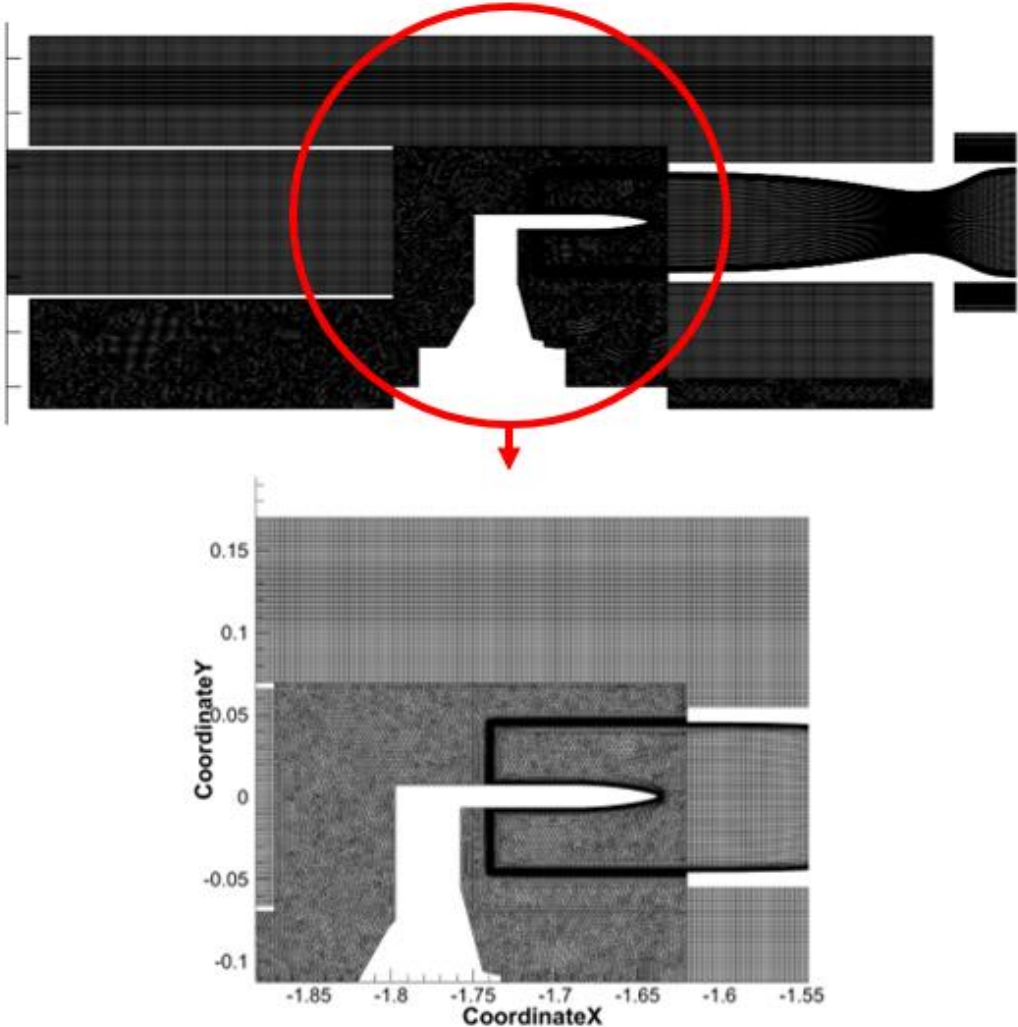


Figure 3-5. Closer View to the Grid of the Test Chamber for Mach 2.5 Free-Jet Nozzle with 8% Blockage.

3.4.1. Fluent CFD Solver Setup

Fluent solver setup provides the following solver settings to solve the HATS solution domain,

- Single-phase fluid motion in steady state
- 3D viscous analyses with coupled pressure-based solver
- Dry air as working fluid
- Compressible flow of air with ideal gas equation

The continuity residual is monitored during the CFD analyses. The inlet and outlet mass flow rates are also compared besides the continuity residual convergence condition. The average iteration number of the analyses is taken as 1500 for the solution to converge in accordance with the conditions that net mass flow rate is almost zero and continuity residuals are at the level of $1e-03$. The CFD solver setup is given in Table 3-1.

Table 3-1. CFD Solver Setup.

Time Dependency	Steady State
Geometry	3D - Half Model
Turbulence Model	SST k- ω
Solution Methods	Double Precision (Coupled Solver)
Pressure Discretization	Second-Order
Density Discretization	Second-Order Upwind
Momentum Discretization	Second-Order Upwind
Turbulent Kinetic Energy Discretization	Second-Order Upwind
Specific Dissipation Rate	Second-Order Upwind
Energy Discretization	Second-Order Upwind

3.4.2. Grid Sensitivity

A grid sensitivity analysis is performed for the test chamber and diffuser system by using coarse, medium and fine mesh for numerical analyses which results around 4.5, 9 and 24 million elements, respectively. The closer view to the grid of the test chamber section of the solution domain on the symmetry plane is given in Figure 3-6, Figure 3-7 and Figure 3-8 for coarse, medium and fine grid, respectively.

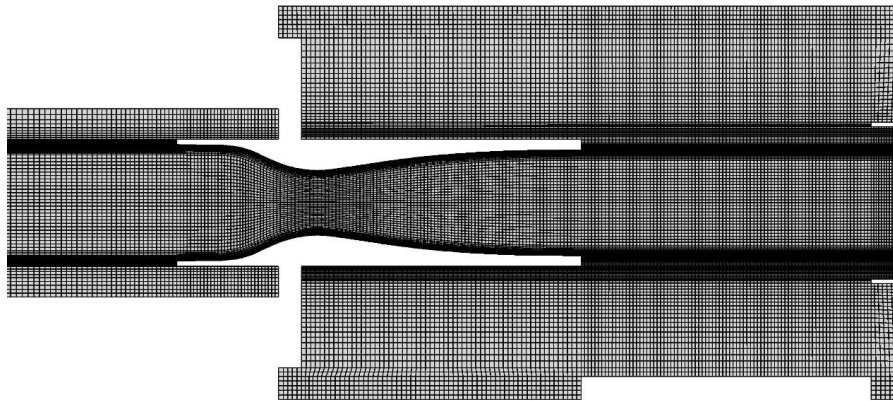


Figure 3-6. Closer View to the Grid of the Test Chamber for Coarse Grid.

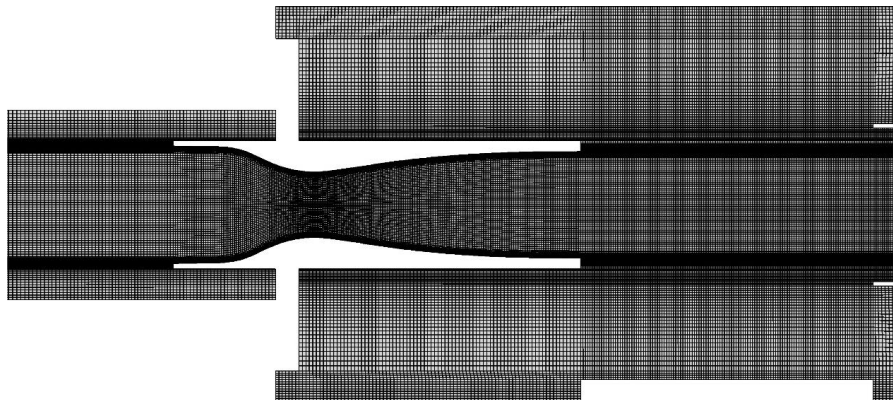


Figure 3-7. Closer View to the Grid of the Test Chamber for Medium Grid.

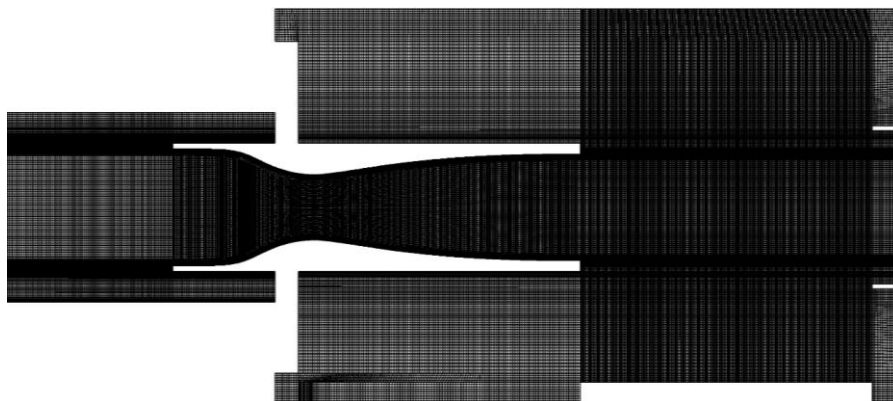


Figure 3-8. Closer View to the Grid of the Test Chamber for Fine Grid.

The grid sensitivity study has been performed only for Mach 2.5 free-jet nozzle and the same grid architecture is used for Mach 2 free-jet nozzle. The grid sensitivity analysis is performed for Mach 2.5 free-jet nozzle with ER of 0.33. The other boundary conditions are also given in Table 3-2.

Table 3-2. Boundary Conditions for Grid Sensitivity Analysis.

Parameter	Value
Free-Jet Nozzle Inlet Pressure, Pa	178500
Free-Jet Nozzle Inlet Temperature, K	290
Entrainment Ratio, ER	0.33
Free-Jet Nozzle Mass Flow Rate, kg/s	1
Test Section Diffuser Outlet Pressure, Pa	25500

The test chamber pressures, that are obtained at the location of the pressure sensor, P3 are predicted as 6375 Pa, 6325 Pa and 6300 Pa for coarse, medium and fine grids, respectively. The number of elements versus the test chamber pressure is given in Figure 3-9.

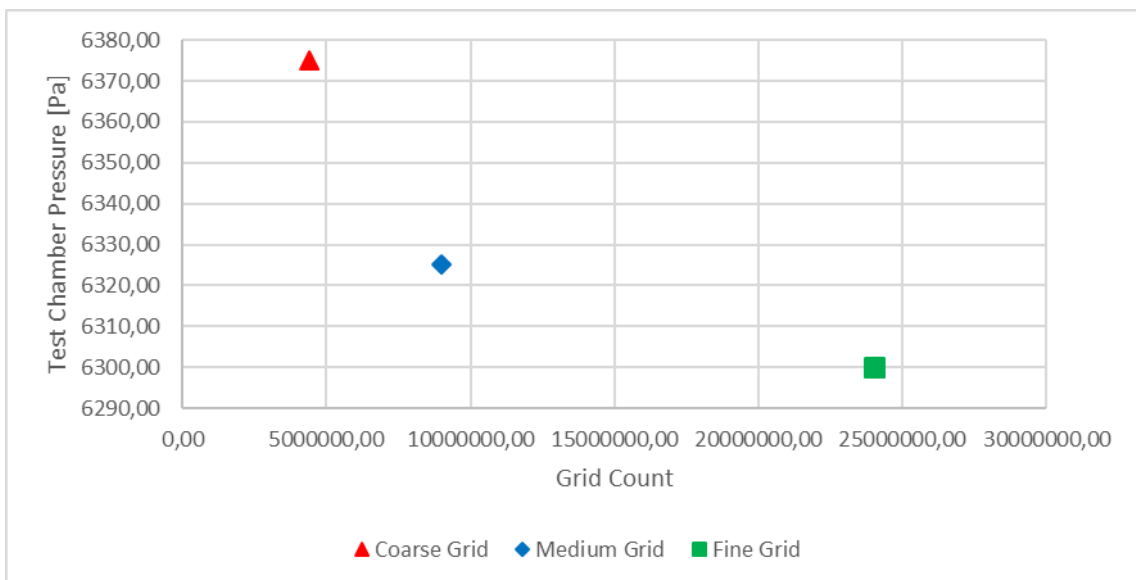


Figure 3-9. Test Chamber Pressure vs. Grid Count.

The test chamber pressure value prediction for coarse grid differs as 0.8% from medium grid and for medium grid differs as 0.4% from the fine grid. The computational time is around one day, two days and five days for 24 processes of parallel solver with 56 physical cores of a computer for coarse, medium and fine grid, respectively.

Mach number variation along the axial direction on the symmetry plane and numerical Schlieren images for coarse, medium and fine grids are given in Figure 3-10.

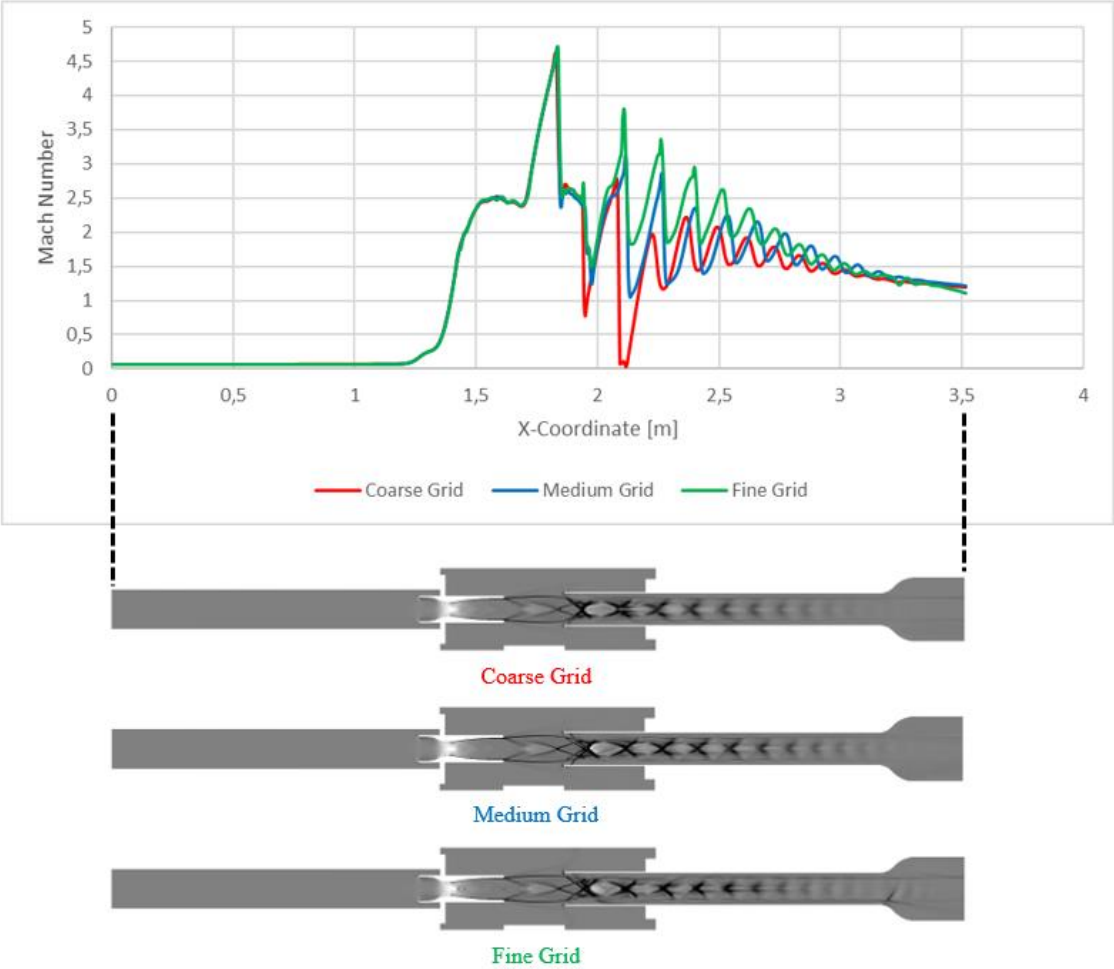


Figure 3-10. Mach Number Variation Along the X-Axis Throughout the Solution Domain and Mach Number Contour Plots for Coarse, Medium and Fine Grids.

While it seems that the coarse grid solution could not catch the trend change, medium and fine grid solutions make similar predictions, which shows that the solution no longer needs to improve the grid. Thus, medium grid is chosen to be used in numerical analyses of the high altitude test system in this thesis.

3.5. Numerical Results

In numerical analyses, different cases are simulated to compare the test chamber static pressure with pressure measurements from the experimental tests. The test chamber pressure is simulated for different test conditions of Mach 2 and 2.5 free-jet nozzles. Solution domain is kept minimum including free-jet nozzle, test chamber and diffuser to reduce the computational time. The numerical simulations for the free-jet nozzles are repeated for different secondary mass flow rates, i.e changing ER with and without blockage. For the numerical simulations, first significant data is the test chamber pressure comparing to the experimental test results.

All numerical simulation results are given in this chapter in terms of the Mach number, static pressure and temperature on the symmetry plane for different test conditions, respectively. The contour plots are given in the way for compatibility with Schlieren images. Static pressure, Mach number and static temperature contour plots are compared under the same category for all of the conditions.

There is much noise in the data for outlet boundary pressure of the solution domain coming from experimental tests, but the mean pressure is used for numerical analyses. If the lower value of this band of the pressure data is taken into consideration, analysis results are closing to the experimental test results for the test chamber pressure value. This is caused from the strong shockwave formation at the outlet boundary condition that is not included properly to the outlet boundary because shockwave is not the cause, it is the result of the high speed flow. Hence, this situation increases the back pressure of the flow at the end of the diffuser section and CFD results get away from the test results.

CFD results are consistent among themselves in the mean of the static pressure, Mach number and static temperature inside the test chamber for Mach 2 and 2.5 free-jet nozzles. Mach 2.5 free-jet nozzle is started for all test conditions. Mach 2.5 free-jet nozzle becomes under-expanded and higher Mach region is formed along the center line of the free-jet nozzle inside the test chamber. On the other hand, it is observed that Mach 2 free-jet nozzle is not started for different cases with and without blockage. It is due to that Mach 2 free-jet nozzle exit diameter is very close to the diffuser entry duct diameter, whole flow is not captured completely and the free-jet flow fills the test chamber. But in CFD analyses, this parameter is not evaluated properly as can be seen

from the results and generally lower static pressure is obtained relatively to the experimental test results. The static pressure on the symmetry plane of the solution domain for the same mass flow rate of the free-jet nozzle with and without blockage test articles is given in Figure 3-11 as an example.

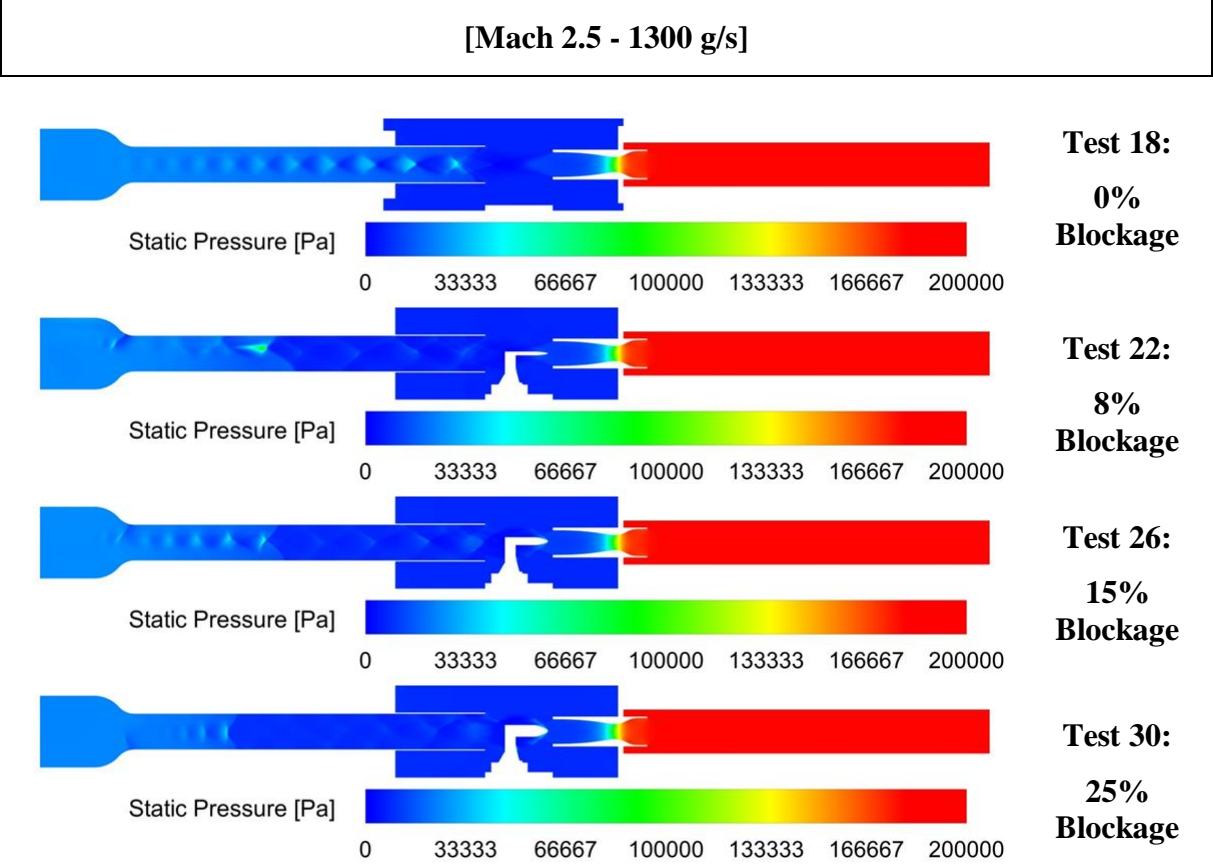


Figure 3-11. Static Pressure Contour Plots for Mach 2.5 Free-Jet Nozzle.

In order to observe the blockage effect on the test chamber pressure, the contour plots are given together according to the increasing blockage rates for the same flow rate of the free-jet nozzle. The flow is choked at the nozzle throat and then expands towards the nozzle exit and the pressure is also lowered. The diffuser inlet static pressure is then starts to increase toward the test section diffuser exit. It is also observed that where the pressure at the entrance of the test section diffuser starts to increase has a similar structure for blockage test articles, but the flow still continues to be at higher speeds at the centerline of the diffuser for the situation where it does not encounter any blockage. The Mach number contour plots are given in Figure 3-12.

[Mach 2.5 - 1300 g/s]

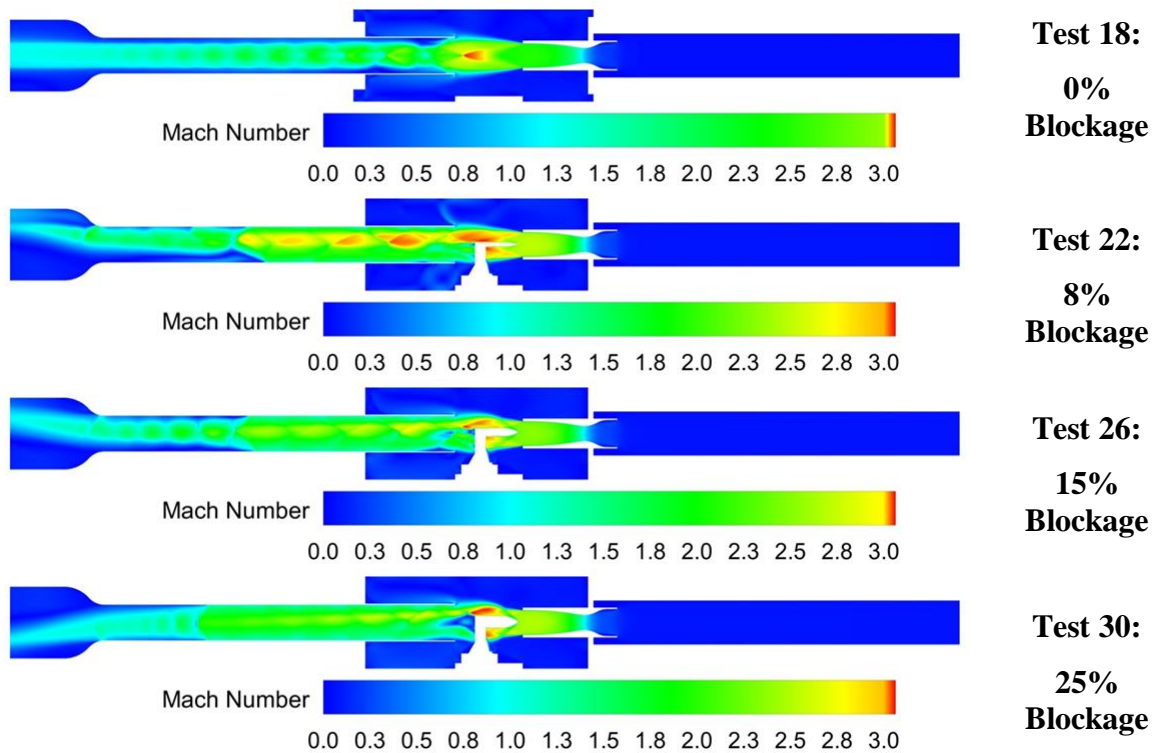


Figure 3-12. Mach Number Contour Plots for Mach 2.5 Free-Jet Nozzle.

It is observed that the flow at low speeds before the free-jet nozzle entrance accelerates through the nozzle and is at Mach 2.5 levels at the nozzle exit for these test conditions given as an example. The oblique shockwaves observed at the nozzle exit form the limits of the testable region for Mach 2.5 test condition at this secondary flow rate. It is seen that test rhombus changes according to the pressure inside the test chamber and the nosecone of the test articles remains within the test rhombus for the test conditions with blockage. The flow is still at supersonic speeds at the entrance of the diffuser and slows down along the test section diffuser.

As another data measured also from the different parts of the test setup during experimental tests, the temperature data is given on the symmetry plane of the solution domain. The static temperature contour plots are given in Figure 3-13.

[Mach 2.5 - 1300 g/s]

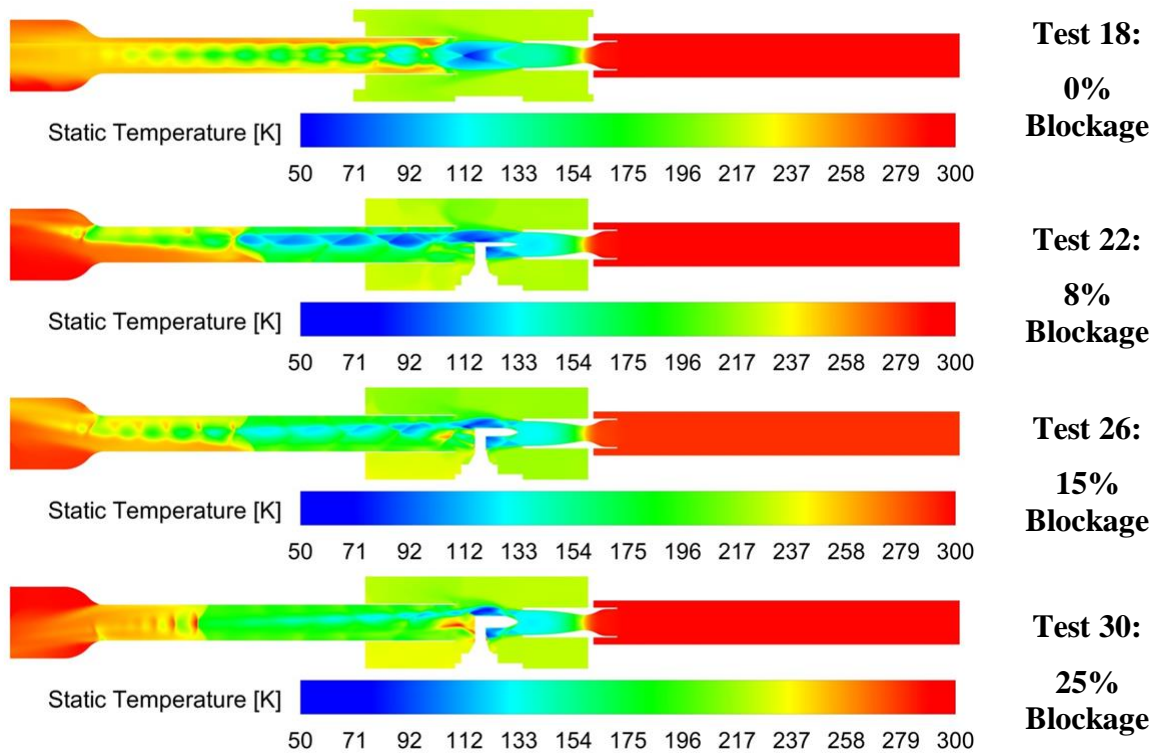


Figure 3-13. Static Temperature Contour Plots for Mach 2.5 Free-Jet Nozzle.

Static temperature of the flow before the free-jet nozzle is known as 290 K as boundary condition for the numerical analyses of the cold flow test condition. The static temperature is decreased along the free-jet nozzle as expected with and without blockage test articles inside the test chamber. And the static temperature is then increased to the almost 290 K at the exit of the test section diffuser.

[Mach 2 - 750 g/s]

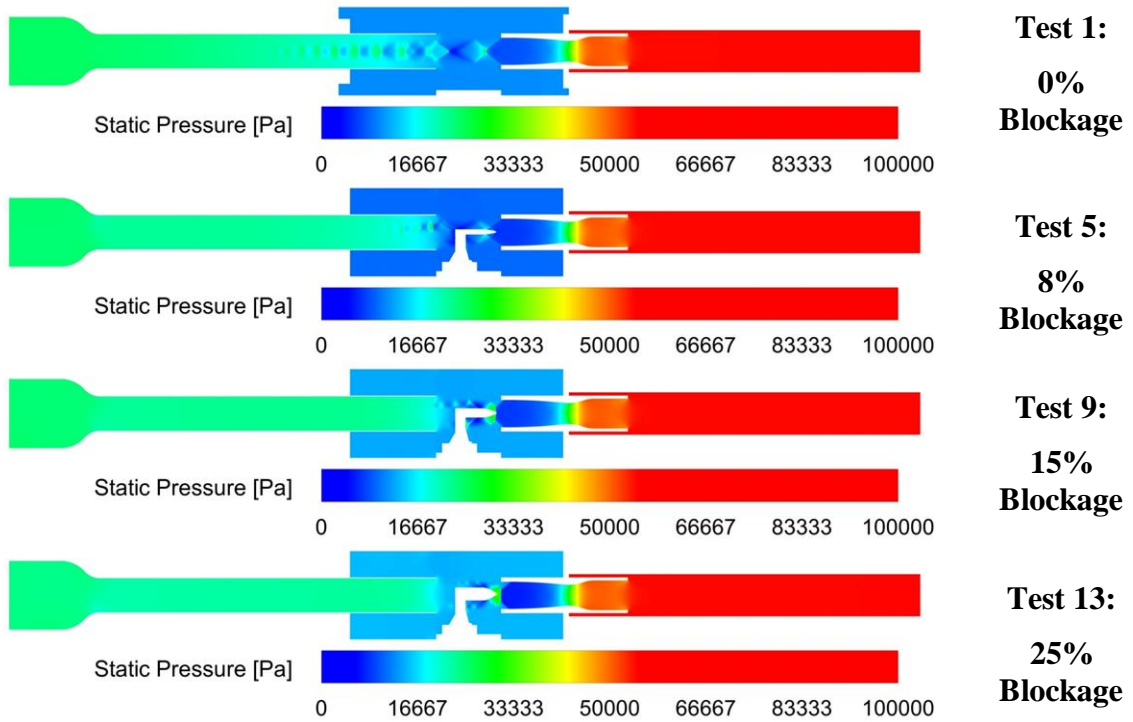


Figure 3-14. Static Pressure Contour Plots [Mach 2 - 750 g/s].

[Mach 2 - 1100 g/s]

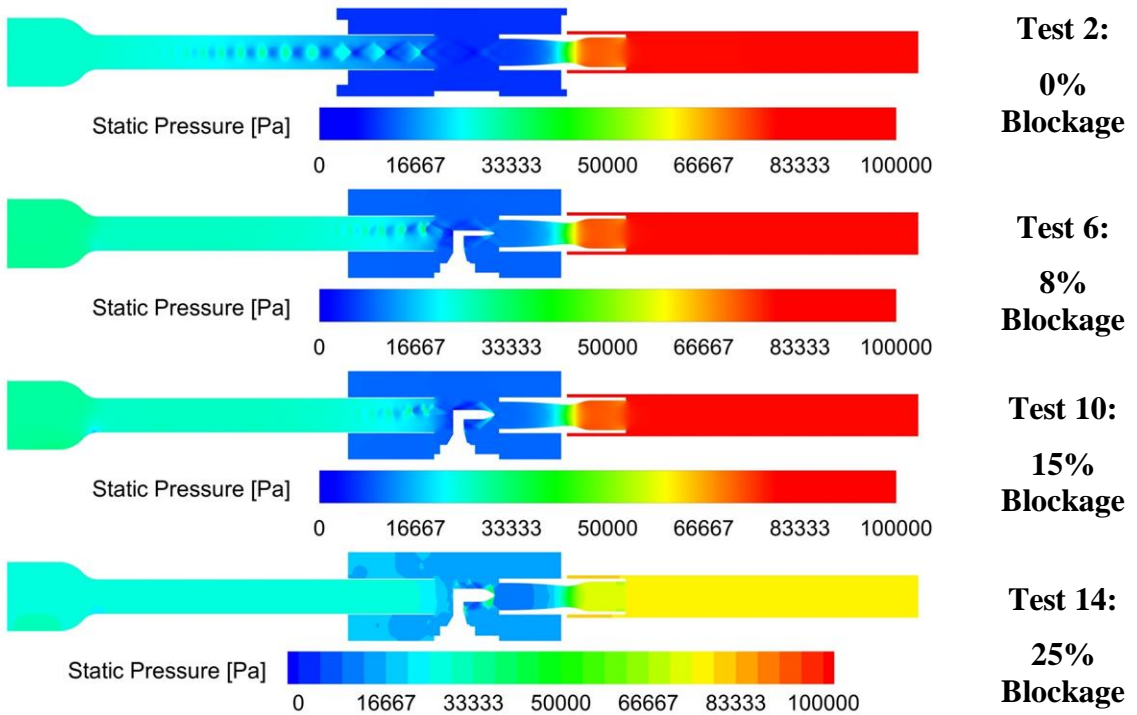


Figure 3-15. Static Pressure Contour Plots [Mach 2 - 1100 g/s].

[Mach 2 - 1500 g/s]

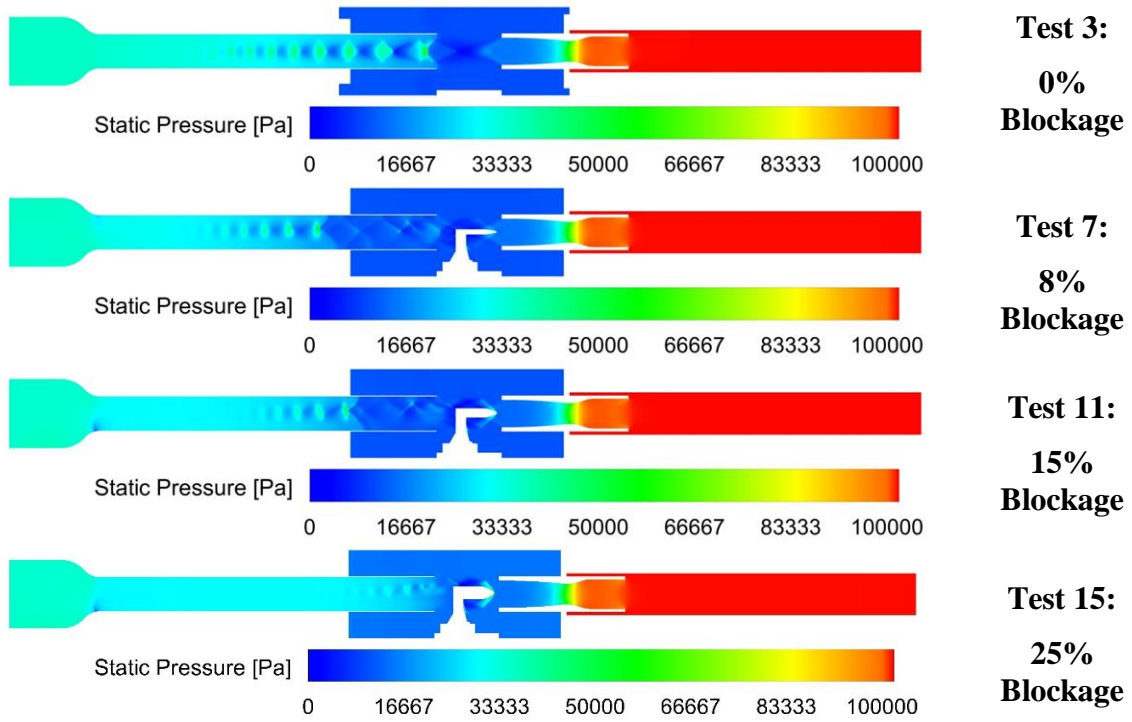


Figure 3-16. Static Pressure Contour Plots [Mach 2 - 1500 g/s].

[Mach 2 - 1900 g/s]

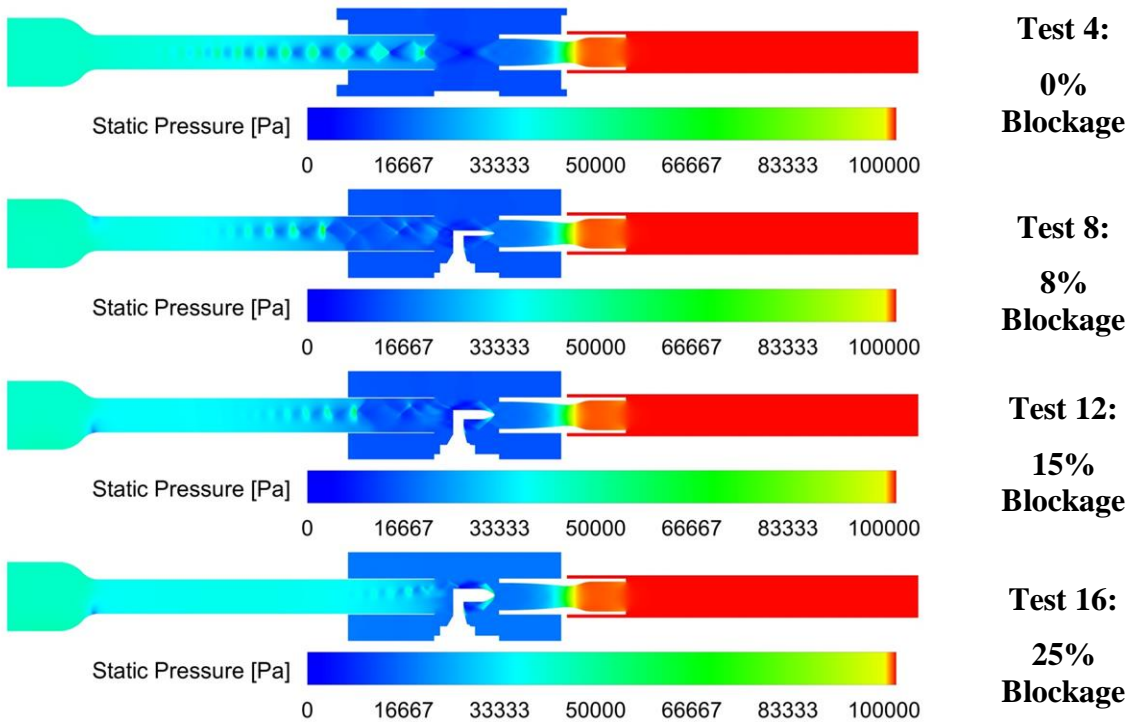


Figure 3-17. Static Pressure Contour Plots [Mach 2 - 1900 g/s].

[Mach 2 - 750 g/s]

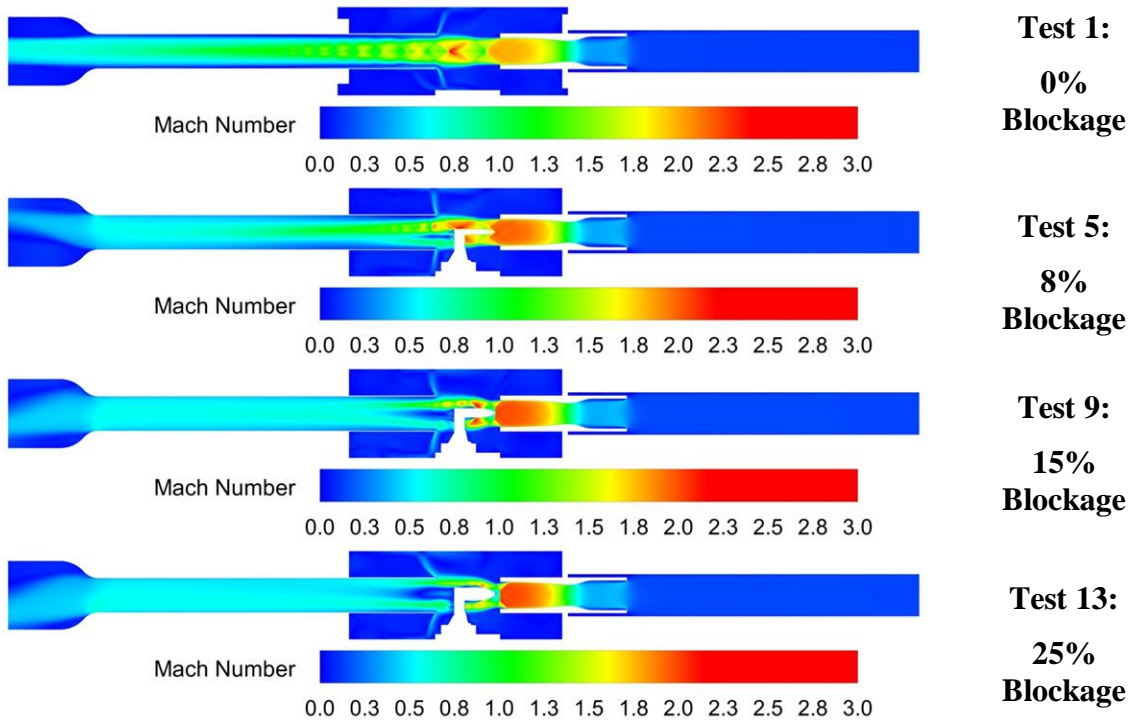


Figure 3-18. Mach Number Contour Plots [Mach 2 - 750 g/s].

[Mach 2 - 1100 g/s]

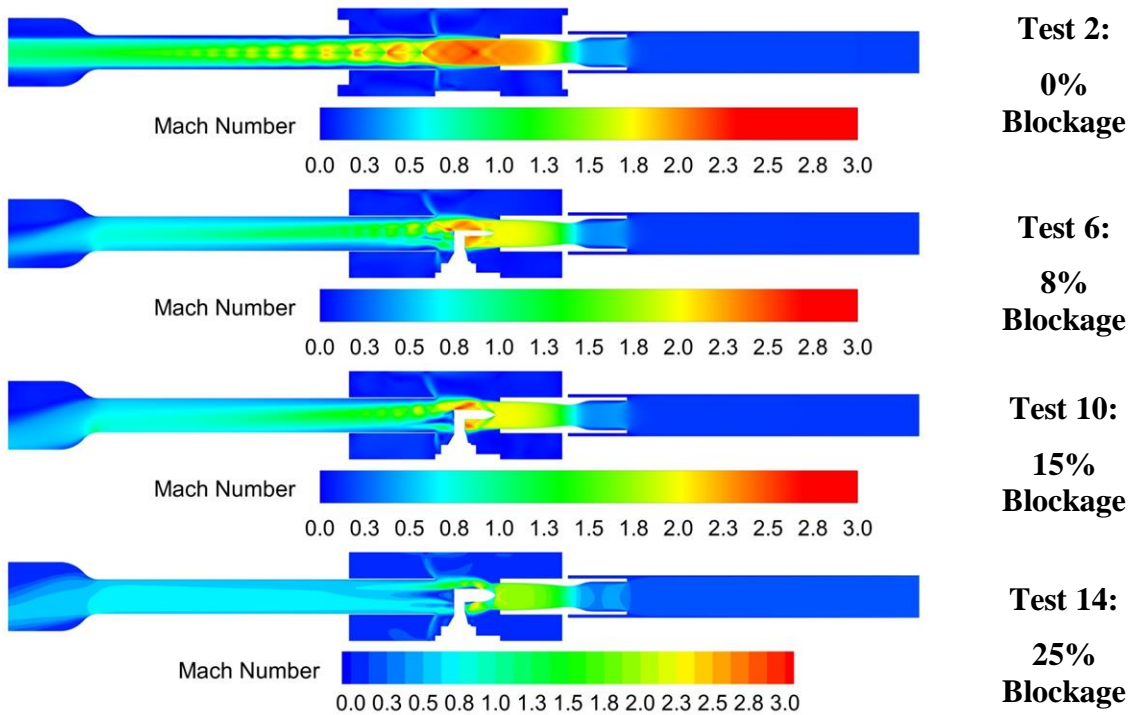


Figure 3-19. Mach Number Contour Plots [Mach 2 - 1100 g/s].

[Mach 2 - 1500 g/s]

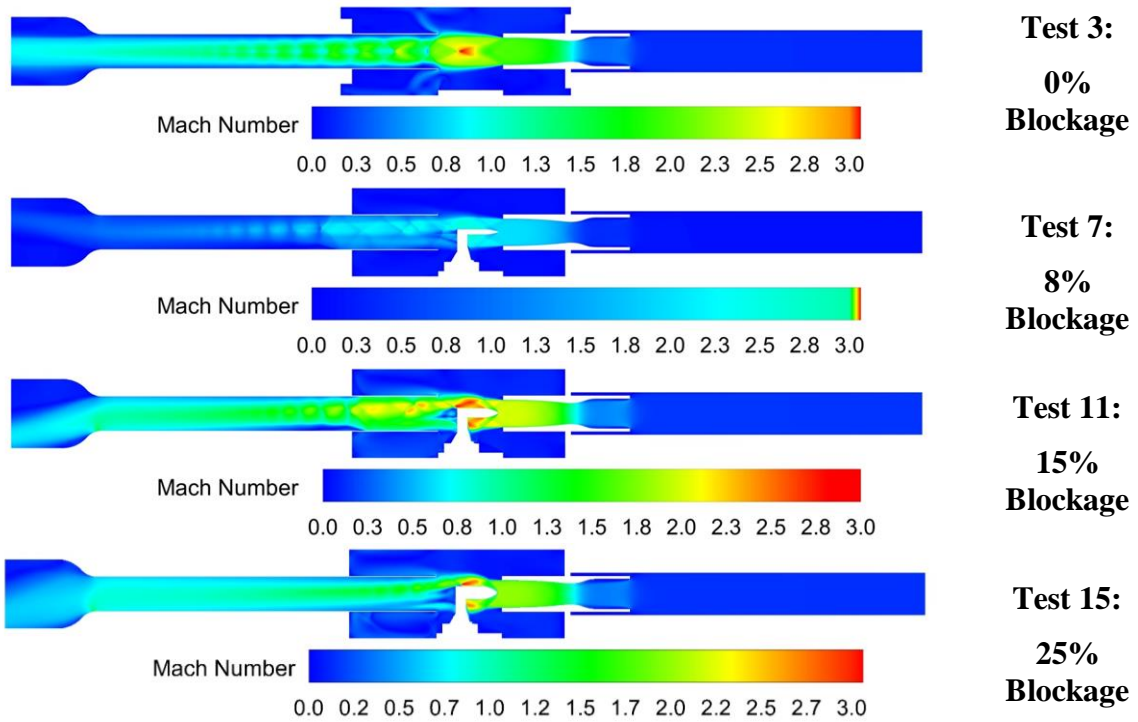


Figure 3-20. Mach Number Contour Plots [Mach 2 - 1500 g/s].

[Mach 2 - 1900 g/s]

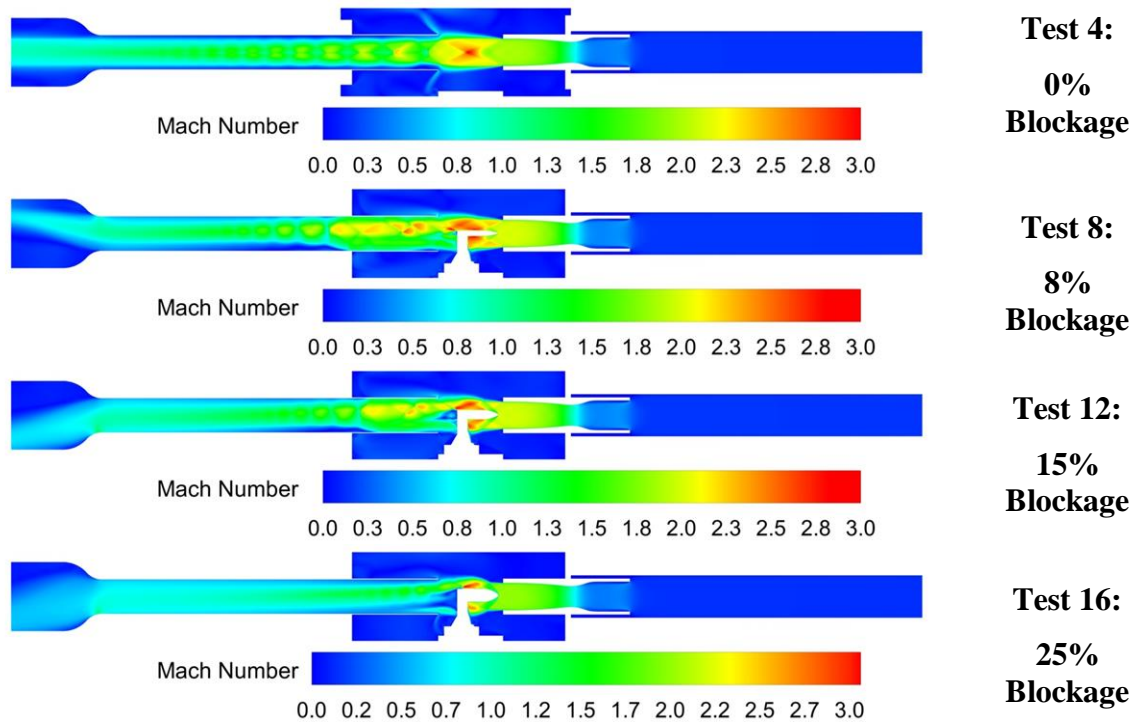


Figure 3-21. Mach Number Contour Plots [Mach 2 - 1900 g/s].

[Mach 2 - 750 g/s]

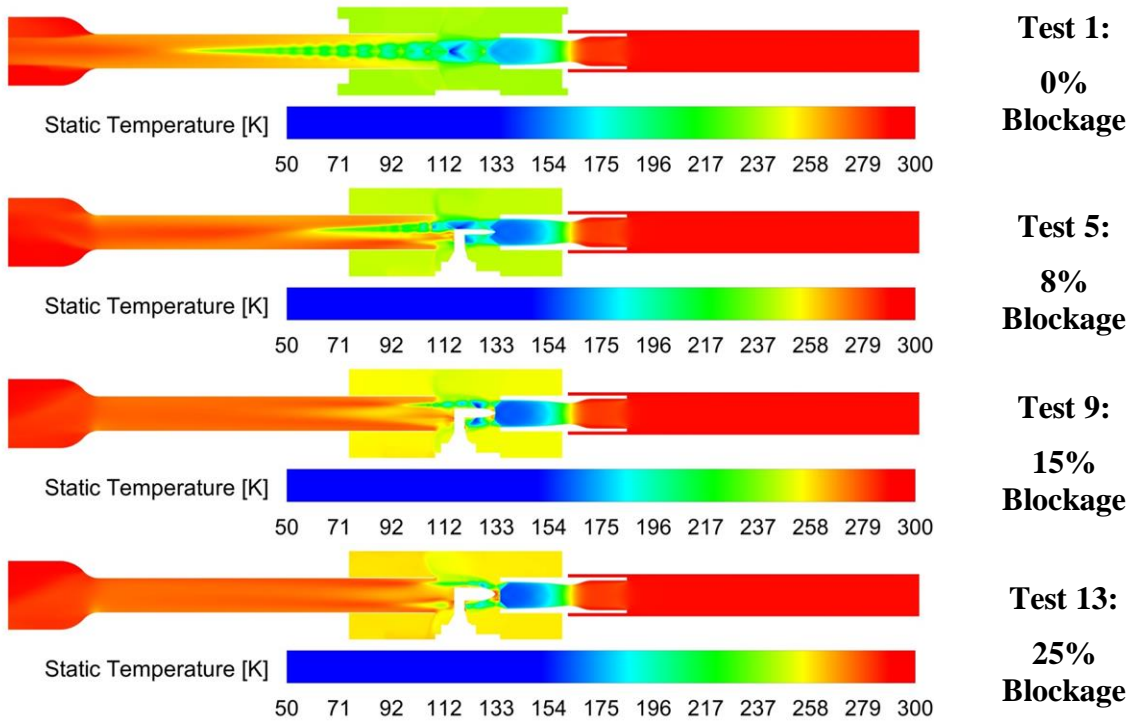


Figure 3-22. Static Temperature Contour Plots [Mach 2 - 750 g/s].

[Mach 2 - 1100 g/s]

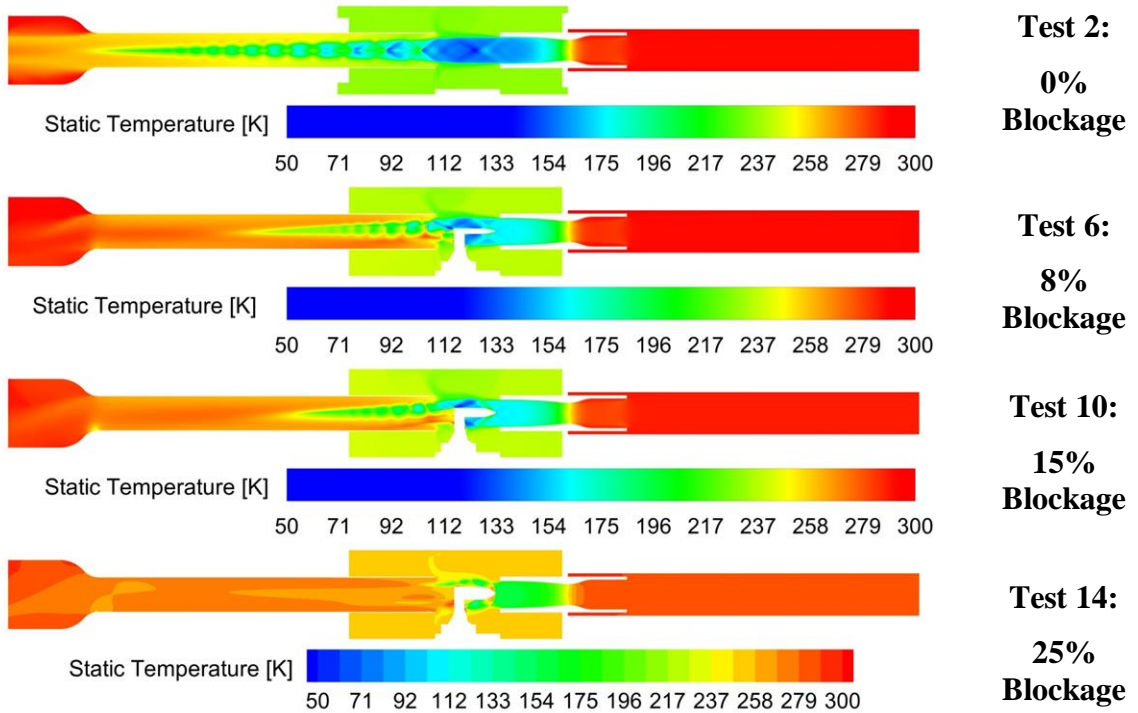


Figure 3-23. Static Temperature Contour Plots [Mach 2 - 1100 g/s].

[Mach 2 - 1500 g/s]

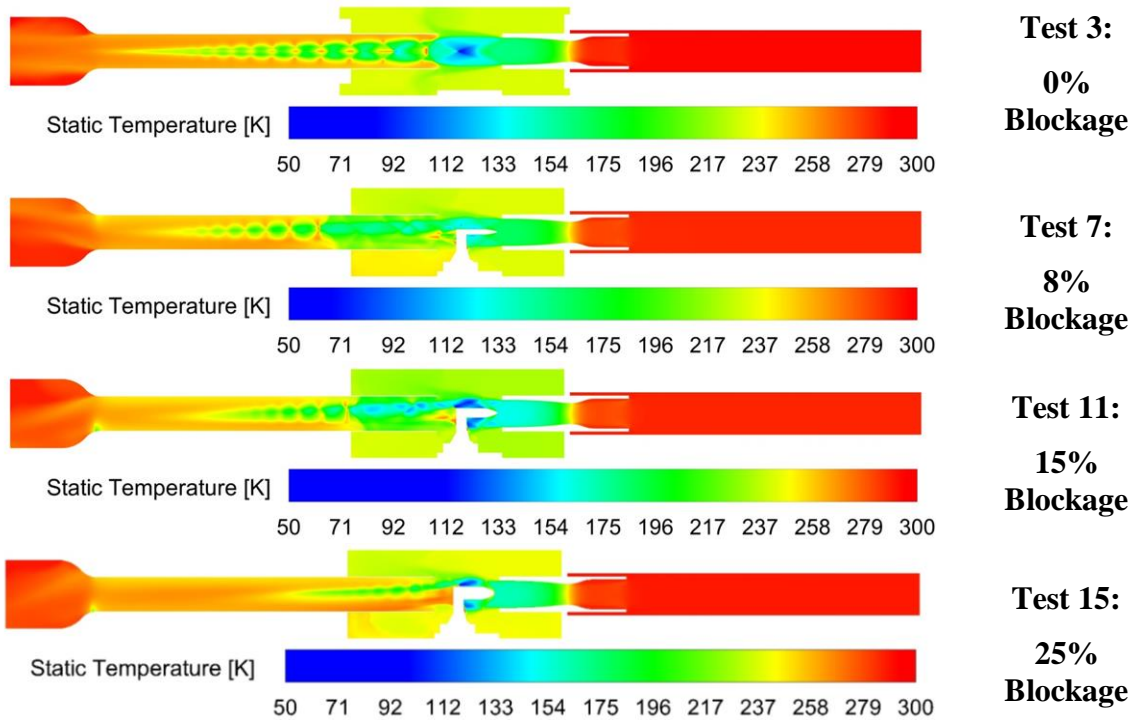


Figure 3-24. Static Temperature Contour Plots [Mach 2 - 1500 g/s].

[Mach 2 - 1900 g/s]

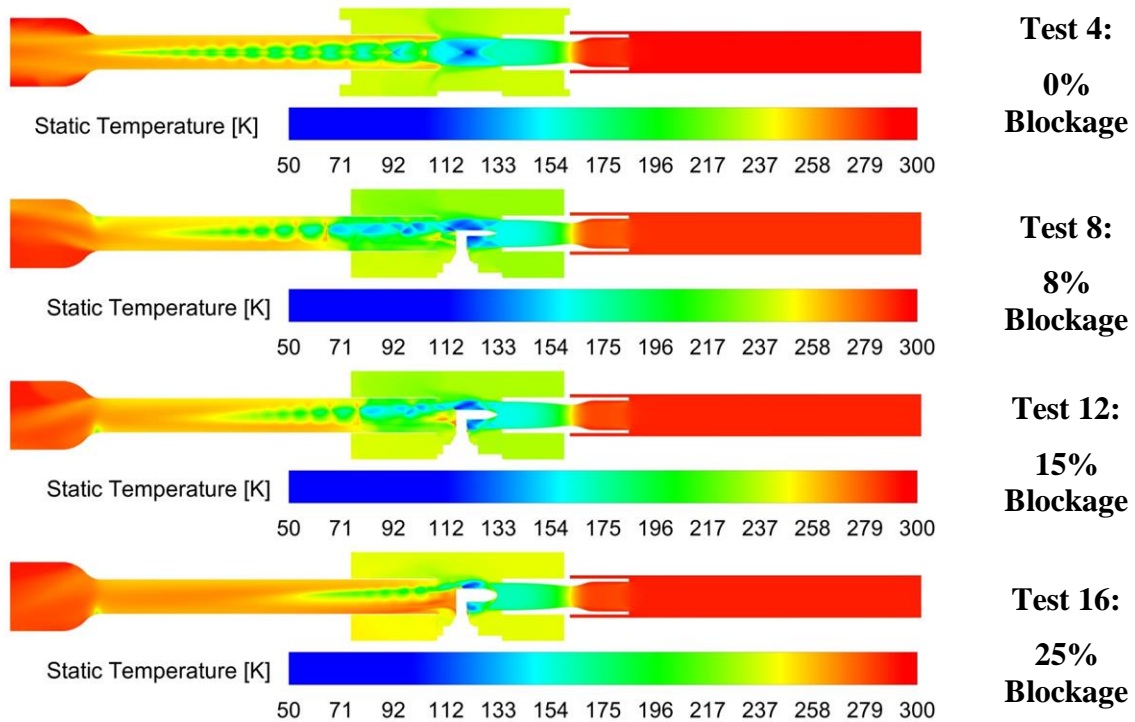


Figure 3-25. Static Temperature Contour Plots [Mach 2 - 1900 g/s].

[Mach 2.5 - 750 g/s]

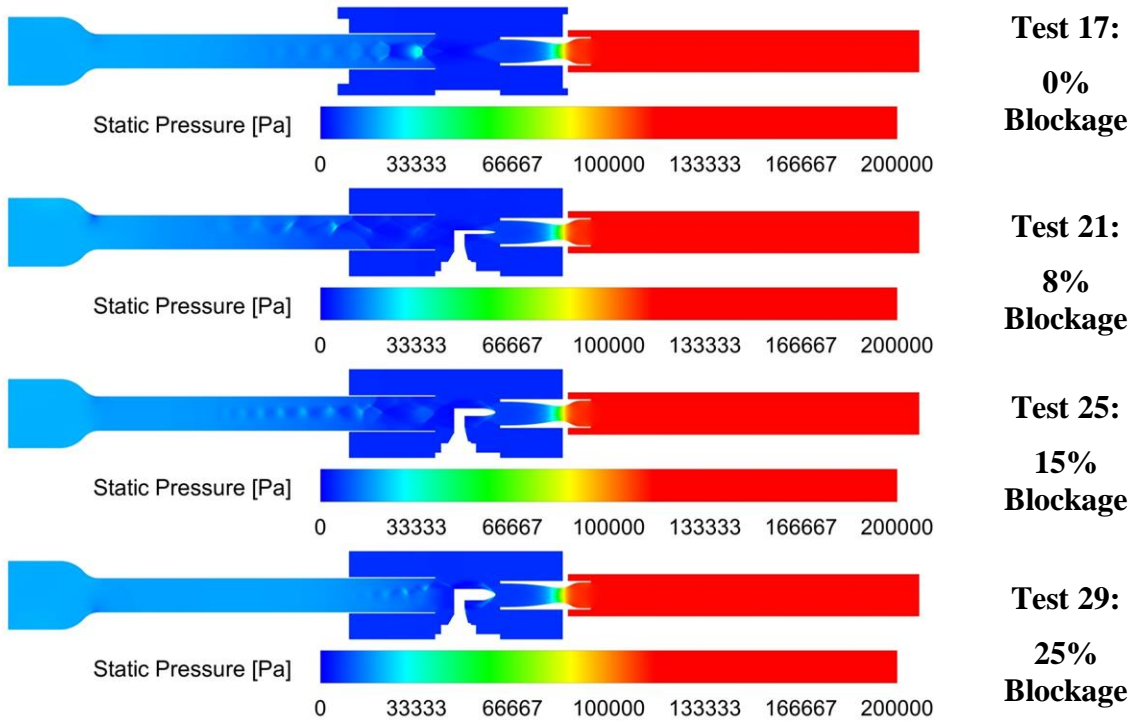


Figure 3-26. Static Pressure Contour Plots [Mach 2.5 - 750 g/s].

[Mach 2.5 - 1300 g/s]

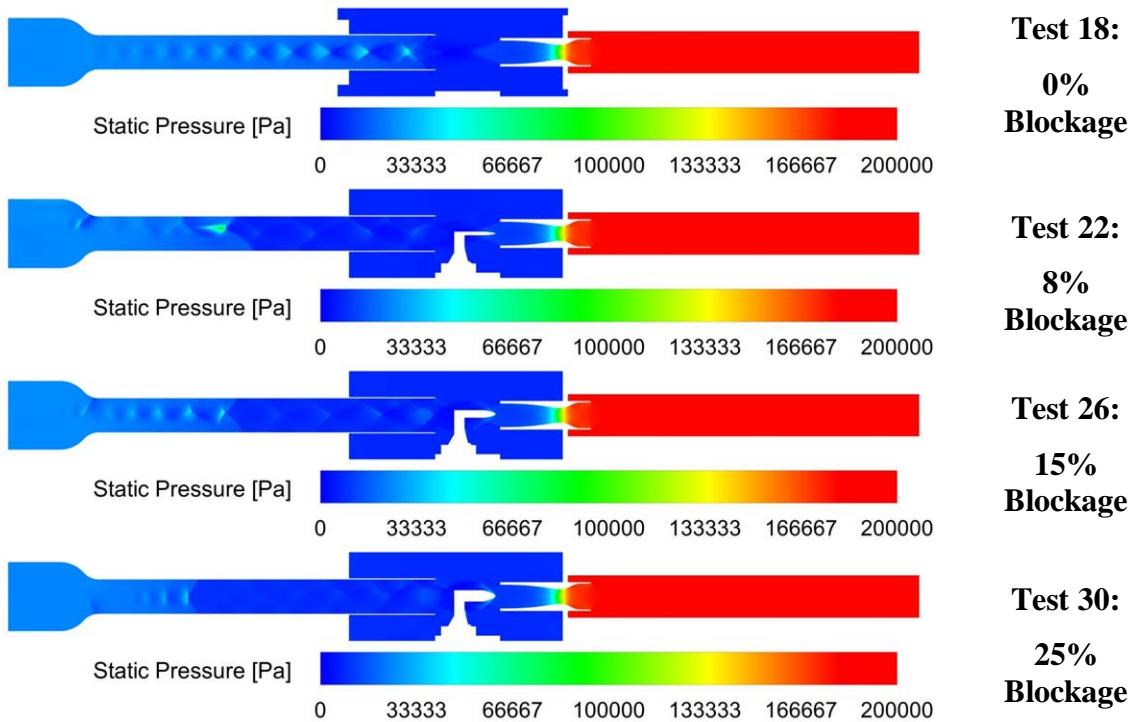


Figure 3-27. Static Pressure Contour Plots [Mach 2.5 - 1300 g/s].

[Mach 2.5 - 1500 g/s]

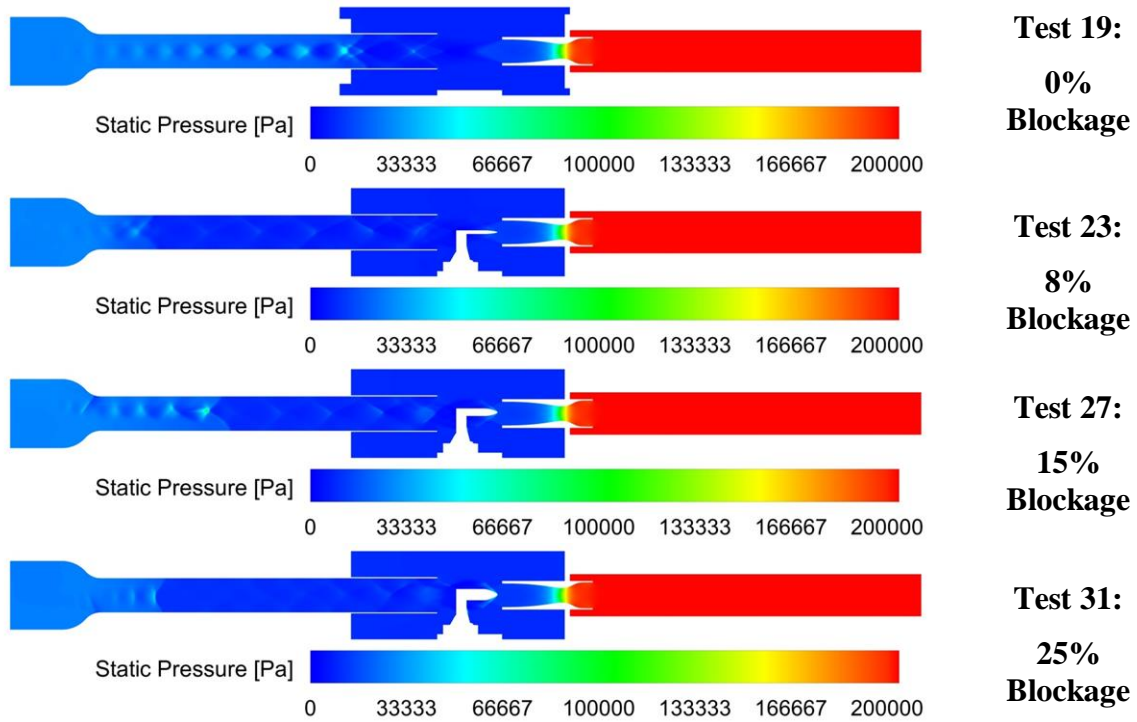


Figure 3-28. Static Pressure Contour Plots [Mach 2.5 - 1500 g/s].

[Mach 2.5 - 1900 g/s]

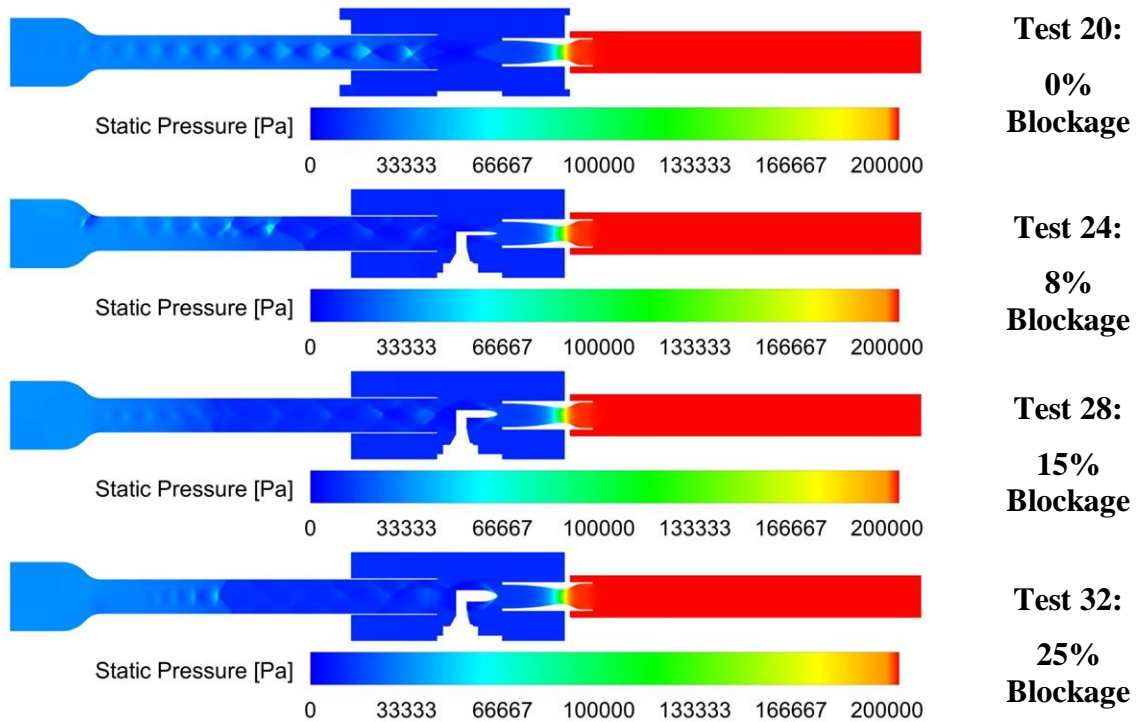


Figure 3-29. Static Pressure Contour Plots [Mach 2.5 - 1900 g/s].

[Mach 2.5 - 750 g/s]

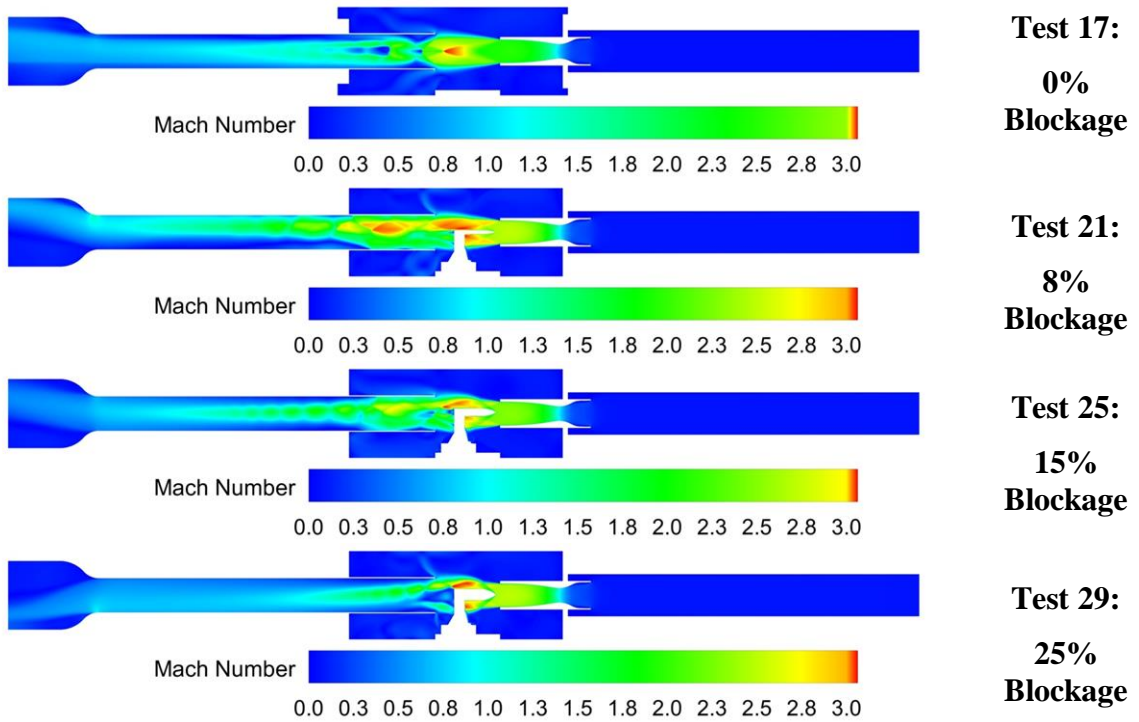


Figure 3-30. Mach Number Contour Plots [Mach 2.5 - 750 g/s].

[Mach 2.5 - 1300 g/s]

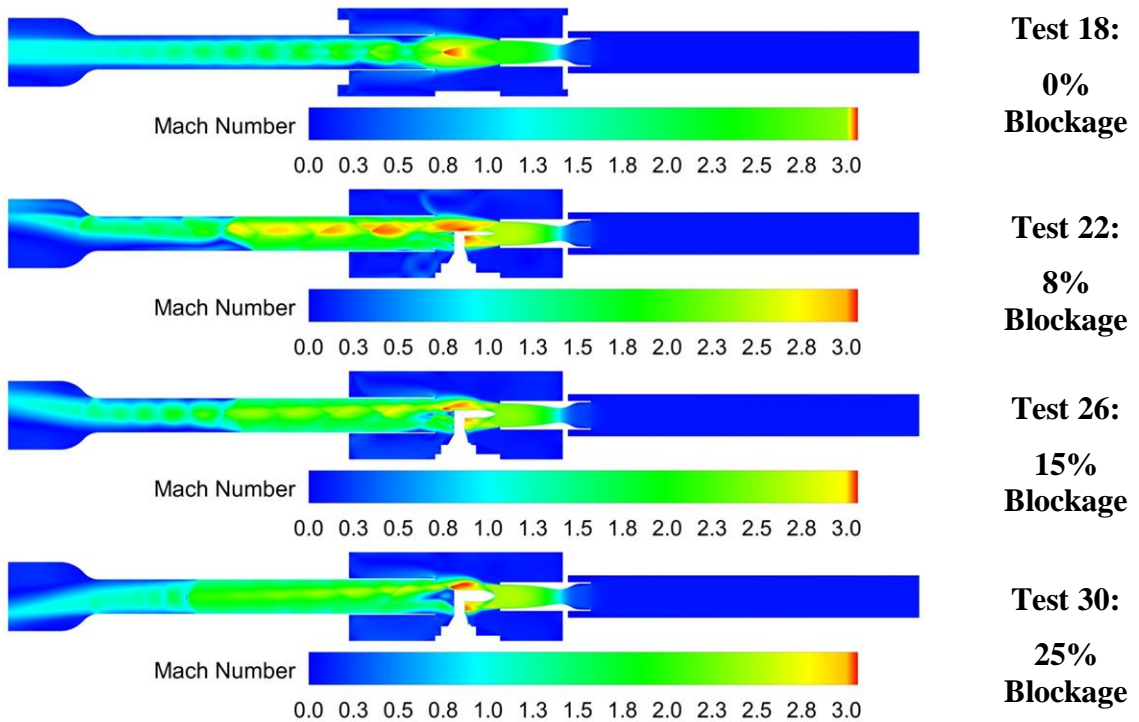


Figure 3-31. Mach Number Contour Plots [Mach 2.5 - 1300 g/s].

[Mach 2.5 - 1500 g/s]

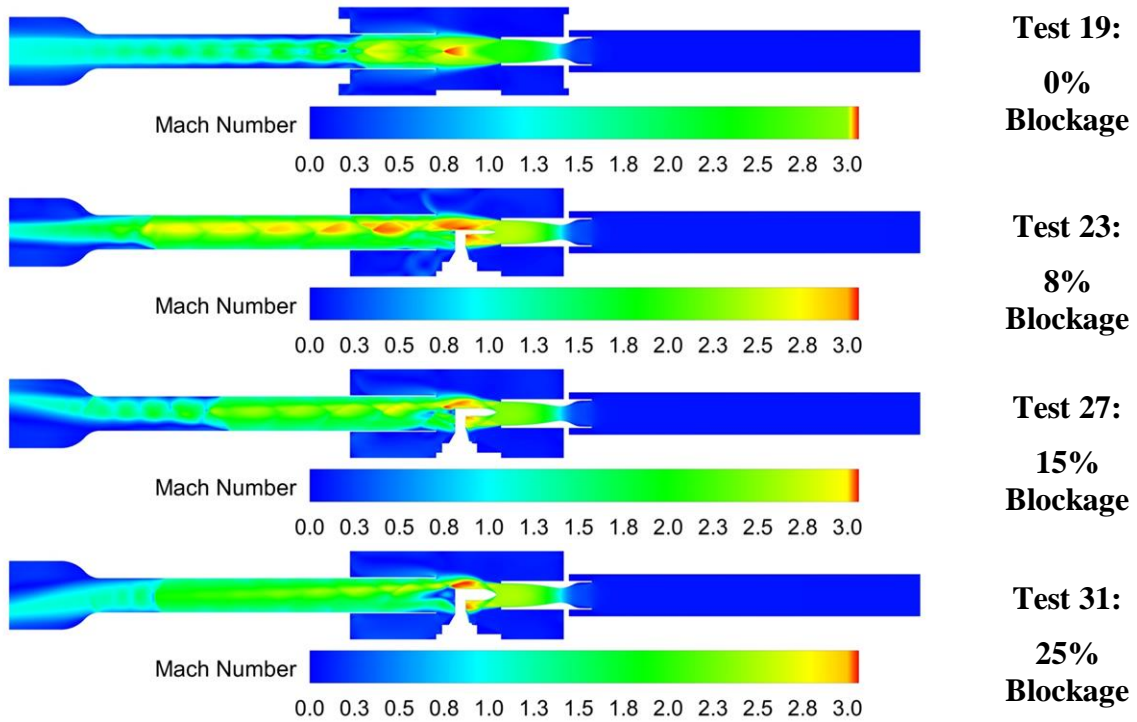


Figure 3-32. Mach Number Contour Plots [Mach 2.5 - 1500 g/s].

[Mach 2.5 - 1900 g/s]

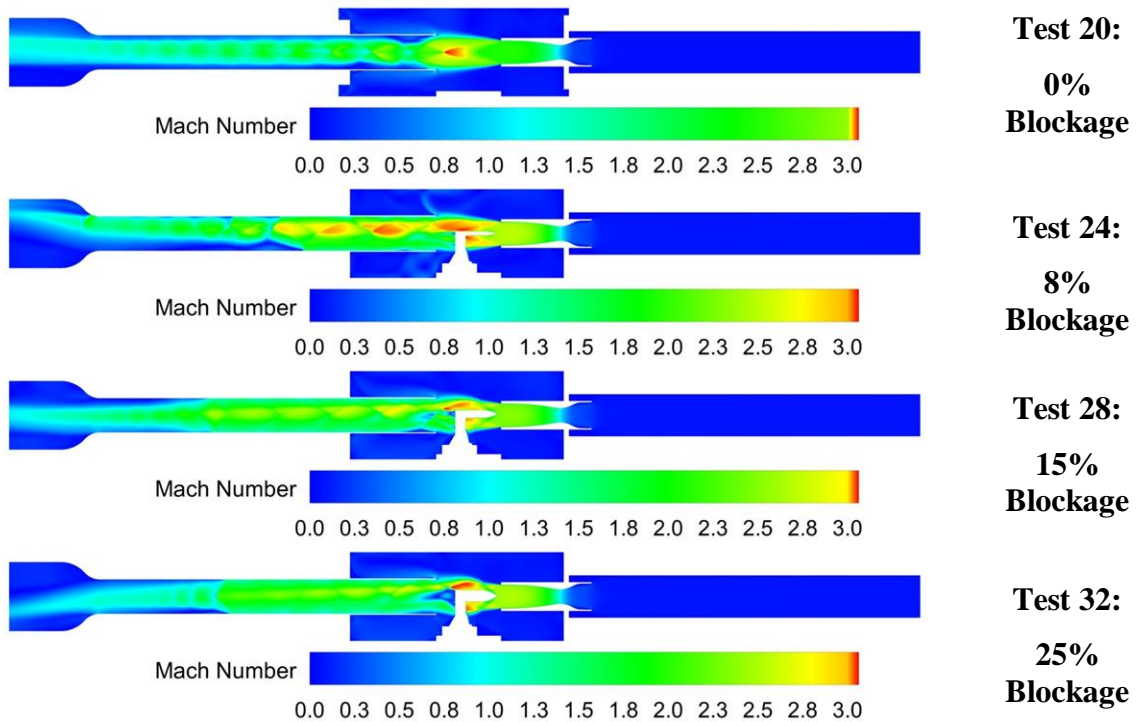


Figure 3-33. Mach Number Contour Plots [Mach 2.5 - 1900 g/s].

[Mach 2.5 - 750 g/s]

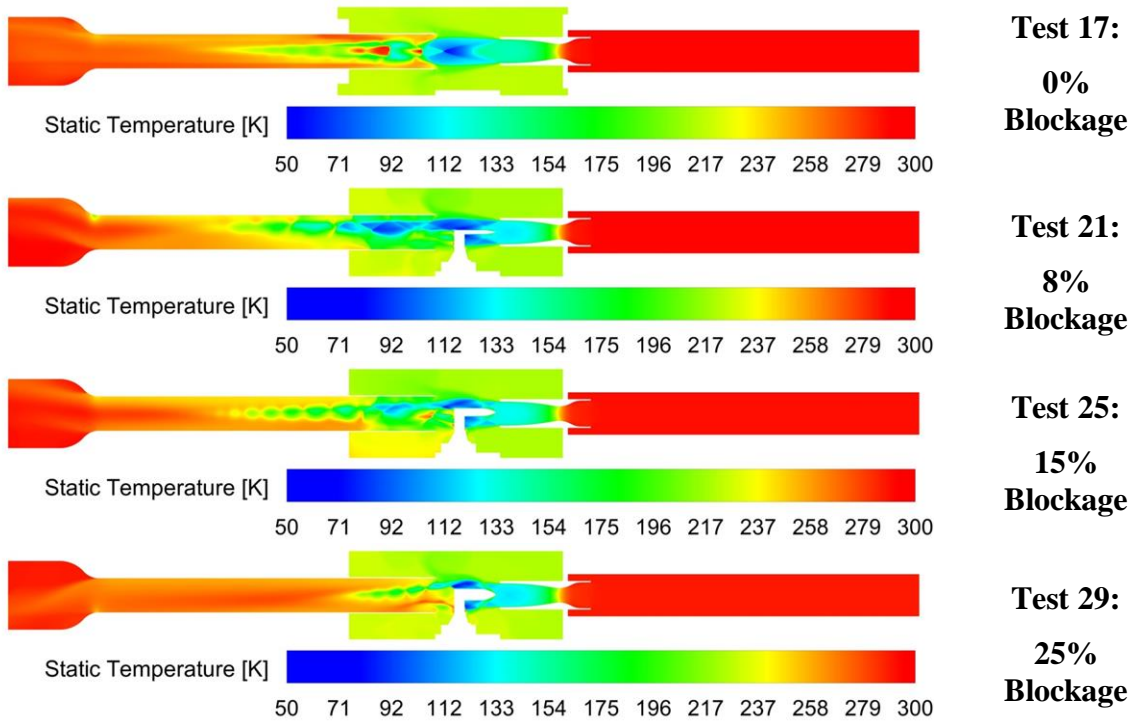


Figure 3-34. Static Temperature Contour Plots [Mach 2.5 - 750 g/s].

[Mach 2.5 - 1300 g/s]

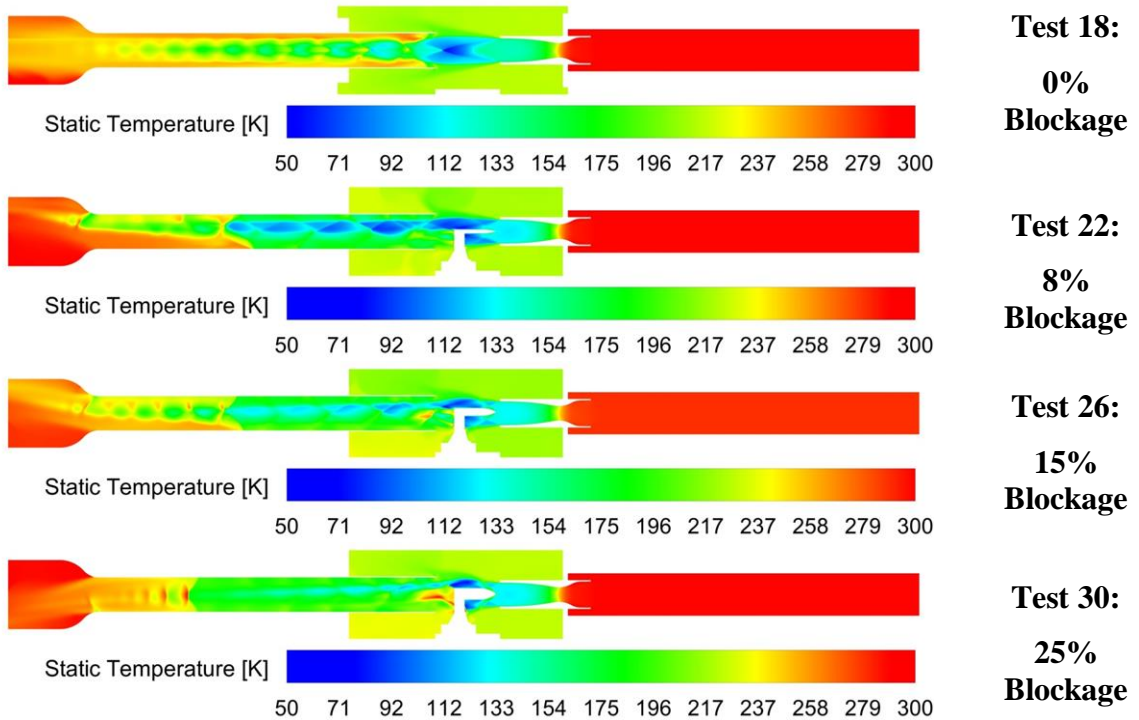


Figure 3-35. Static Temperature Contour Plots [Mach 2.5 - 1300 g/s].

[Mach 2.5 - 1500 g/s]

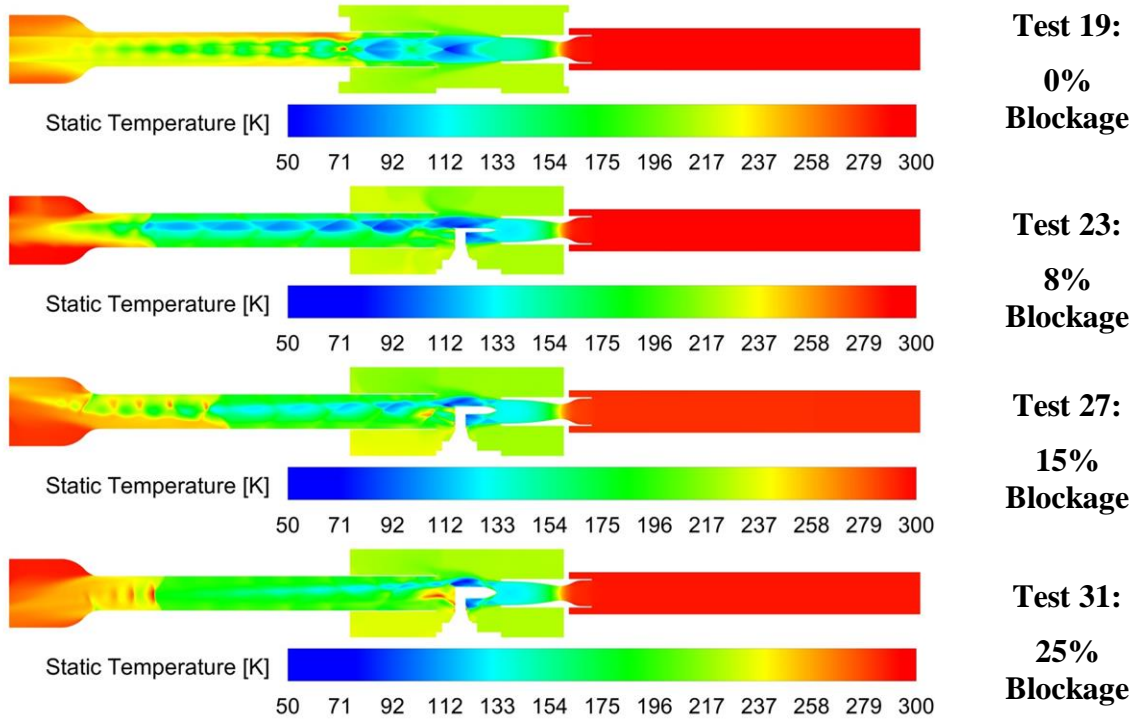


Figure 3-36. Static Temperature Contour Plots [Mach 2.5 - 1500 g/s].

[Mach 2.5 - 1900 g/s]

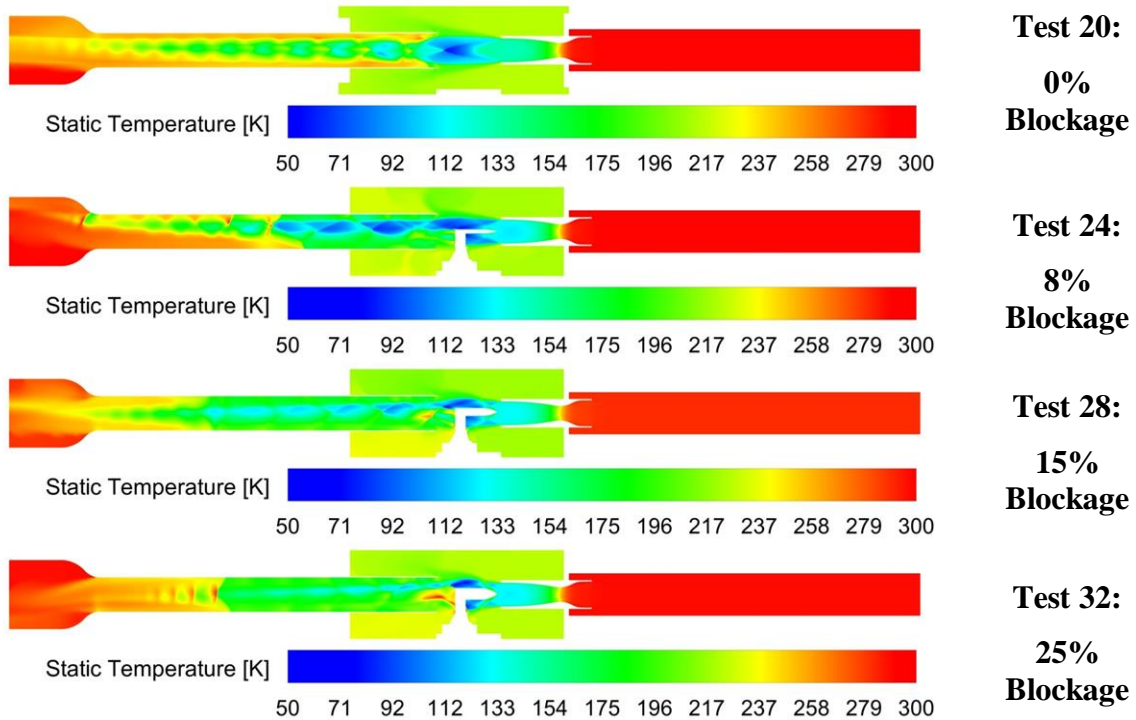


Figure 3-37. Static Temperature Contour Plots [Mach 2.5 - 1900 g/s].

3.6. Comparison of the Experimental and Numerical Results

The most important data is considered as the test chamber pressure and Schlieren images among all test data to determine the working characteristics of the experimental test setup. The comparison of the results are given in the context of test chamber pressure and Schlieren image in this section.

3.6.1. Test Chamber Pressure

Test chamber pressure comparison between experimental tests and numerical analysis results are performed in this section. Exact locations of the pressure sensors are given in Figure 3-38.

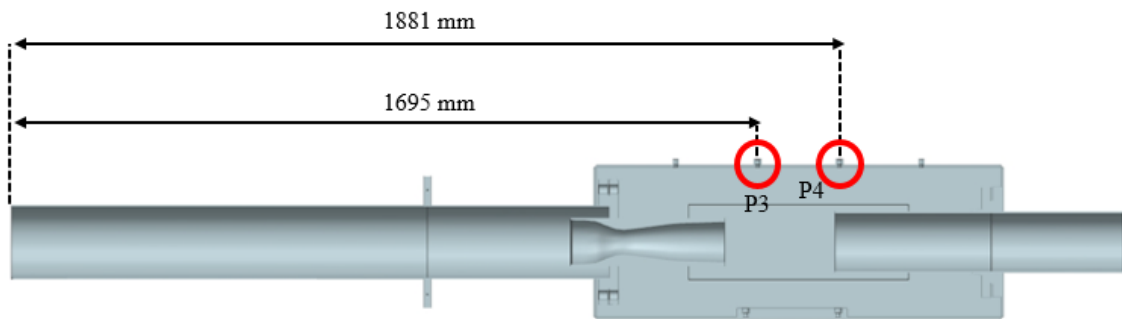


Figure 3-38. Test Chamber Pressure Sensor Locations.

Reference point is taken as the point where the free-jet nozzle inlet pressure sensor is installed and this plane is also used for inlet pressure boundary in the numerical analyses. In numerical analyses, pressure data is collected over the line between pressure sensor points along the x-direction values on the symmetry plane. At the beginning and end points of the line, pressure sensor values obtained from the experimental tests with error bar coming from the waving of the pressure data can also be used for the comparison of the CFD and test results. As an example, pressure data comparison for the case of Mach 2.5 and 15% blockage with 1300 g/s free-jet nozzle mass flow rate is shown in Figure 3-39.

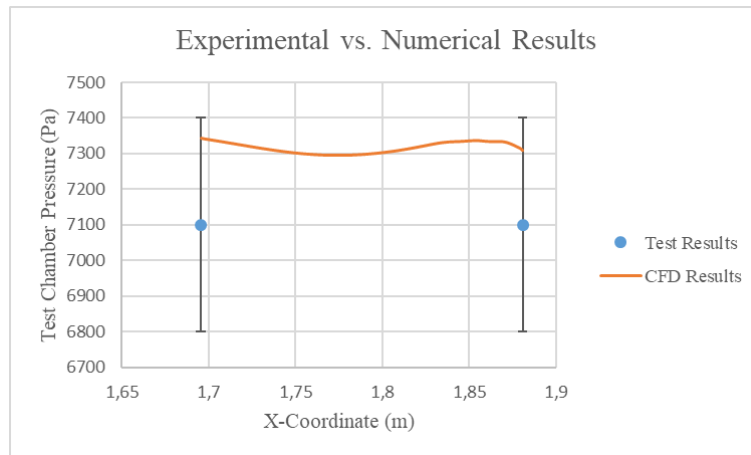
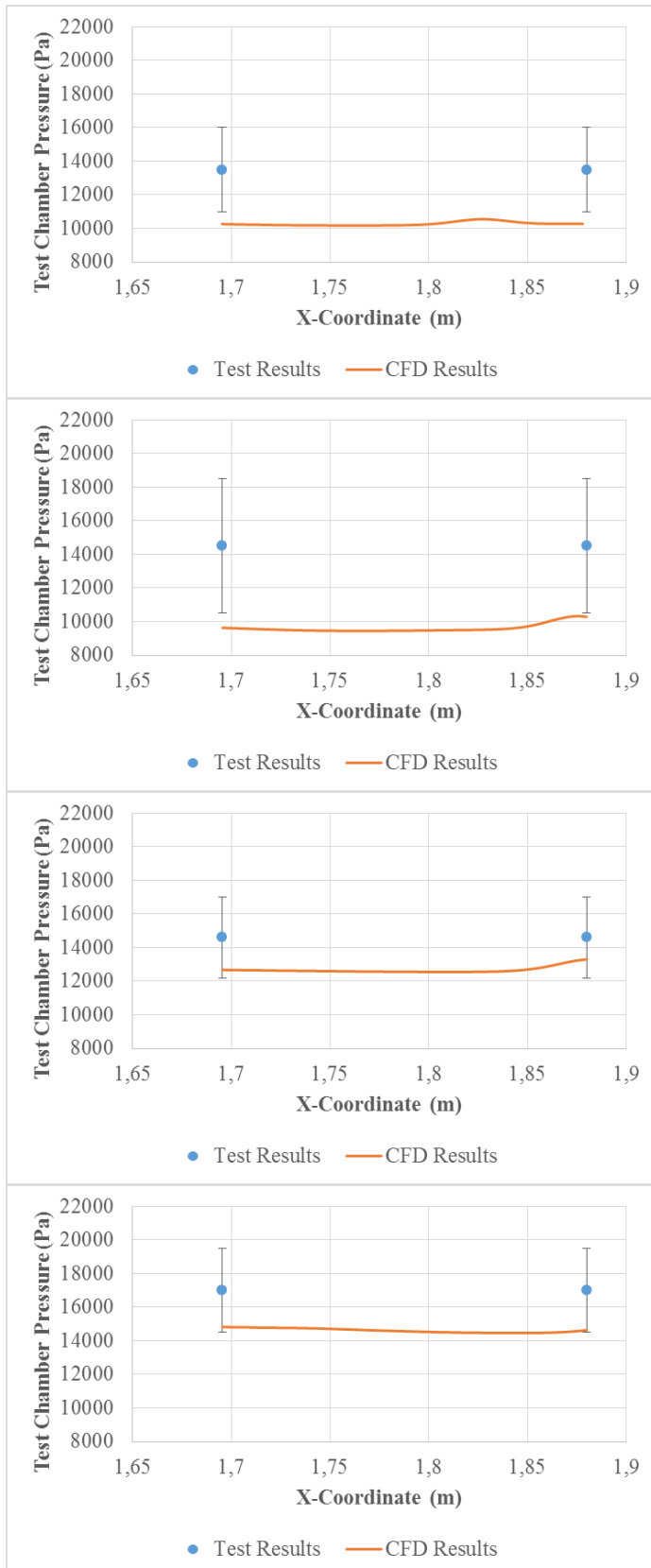


Figure 3-39. Comparison of the Test Chamber Pressure for Mach 2.5 and 15% Blockage Ratio.

It is obvious that numerical analyses for Mach 2.5 free-jet nozzle can be considered as very close to the test results in the mean of the test chamber pressure with absolute error of 4% in average. This is because of the start status of both ejector and free-jet nozzle. On the other hand, numerical analyses for Mach 2 free-jet nozzle give poor results relatively to the results of Mach 2.5 free-jet nozzle with absolute error of 20% in average. Average absolute pressure error is 20% and 4% for Mach 2 and 2.5 free-jet nozzles, respectively. It is necessary that exit pressure of the free-jet nozzle should be equal or higher than the test chamber pressure. This is achieved for Mach 2.5 free-jet nozzle and on the other hand, Mach 2 free-jet nozzle cannot provide this competence for most cases as shown in Appendix-3. As a result of this incompetence, static test chamber pressure for Mach 2 free-jet nozzle approaches to the experimental test results with more errors than Mach 2.5 free-jet nozzle.

Figure 3-40. Experimental vs. Numerical Test Chamber Pressure.

[Mach 2 - 750 g/s]



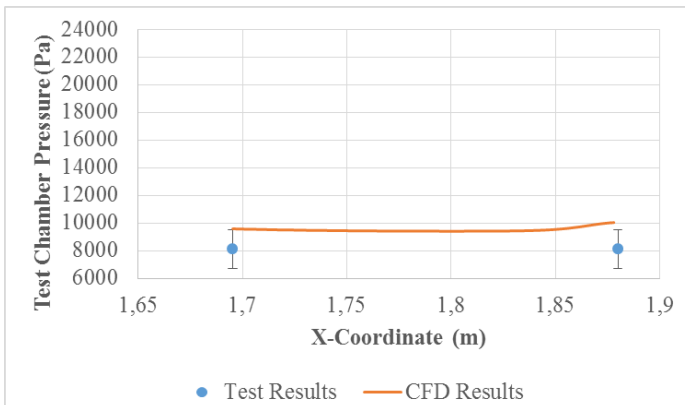
**Test 1:
0% Blockage**

**Test 5:
8% Blockage**

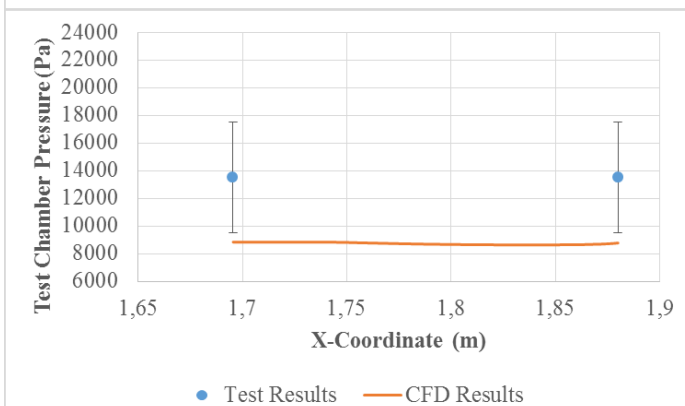
**Test 9:
15% Blockage**

**Test 13:
25% Blockage**

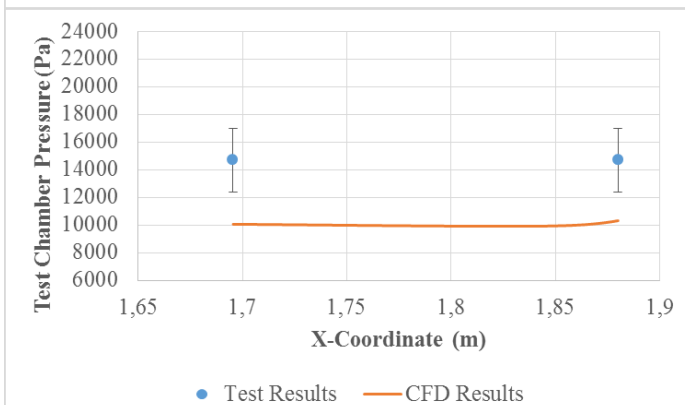
[Mach 2 - 1100 g/s]



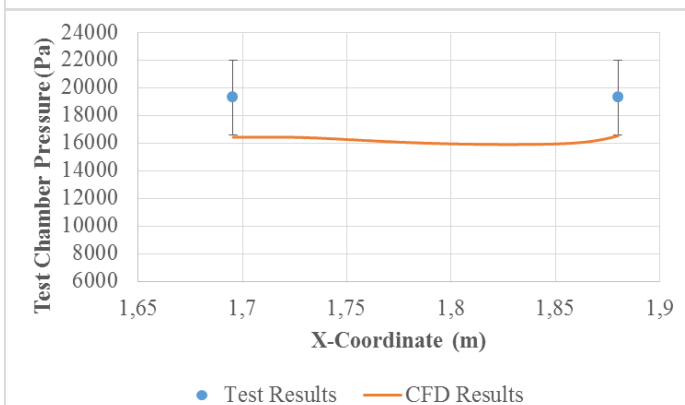
**Test 2:
0% Blockage**



**Test 6:
8% Blockage**

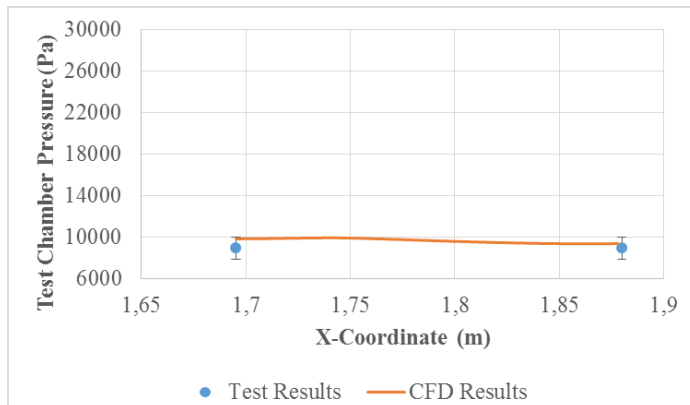


**Test 10:
15% Blockage**

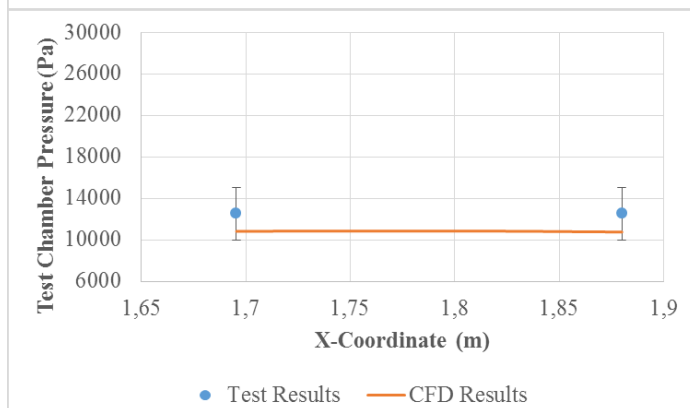


**Test 14:
25% Blockage**

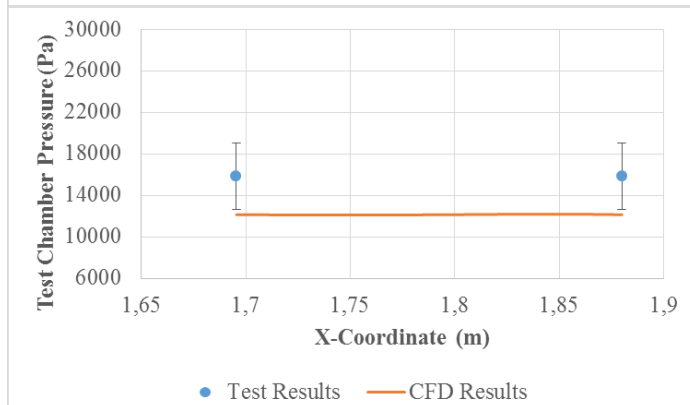
[Mach 2 - 1500 g/s]



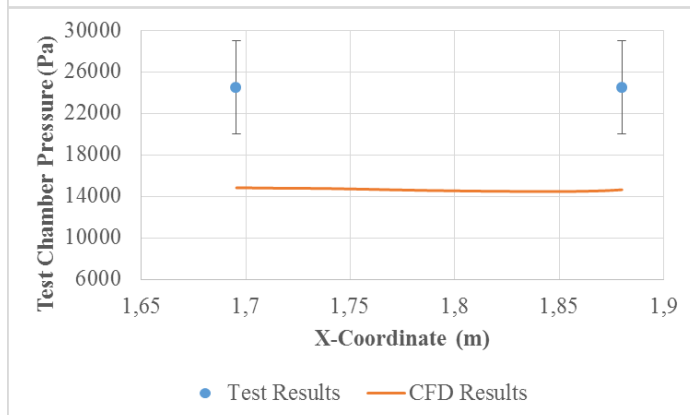
**Test 3:
0% Blockage**



**Test 7:
8% Blockage**

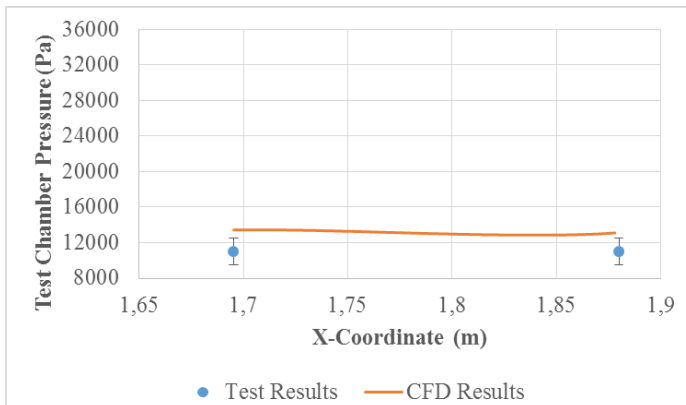


**Test 11:
15% Blockage**

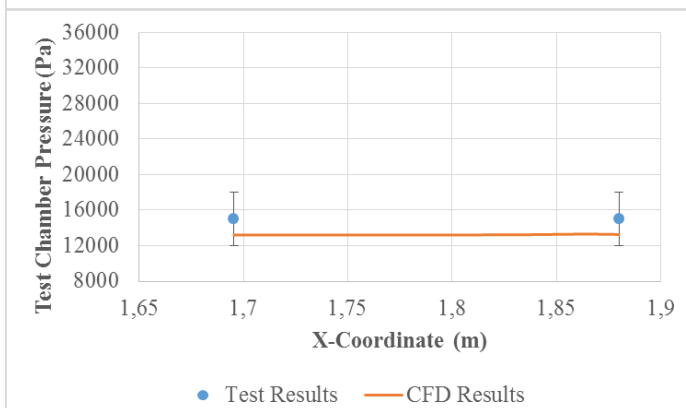


**Test 15:
25% Blockage**

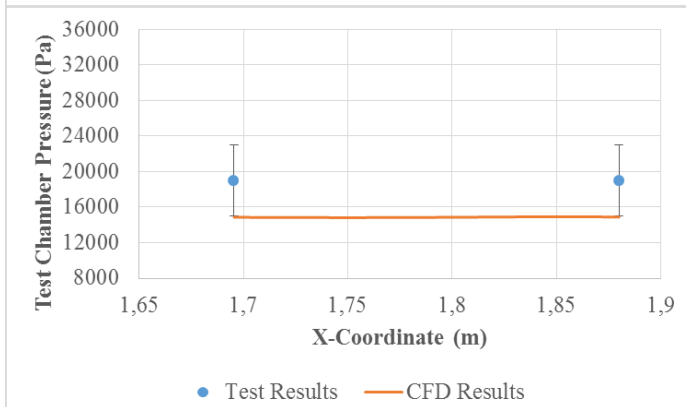
[Mach 2 - 1900 g/s]



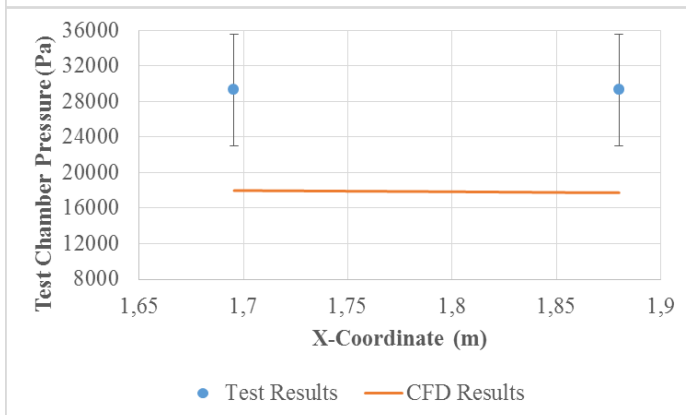
**Test 4:
0% Blockage**



**Test 8:
8% Blockage**

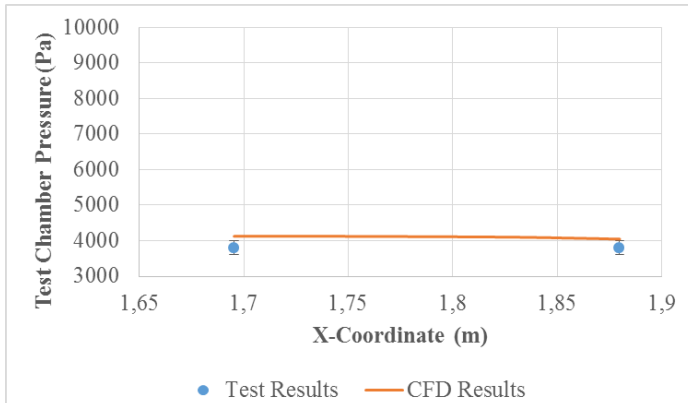


**Test 12:
15% Blockage**

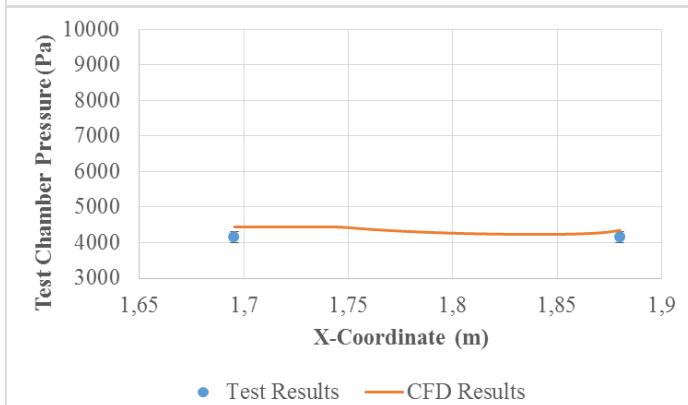


**Test 16:
25% Blockage**

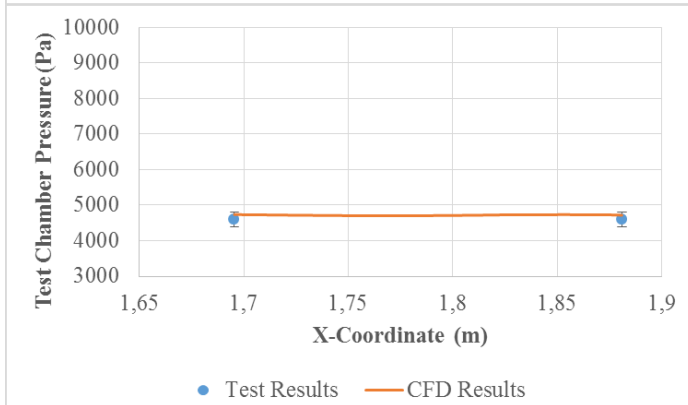
[Mach 2.5 - 750 g/s]



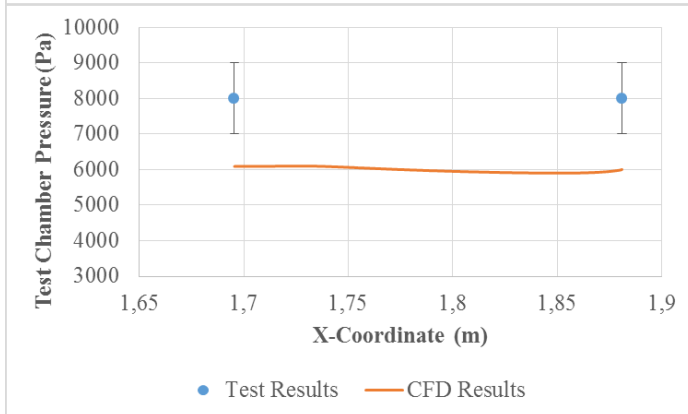
**Test 17:
0% Blockage**



**Test 21:
8% Blockage**

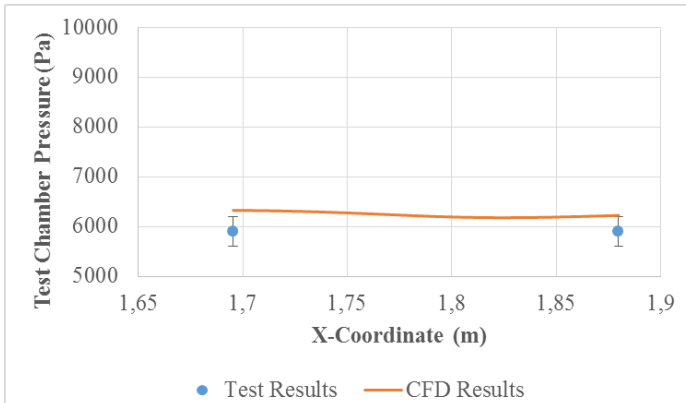


**Test 25:
15% Blockage**

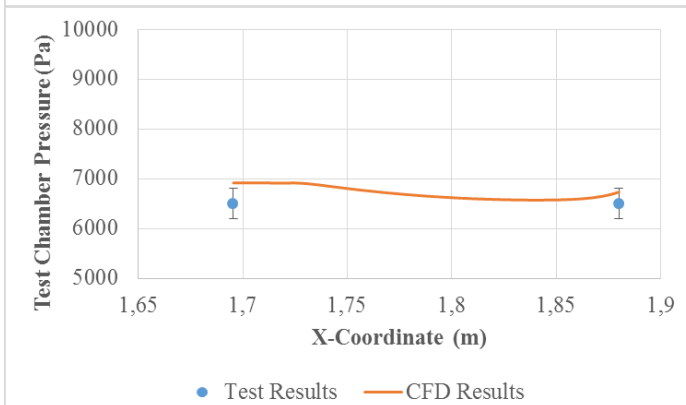


**Test 29:
25% Blockage**

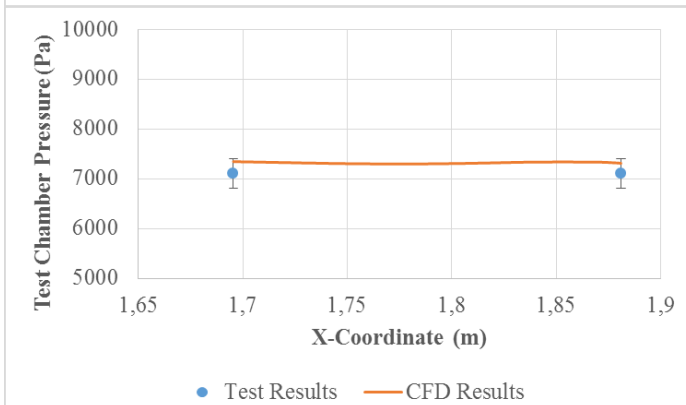
[Mach 2.5 - 1300 g/s]



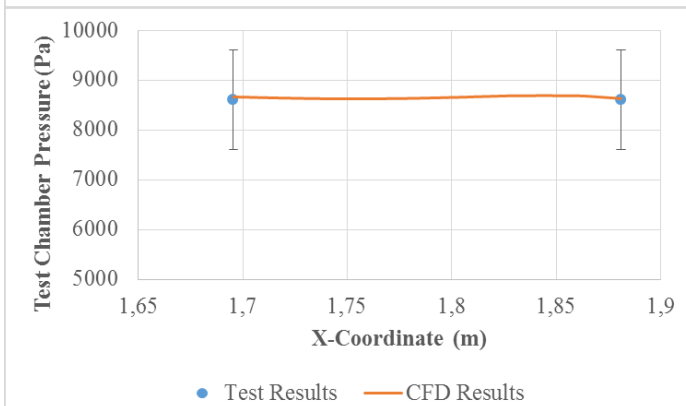
**Test 18:
0% Blockage**



**Test 22:
8% Blockage**

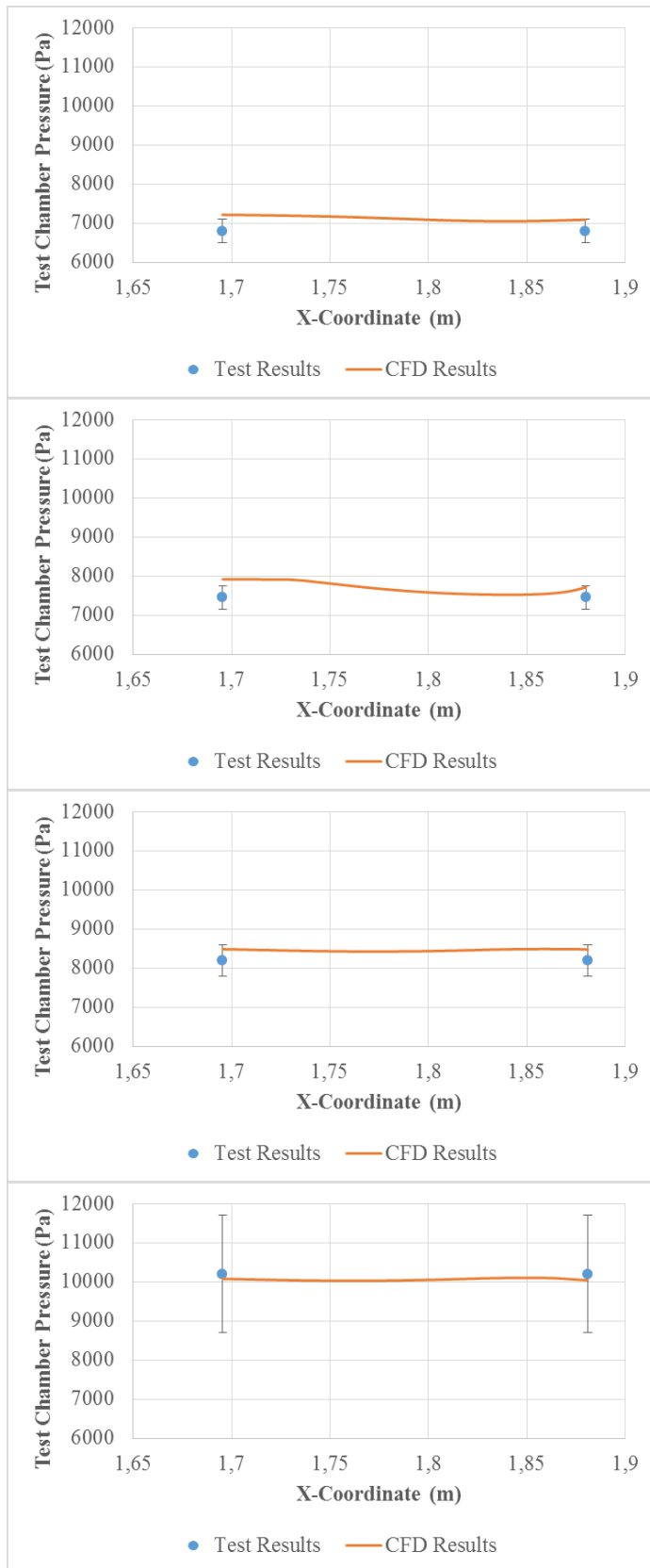


**Test 26:
15% Blockage**



**Test 30:
25% Blockage**

[Mach 2.5 - 1500 g/s]



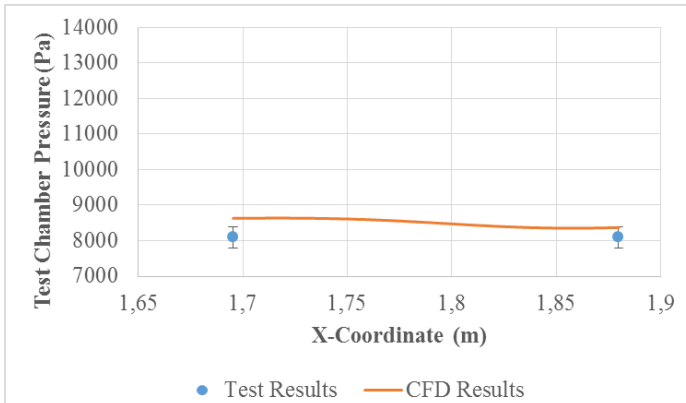
Test 19:
0% Blockage

Test 23:
8% Blockage

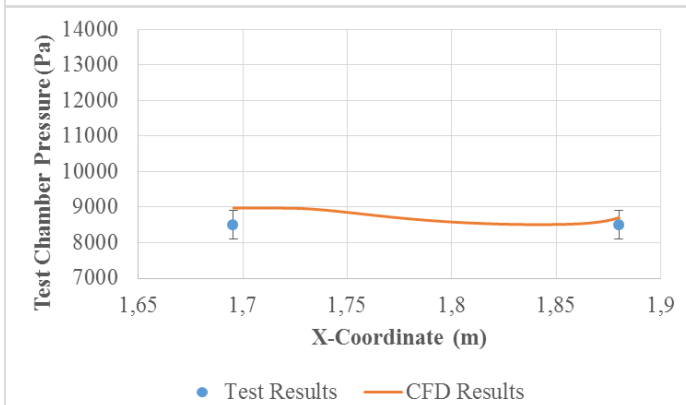
Test 27:
15% Blockage

Test 31:
25% Blockage

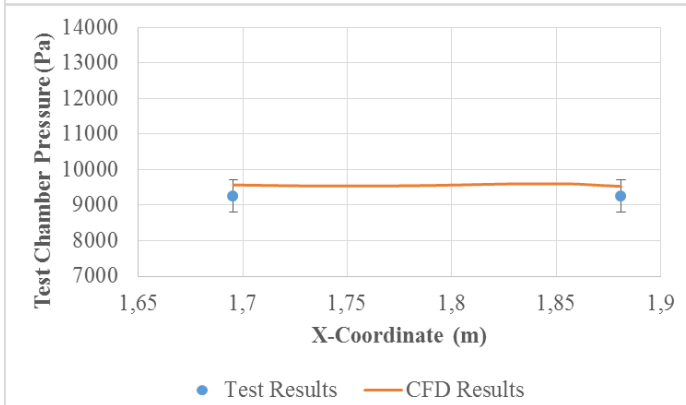
[Mach 2.5 - 1900 g/s]



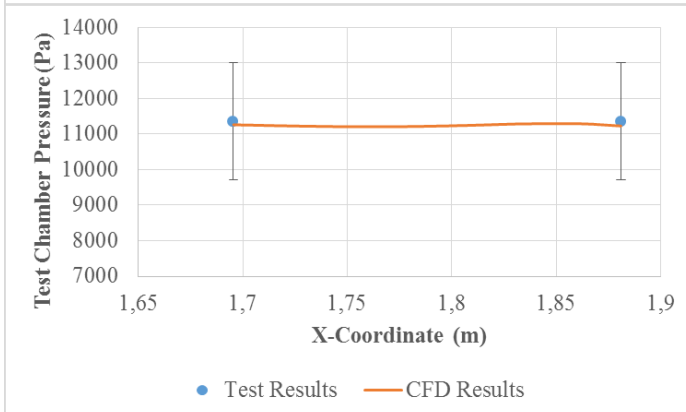
**Test 20:
0% Blockage**



**Test 24:
8% Blockage**



**Test 28:
15% Blockage**



**Test 32:
25% Blockage**

3.6.2. Schlieren Imaging

Another comparison between the experimental and numerical results can be made with Schlieren images for different test conditions. Numerical Schlieren illustrations and images captured by using Schlieren method during experiments give also good convergence for different mass flow rate and blockage test article conditions. All numerical Schlieren images compared with Schlieren images captured during experimental tests are also given in this section.

The comparison includes the angle of the shockwaves and determining the test region where the nose of the test article is located in. Some strong shockwave and weak expansion waves can also be compared in terms of the location and length of the waves using these results. The test rhombus of the free-jet nozzle varies according to the nozzles designed for different Mach numbers and altitude conditions. Mach cone is the conical pressure wave occurred at the exit of the nozzle which exit speed is greater than that of sound. Mach cone angle can be calculated as given in Equation 3-17.

$$\theta = \sin^{-1}\left(\frac{1}{M}\right) \quad (3-17)$$

The tabulated Mach cone angles for Mach 2 and 2.5 free-jet nozzles are given theoretically in Table 3-3.

Table 3-3. Mach Cone Angle for Mach 2 and 2.5 Free-Jet Nozzles.

Mach Number	Angle Notation	Mach Cone Angle (°)
2	θ_1	30
2.5	θ_2	23.56

It is seen that the test rhombus increases as the Mach number increases for nozzles with the same exit diameter. The sketch of the test rhombus for both of Mach 2 and 2.5 free-jet nozzles are also given in Figure 3-41.

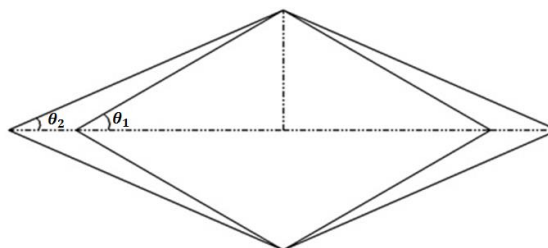


Figure 3-41. Sketch of the Test Rhombus for Mach 2 and 2.5 Free-Jet Nozzles.

It is seen that the testable length of the test article increases when it is positioned into the free-jet nozzle. But, this length is also related to the nosecone of the test article. In addition to keeping the test article inside the test rhombus, the bow shock that will occur due to the nosecone geometry must also be outside the free-jet nozzle. This situation is shown in Figure 3-42.

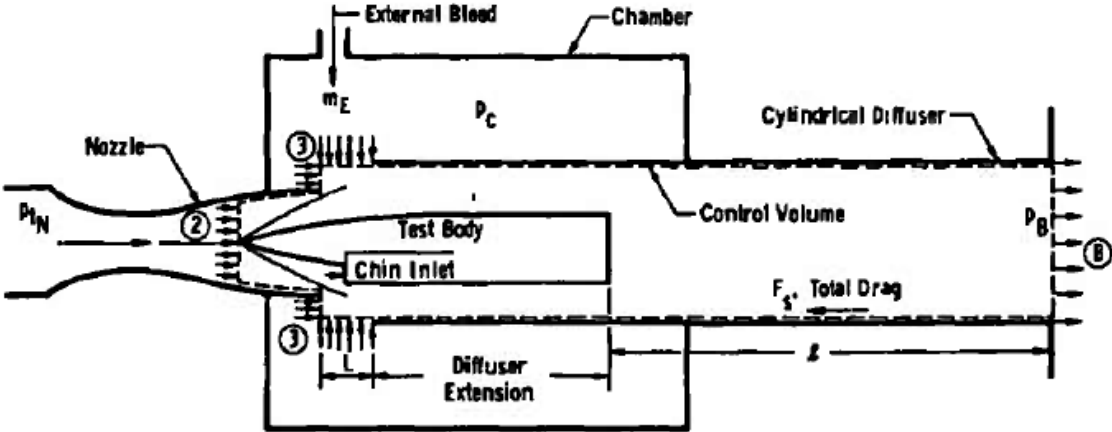


Figure 3-42. Sketch of Positioning the Test Article Inside the Test Chamber [10].

In this study, in order to clearly see the shock formations formed on the test article, the test article is placed out of the free-jet nozzle provided that it is still within the test rhombus. Thus, shockwaves reflected from both the free-jet nozzle and the nosecone of the test article can be observed using Schlieren method.

During experimental tests, Schlieren images are recorded by projecting on the high speed camera for each test separately. When the secondary flow rate of the free-jet nozzle reaches at its predetermined testing value and the oscillations in the mass flow rate data is lowered, video recording with high speed camera starts. Since Schlieren images are received in high resolution and high frame per second, fps, video recording can be performed for a limited time of about 3 seconds on average. Therefore, 15000 frames are obtained for each test separately. Then, an average image is obtained with the help of 'ImageJ' computer program by selecting 100, 200, 500, 1000 and 2000 of the obtained images, respectively for a test condition. When the average image results are compared, it is seen that the image obtained from 500 frames gives a good result, then it is continued by averaging the same number of frames for the other test conditions.

After obtaining average intensity image, the Mach cone angle of the free-jet nozzle and the oblique shock angle at the nosecone of the test article is calculated for each test condition. Mach cone angle, α_1 and oblique shock angle, α_2 express the angles on the Schlieren image obtained according to the experimental test results and numerical analyses. An example illustration of the comparison according to the shock angles and Schlieren images is given in Figure 3-43.

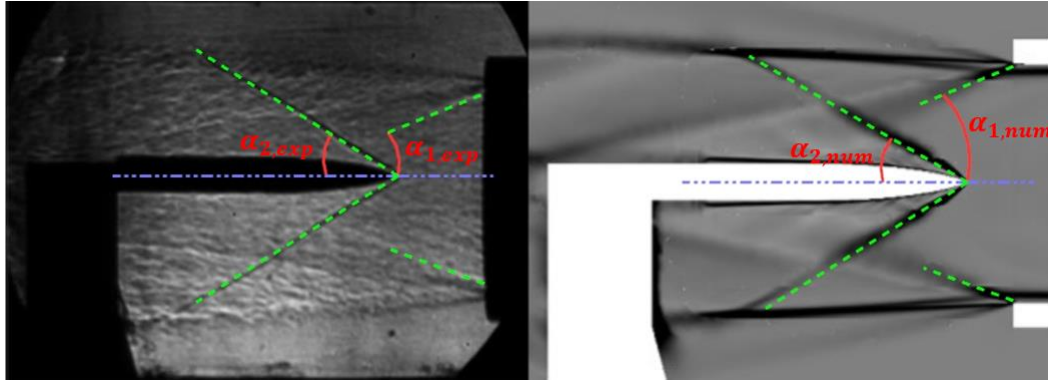


Figure 3-43. Example Comparison of the Schlieren Images and Shock Angles.

The comparisons for all test conditions are made with the same manner and the results are given in the following tables. In some cases, where there is no blockage or the free-jet nozzle does not start, that is, a normal shock occurs at the nozzle outlet, some angle values given in the tables could not be calculated. However, for all other test conditions, approximate angle values have been tried to be given for both experimental and numerical Schlieren images. The percentage absolute error can also be calculated to determine how much the shock angles obtained using numerical Schlieren images differ from the experimental Schlieren shock angles using Equation 3.18.

$$Percentage\ Absolute\ Error = \frac{|\alpha_{num} - \alpha_{exp}|}{\alpha_{exp}} \times 100\% \quad (3-18)$$

It is observed that there are differences between the experimental and numerical Schlieren images obtained in some test conditions for Mach 2 free-jet nozzle designed and manufactured in the study of [2]. One reason for this situation can be evaluated as there are differences in the dimensions of Mach 2 free-jet nozzle manufactured and because it is not manufactured as designed, the free-jet nozzle exit pressure may change. Another reason may be that the entire test setup with ejector system is not solved in numerical analyses. In this case, the pressure outlet boundary condition used for numerical analyses may not be given exactly to simulate the operation of the ejector

system. The test chamber pressure is higher than the free-jet nozzle exit pressure for both situations, the free-jet nozzle is over-expanded and the flow separates towards the free-jet nozzle exit and a normal shock occurs at the free-jet nozzle exit.

As the free-jet nozzle outlet pressure increases with the increasing inlet pressure, the normal shock occurring at the free-jet nozzle exit is defeated and the free-jet nozzle works as ideally expanded. Test-5 can be shown for Mach 2 free-jet nozzle as an example. When the free-jet nozzle theoretical pressure and test chamber pressure given in Appendix-3 are compared, it is seen for Test-5 that the test chamber pressure is approximately twice the free-jet nozzle exit pressure. The same situation can also be evaluated for Test-15 and Test-16. Experimental and numerical Schlieren images are given in Figure 3-44 for Test-5 as an example.

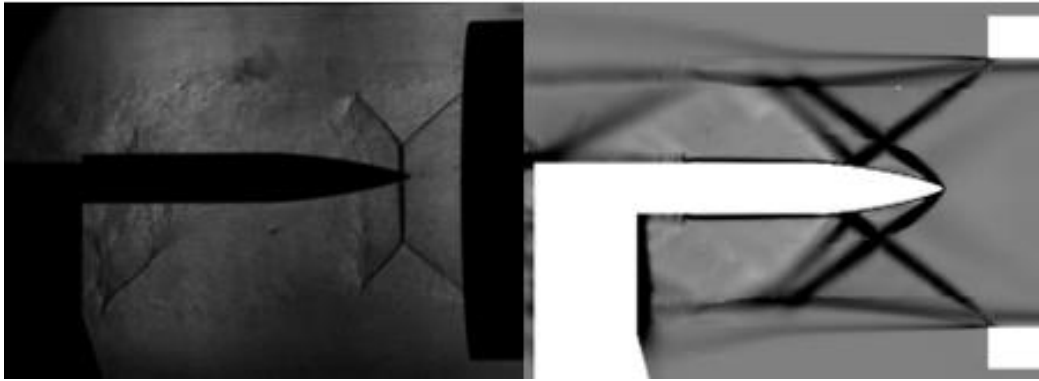


Figure 3-44. Experimental vs. Numerical Schlieren Image [Test-5].

Although the test chamber pressure is predicted as 10500 Pa in numerical analyses, it is measured as approximately 14500 Pa in experimental tests. The free-jet nozzle exit pressure theoretically is calculated as 7000 Pa. In this case, differences occur in the experimental and numerical Schlieren images for Test-5 as seen in Figure 3-44. It is also seen that both experimental and numerical schlieren images of Mach 2.5 free-jet nozzle designed and manufactured in this thesis are similar for all test conditions.

Table 3-4. Experimental vs. Numerical Schlieren Image [Test-1].

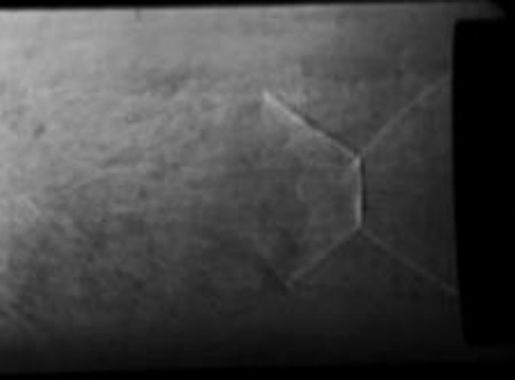
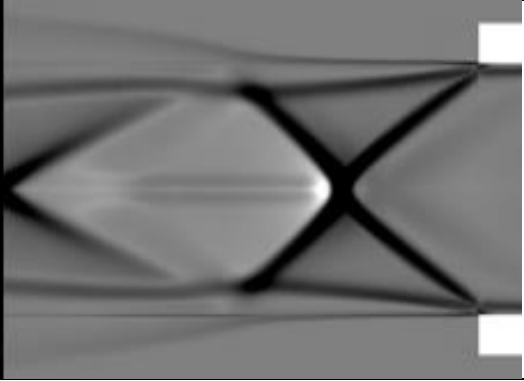
Experimental Schlieren		Numerical Schlieren	
$\alpha_{1,exp}(\text{°})$	$\alpha_{2,exp}(\text{°})$	$\alpha_{1,num}(\text{°})$	$\alpha_{2,num}(\text{°})$
41	-	38	-
Percentage Absolute Error, %			
α_1		α_2	
7.3		-	
			
Test-1: [Mach 2 - 750 g/s - 0% Blockage]			

Table 3-5. Experimental vs. Numerical Schlieren Image [Test-2].

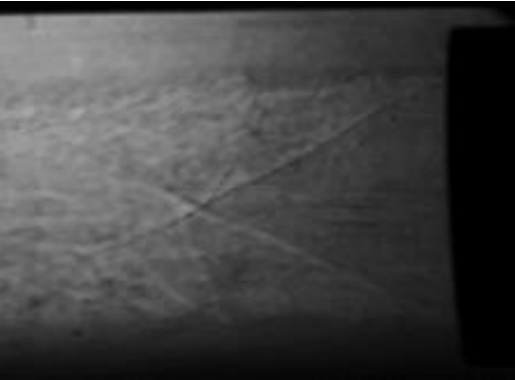
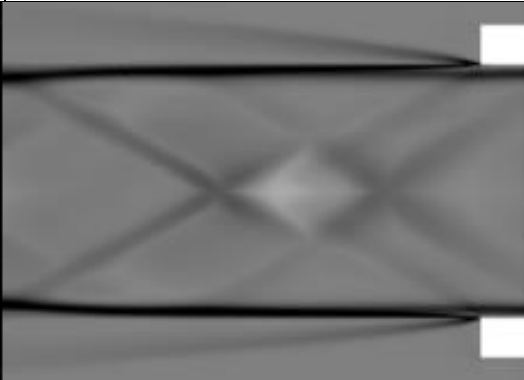
Experimental Schlieren		Numerical Schlieren	
$\alpha_{1,exp}(\text{°})$	$\alpha_{2,exp}(\text{°})$	$\alpha_{1,num}(\text{°})$	$\alpha_{2,num}(\text{°})$
27	-	26	-
Percentage Absolute Error, %			
α_1		α_2	
3.7		-	
			
Test-2: [Mach 2 - 1100 g/s - 0% Blockage]			

Table 3-6. Experimental vs. Numerical Schlieren Image [Test-3].


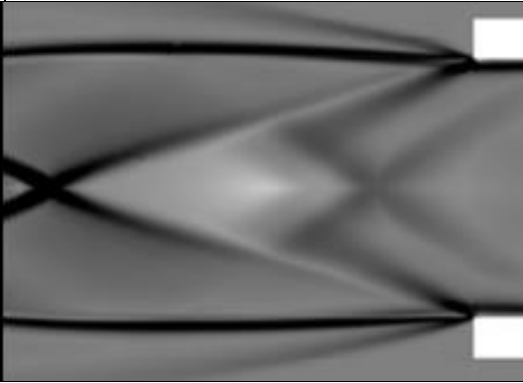
Experimental Schlieren		Numerical Schlieren	
$\alpha_{1,exp}(\text{°})$	$\alpha_{2,exp}(\text{°})$	$\alpha_{1,num}(\text{°})$	$\alpha_{2,num}(\text{°})$
24	-	23	-
Percentage Absolute Error, %			
α_1		α_2	
4.2		-	
			
Test-3: [Mach 2 - 1500 g/s - 0% Blockage]			

Table 3-7. Experimental vs. Numerical Schlieren Image [Test-4].

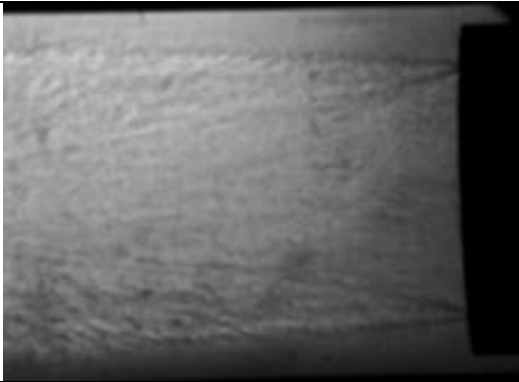
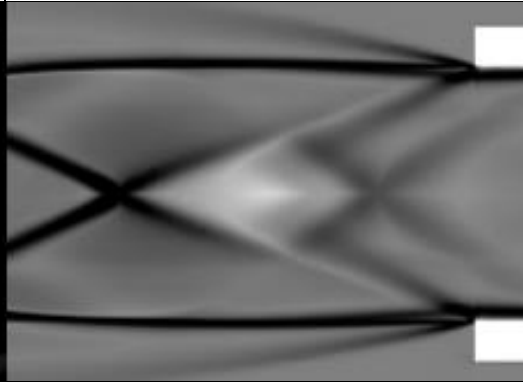
Experimental Schlieren		Numerical Schlieren	
$\alpha_{1,exp}(\text{°})$	$\alpha_{2,exp}(\text{°})$	$\alpha_{1,num}(\text{°})$	$\alpha_{2,num}(\text{°})$
21	-	23	-
Percentage Absolute Error, %			
α_1		α_2	
9.5		-	
			
Test-4: [Mach 2 - 1900 g/s - 0% Blockage]			

Table 3-8. Experimental vs. Numerical Schlieren Image [Test-5].

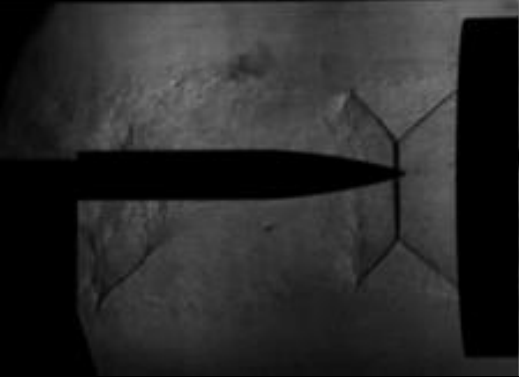
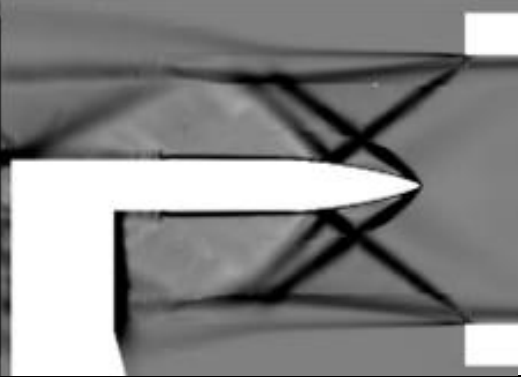
Experimental Schlieren		Numerical Schlieren	
$\alpha_{1,exp}(\text{°})$	$\alpha_{2,exp}(\text{°})$	$\alpha_{1,num}(\text{°})$	$\alpha_{2,num}(\text{°})$
39	-	37	37
Percentage Absolute Error, %			
α_1		α_2	
5.1		-	
			
Test-5: [Mach 2 - 750 g/s - 8% Blockage]			

Table 3-9. Experimental vs. Numerical Schlieren Image [Test-6].

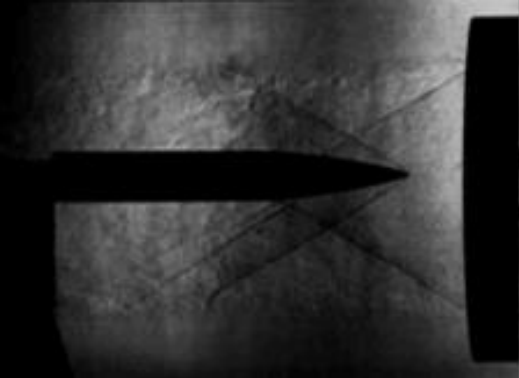
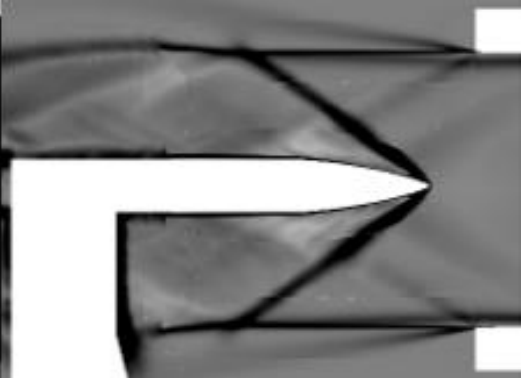
Experimental Schlieren		Numerical Schlieren	
$\alpha_{1,exp}(\text{°})$	$\alpha_{2,exp}(\text{°})$	$\alpha_{1,num}(\text{°})$	$\alpha_{2,num}(\text{°})$
30	30	29	36
Percentage Absolute Error, %			
α_1		α_2	
3.3		20.0	
			
Test-6: [Mach 2 - 1100 g/s - 8% Blockage]			

Table 3-10. Experimental vs. Numerical Schlieren Image [Test-7].

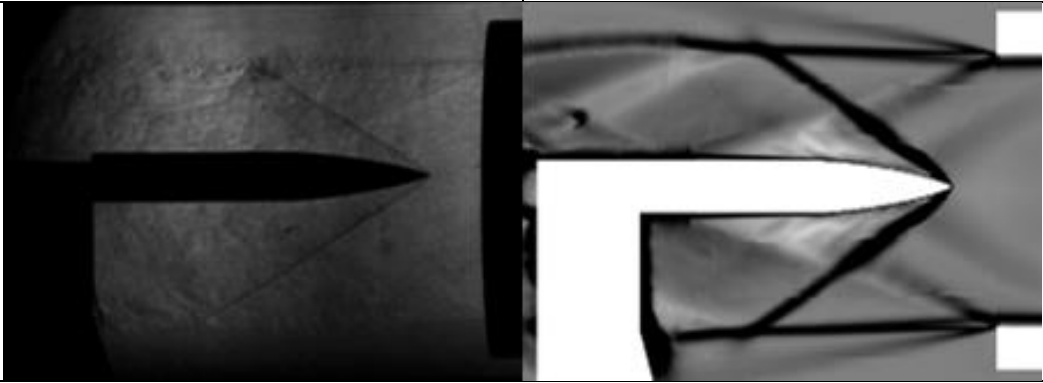
Experimental Schlieren		Numerical Schlieren	
$\alpha_{1,exp}(\text{°})$	$\alpha_{2,exp}(\text{°})$	$\alpha_{1,num}(\text{°})$	$\alpha_{2,num}(\text{°})$
21	32	21	36
Percentage Absolute Error, %			
α_1		α_1	
0.0		12.5	
			
Test-7: [Mach 2 - 1500 g/s - 8% Blockage]			

Table 3-11. Experimental vs. Numerical Schlieren Image [Test-8].

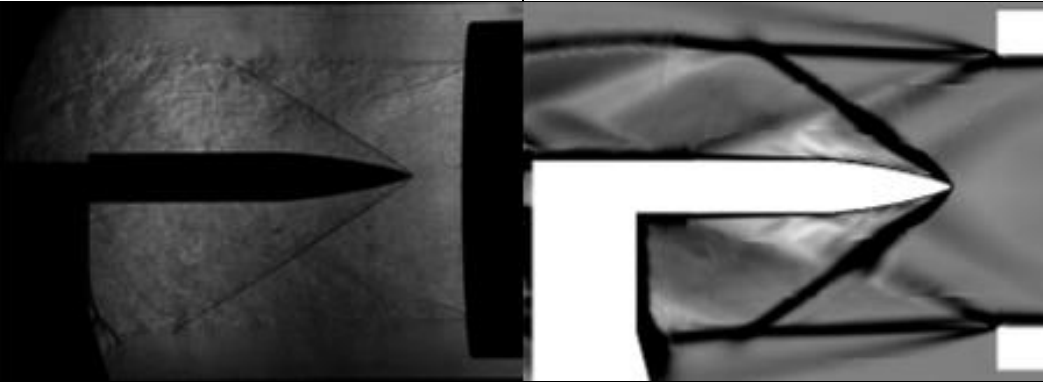
Experimental Schlieren		Numerical Schlieren	
$\alpha_{1,exp}(\text{°})$	$\alpha_{2,exp}(\text{°})$	$\alpha_{1,num}(\text{°})$	$\alpha_{2,num}(\text{°})$
20	33	19	36
Percentage Absolute Error, %			
α_1		α_1	
5.0		9.1	
			
Test-8: [Mach 2 - 1900 g/s - 8% Blockage]			

Table 3-12. Experimental vs. Numerical Schlieren Image [Test-9].

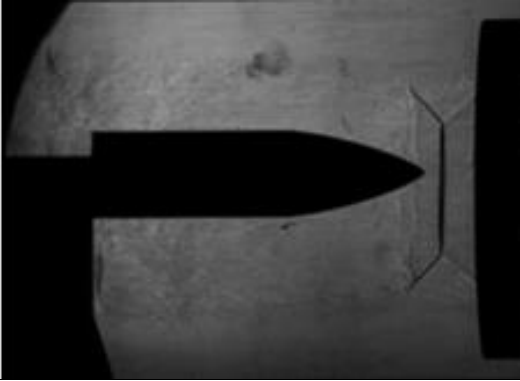
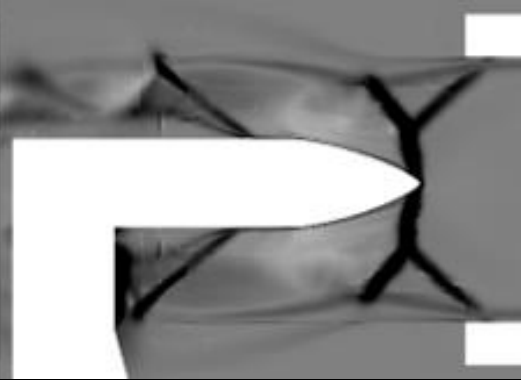
Experimental Schlieren		Numerical Schlieren	
$\alpha_{1,exp}(\text{°})$	$\alpha_{2,exp}(\text{°})$	$\alpha_{1,num}(\text{°})$	$\alpha_{2,num}(\text{°})$
39	-	40	-
Percentage Absolute Error, %			
α_1		α_1	
2.6		-	
			
Test-9: [Mach 2 - 750 g/s - 15% Blockage]			

Table 3-13. Experimental vs. Numerical Schlieren Image [Test-10].

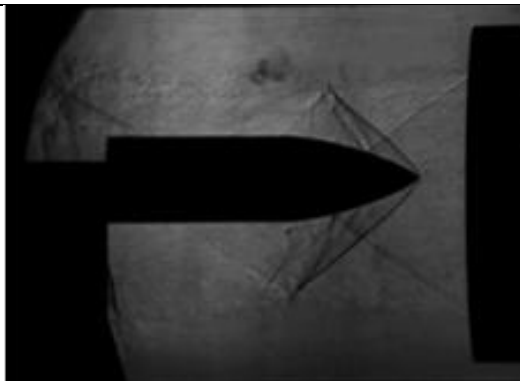
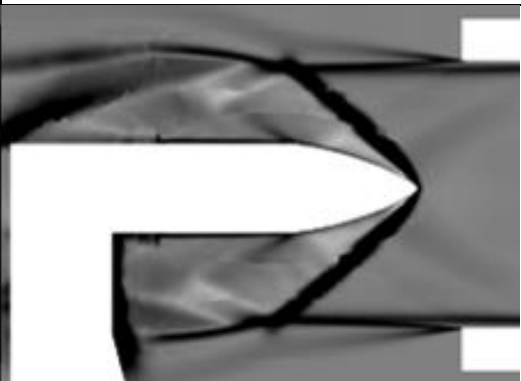
Experimental Schlieren		Numerical Schlieren	
$\alpha_{1,exp}(\text{°})$	$\alpha_{2,exp}(\text{°})$	$\alpha_{1,num}(\text{°})$	$\alpha_{2,num}(\text{°})$
35	44	31	45
Percentage Absolute Error, %			
α_1		α_1	
11.4		2.3	
			
Test-10: [Mach 2 - 1100 g/s - 15% Blockage]			

Table 3-14. Experimental vs. Numerical Schlieren Image [Test-11].


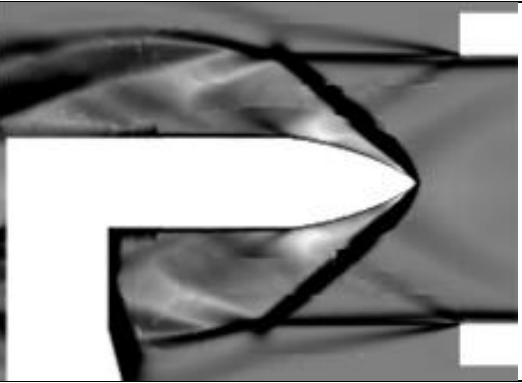
Experimental Schlieren		Numerical Schlieren	
$\alpha_{1,exp}(\text{°})$	$\alpha_{2,exp}(\text{°})$	$\alpha_{1,num}(\text{°})$	$\alpha_{2,num}(\text{°})$
29	42	27	44
Percentage Absolute Error, %			
α_1		α_1	
6.9		4.8	
			
Test-11: [Mach 2 - 1500 g/s - 15% Blockage]			

Table 3-15. Experimental vs. Numerical Schlieren Image [Test-12].


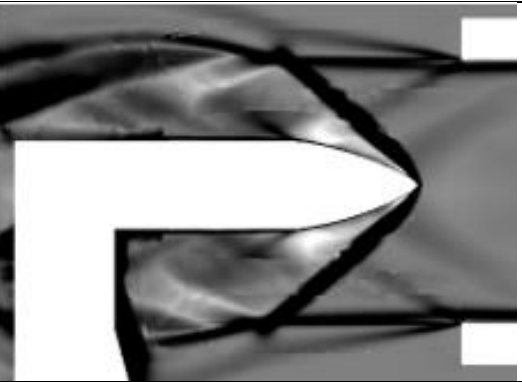
Experimental Schlieren		Numerical Schlieren	
$\alpha_{1,exp}(\text{°})$	$\alpha_{2,exp}(\text{°})$	$\alpha_{1,num}(\text{°})$	$\alpha_{2,num}(\text{°})$
31	42	30	43
Percentage Absolute Error, %			
α_1		α_1	
3.2		2.4	
			
Test-12: [Mach 2 - 1900 g/s - 15% Blockage]			

Table 3-16. Experimental vs. Numerical Schlieren Image [Test-13].


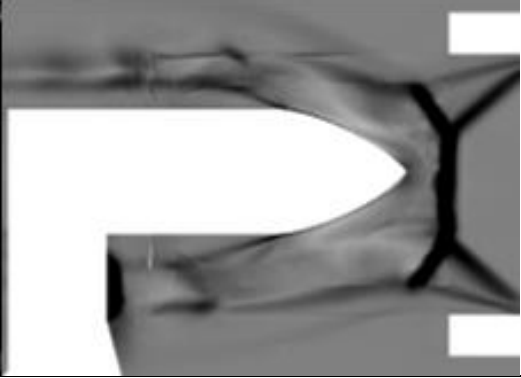
Experimental Schlieren		Numerical Schlieren	
$\alpha_{1,exp}(\text{°})$	$\alpha_{2,exp}(\text{°})$	$\alpha_{1,num}(\text{°})$	$\alpha_{2,num}(\text{°})$
-	-	39	-
Percentage Absolute Error, %			
α_1		α_1	
-		-	
			
Test-13: [Mach 2 - 750 g/s - 25% Blockage]			

Table 3-17. Experimental vs. Numerical Schlieren Image [Test-14].



Experimental Schlieren		Numerical Schlieren	
$\alpha_{1,exp}(\text{°})$	$\alpha_{2,exp}(\text{°})$	$\alpha_{1,num}(\text{°})$	$\alpha_{2,num}(\text{°})$
-	-	39	-
Percentage Absolute Error, %			
α_1		α_1	
-		-	
			
Test-14: [Mach 2 - 1100 g/s - 25% Blockage]			

Table 3-18. Experimental vs. Numerical Schlieren Image [Test-15].

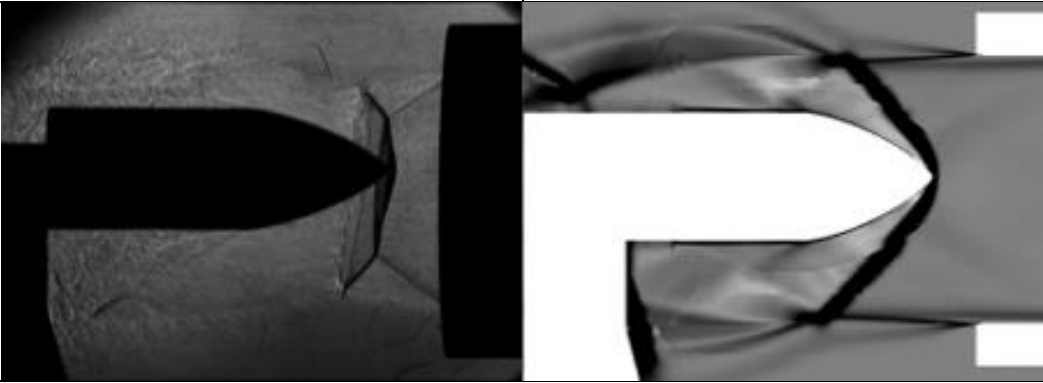
Experimental Schlieren		Numerical Schlieren	
$\alpha_{1,exp}(\text{°})$	$\alpha_{2,exp}(\text{°})$	$\alpha_{1,num}(\text{°})$	$\alpha_{2,num}(\text{°})$
34	-	36	53
Percentage Absolute Error, %			
α_1		α_1	
5.9		-	
			
Test-15: [Mach 2 - 1500 g/s - 25% Blockage]			

Table 3-19. Experimental vs. Numerical Schlieren Image [Test-16].

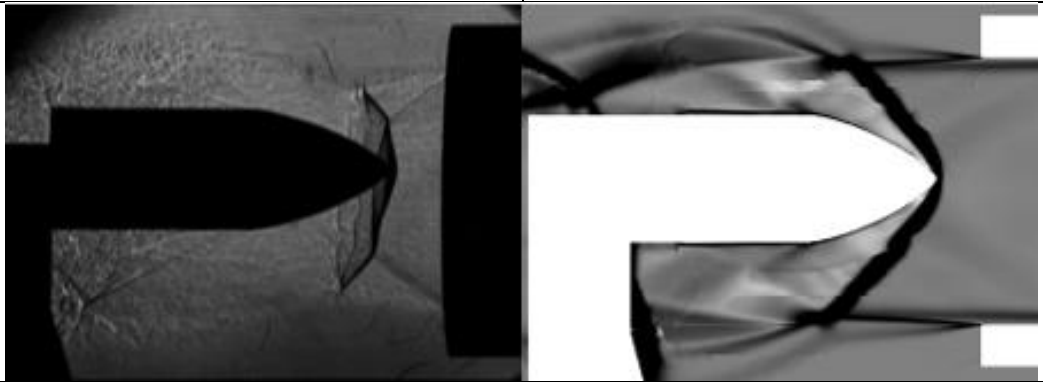
Experimental Schlieren		Numerical Schlieren	
$\alpha_{1,exp}(\text{°})$	$\alpha_{2,exp}(\text{°})$	$\alpha_{1,num}(\text{°})$	$\alpha_{2,num}(\text{°})$
37	-	35	53
Percentage Absolute Error, %			
α_1		α_1	
5.4		-	
			
Test-16: [Mach 2 - 1900 g/s - 25% Blockage]			

Table 3-20. Experimental vs. Numerical Schlieren Image [Test-17].

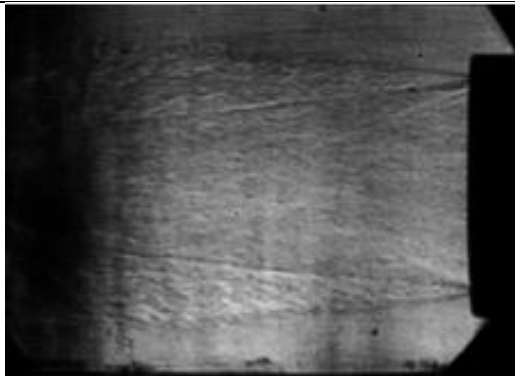
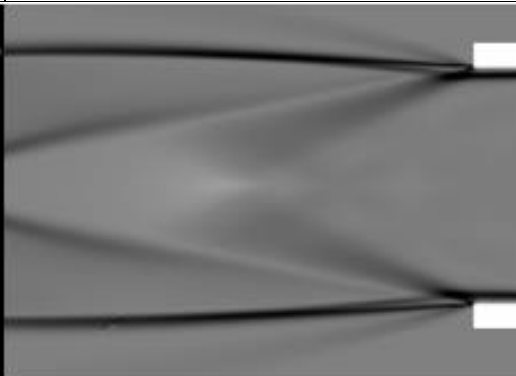
Experimental Schlieren		Numerical Schlieren	
$\alpha_{1,exp}(\text{°})$	$\alpha_{2,exp}(\text{°})$	$\alpha_{1,num}(\text{°})$	$\alpha_{2,num}(\text{°})$
22	-	24	-
Percentage Absolute Error, %			
α_1		α_1	
9.1		-	
			
Test-17: [Mach 2.5 - 750 g/s - 0% Blockage]			

Table 3-21. Experimental vs. Numerical Schlieren Image [Test-18].

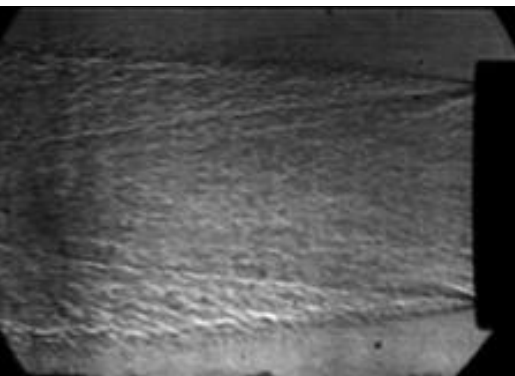
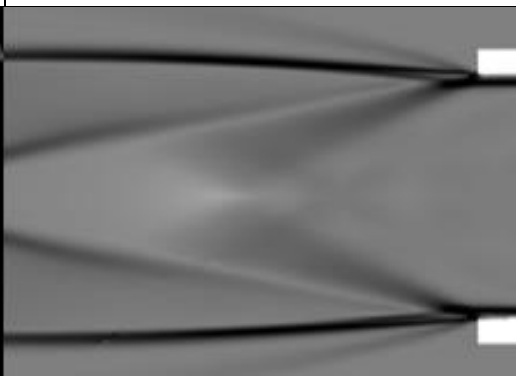
Experimental Schlieren		Numerical Schlieren	
$\alpha_{1,exp}(\text{°})$	$\alpha_{2,exp}(\text{°})$	$\alpha_{1,num}(\text{°})$	$\alpha_{2,num}(\text{°})$
23	-	26	-
Percentage Absolute Error, %			
α_1		α_1	
13.0		-	
			
Test-18: [Mach 2.5 - 1300 g/s - 0% Blockage]			

Table 3-22. Experimental vs. Numerical Schlieren Image [Test-19].

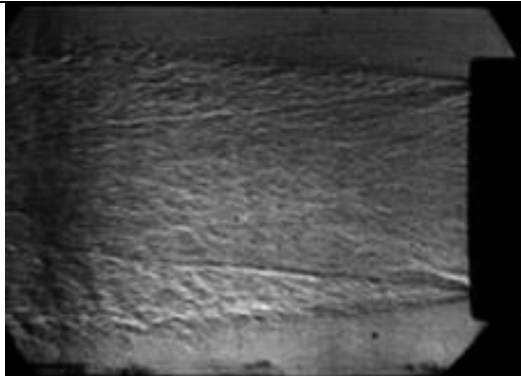
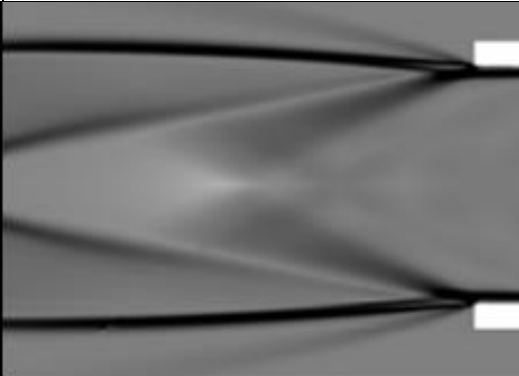
Experimental Schlieren		Numerical Schlieren	
$\alpha_{1,exp}(\text{°})$	$\alpha_{2,exp}(\text{°})$	$\alpha_{1,num}(\text{°})$	$\alpha_{2,num}(\text{°})$
20	-	25	-
Percentage Absolute Error, %			
α_1		α_1	
25.0		-	
			
Test-19: [Mach 2.5 - 1500 g/s - 0% Blockage]			

Table 3-23. Experimental vs. Numerical Schlieren Image [Test-20].

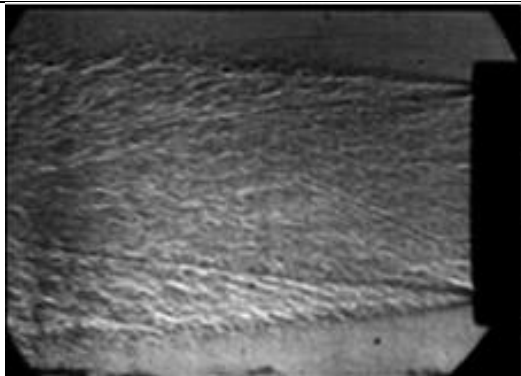
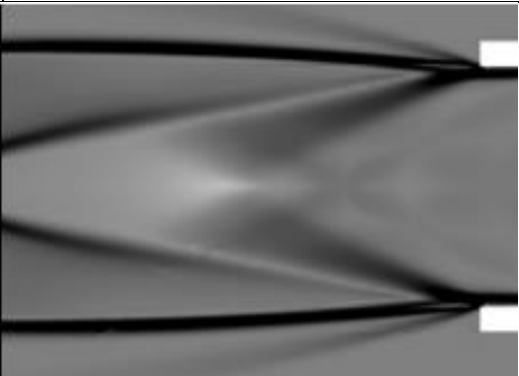
Experimental Schlieren		Numerical Schlieren	
$\alpha_{1,exp}(\text{°})$	$\alpha_{2,exp}(\text{°})$	$\alpha_{1,num}(\text{°})$	$\alpha_{2,num}(\text{°})$
21	-	25	-
Percentage Absolute Error, %			
α_1		α_1	
19.0		-	
			
Test-20: [Mach 2.5 - 1900 g/s - 0% Blockage]			

Table 3-24. Experimental vs. Numerical Schlieren Image [Test-21].

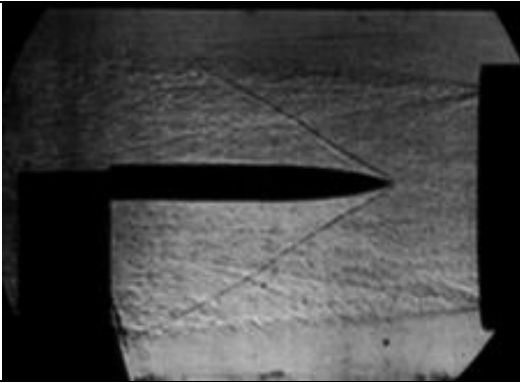
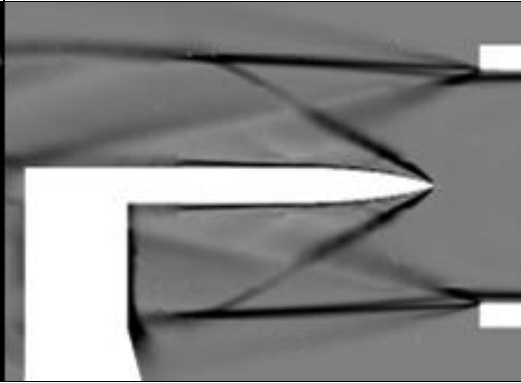
Experimental Schlieren		Numerical Schlieren	
$\alpha_{1,exp}(\text{°})$	$\alpha_{2,exp}(\text{°})$	$\alpha_{1,num}(\text{°})$	$\alpha_{2,num}(\text{°})$
20	31	21	30
Percentage Absolute Error, %			
α_1		α_1	
5.0		3.2	
			
Test-21: [Mach 2.5 - 750 g/s - 8% Blockage]			

Table 3-25. Experimental vs. Numerical Schlieren Image [Test-22].

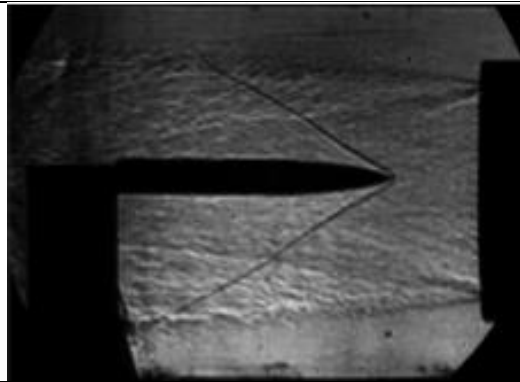
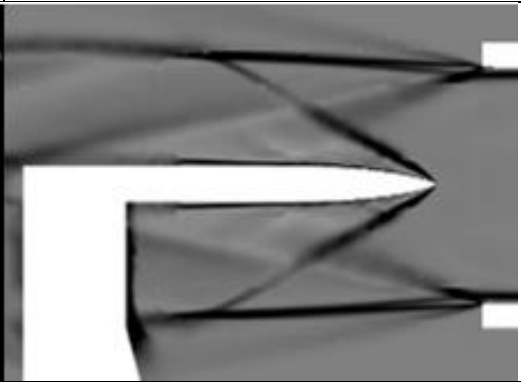
Experimental Schlieren		Numerical Schlieren	
$\alpha_{1,exp}(\text{°})$	$\alpha_{2,exp}(\text{°})$	$\alpha_{1,num}(\text{°})$	$\alpha_{2,num}(\text{°})$
22	32	22	30
Percentage Absolute Error, %			
α_1		α_1	
0.0		6.25	
			
Test-22: [Mach 2.5 - 1300 g/s - 8% Blockage]			

Table 3-26. Experimental vs. Numerical Schlieren Image [Test-23].

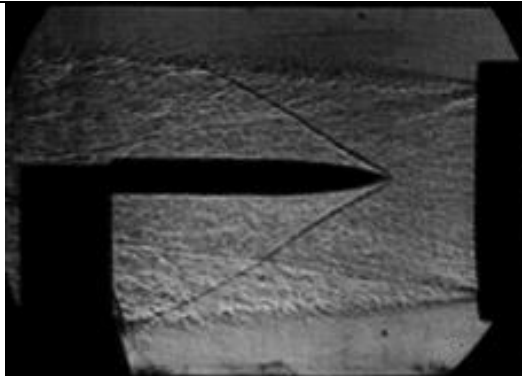
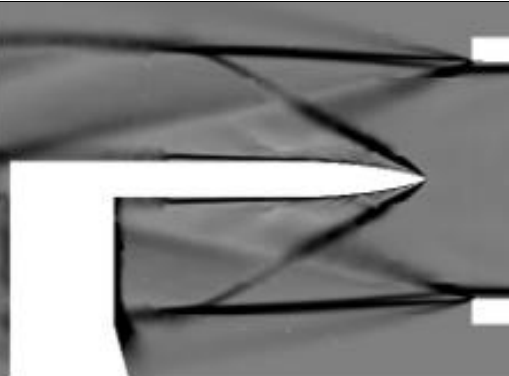
Experimental Schlieren		Numerical Schlieren	
$\alpha_{1,exp}(\text{°})$	$\alpha_{2,exp}(\text{°})$	$\alpha_{1,num}(\text{°})$	$\alpha_{2,num}(\text{°})$
21	31	22	30
Percentage Absolute Error, %			
α_1		α_1	
4.8		3.2	
			
Test-23: [Mach 2.5 - 1500 g/s - 8% Blockage]			

Table 3-27. Experimental vs. Numerical Schlieren Image [Test-24].

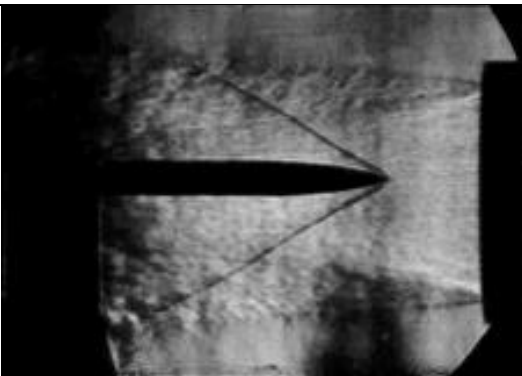
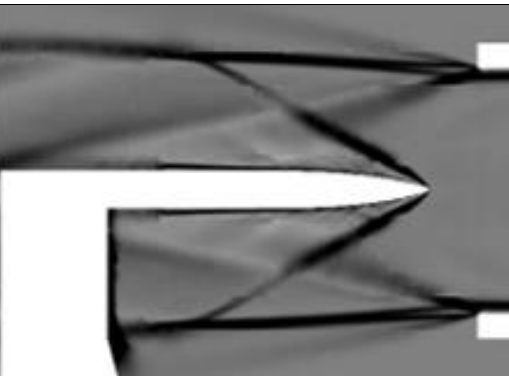
Experimental Schlieren		Numerical Schlieren	
$\alpha_{1,exp}(\text{°})$	$\alpha_{2,exp}(\text{°})$	$\alpha_{1,num}(\text{°})$	$\alpha_{2,num}(\text{°})$
18	30	24	30
Percentage Absolute Error, %			
α_1		α_1	
33.3		0.0	
			
Test-24: [Mach 2.5 - 1900 g/s - 8% Blockage]			

Table 3-28. Experimental vs. Numerical Schlieren Image [Test-25].



Experimental Schlieren		Numerical Schlieren	
$\alpha_{1,exp}(\text{°})$	$\alpha_{2,exp}(\text{°})$	$\alpha_{1,num}(\text{°})$	$\alpha_{2,num}(\text{°})$
21	40	23	39
Percentage Absolute Error, %			
α_1		α_1	
9.5		2.5	
			
Test-25: [Mach 2.5 - 750 g/s - 15% Blockage]			

Table 3-29. Experimental vs. Numerical Schlieren Image [Test-26].

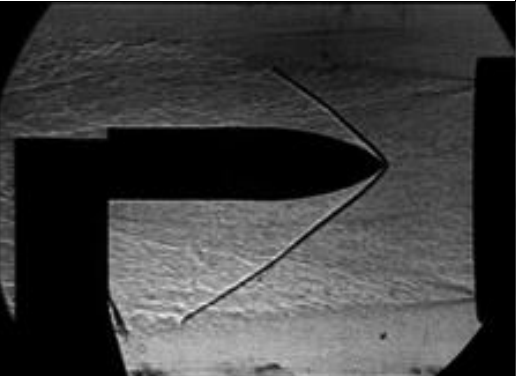

Experimental Schlieren		Numerical Schlieren	
$\alpha_{1,exp}(\text{°})$	$\alpha_{2,exp}(\text{°})$	$\alpha_{1,num}(\text{°})$	$\alpha_{2,num}(\text{°})$
20	40	20	38
Percentage Absolute Error, %			
α_1		α_1	
0.0		5.0	
			
Test-26: [Mach 2.5 - 1300 g/s - 15% Blockage]			

Table 3-30. Experimental vs. Numerical Schlieren Image [Test-27].

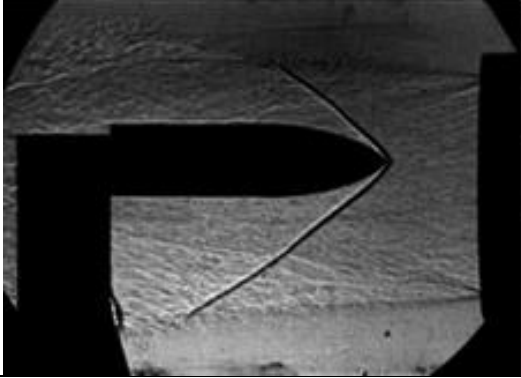

Experimental Schlieren		Numerical Schlieren	
$\alpha_{1,exp}(\text{°})$	$\alpha_{2,exp}(\text{°})$	$\alpha_{1,num}(\text{°})$	$\alpha_{2,num}(\text{°})$
21	40	20	39
Percentage Absolute Error, %			
α_1		α_1	
4.8		2.5	
			
Test-27: [Mach 2.5 - 1500 g/s - 15% Blockage]			

Table 3-31. Experimental vs. Numerical Schlieren Image [Test-28].



Experimental Schlieren		Numerical Schlieren	
$\alpha_{1,exp}(\text{°})$	$\alpha_{2,exp}(\text{°})$	$\alpha_{1,num}(\text{°})$	$\alpha_{2,num}(\text{°})$
21	42	23	39
Percentage Absolute Error, %			
α_1		α_1	
9.5		7.1	
			
Test-28: [Mach 2.5 - 1900 g/s - 15% Blockage]			

Table 3-32. Experimental vs. Numerical Schlieren Image [Test-29].



Experimental Schlieren		Numerical Schlieren	
$\alpha_{1,exp}(\text{°})$	$\alpha_{2,exp}(\text{°})$	$\alpha_{1,num}(\text{°})$	$\alpha_{2,num}(\text{°})$
25	45	26	44
Percentage Absolute Error, %			
α_1		α_1	
4.0		2.2	
			
Test-29: [Mach 2.5 - 750 g/s - 25% Blockage]			

Table 3-33. Experimental vs. Numerical Schlieren Image [Test-30].

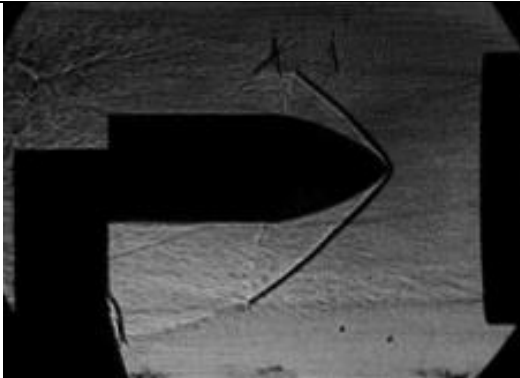

Experimental Schlieren		Numerical Schlieren	
$\alpha_{1,exp}(\text{°})$	$\alpha_{2,exp}(\text{°})$	$\alpha_{1,num}(\text{°})$	$\alpha_{2,num}(\text{°})$
21	45	23	45
Percentage Absolute Error, %			
α_1		α_1	
9.5		0.0	
			
Test-30: [Mach 2.5 - 1300 g/s - 25% Blockage]			

Table 3-34. Experimental vs. Numerical Schlieren Image [Test-31].

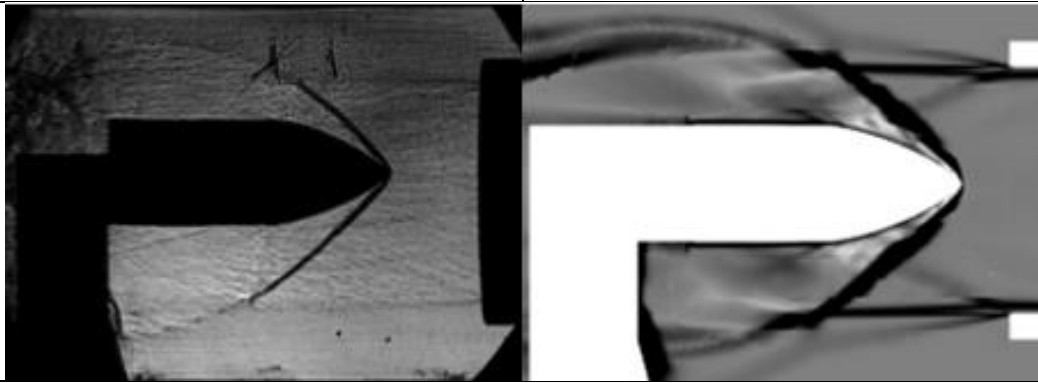
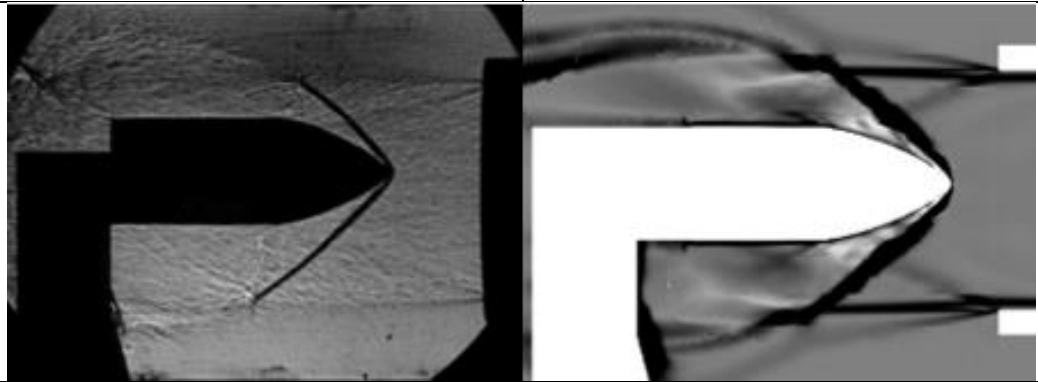
Experimental Schlieren		Numerical Schlieren	
$\alpha_{1,exp}(\text{°})$	$\alpha_{2,exp}(\text{°})$	$\alpha_{1,num}(\text{°})$	$\alpha_{2,num}(\text{°})$
20	44	22	45
Percentage Absolute Error, %			
α_1		α_1	
10.0		2.3	
			
Test-31: [Mach 2.5 - 1500 g/s - 25% Blockage]			

Table 3-35. Experimental vs. Numerical Schlieren Image [Test-32].

Experimental Schlieren		Numerical Schlieren	
$\alpha_{1,exp}(\text{°})$	$\alpha_{2,exp}(\text{°})$	$\alpha_{1,num}(\text{°})$	$\alpha_{2,num}(\text{°})$
20	44	23	45
Percentage Absolute Error, %			
α_1		α_1	
15.0		2.3	
			
Test-32: [Mach 2.5 - 1900 g/s - 25% Blockage]			

4. CONCLUSION AND FUTURE STUDY

4.1. Conclusion

In this thesis, test section of the high altitude test system was investigated with/without blockage test articles experimentally and numerically. Ejector section of the high altitude test system was not the part of this study and just used for the outlet pressure boundary condition in the numerical analyses and considered working at its optimum condition around 20 bar ejector nozzle inlet total pressure for successful starting of the free-jet nozzle in the experimental tests. Mach 2.5 free-jet nozzle was designed using one-dimensional theory of nozzle besides Mach 2 free-jet nozzle to test different Mach number and altitude conditions. Free-jet nozzle calculations were performed with entrainment ratio of 0.33 as around 1 kg/s in accordance with the ejector nozzle mass flow rate as around 3 kg/s. Mass flow rate of 1 kg/s test condition for the free-jet nozzle was the main subject of the experimental tests. This condition is coming from the thesis result about determining design parameters of the high altitude test system established in TÜBİTAK-SAGE [2]. Lower and higher mass flow rates than 1 kg/s were also chosen for the mass flow rate of the free-jet nozzle inlet to characterize and show diversities in the test chamber pressure. Both of the free-jet nozzles were installed into the test chamber to ensure the high altitude pressure environment and so to test the articles in the vacuum pressure environment. High altitude test system did not start as expected for the lower mass flow rates of free-jet nozzle and in some situations with higher blockage test articles test chamber pressure was not also lowered to start the test system.

The test articles with three different blockage ratios according to both of the free-jet nozzles were designed with a special nosecone geometry. The supporting mechanism was also designed. These supporting mechanism and test articles were installed for different test conditions inside the test chamber. The experimental tests were conducted in HATS established in the test facility. Pressure, temperature and mass flow rate data were collected during these experimental tests. Vacuum pressure in the test section diffuser was measured from the wall used for pressure outlet boundary condition in numerical analyses. The weighted average pressure at this plane obtained from the experimental tests can be lower in reality to be used for CFD analyses as pressure outlet

boundary condition because of the high speed flow occurring at the centerline of the test section diffuser outlet.

It is observed that there are high fluctuations in the pressure data sampled during some of the experimental tests. When the free-jet nozzle exit pressure is lower than the test chamber pressure, the amplitude of the pressure oscillations becomes higher. Amplitude of the fluctuations in the pressure data increases for fixed geometry of the ejector system for Mach 2 compared to Mach 2.5 free-jet nozzle because of that free-jet nozzle and diffuser are at unstarted mode or moderately started mode and pressure oscillates due to the moving waves inside the system. The diameter of the ejector diffuser is calculated for a given total mass flow rate that is the sum of the primary and secondary mass flow rates. If this determined mass flow rate increases, ejector cannot show good performance and test section diffuser and test chamber pressure also increase.

Schlieren method were used to visually inspect the fluid flow properties like shockwaves. The mass flow rate and blockage ratio effects on the test chamber pressure were compared by using experimental test results and numerical simulation results. The numerical analyses were performed with the help of the data obtained from the experimental tests for the same conditions. The fluid flow properties were compared obtained from numerical analyses with experimental tests including Schlieren images. The altitude condition low pressure environment between 9000 and 17000 meters for Mach 2 free-jet nozzle and between 15000 and 22000 meters for Mach 2.5 free-jet nozzle were simulated in this study. Sea level or other altitude conditions can also be simulated for different flow rates of the free-jet nozzles. Atmospheric pressure data is also given in Appendix-2 in detail. Mach 2 free-jet nozzle was used in this study, which is a continuation of the thesis about design parameter of the HATS [2]. Then, it was concluded that for most test conditions this Mach 2 free-jet nozzle was not started and test chamber pressure does not appear to decrease. Hence, this can be said as a result that another free-jet nozzle with lower nozzle exit diameter may be used to test also Mach 2 test conditions. Mach 2.5 free-jet nozzle was designed and tested in this study. Its exit diameter was lowered and exit pressure was always higher than the test chamber pressure for all cases except 25% blockage with the lowest mass flow rate.

It was also observed that one of the crucial factors is the diffuser diameter. The ratio of the free-jet nozzle exit diameter to the test section diffuser diameter is around 80% for Mach 2 free-jet nozzle and around 70% for Mach 2.5 free-jet nozzle. Then, it was the result of this ratio that Mach 2 free-jet nozzle is not started and does not lower the test chamber pressure at the desired levels. This difference for Mach 2 free-jet nozzle compared to the Mach 2.5 free-jet nozzle can also be seen from the experimental test results that very high pressure oscillations occur for the test chamber pressure and this oscillation is getting higher for higher free-jet nozzle inlet pressure. This is due to this reason that free-jet nozzle exit diameter is very close to the test section diffuser diameter and flow coming from the free-jet nozzle is not captured totally by the test section diffuser and fills the test chamber. To lower this test chamber pressure, the exit diameter of the free-jet nozzle should also be decreased for a fixed diameter of the diffuser to capture the whole flow.

4.2. Future Study

Proposed study examples given below can be used for future studies,

- Hot flow conditions can be tested by supplying high temperature airflow to the test articles
- Different free-jet nozzles can be used to test different Mach number conditions
- Color Schlieren Photography Method, 'CSPM' can be used to obtain more and sensitive data in shockwave researchs
- Positive and/or negative angle of attack can be given to the test articles to observe the effects of the angle and so higher blockage ratios
- The free-jet nozzle exit diameter according to the diffuser entry duct diameter can be studied both experimentally and numerically
- Mixing characteristics of the flow from the free-jet nozzle and ejector nozzle can be studied using Particle Image Velocimetry, 'PIV'

5. REFERENCES

- [1] H. B. Goethert, "High Altitude and Space Simulation Testing," ARS Space Flight Report to the Nation, 1962.
- [2] A. Aydogdu, "Design of a Test Setup for Altitude Simulation," *Master Thesis, METU*, 2019.
- [3] D. T. Daniel, "A General Simulation of an Air Ejector Diffuser System," *Master Thesis, University of Tennessee*, 2010.
- [4] Manikanda Kumaran R., Vivekanand P. K., Sundararajan T., "Analysis of Diffuser and Ejector Performance in a High Altitude Test Facility," *AIAA 2009-5008*.
- [5] Bruce Ralphin Rose J., Jinu GR, Brindha CJ, "A Numerical Optimization of High Altitude Testing Facility for Wind Tunnel Experiments," *Chinese Journal of Aeronautics*, 2015.
- [6] R. C. German, R. C. Bauer, Panesci J. H., "Methods for Determining the Performance of Ejector-Diffuser Systems Used in Rocket Altitude Simulation," 1964.
- [7] Kracik Jan, Dvorak Vaclav, "Preliminary Study of the Primary Nozzle Position of a Supersonic Air Ejector with a Constant-Area Mixing Chamber," EPJ Web of Conferences 143, 02056, EFM, 2016.
- [8] Pruitt D., Bates L., "Starting and Test Rhombus Characteristics of Two-Dimensional Supersonic Free-Jet Nozzle/Generic Supersonic Aircraft Inlet Configurations," *AIAA 92-5091*.
- [9] P. A. Czysz, "Correlation of Wind Tunnel Blockage Data," Technical Documentary Report, ASD-TDR-63-230, 1963.
- [10] Bauer R. C., Muse W. W., Tisley C. R., "Simulation of Flow Approaching the Chin Inlet of a Ramjet Missile," AEDC-TR-74-5, 1974.
- [11] Manikanda Kumaran R., Vivekanand P. K., Sundararajan T., "Optimization of Second Throat Ejectors for High-Altitude Test Facility," *Journal of Propulsion and Power*, vol. 25, no. 3, 2009.
- [12] Fernando D. X., Sivaranjan S., Santosh Raj G., Prithiv Kumar C., "Design and Analysis of Second Throat Diffuser System at Different Back Pressures for High Altitude Test," *Journal of Basic and Applied Engineering Research*, vol. 1, no. 5, pp. 67-70, 2014.

- [13] Robert E. Smith Jr., Joel Ferrell Jr., "High-Altitude Tests of Rocket Engines in Ground Test Facilities," *SAE International*, vol. 73, pp. 400-415, 1965.
- [14] Kronmueller H., Schaefer K., Zimmermann H., Stark R., "Cold Gas Subscale Test Facility P6.2 at DLR Lampoldshausen," *Institute of Space Propulsion*, 2002.
- [15] Zou Jian-Jun, Zhou Jin, Lu Hui-Qiang, Hu Yong, "Experimental Investigation on Starting Process of Supersonic Single-Stage Air Ejector," *Journal of Thermal Science*, vol. 21, no. 4, 2012.
- [16] A. Bachmann, "Measurement of the Plasma Radius in a Vapor Cell Using Schlieren Imaging," *Master Thesis in Physics, Heinrich-Heine University*, 2016.
- [17] "Nozzle Theory," 14 April 2015. [Online]. Available: http://www.nakka-rocketry.net/th_nozz.html. [Accessed 5 September 2021].
- [18] ANSYS, "ANSYS Fluent Theory Guide," 2013.
- [19] Y. Bartosiewicz, "Numerical and Experimental Investigations on Supersonic Ejectors," *Int. J. Heat Fluid Flow*, vol. 26, pp. 56-70, 2005.
- [20] Kolar J., Dvorak V., "Verification of k- ω SST Turbulence Model for Supersonic Internal Flows," *Int. J. Mech. Aerospace, Ind. Mechatron Manuf. Eng.*, vol. 5, no. 9, pp. 1715-1719, 2011.
- [21] "SST K-Omega Turbulence Models," 2019. [Online]. Available: <https://knowledge.autodesk.com/support/cfd>. [Accessed 5 January 2021].
- [22] "Turbulence Length Scale," 15 June 2012. [Online]. Available: https://www.cfd-online.com/Wiki/Turbulence_length_scale. [Accessed 5 September 2021].
- [23] F. M. White, *Viscous Fluid Flow*, McGraw-Hill, 1991.

APPENDIX

1 - Test Setup and Measurement Locations



Figure 1-1. Free-Jet Nozzle Inlet Pressure Measurement Locations.

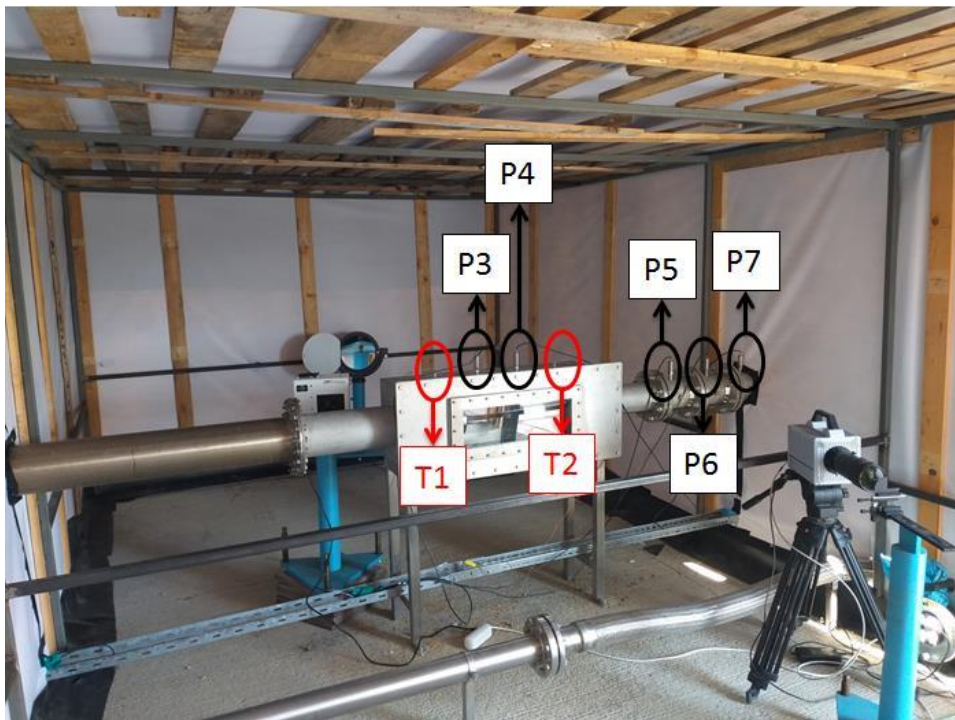


Figure 1-2. Test Chamber and Test Section Diffuser Pressure and Temperature Measurement Locations.

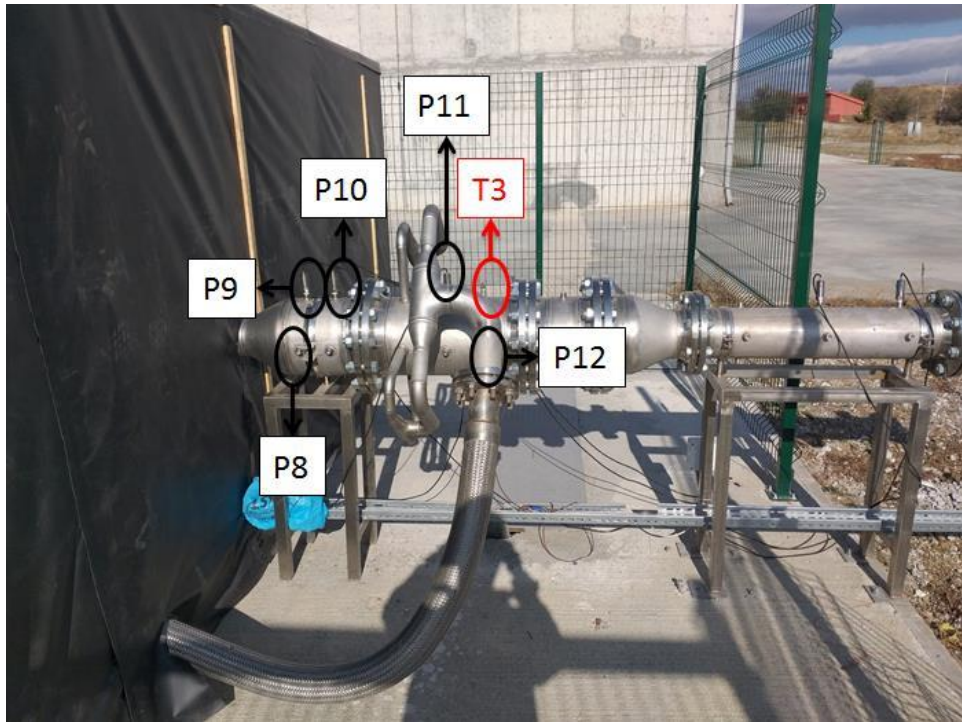


Figure 1-3. Test Section Diffuser-Ejector Nozzle Feed Manifold Connection and Ejector Nozzle Inlet Pressure and Temperature Measurement Locations.

Table 1-1. Measurement Location Numbers.

Pressure Transducers	Thermocouples
P1-P2-P3-P4-P5-P6-P7-P8-P9-P10-P11-P12	T1-T2-T3

2 - Atmospheric Pressure Data

Table 2-1. Atmospheric Pressure Data.

Altitude, m	Atmospheric Pressure, Pa	Altitude, m	Atmospheric Pressure, Pa
0	101325	3048.0	69682
15.240	101142	4572.0	57182
30.480	100959	6096.0	46563
60.960	100595	7620.0	37601
91.440	100231	9144.0	30090
121.92	99869	10668	23842
152.40	99506	12192	18754
182.88	99147	13716	14748
213.36	98788	15240	11597
243.84	98430	16764	9120
274.32	98072	18288	7172
304.80	97717	19812	5640
609.60	94213	21336	4438
914.40	90812	22860	3498
1219.2	87511	24384	2762
1524.0	84307	25908	2184
1828.8	81200	27432	1730
2133.6	78185	28956	1372
2438.4	75262	30480	1090
2743.2	72429		

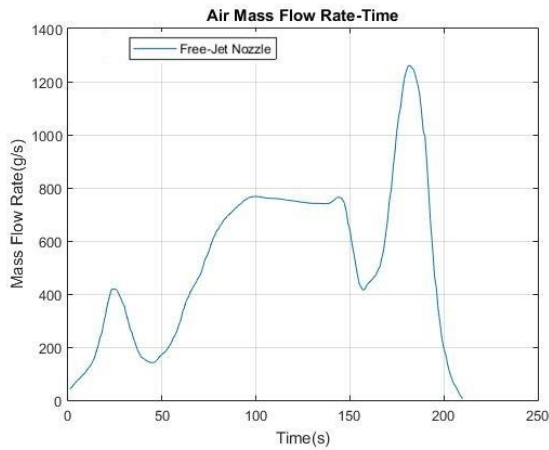
3 - Test Matrix

Table 3-1. Test Matrix.

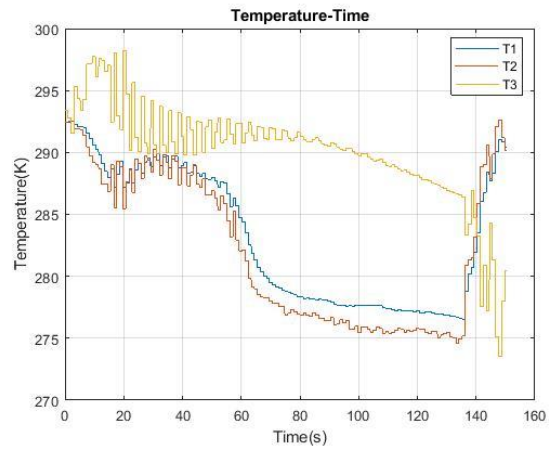
	Mach Number	Free-Jet Nozzle Mass Flow Rate (g/s)	Free-Jet Nozzle Inlet Pressure (Pa)	Free-Jet Nozzle Outlet Pressure (Pa)	Blockage Ratio (%)	Test Chamber Static Pressure (Pa)
Test-1	2	750	55500	7095	0	13500
Test-2	2	1100	79500	10160	0	8100
Test-3	2	1500	112500	14380	0	8900
Test-4	2	1900	138000	17640	0	11000
Test-5	2	750	55000	7030	8	14500
Test-6	2	1100	80000	10225	8	13500
Test-7	2	1500	112000	14315	8	12500
Test-8	2	1900	140000	17895	8	15000
Test-9	2	750	55000	7030	15	14600
Test-10	2	1100	80000	10225	15	14700
Test-11	2	1500	112000	14315	15	15800
Test-12	2	1900	138000	17640	15	19000
Test-13	2	750	54000	6900	25	17000
Test-14	2	1100	80000	10225	25	19300
Test-15	2	1500	112000	14315	25	24500
Test-16	2	1900	138000	17640	25	29300

	Mach Number	Free-Jet Nozzle Mass Flow Rate (g/s)	Free-Jet Nozzle Inlet Pressure (Pa)	Free-Jet Nozzle Outlet Pressure (Pa)	Blockage Ratio (%)	Test Chamber Static Pressure (Pa)
Test-17	2.5	750	115500	6760	0	3800
Test-18	2.5	1300	178500	10450	0	5900
Test-19	2.5	1500	206000	12060	0	6800
Test-20	2.5	1900	245000	14340	0	8100
Test-21	2.5	750	114000	6670	8	4150
Test-22	2.5	1300	178000	10400	8	6500
Test-23	2.5	1500	206000	12050	8	7450
Test-24	2.5	1900	234000	13695	8	8500
Test-25	2.5	750	115000	6730	15	4600
Test-26	2.5	1300	180000	10535	15	7100
Test-27	2.5	1500	208000	12170	15	8200
Test-28	2.5	1900	235000	13750	15	9250
Test-29	2.5	750	116000	6790	25	8000
Test-30	2.5	1300	180000	10535	25	8600
Test-31	2.5	1500	210000	12290	25	10200
Test-32	2.5	1900	235000	13750	25	11350

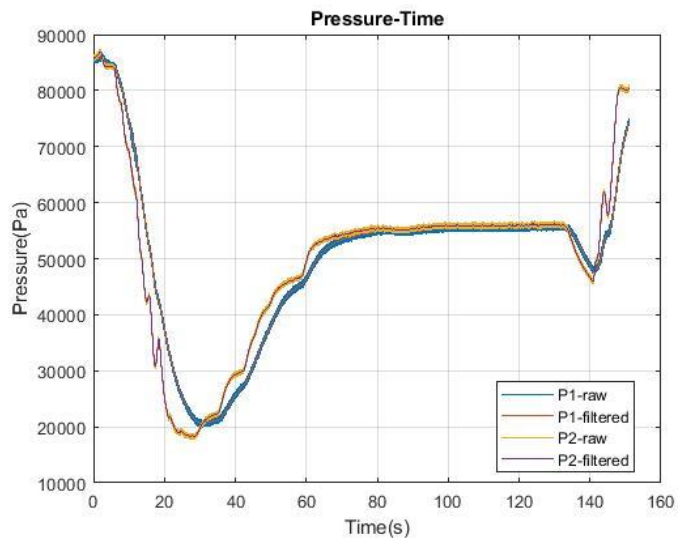
4 - Experimental Data from Tests



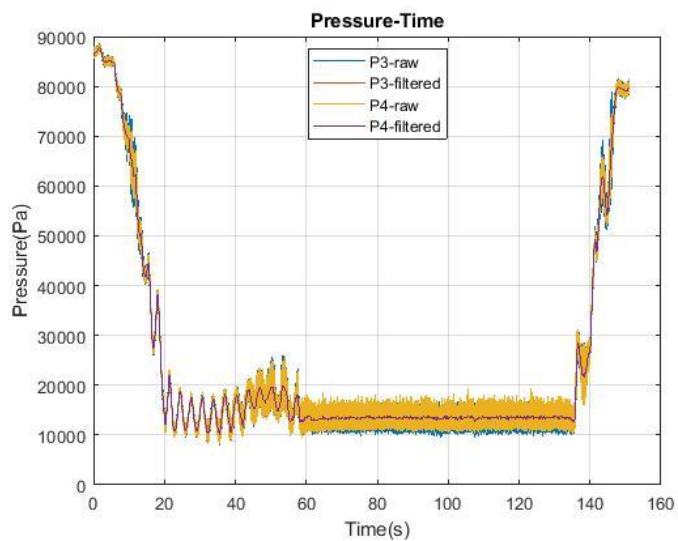
Free-Jet Nozzle Air Mass Flow Rate



Test Chamber and Ejector Nozzle Feed Manifold Connection Temperature

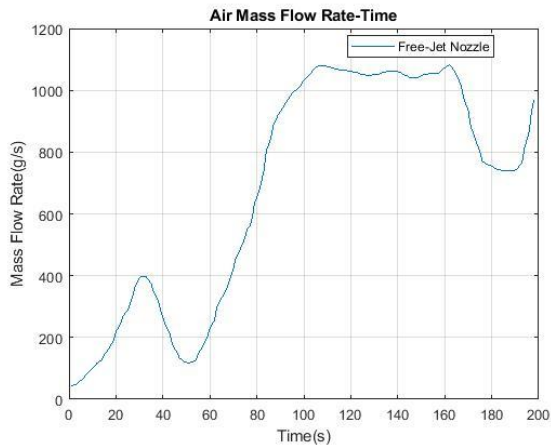


Free-Jet Nozzle Inlet Pressure

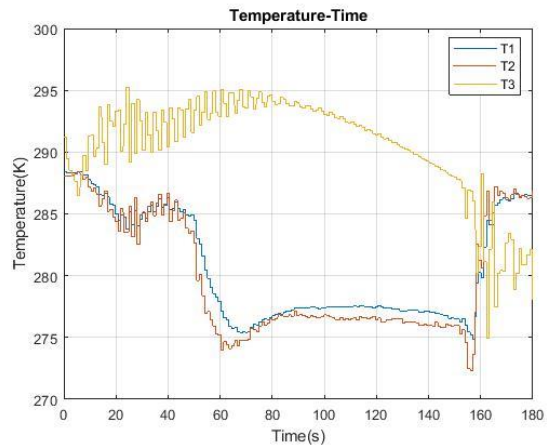


Test Chamber Pressure

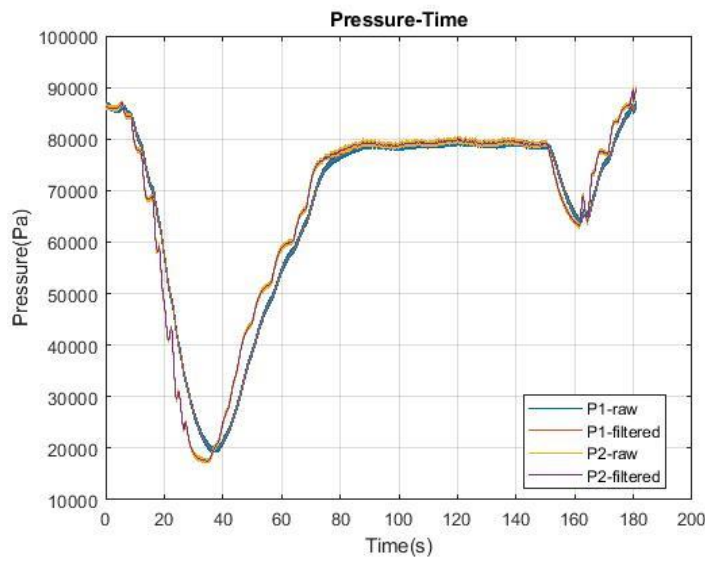
Figure 4-1. Test-1: [Mach 2 - 750 g/s - 0% Blockage].



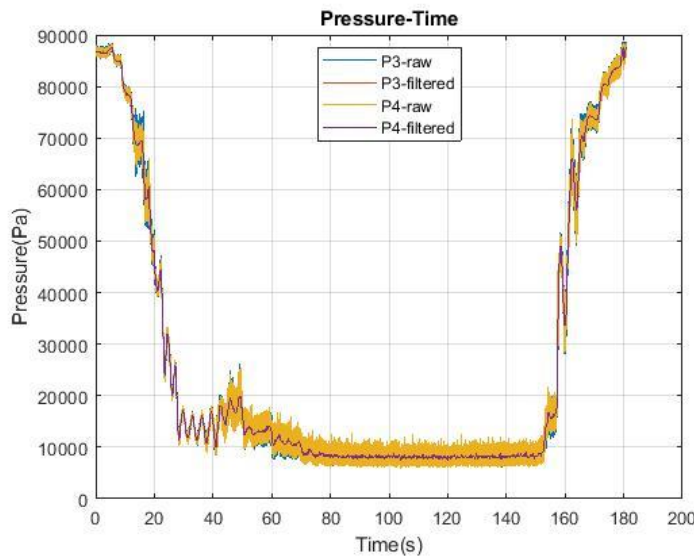
Free-Jet Nozzle Air Mass Flow Rate



Test Chamber and Ejector Nozzle Feed Manifold Connection Temperature

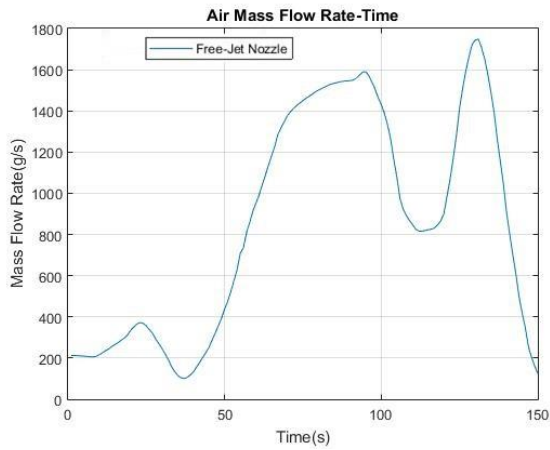


Free-Jet Nozzle Inlet Pressure

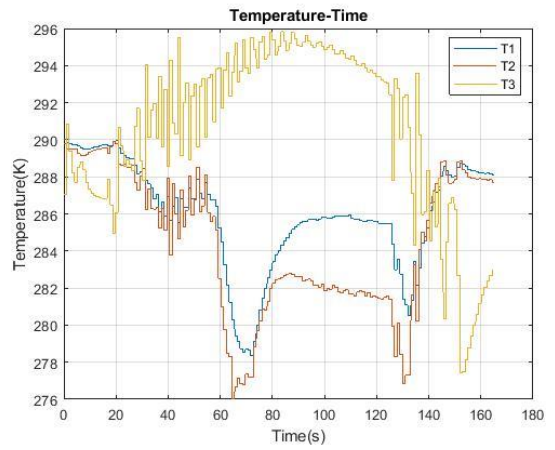


Test Chamber Pressure

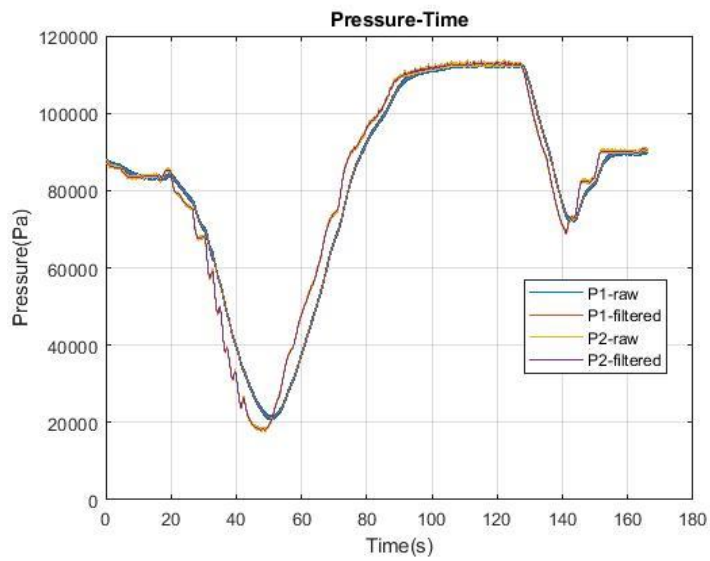
Figure 4-2. Test-2: [Mach 2 - 1100 g/s - 0% Blockage].



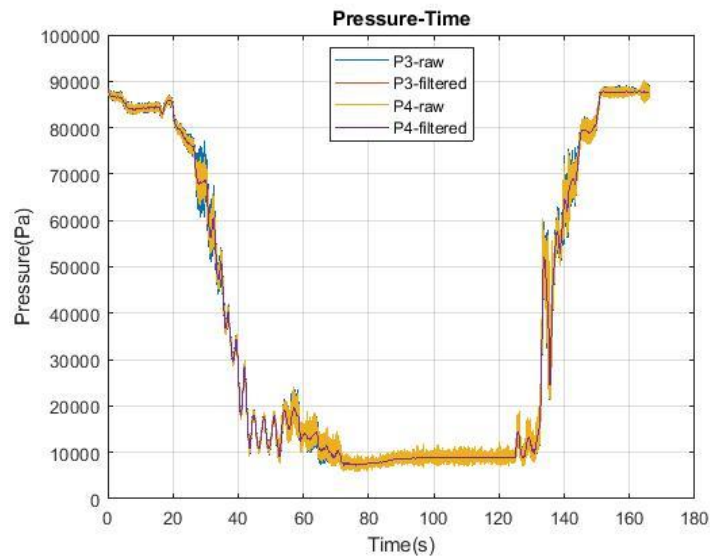
Free-Jet Nozzle Air Mass Flow Rate



Test Chamber and Ejector Nozzle Feed Manifold Connection Temperature

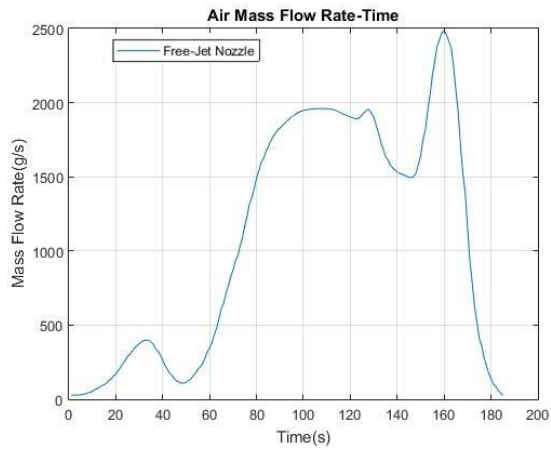


Free-Jet Nozzle Inlet Pressure

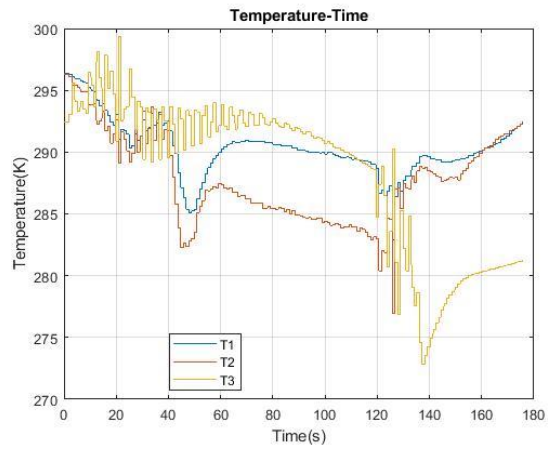


Test Chamber Pressure

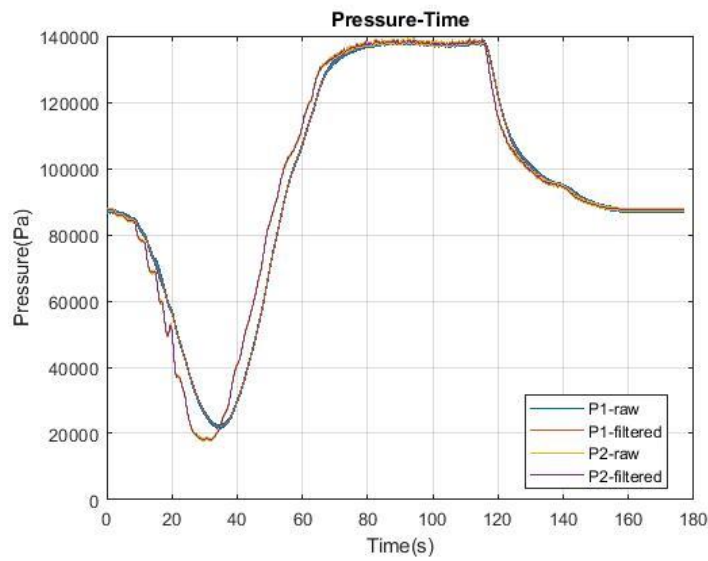
Figure 4-3. Test-3: [Mach 2 - 1500 g/s - 0% Blockage].



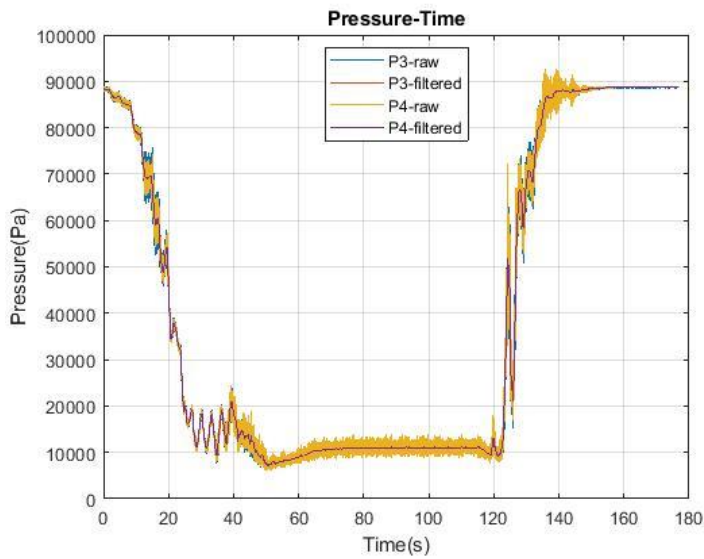
Free-Jet Nozzle Air Mass Flow Rate



Test Chamber and Ejector Nozzle Feed Manifold Connection Temperature

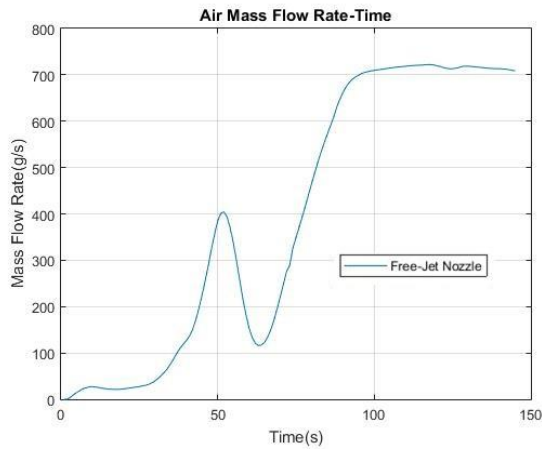


Free-Jet Nozzle Inlet Pressure

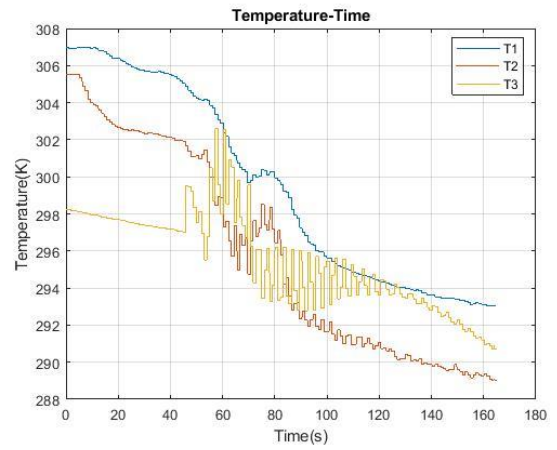


Test Chamber Pressure

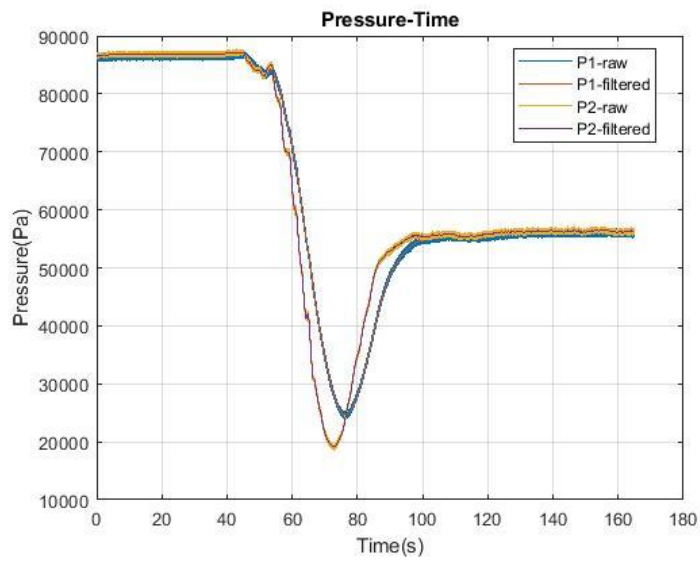
Figure 4-4. Test-4: [Mach 2 - 1900 g/s - 0% Blockage].



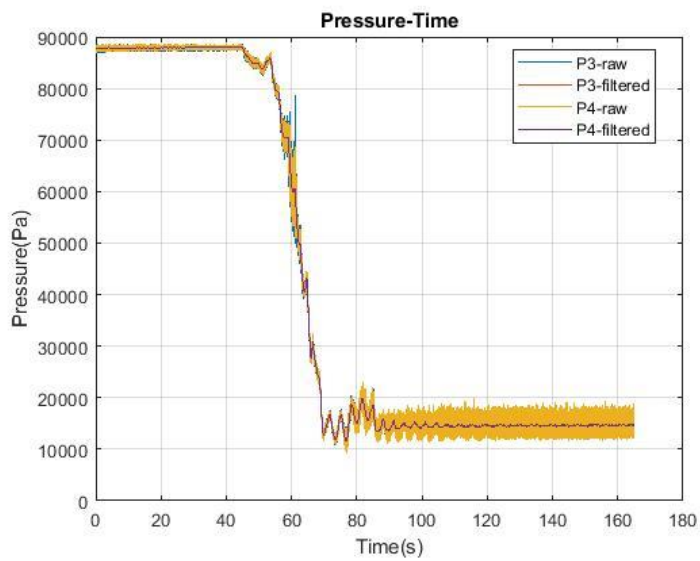
Free-Jet Nozzle Air Mass Flow Rate



Test Chamber and Ejector Nozzle Feed Manifold Connection Temperature

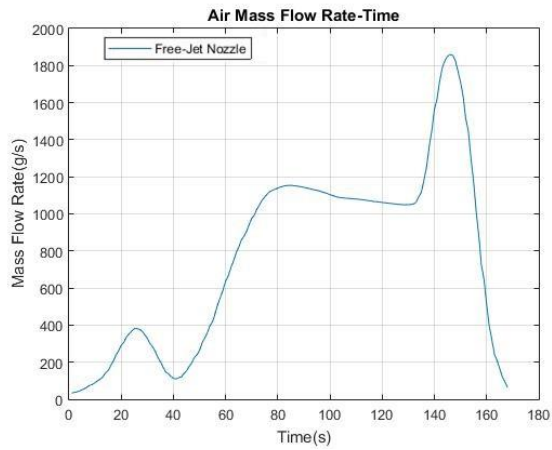


Free-Jet Nozzle Inlet Pressure

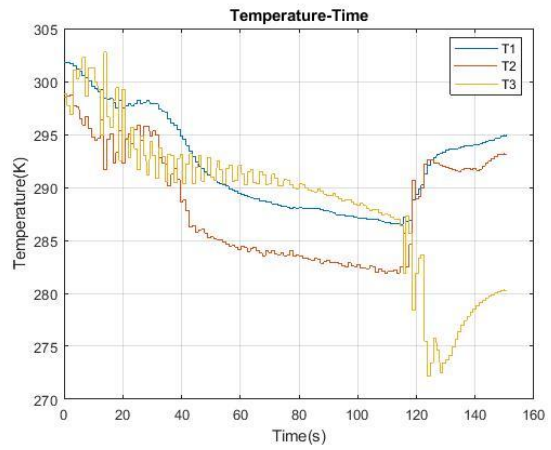


Test Chamber Pressure

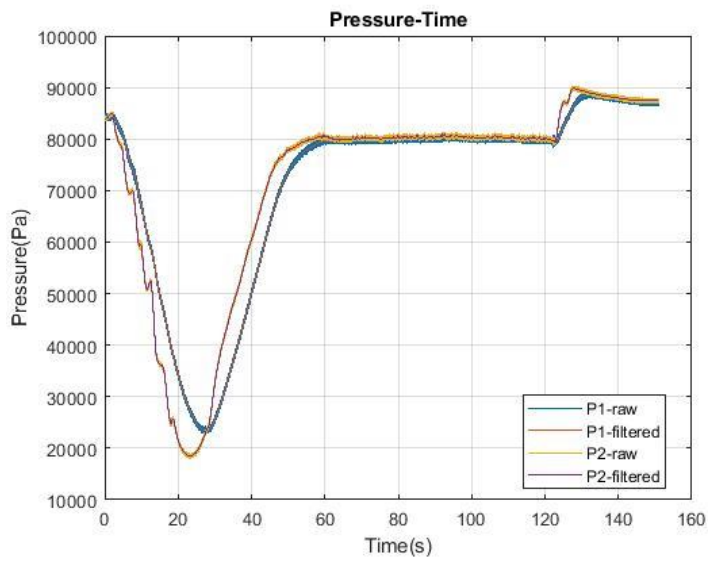
Figure 4-5. Test-5: [Mach 2 - 750 g/s - 8% Blockage].



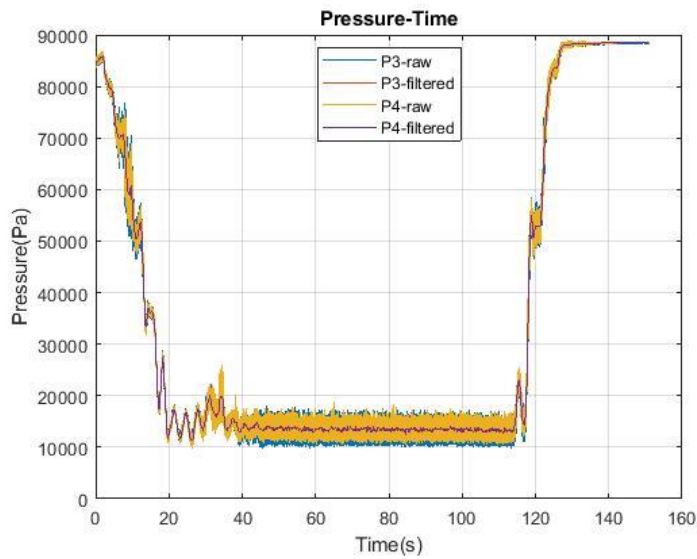
Free-Jet Nozzle Air Mass Flow Rate



Test Chamber and Ejector Nozzle Feed Manifold Connection Temperature

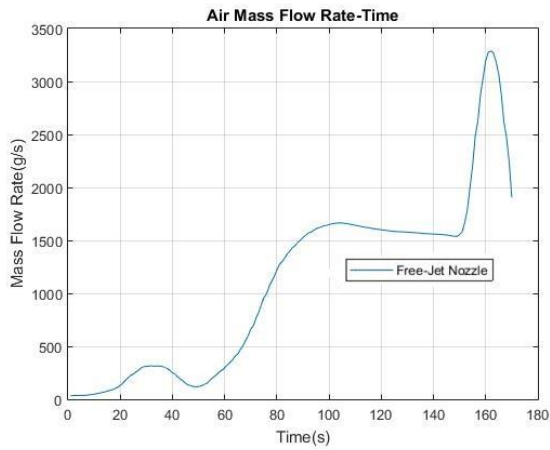


Free-Jet Nozzle Inlet Pressure

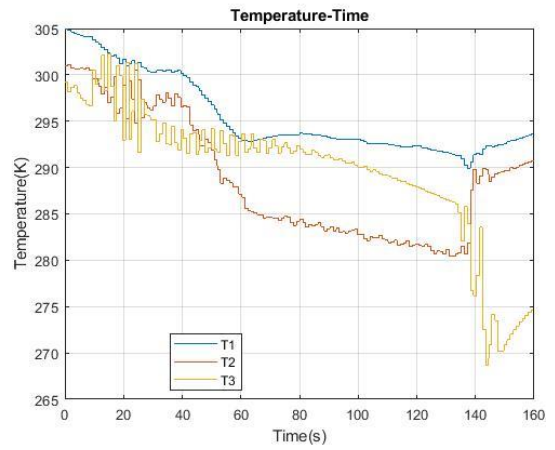


Test Chamber Pressure

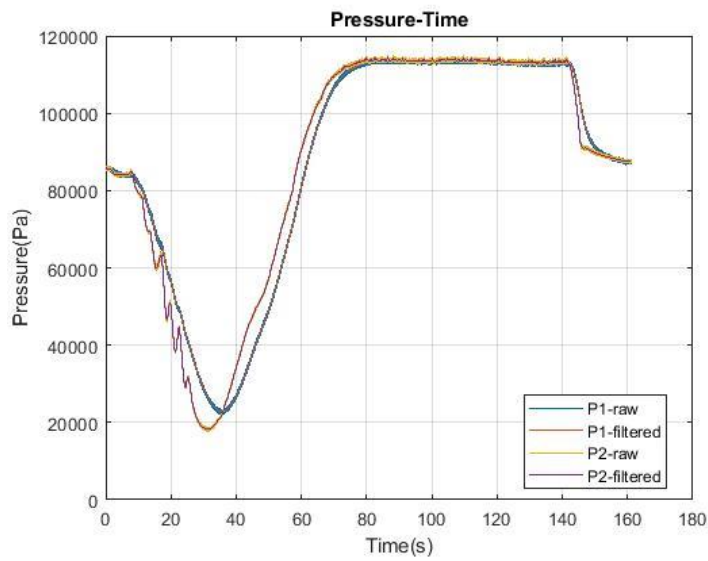
Figure 4-6. Test-6: [Mach 2 - 1100 g/s - 8% Blockage].



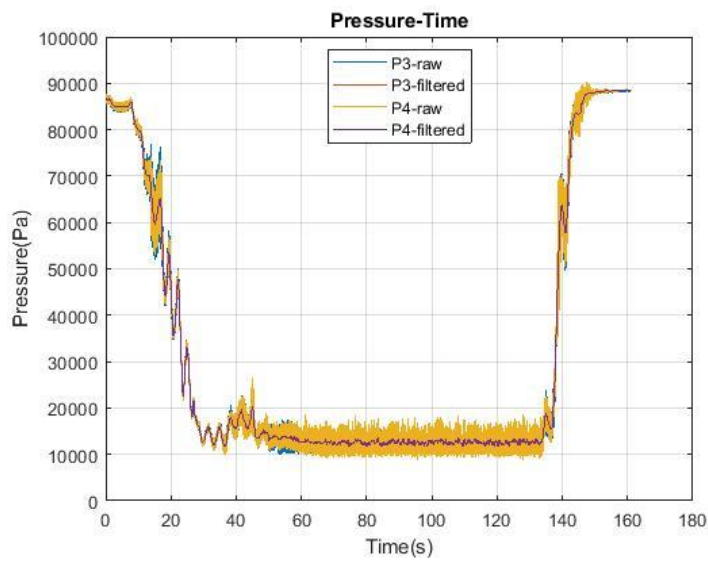
Free-Jet Nozzle Air Mass Flow Rate



Test Chamber and Ejector Nozzle Feed Manifold Connection Temperature

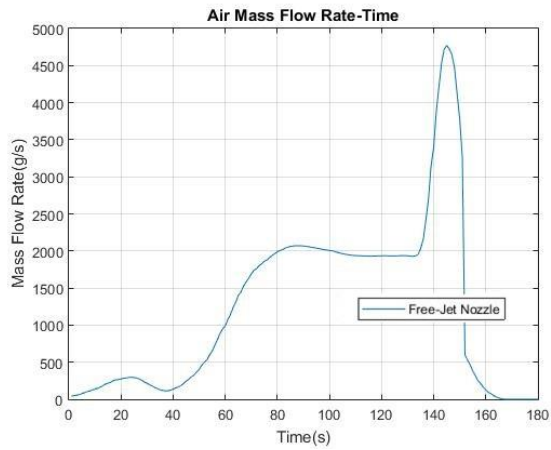


Free-Jet Nozzle Inlet Pressure

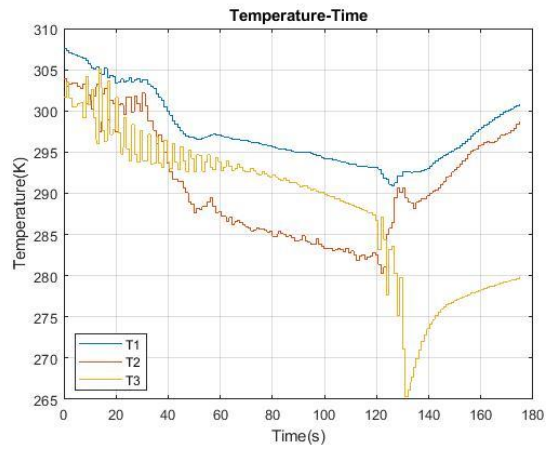


Test Chamber Pressure

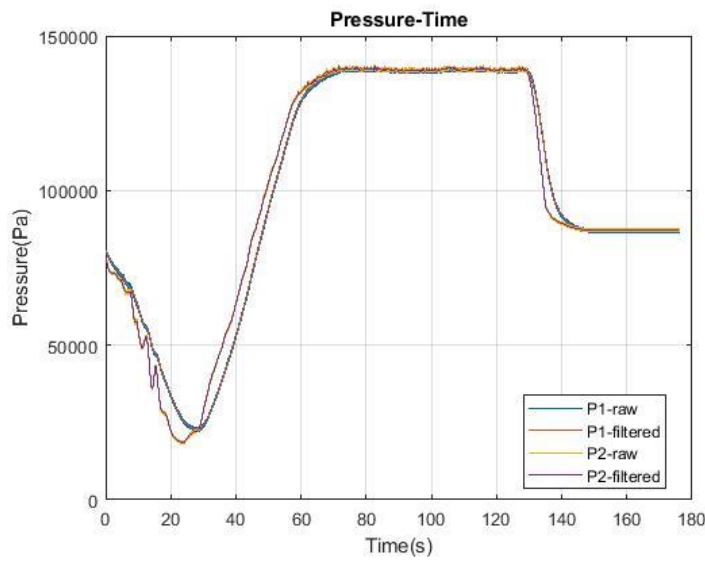
Figure 4-7. Test-7: [Mach 2 - 1500 g/s - 8% Blockage].



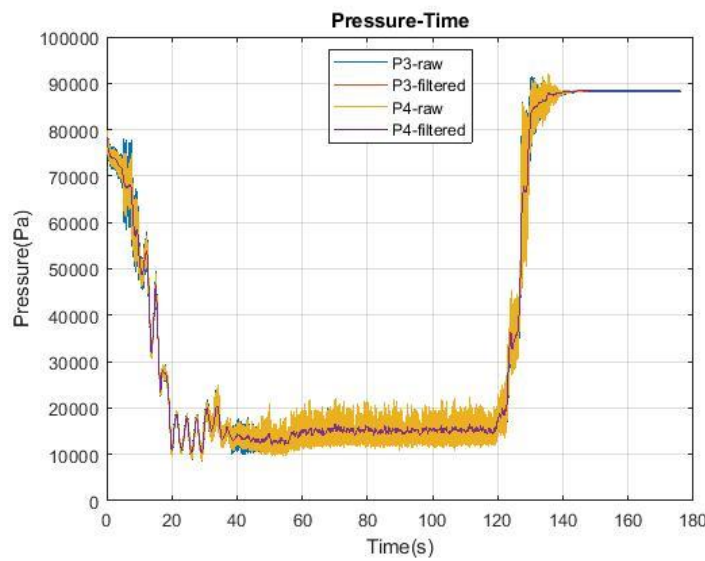
Free-Jet Nozzle Air Mass Flow Rate



Test Chamber and Ejector Nozzle Feed Manifold Connection Temperature

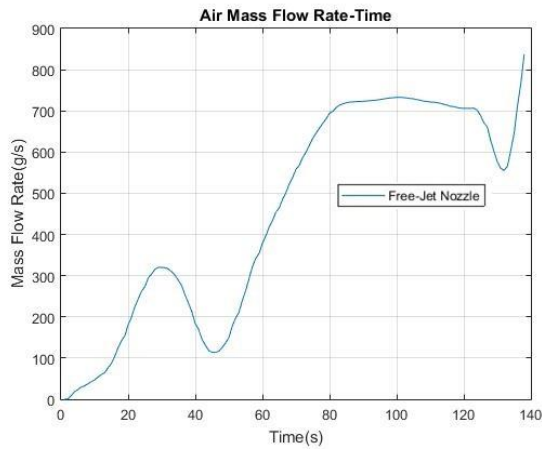


Free-Jet Nozzle Inlet Pressure

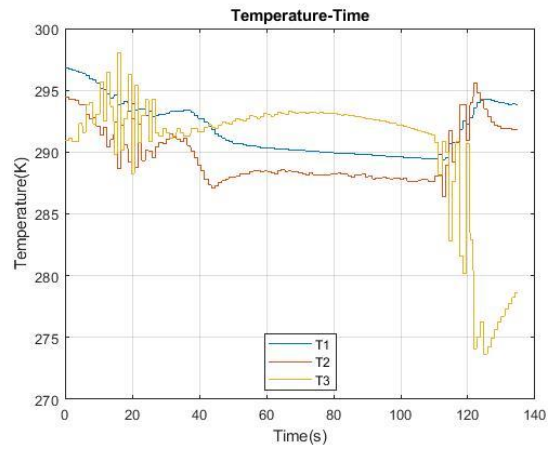


Test Chamber Pressure

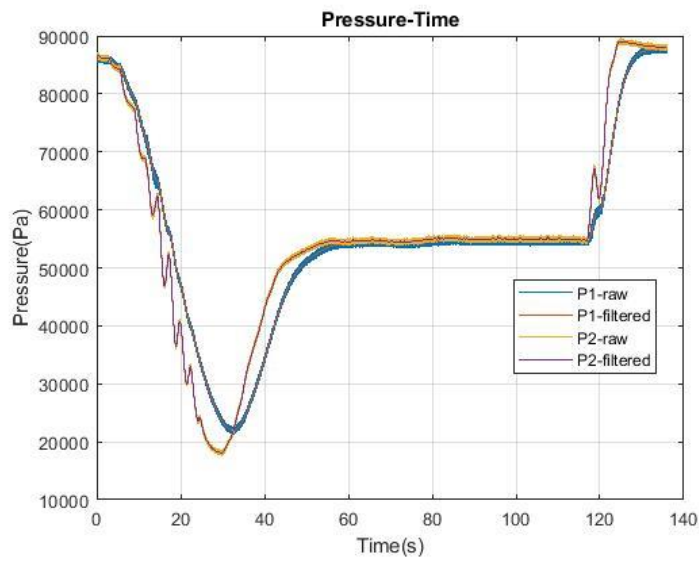
Figure 4-8. Test-8: [Mach 2 - 1900 g/s - 8% Blockage].



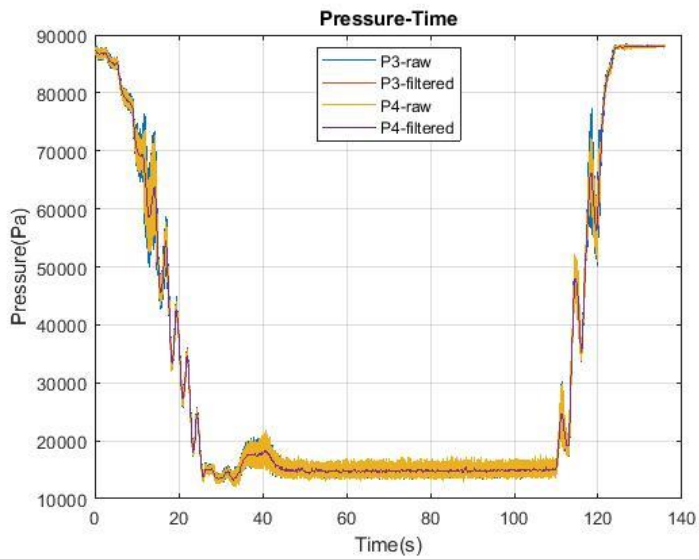
Free-Jet Nozzle Air Mass Flow Rate



Test Chamber and Ejector Nozzle Feed Manifold Connection Temperature

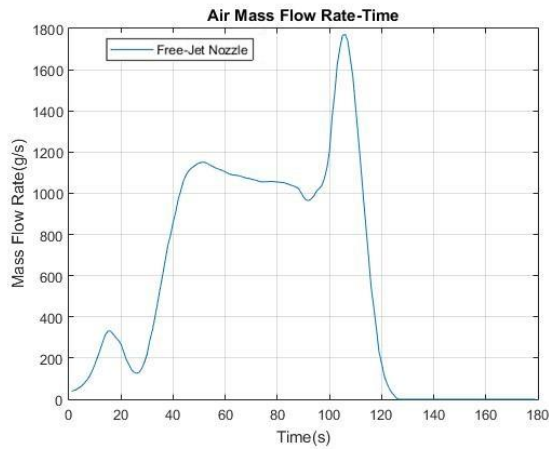


Free-Jet Nozzle Inlet Pressure

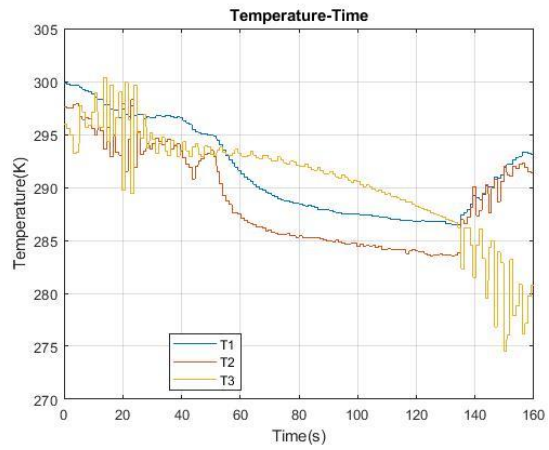


Test Chamber Pressure

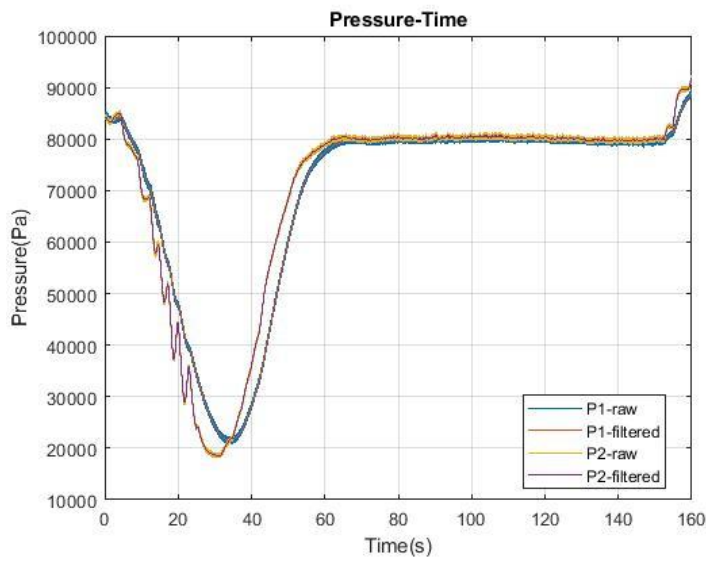
Figure 4-9. Test-9: [Mach 2 - 750 g/s - 15% Blockage].



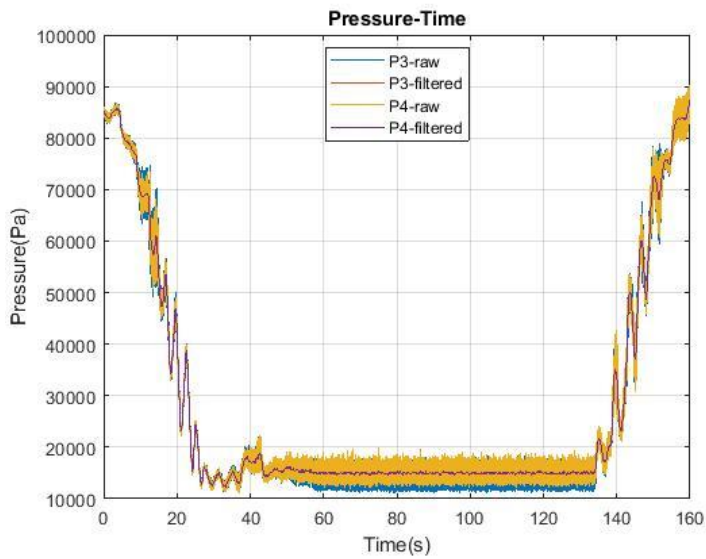
Free-Jet Nozzle Air Mass Flow Rate



Test Chamber and Ejector Nozzle Feed Manifold Connection Temperature

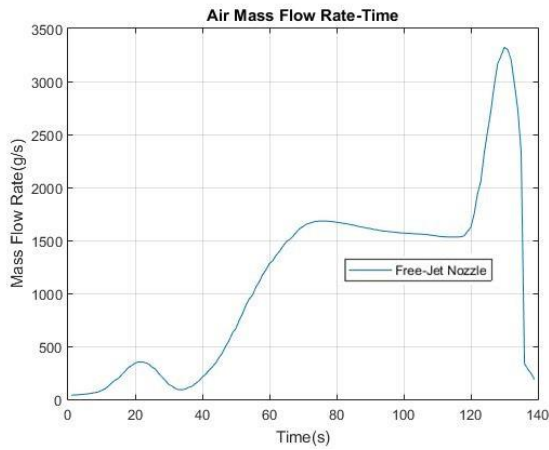


Free-Jet Nozzle Inlet Pressure

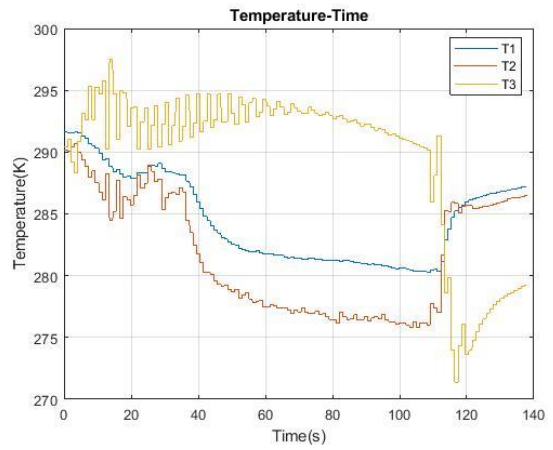


Test Chamber Pressure

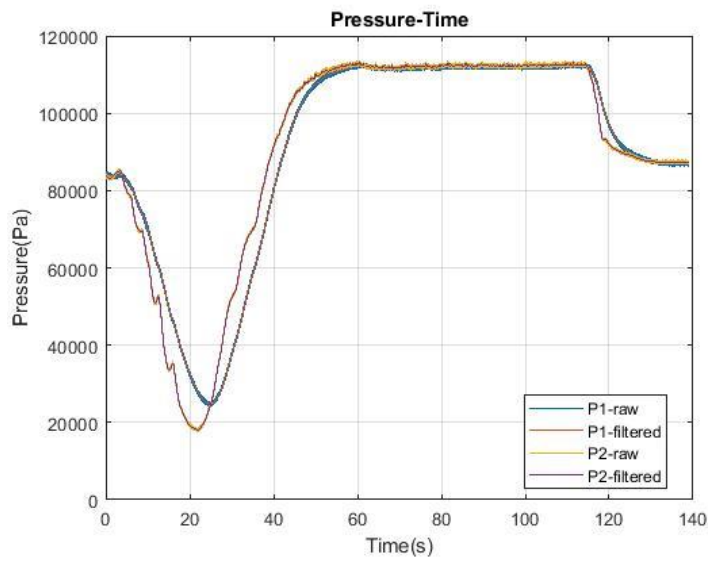
Figure 4-10. Test-10: [Mach 2 - 1100 g/s - 15% Blockage].



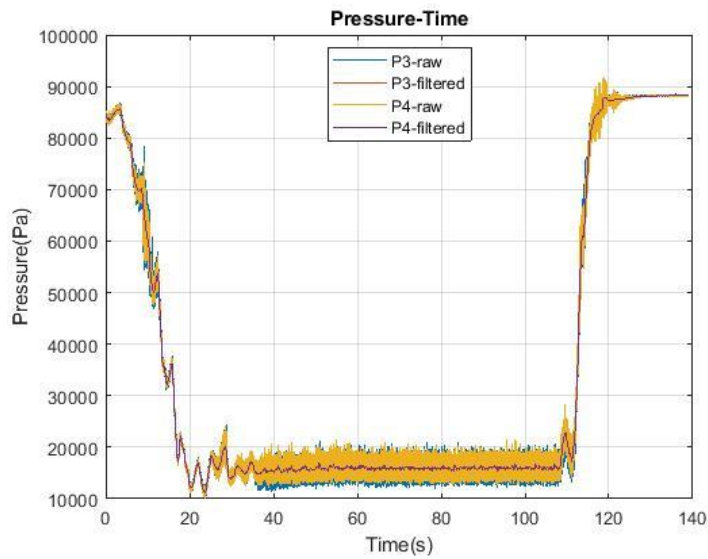
Free-Jet Nozzle Air Mass Flow Rate



Test Chamber and Ejector Nozzle Feed Manifold Connection Temperature

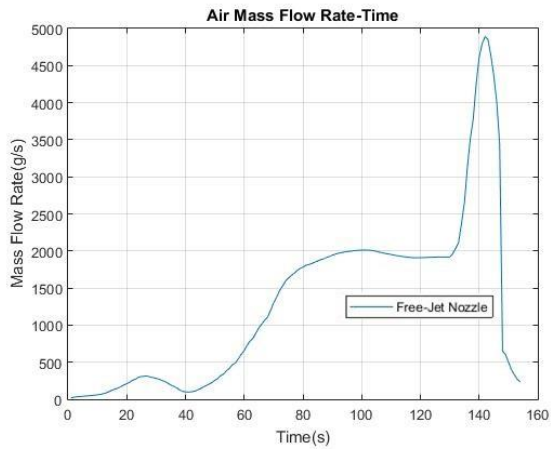


Free-Jet Nozzle Inlet Pressure

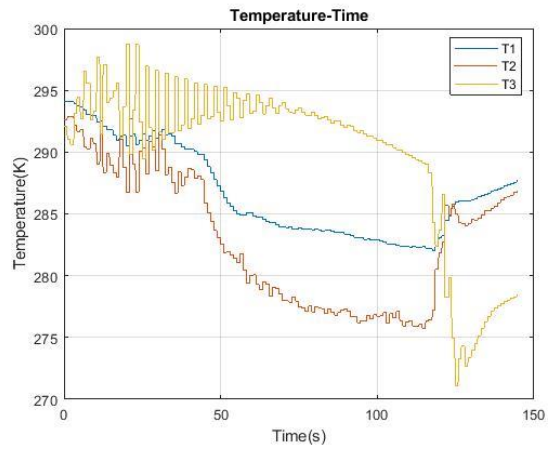


Test Chamber Pressure

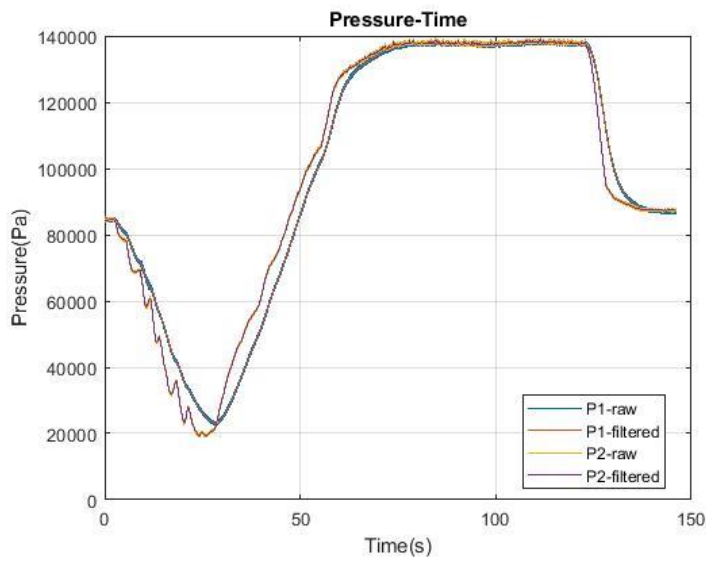
Figure 4-11. Test-11: [Mach 2 - 1500 g/s - 15% Blockage].



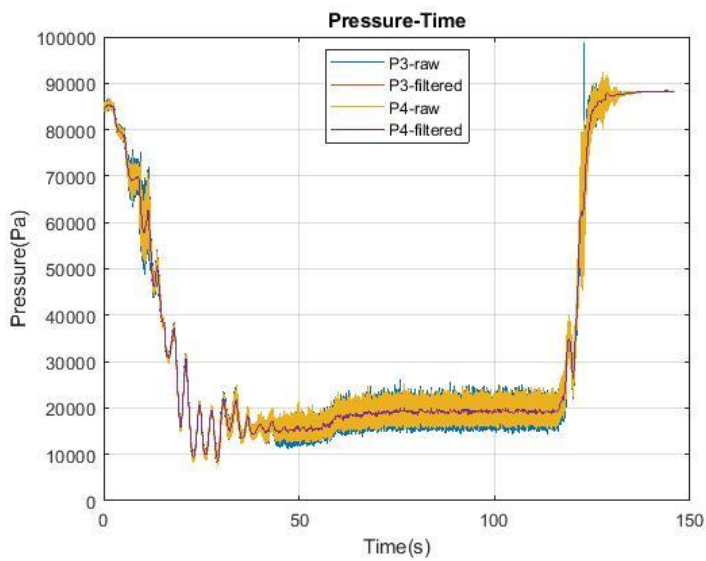
Free-Jet Nozzle Air Mass Flow Rate



Test Chamber and Ejector Nozzle Feed Manifold Connection Temperature

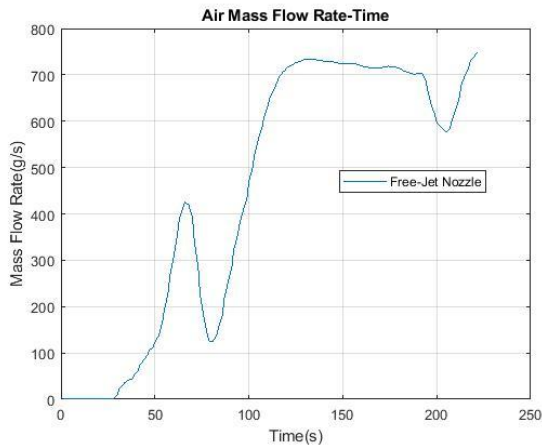


Free-Jet Nozzle Inlet Pressure

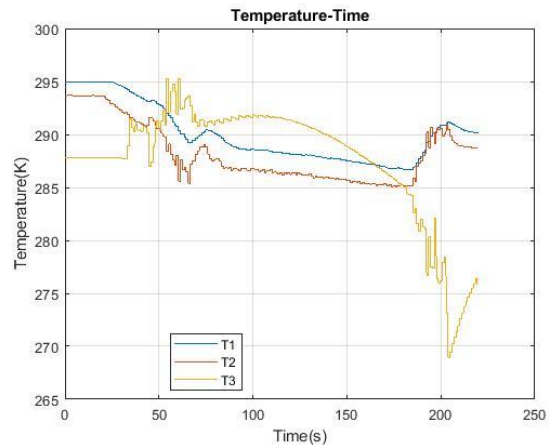


Test Chamber Pressure

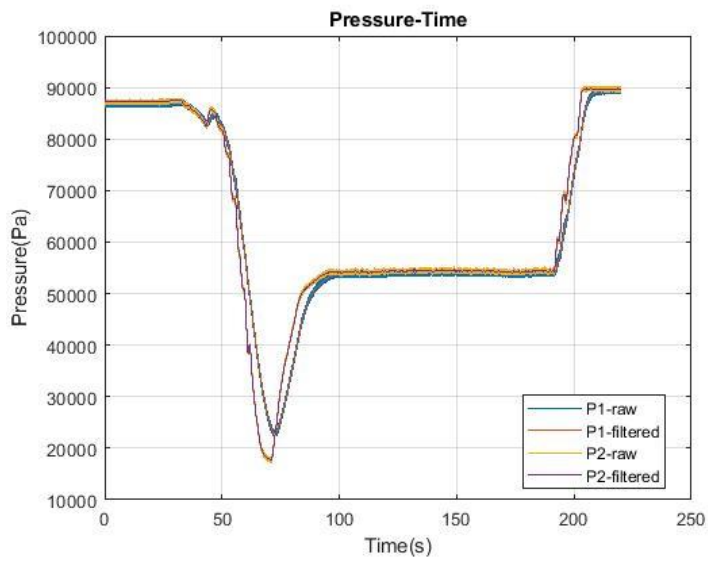
Figure 4-12. Test-12: [Mach 2 - 1900 g/s - 15% Blockage].



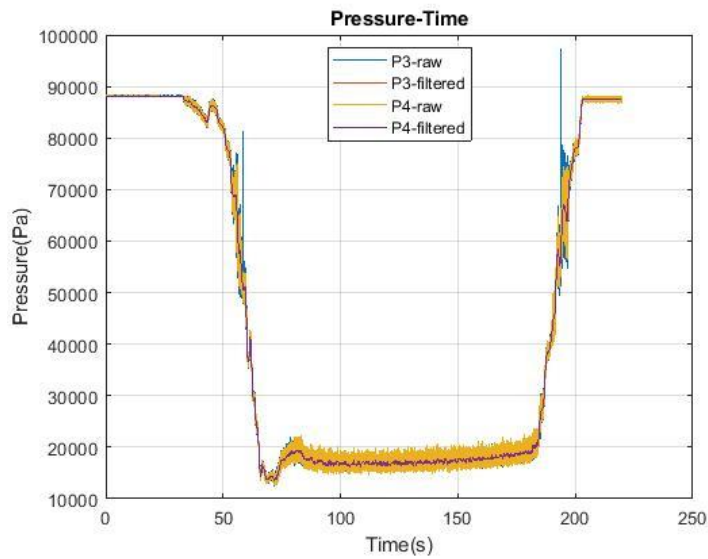
Free-Jet Nozzle Air Mass Flow Rate



Test Chamber and Ejector Nozzle Feed Manifold Connection Temperature

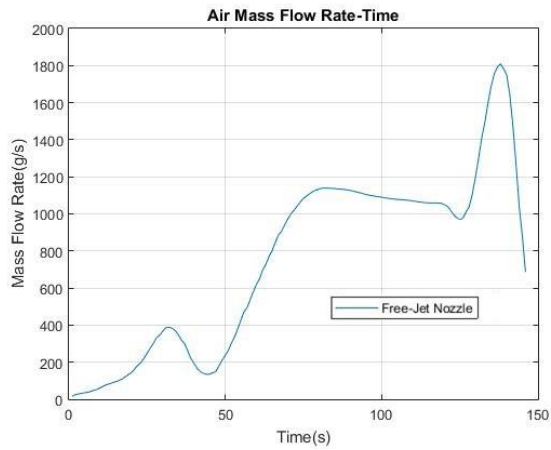


Free-Jet Nozzle Inlet Pressure

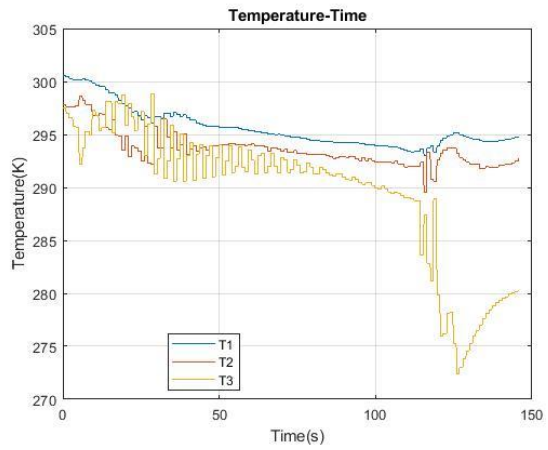


Test Chamber Pressure

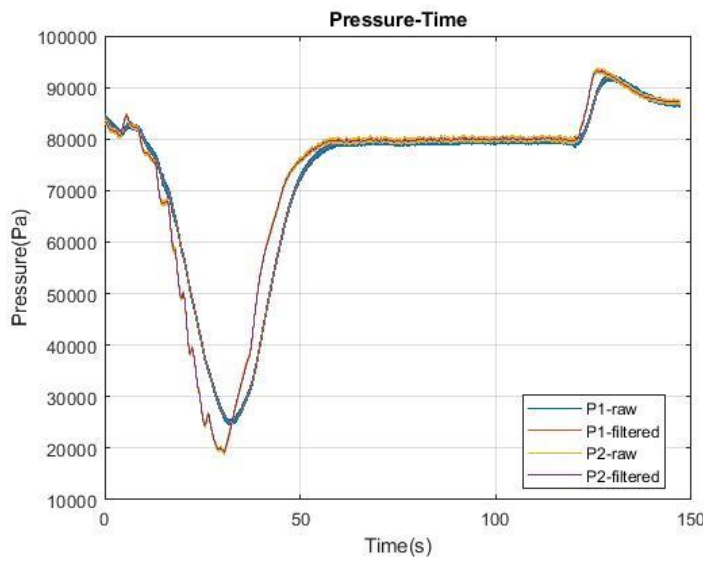
Figure 4-13. Test-13: [Mach 2 - 750 g/s - 25% Blockage].



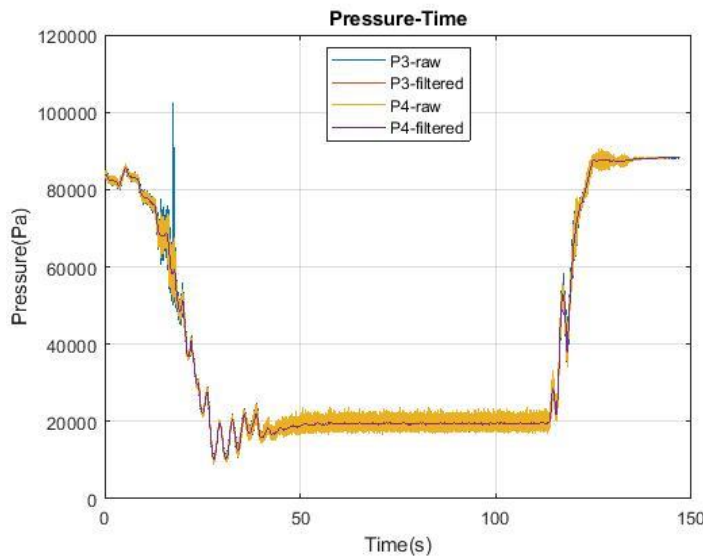
Free-Jet Nozzle Air Mass Flow Rate



Test Chamber and Ejector Nozzle Feed Manifold Connection Temperature

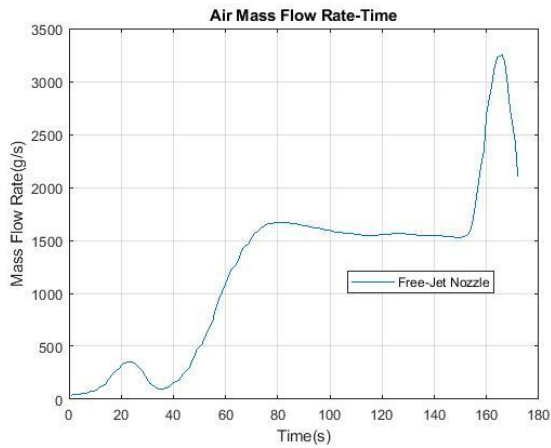


Free-Jet Nozzle Inlet Pressure

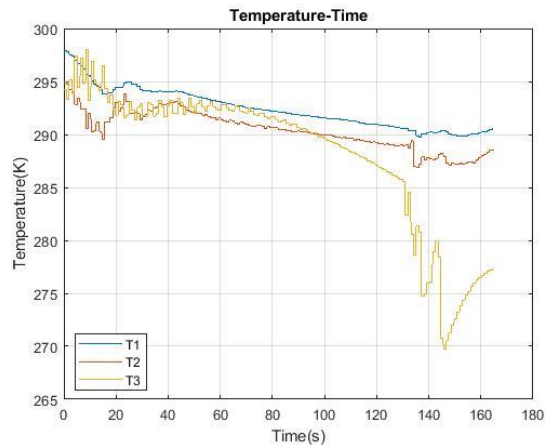


Test Chamber Pressure

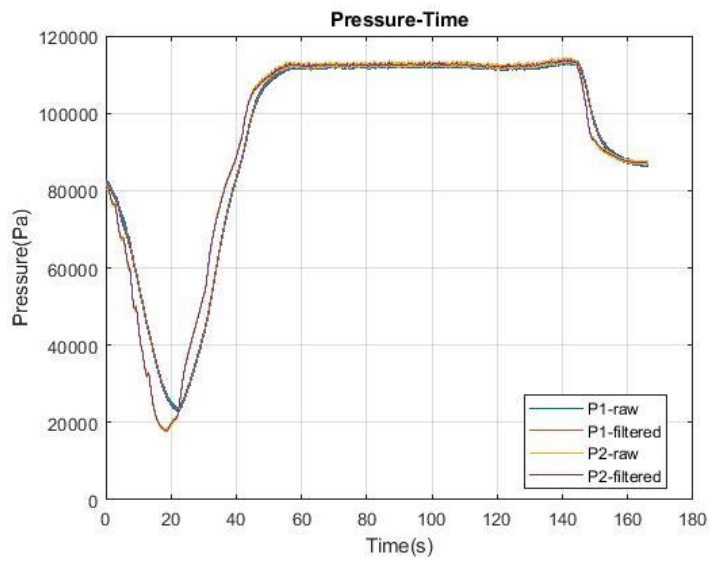
Figure 4-14. Test-14: [Mach 2 - 1100 g/s - 25% Blockage].



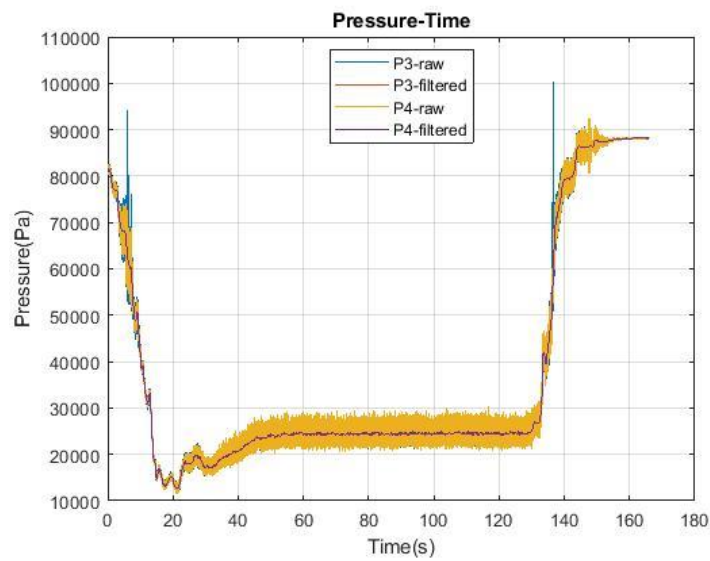
Free-Jet Nozzle Air Mass Flow Rate



Test Chamber and Ejector Nozzle Feed Manifold Connection Temperature

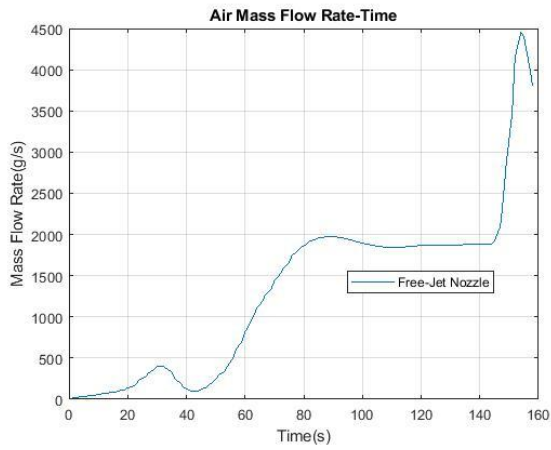


Free-Jet Nozzle Inlet Pressure

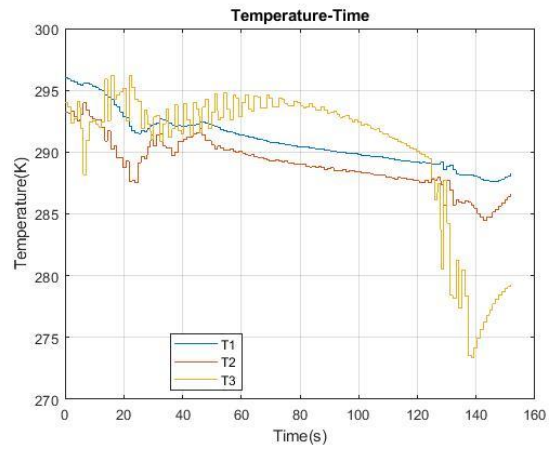


Test Chamber Pressure

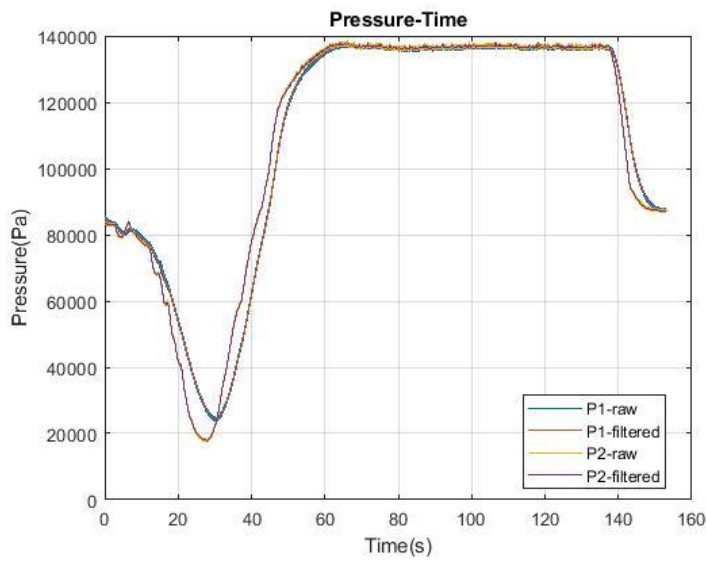
Figure 4-15. Test-15: [Mach 2 - 1500 g/s - 25% Blockage].



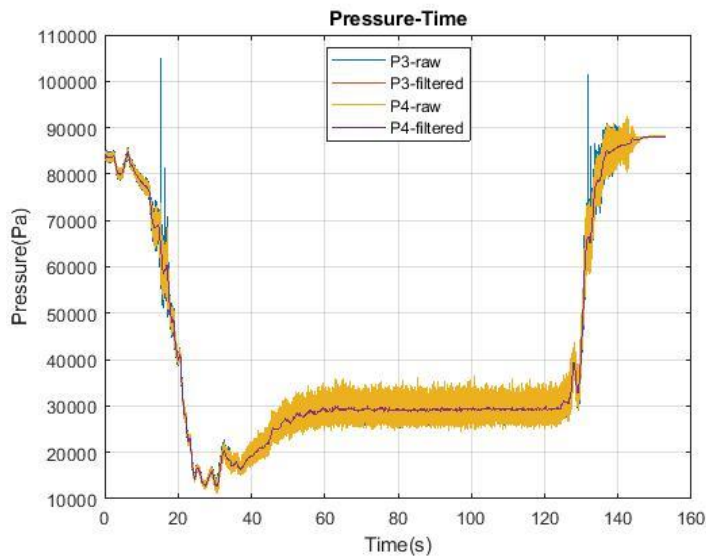
Free-Jet Nozzle Air Mass Flow Rate



Test Chamber and Ejector Nozzle Feed Manifold Connection Temperature

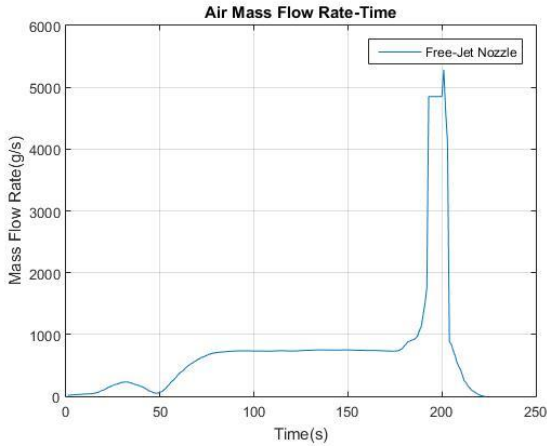


Free-Jet Nozzle Inlet Pressure

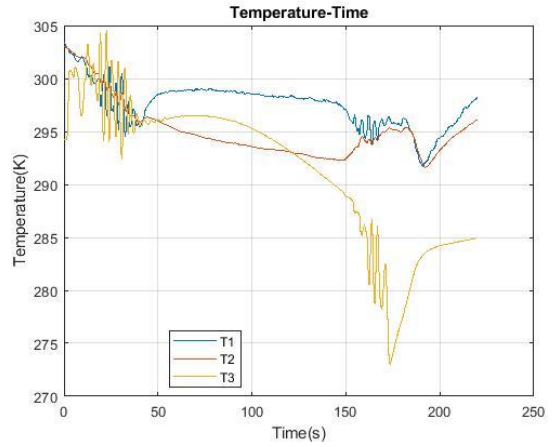


Test Chamber Pressure

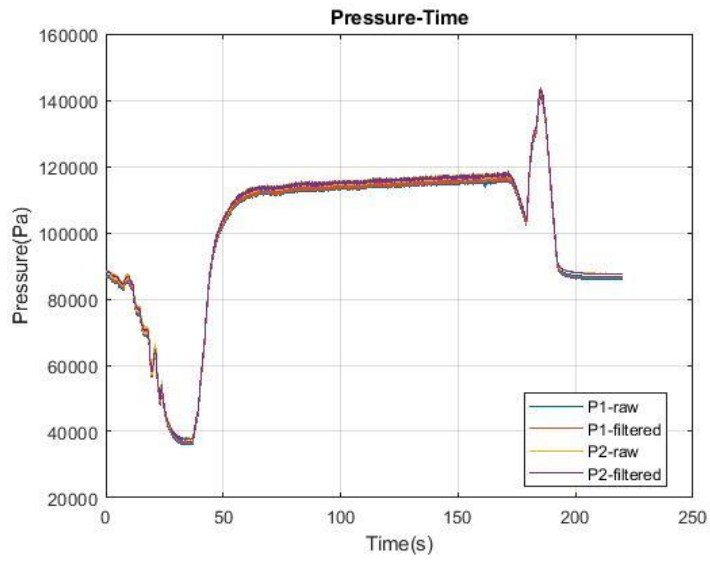
Figure 4-16. Test-16: [Mach 2 - 1900 g/s - 25% Blockage].



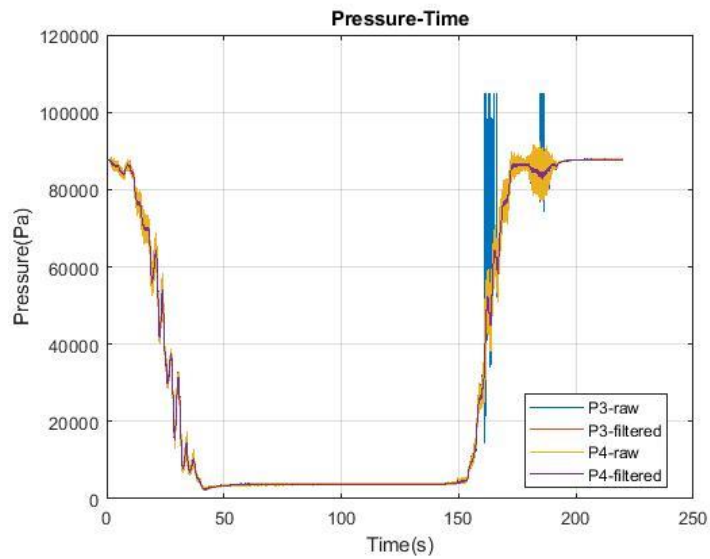
Free-Jet Nozzle Air Mass Flow Rate



Test Chamber and Ejector Nozzle Feed Manifold Connection Temperature

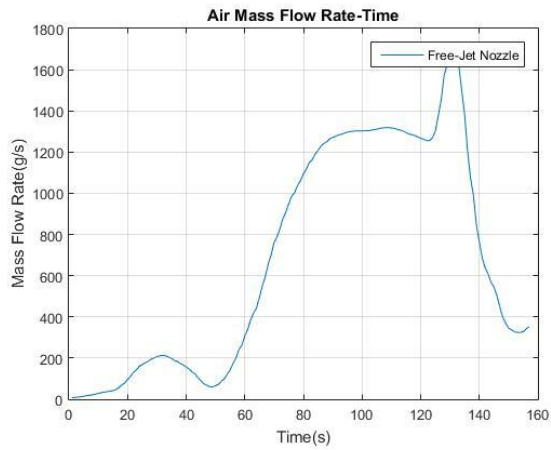


Free-Jet Nozzle Inlet Pressure

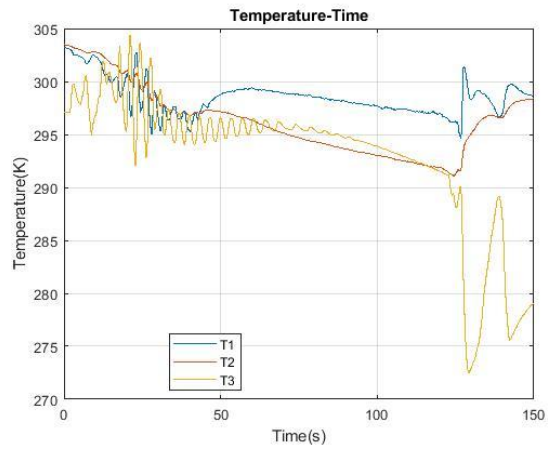


Test Chamber Pressure

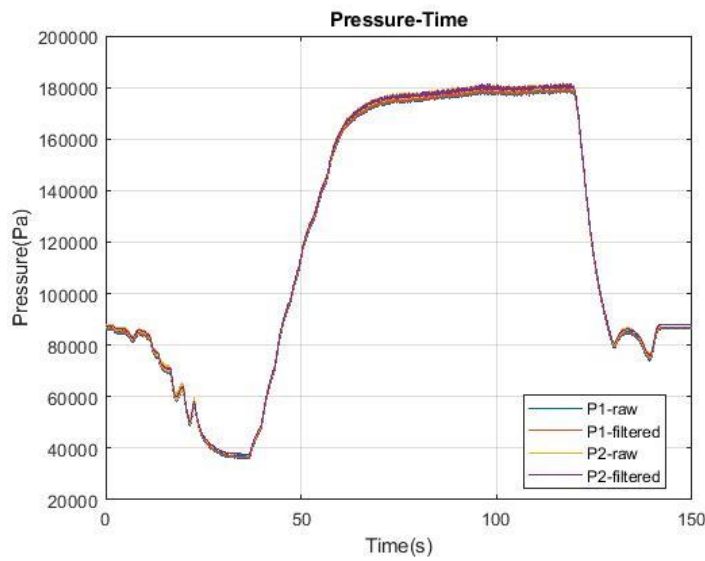
Figure 4-17. Test-17: [Mach 2.5 - 750 g/s - 0% Blockage].



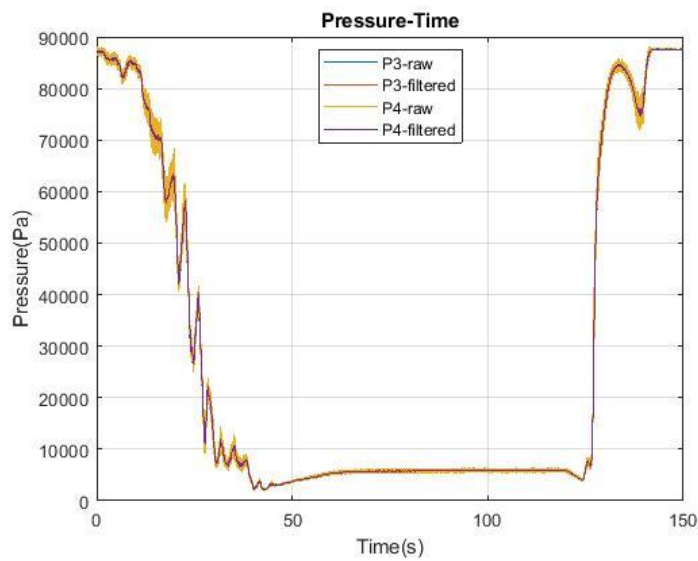
Free-Jet Nozzle Air Mass Flow Rate



Test Chamber and Ejector Nozzle Feed Manifold Connection Temperature

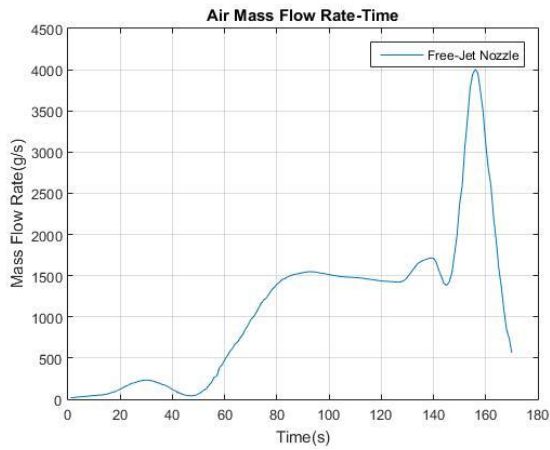


Free-Jet Nozzle Inlet Pressure

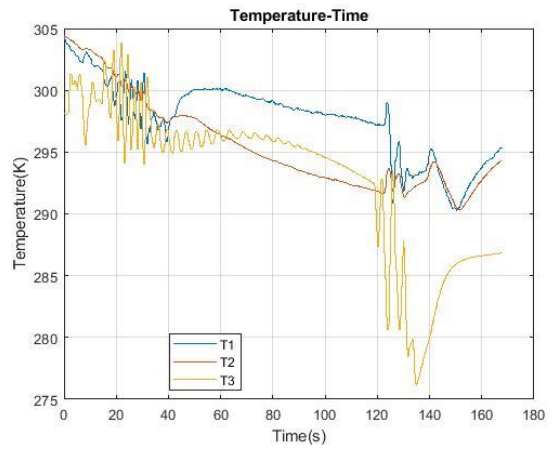


Test Chamber Pressure

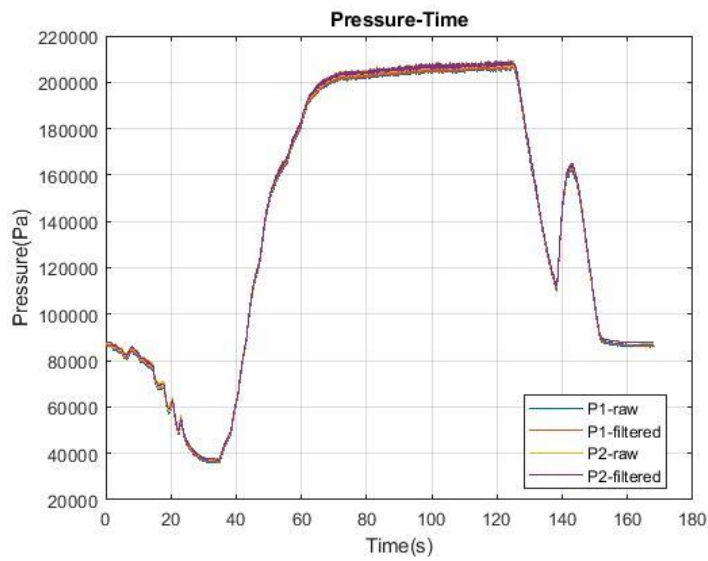
Figure 4-18. Test-18: [Mach 2.5 - 1300 g/s - 0% Blockage].



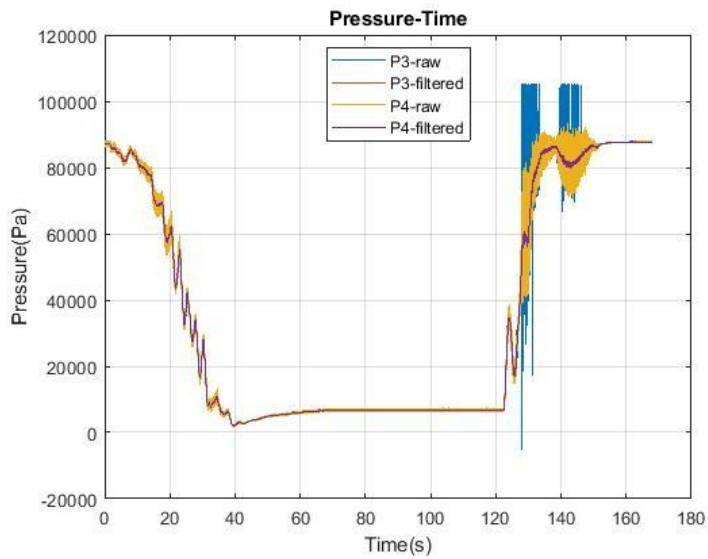
Free-Jet Nozzle Air Mass Flow Rate



Test Chamber and Ejector Nozzle Feed Manifold Connection Temperature

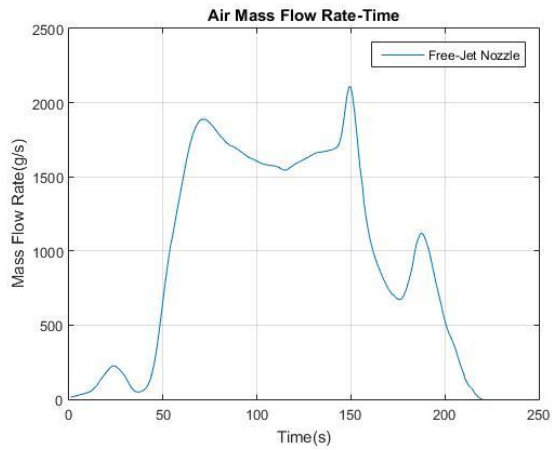


Free-Jet Nozzle Inlet Pressure

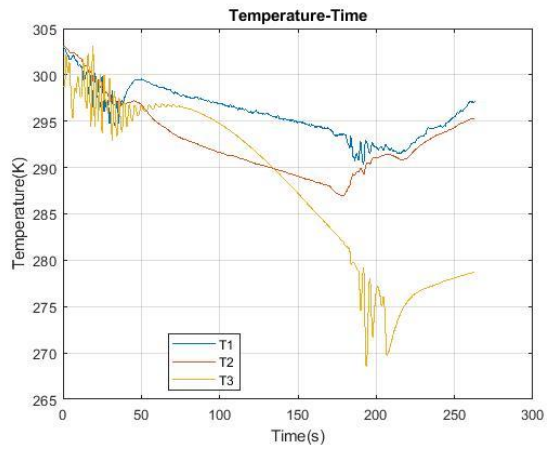


Test Chamber Pressure

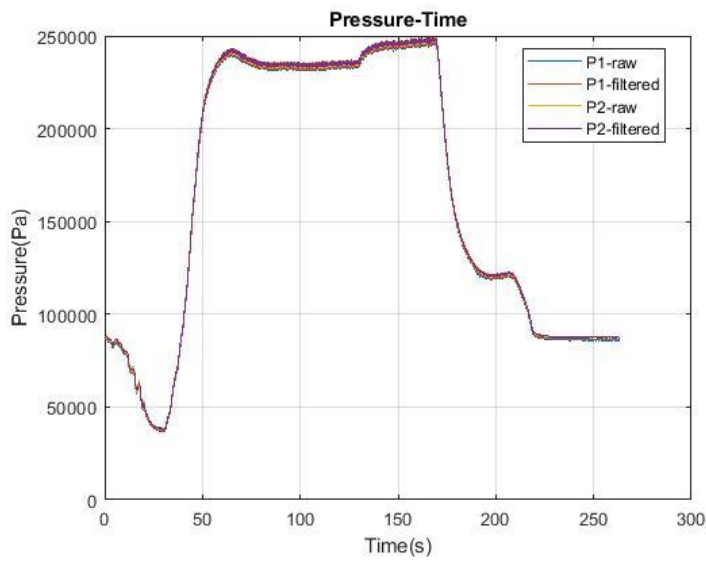
Figure 4-19. Test-19: [Mach 2.5 - 1500 g/s - 0% Blockage].



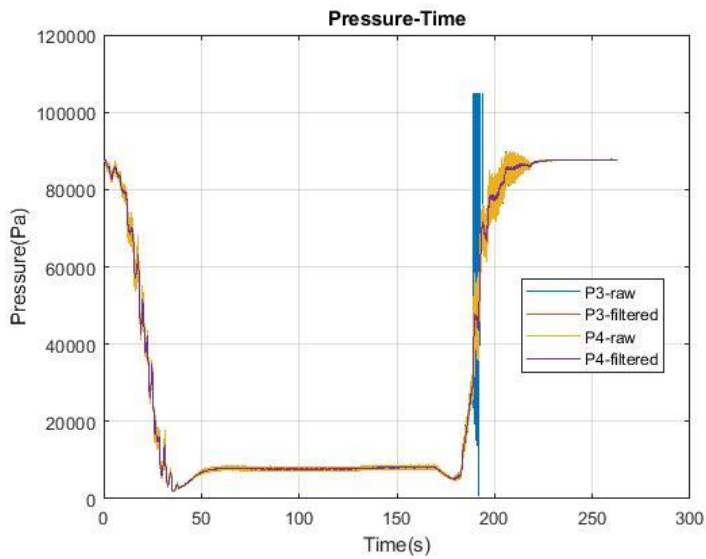
Free-Jet Nozzle Air Mass Flow Rate



Test Chamber and Ejector Nozzle Feed
Manifold Connection Temperature

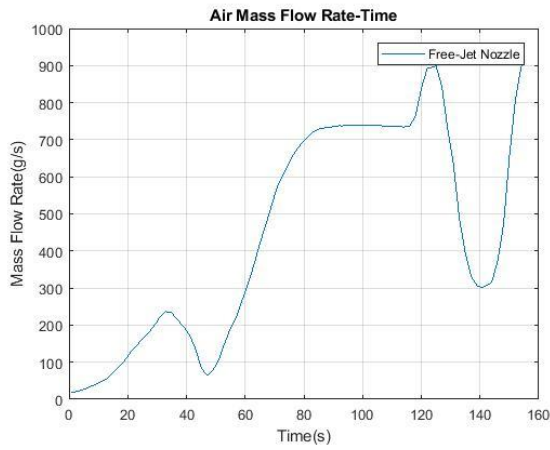


Free-Jet Nozzle Inlet Pressure

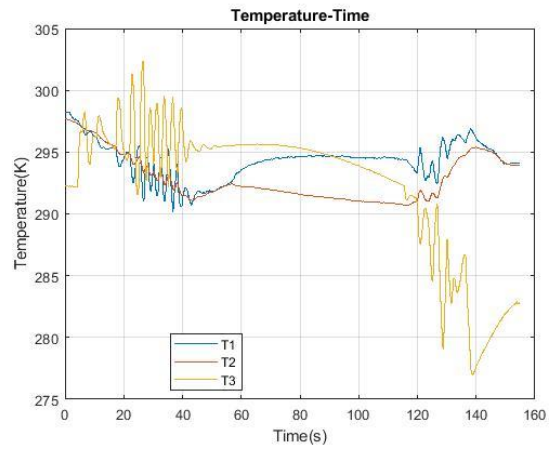


Test Chamber Pressure

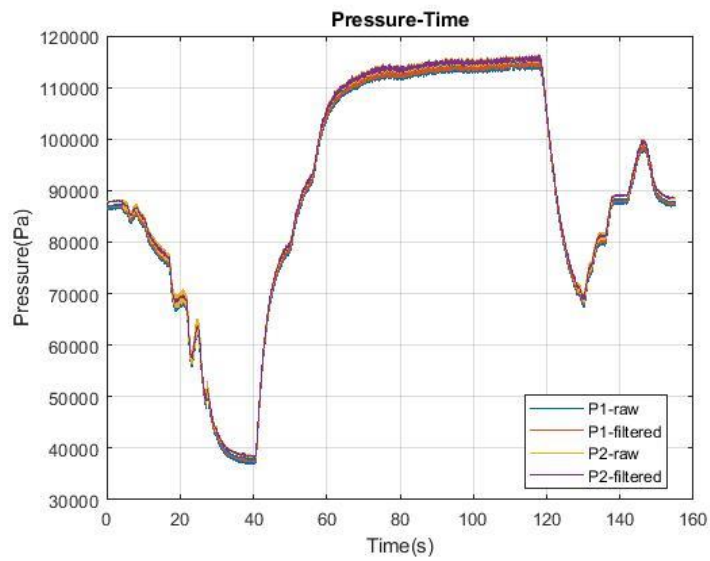
Figure 4-20. Test-20: [Mach 2.5 - 1900 g/s - 0% Blockage].



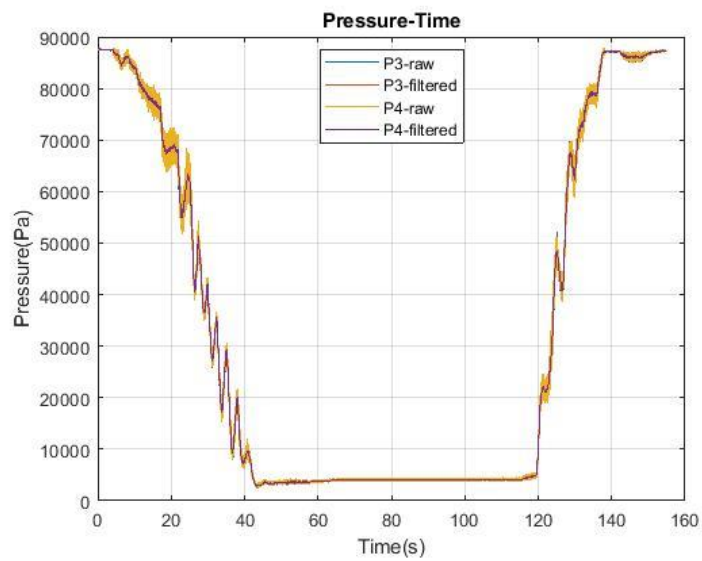
Free-Jet Nozzle Air Mass Flow Rate



Test Chamber and Ejector Nozzle Feed Manifold Connection Temperature

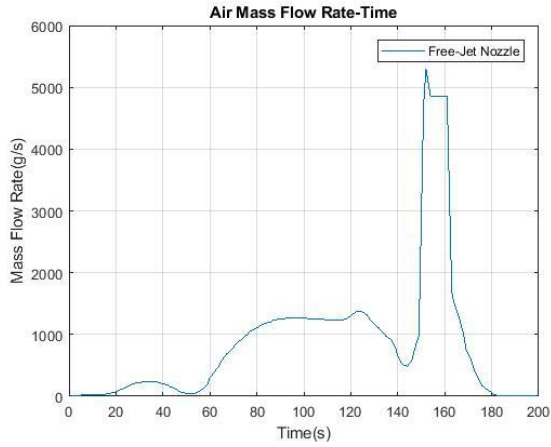


Free-Jet Nozzle Inlet Pressure

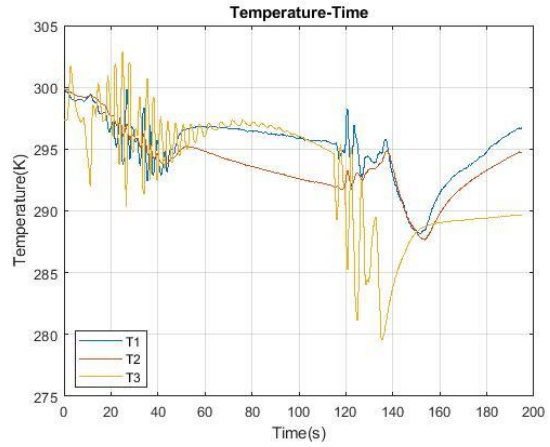


Test Chamber Pressure

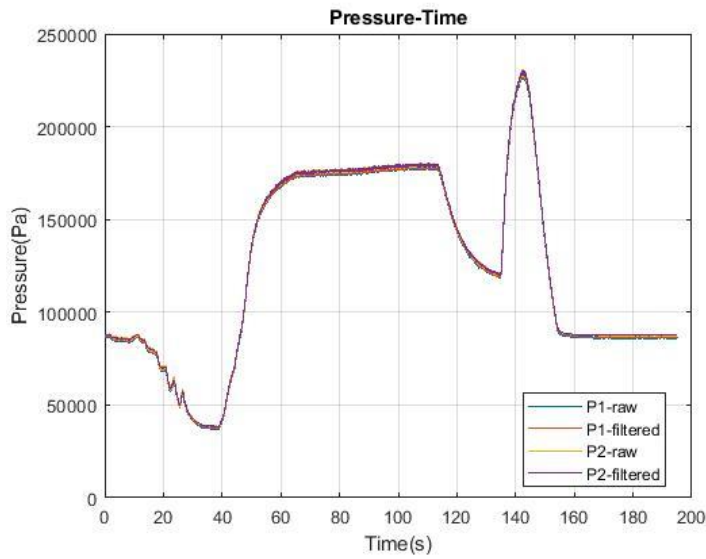
Figure 4-21. Test-21: [Mach 2.5 - 750 g/s - 8% Blockage].



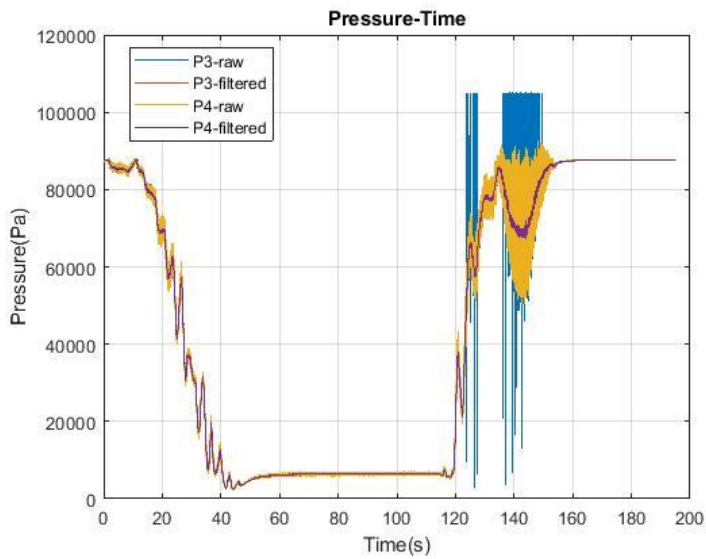
Free-Jet Nozzle Air Mass Flow Rate



Test Chamber and Ejector Nozzle Feed Manifold Connection Temperature

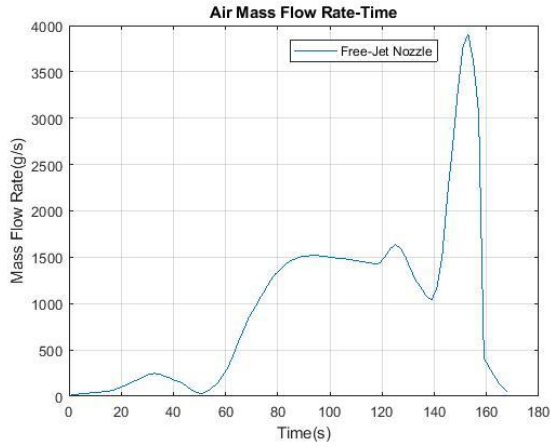


Free-Jet Nozzle Inlet Pressure

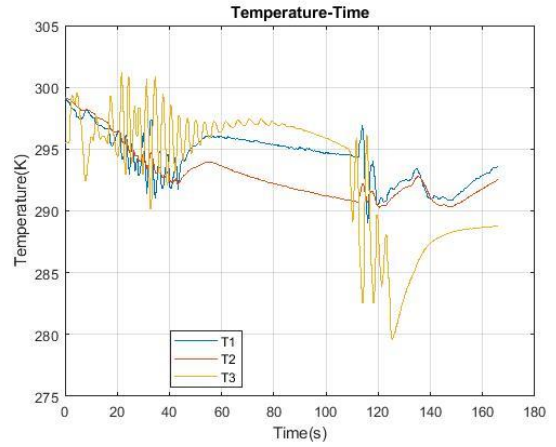


Test Chamber Pressure

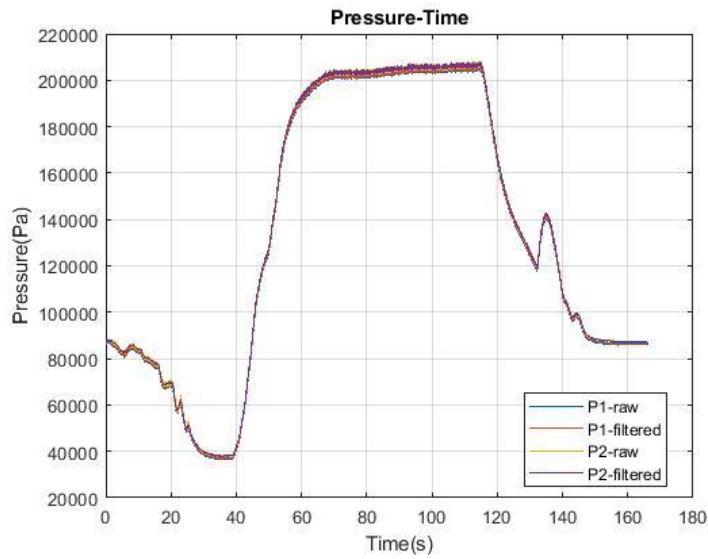
Figure 4-22. Test-22: [Mach 2.5 - 1300 g/s - 8% Blockage].



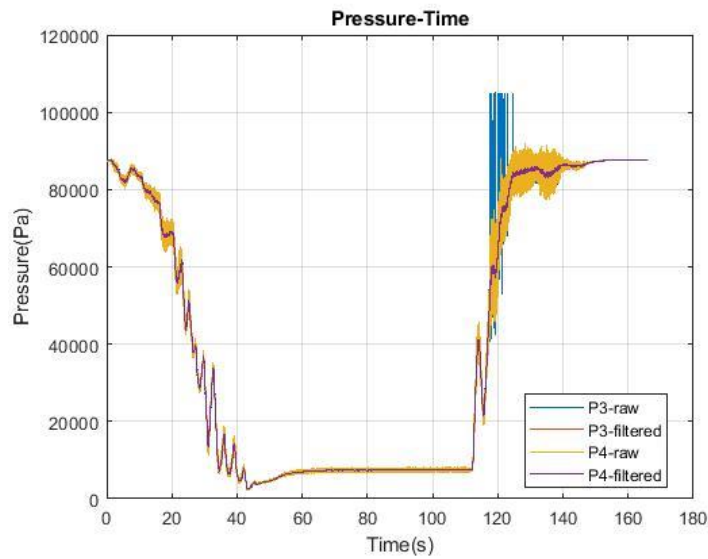
Free-Jet Nozzle Air Mass Flow Rate



Test Chamber and Ejector Nozzle Feed Manifold Connection Temperature

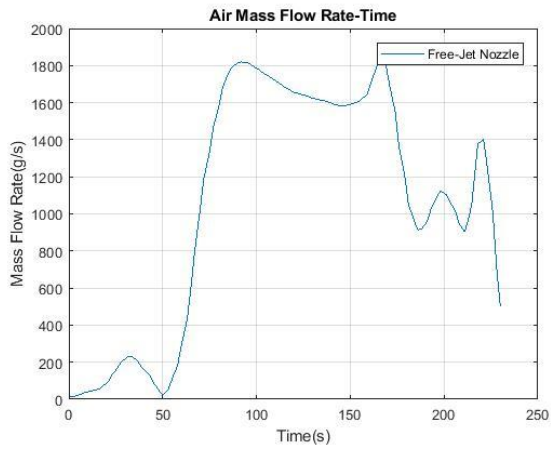


Free-Jet Nozzle Inlet Pressure

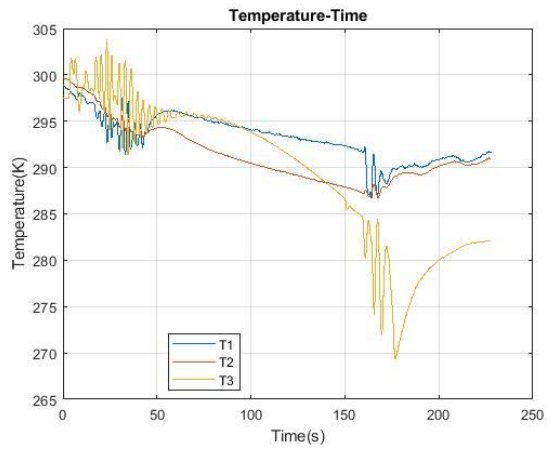


Test Chamber Pressure

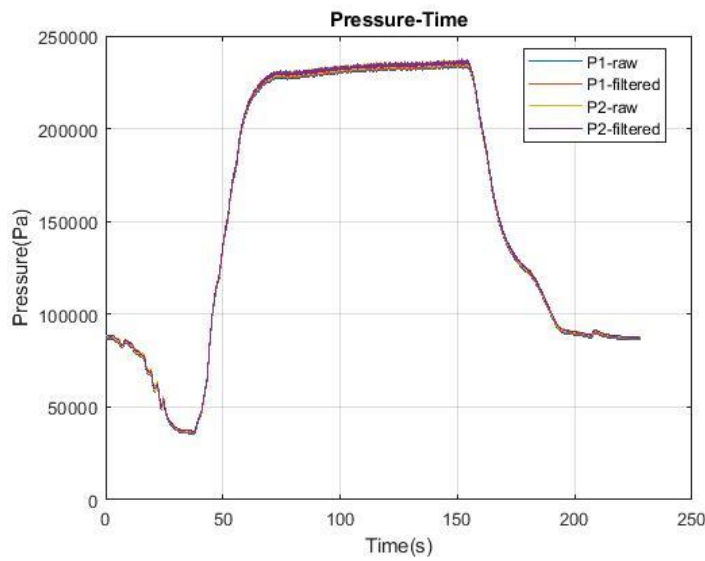
Figure 4-23. Test-23: [Mach 2.5 - 1500 g/s - 8% Blockage].



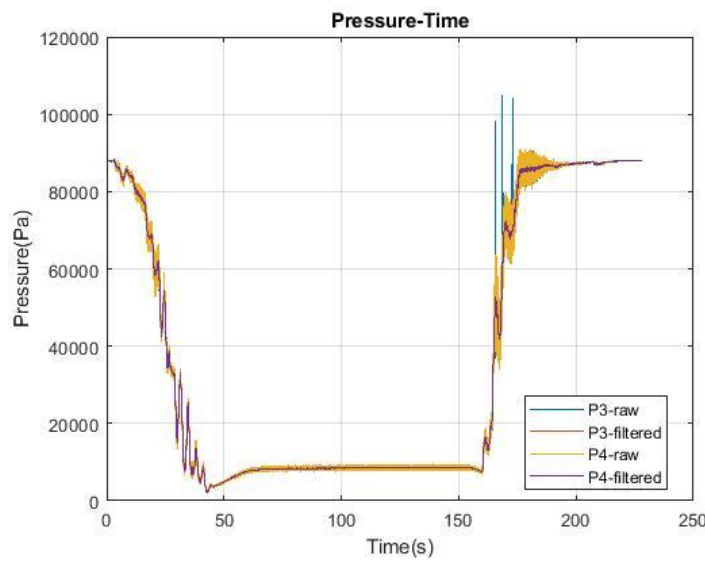
Free-Jet Nozzle Air Mass Flow Rate



Test Chamber and Ejector Nozzle Feed Manifold Connection Temperature

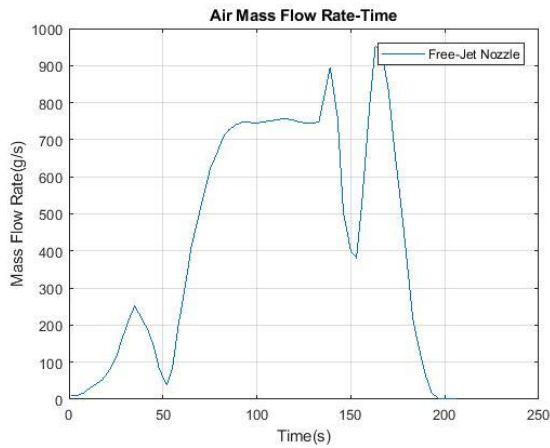


Free-Jet Nozzle Inlet Pressure

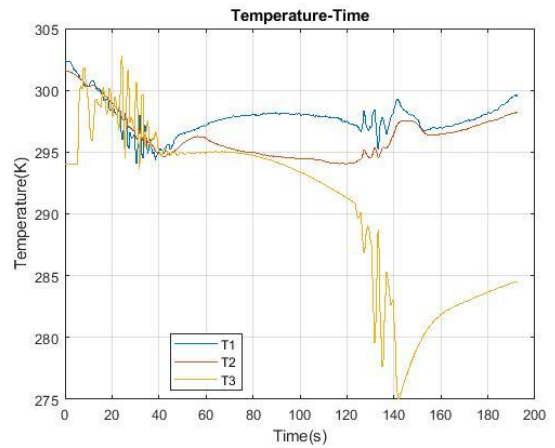


Test Chamber Pressure

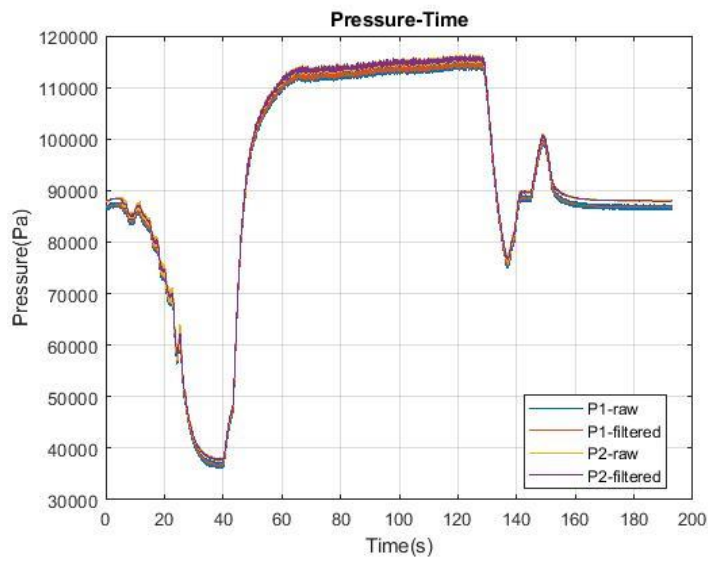
Figure 4-24. Test-24: [Mach 2.5 - 1900 g/s - 8% Blockage].



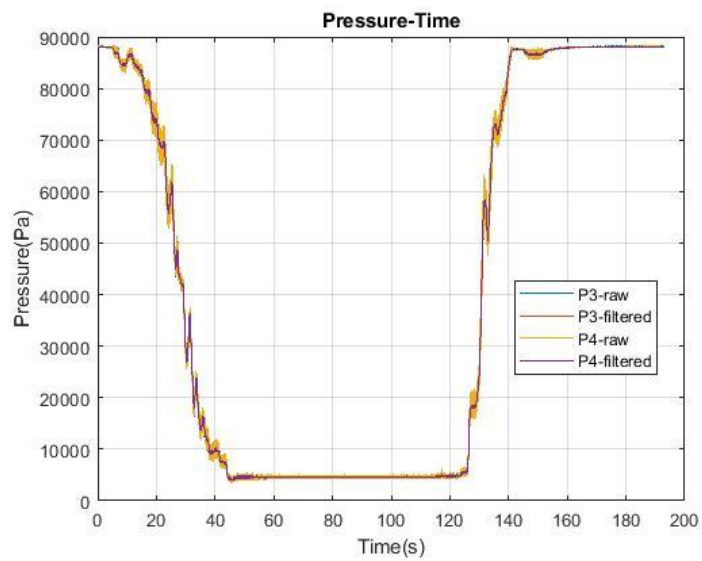
Free-Jet Nozzle Air Mass Flow Rate



Test Chamber and Ejector Nozzle Feed Manifold Connection Temperature

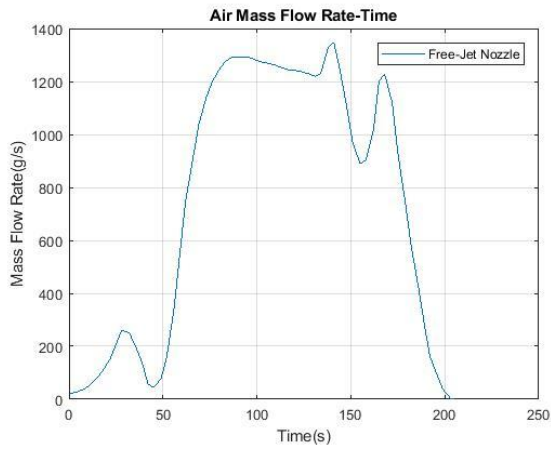


Free-Jet Nozzle Inlet Pressure

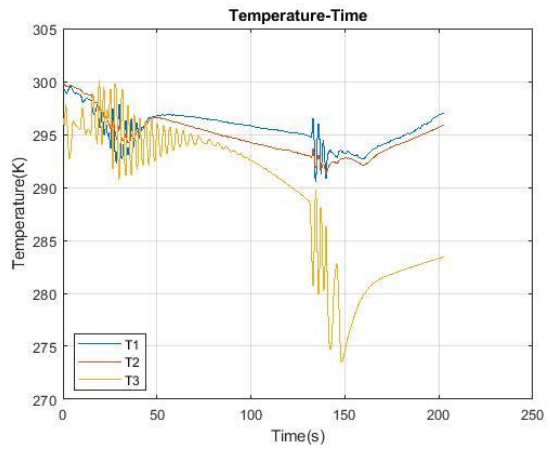


Test Chamber Pressure

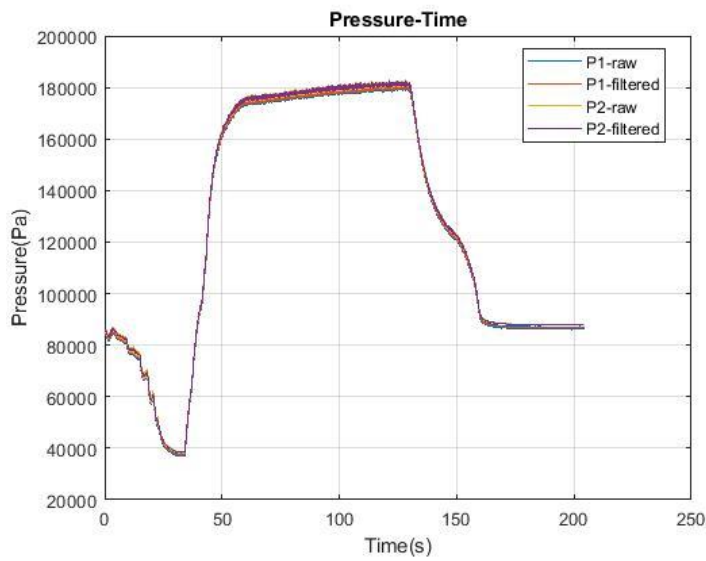
Figure 4-25. Test-25: [Mach 2.5 - 750 g/s - 15% Blockage].



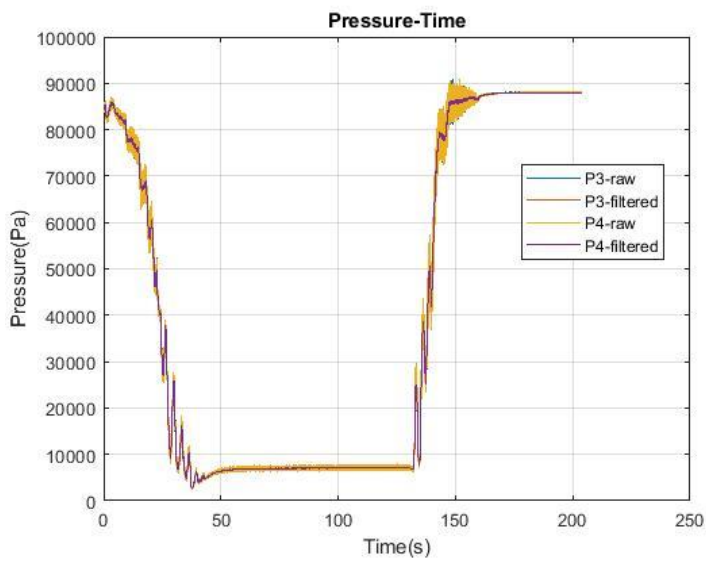
Free-Jet Nozzle Air Mass Flow Rate



Test Chamber and Ejector Nozzle Feed Manifold Connection Temperature

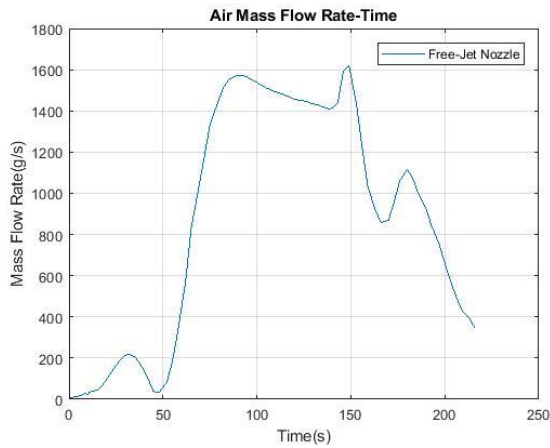


Free-Jet Nozzle Inlet Pressure

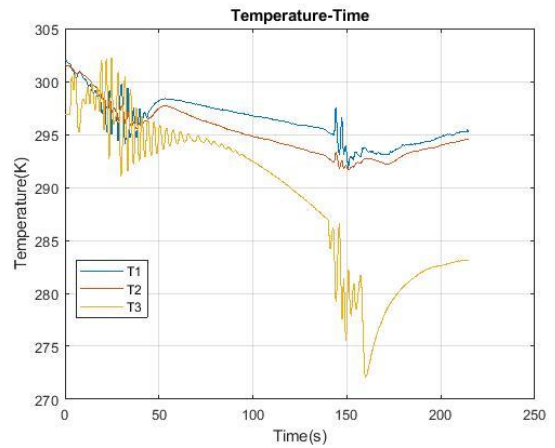


Test Chamber Pressure

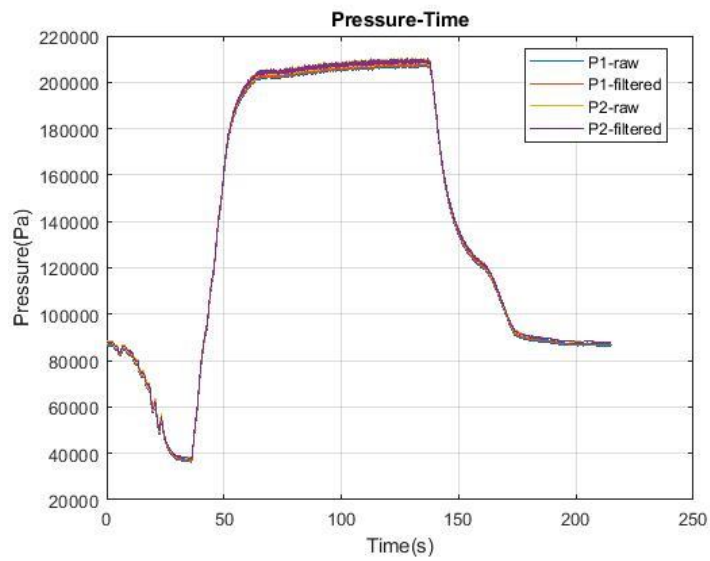
Figure 4-26. Test-26: [Mach 2.5 - 1300 g/s - 15% Blockage].



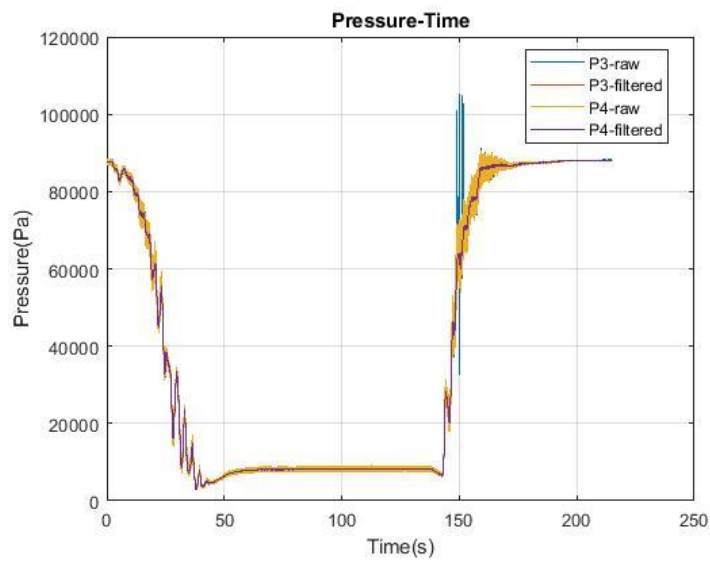
Free-Jet Nozzle Air Mass Flow Rate



Test Chamber and Ejector Nozzle Feed Manifold Connection Temperature

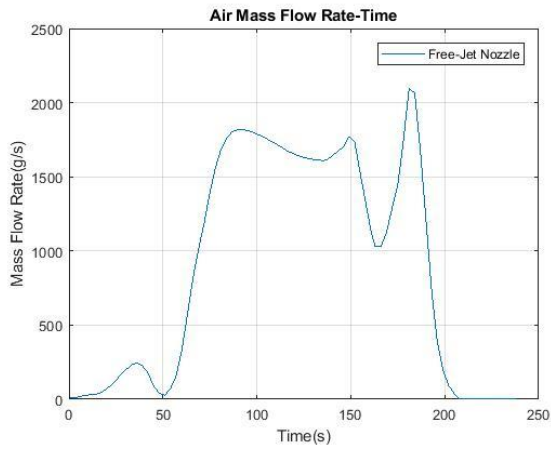


Free-Jet Nozzle Inlet Pressure

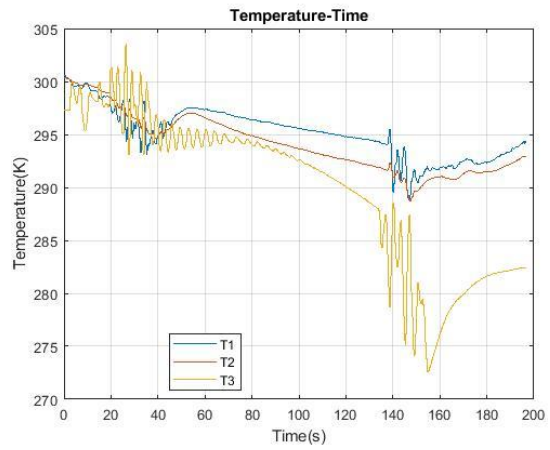


Test Chamber Pressure

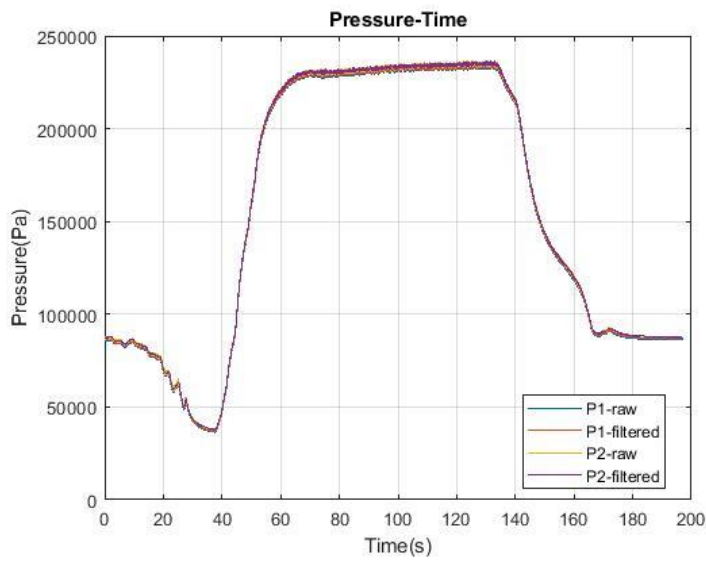
Figure 4-27. Test-27: [Mach 2.5 - 1500 g/s - 15% Blockage].



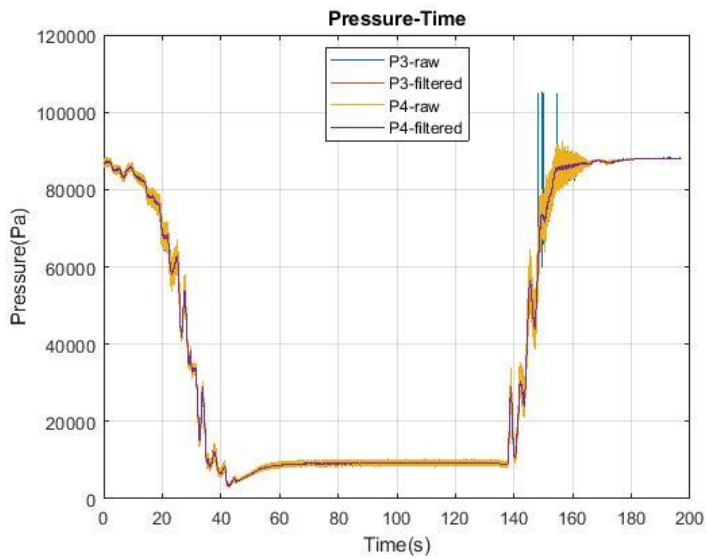
Free-Jet Nozzle Air Mass Flow Rate



Test Chamber and Ejector Nozzle Feed Manifold Connection Temperature

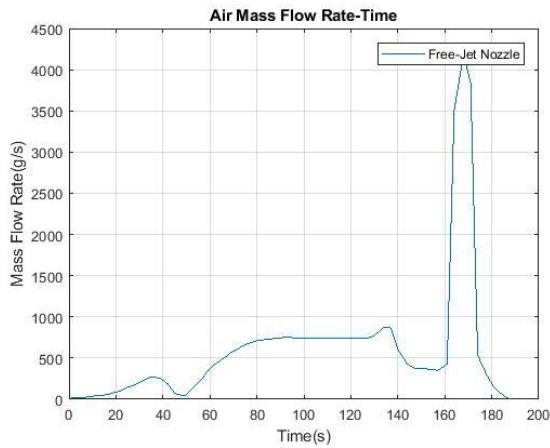


Free-Jet Nozzle Inlet Pressure

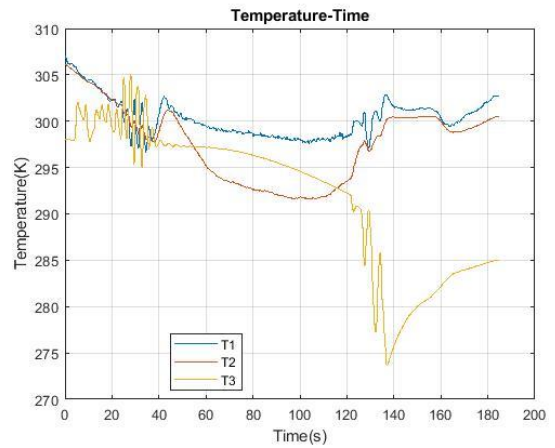


Test Chamber Pressure

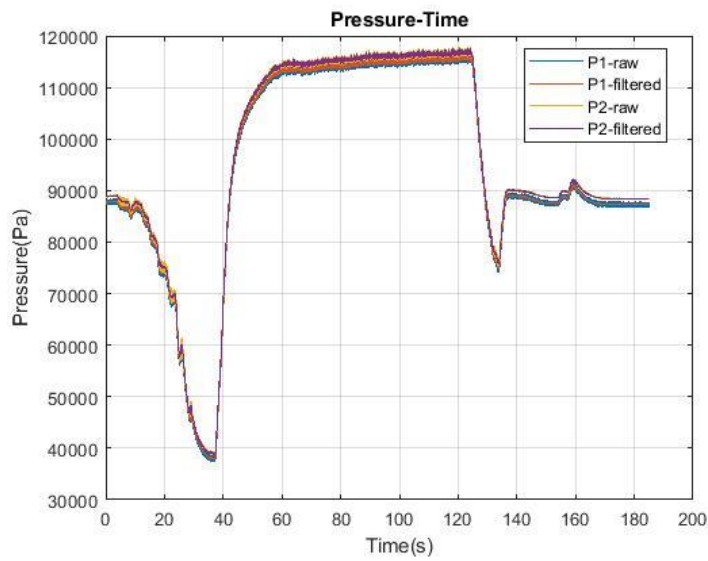
Figure 4-28. Test-28: [Mach 2.5 - 1900 g/s - 15% Blockage].



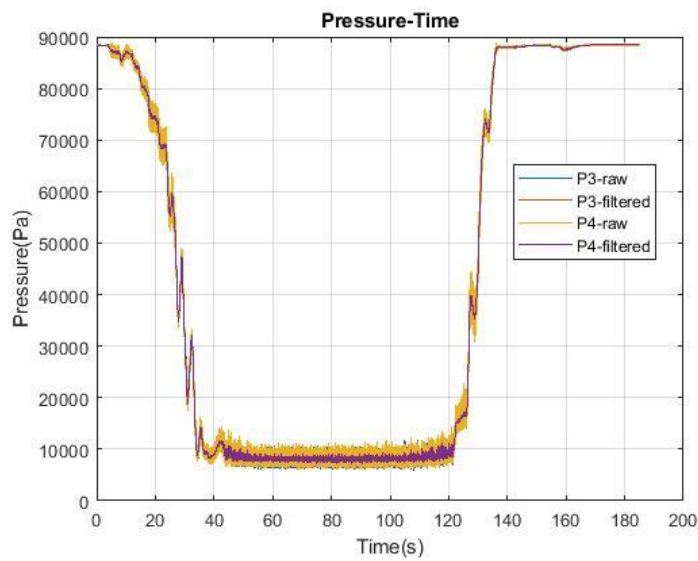
Free-Jet Nozzle Air Mass Flow Rate



Test Chamber and Ejector Nozzle Feed Manifold Connection Temperature

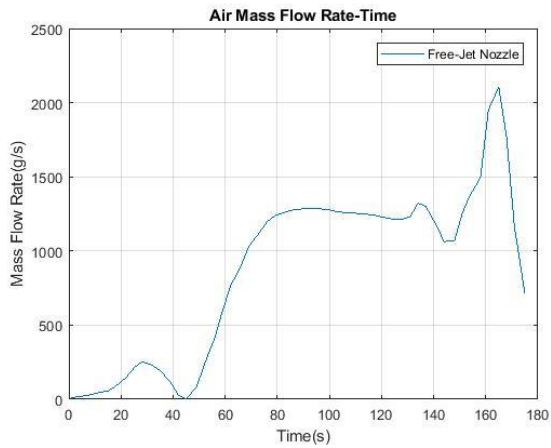


Free-Jet Nozzle Inlet Pressure

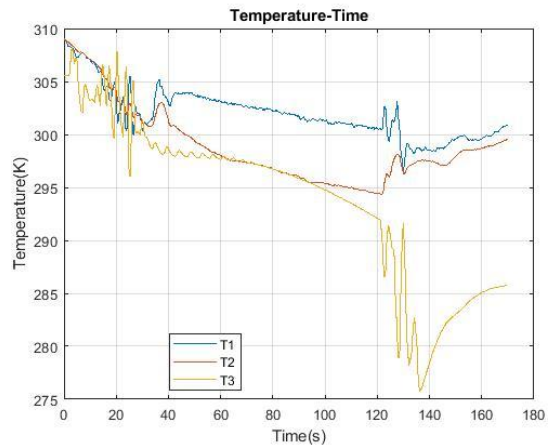


Test Chamber Pressure

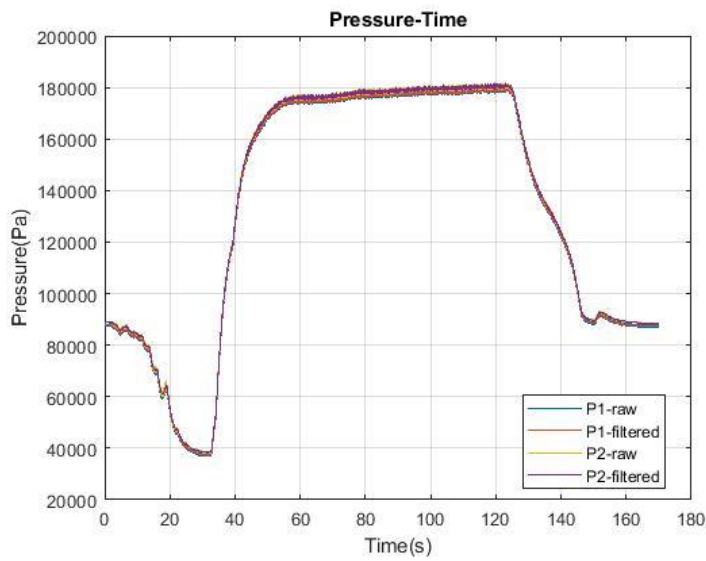
Figure 4-29. Test-29: [Mach 2.5 - 750 g/s - 25% Blockage].



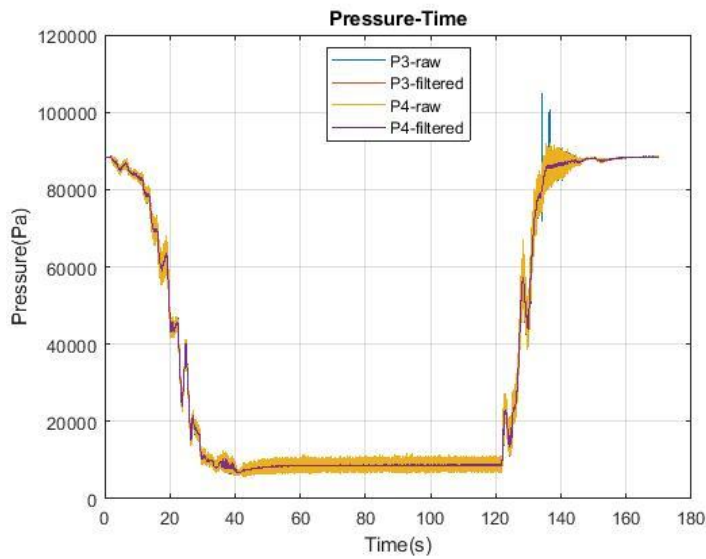
Free-Jet Nozzle Air Mass Flow Rate



Test Chamber and Ejector Nozzle Feed Manifold Connection Temperature

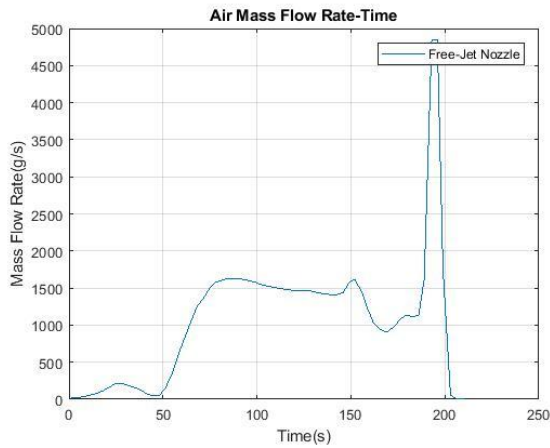


Free-Jet Nozzle Inlet Pressure

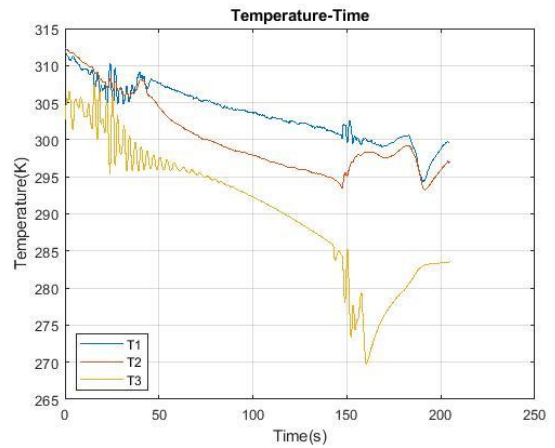


Test Chamber Pressure

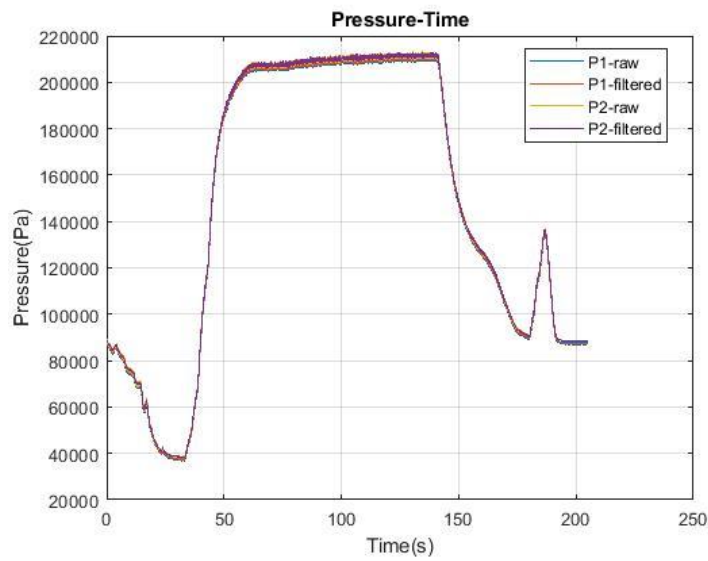
Figure 4-30. Test-30: [Mach 2.5 - 1300 g/s - 25% Blockage].



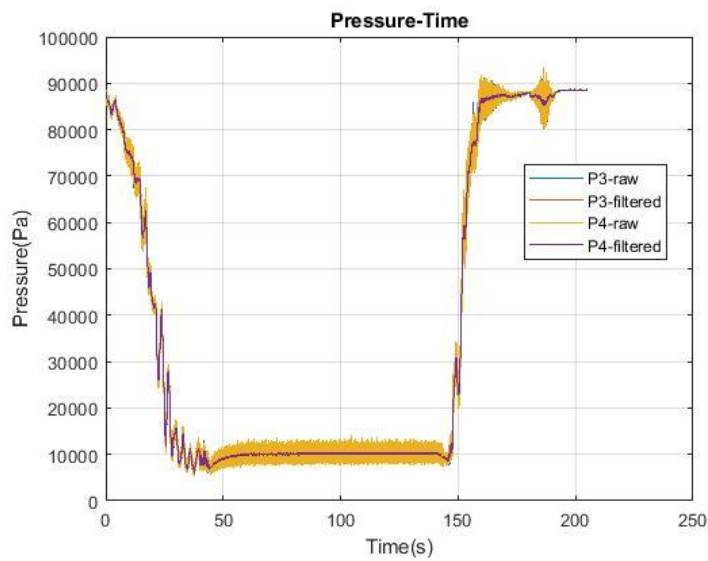
Free-Jet Nozzle Air Mass Flow Rate



Test Chamber and Ejector Nozzle Feed Manifold Connection Temperature

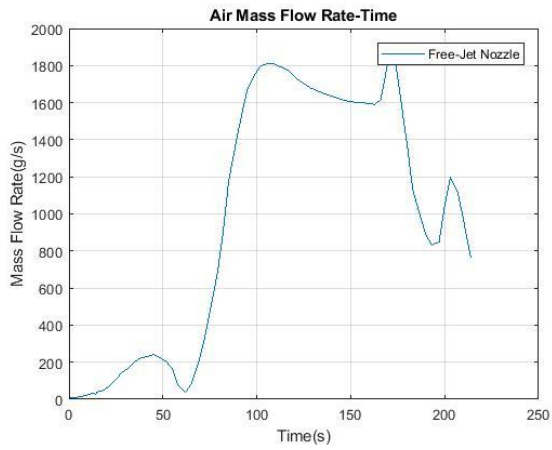


Free-Jet Nozzle Inlet Pressure

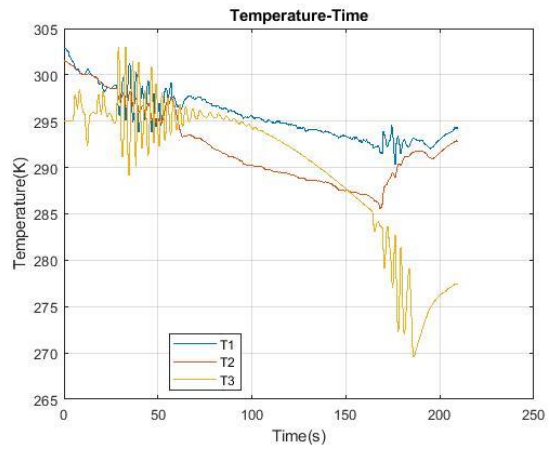


Test Chamber Pressure

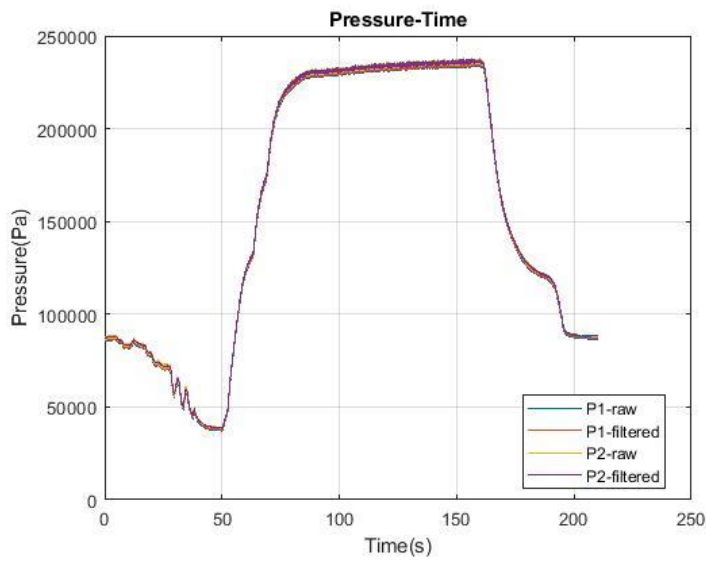
Figure 4-31. Test-31: [Mach 2.5 - 1500 g/s - 25% Blockage].



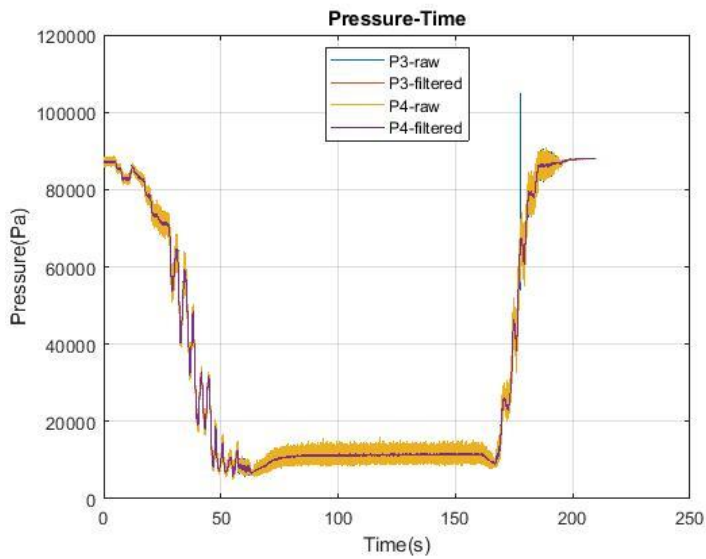
Free-Jet Nozzle Air Mass Flow Rate



Test Chamber and Ejector Nozzle Feed Manifold Connection Temperature



Free-Jet Nozzle Inlet Pressure



Test Chamber Pressure

Figure 4-32. Test-32: [Mach 2.5 - 1900 g/s - 25% Blockage].

